



Terms and Conditions of Use of Digitised Theses from Trinity College Library Dublin

Copyright statement

All material supplied by Trinity College Library is protected by copyright (under the Copyright and Related Rights Act, 2000 as amended) and other relevant Intellectual Property Rights. By accessing and using a Digitised Thesis from Trinity College Library you acknowledge that all Intellectual Property Rights in any Works supplied are the sole and exclusive property of the copyright and/or other IPR holder. Specific copyright holders may not be explicitly identified. Use of materials from other sources within a thesis should not be construed as a claim over them.

A non-exclusive, non-transferable licence is hereby granted to those using or reproducing, in whole or in part, the material for valid purposes, providing the copyright owners are acknowledged using the normal conventions. Where specific permission to use material is required, this is identified and such permission must be sought from the copyright holder or agency cited.

Liability statement

By using a Digitised Thesis, I accept that Trinity College Dublin bears no legal responsibility for the accuracy, legality or comprehensiveness of materials contained within the thesis, and that Trinity College Dublin accepts no liability for indirect, consequential, or incidental, damages or losses arising from use of the thesis for whatever reason. Information located in a thesis may be subject to specific use constraints, details of which may not be explicitly described. It is the responsibility of potential and actual users to be aware of such constraints and to abide by them. By making use of material from a digitised thesis, you accept these copyright and disclaimer provisions. Where it is brought to the attention of Trinity College Library that there may be a breach of copyright or other restraint, it is the policy to withdraw or take down access to a thesis while the issue is being resolved.

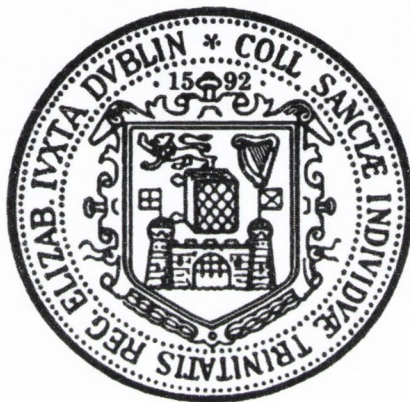
Access Agreement

By using a Digitised Thesis from Trinity College Library you are bound by the following Terms & Conditions. Please read them carefully.

I have read and I understand the following statement: All material supplied via a Digitised Thesis from Trinity College Library is protected by copyright and other intellectual property rights, and duplication or sale of all or part of any of a thesis is not permitted, except that material may be duplicated by you for your research use or for educational purposes in electronic or print form providing the copyright owners are acknowledged using the normal conventions. You must obtain permission for any other use. Electronic or print copies may not be offered, whether for sale or otherwise to anyone. This copy has been supplied on the understanding that it is copyright material and that no quotation from the thesis may be published without proper acknowledgement.

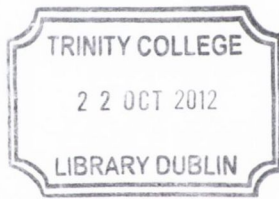
**MRI as an analytical tool in
three models of neuroinflammation**

Ronan J. Kelly



A thesis submitted to
Trinity College Dublin
for the degree of
Doctor of Philosophy

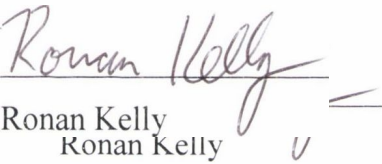
Supervisor: Professor Marina A. Lynch
Department of Physiology
Trinity College Dublin
2012



Thesis 9777

I. Declaration of Authorship

I declare that this thesis has not been submitted as an exercise for a degree at this or any other university. It is entirely my own work, with the following exceptions: certain results were kindly donated by Tara Browne. I agree to deposit this thesis in the University's open access institutional repository or allow Trinity College Library to do so on my behalf.


Ronan Kelly
Ronan Kelly

II. Acknowledgements

Firstly, I'd like to thank my supervisor, Professor Marina Lynch for her unwavering support, advice, patience and humour throughout the last three years. The motivation and encouragement she imparted to me are just immeasurable. She instilled in me the drive and belief that was required to carry out this project and this is greatly appreciated.

I'd like to thank everyone in MAL lab, both present and past, for their help and support throughout my project. These include, in no particular order; Aedín, Anto, Downer, Thelma, Derek, Niamh, Anne-Marie, Rodrigo, Dónal, Belinda, Steph, Raasay, Tara, James and Roisín. Special thanks much be extended to Belinda for helping me out right at the beginning when I needed it most. The expertise she provided and the time she invested in me went far beyond the call of asking, and this is enormously appreciated. I'd also like to thank Dr. Aedín Minogue for her support and advice over my three years, and whose head I nearly wrecked asking for help all the time. She was never too busy to help me out, and was a great source of advice and support throughout my three years.

I would like to thank the staff of the Department of Physiology; in particular Lesley Penney and Ann Connick, as well as my funding providers Science Foundation Ireland. I would like to acknowledge Rustam Rakhmatullin for his assistance with the MRI work, and Dr. Matthew Campbell for providing the siRNA compounds and for being incredibly helpful throughout the BBB project. Thanks to Christoph for his invaluable assistance and guidance throughout the scanning sessions too. Special mention must also be given to Joe and Mike for sharing their know-how and expertise all things MR-related during my pre-PhD days. And for those musical collaborations, we're sure to make it big one day.

A big shout-out to Dónal, Luke and Bursney whose company I couldn't have done without, whether it was our daily cups of tea, the thought-provoking chats, or our weekend retreats. Thanks to Ronan, Diarmuid, Ella, Dominic and Sophie for keeping me level-headed and relaxed when things got hectic and stressful, especially at the end. Thanks to Downer for the write-up pep talks, much appreciated.

It takes patience to put up with the everyday demands of lab work and thesis writing, so I have Nicola to thank for being an incredibly patient, reassuring and calming influence, and her usual amazing self.

Finally, I'd like to thank my parents and my sister Catherine for their constant encouragement and positive attitude, especially during this PhD when it mattered most. I've been very lucky to have you at the end of the phone whenever needed. This is dedicated to you.

III. Abstract

It is well established that inflammatory changes in the brain accompany the ageing process and neurodegenerative disorders. These changes are largely mediated by activation of microglial and astrocytic cells, which is characterized by an increase in cell surface markers and the release of pro-inflammatory cytokines. CD200 is a cell surface protein widely expressed on a variety of cells, including neurons, astrocytes and endothelial cells. However, expression of CD200 receptor is reserved for cells of the myeloid lineage, including microglia. Several studies have shown that ligation of the CD200R by its endogenous ligand helps preserve microglia in a quiescent state, and that microglia are restrained from tissue-damaging activation through CD200R signalling.

The development of MRI as a clinical tool has led to its ability to detect subtle changes in the tissue water environment under examination through assessment of T_1 and T_2 relaxation times. The presence of iron in activated microglial cells could render T_2 relaxometry a useful biomarker of microglial activation, while it has been previously shown that T_1 hyperintensities reflect acute astrocytosis.

The findings in this study suggest that CD200 has anti-inflammatory actions in the CNS, since age and LPS treatment induced exacerbated inflammation in CD200-deficient mice. The data reveal that the age-related increase in microglial activation is markedly enhanced in CD200-deficient mice. There was an age-related decrease in T_2 relaxometry in both WT and CD200-deficient mice; however, this decrease was not exacerbated in CD200^{-/-} mice. Treatment with LPS induced significantly greater microglial activation in CD200^{-/-}, compared with WT, mice. T_2 relaxometry did not show the predicted decrease following LPS treatment, indicating that the age-related decrease in T_2 may be reflective of the increase in overall iron accumulation, which was not correlated with the extent of activation of microglial cells. However, treatment with LPS induced increases in both astrocytosis and T_1 relaxometry, confirming the already established association between acute astrocytic activation and T_1 relaxation times.

Blood-brain barrier (BBB) permeability to the gadolinium-based contrast agent Magnevist was assessed using a novel tail-vein cannulation technique. The data reveal that BBB permeability was increased in LPS-treated WT and CD200^{-/-} mice. This was coupled with a decrease in occludin and claudins 5 and 12 messenger ribonucleic acid

(mRNA). Moreover, BBB permeability was also increased in control-treated CD200^{-/-}, compared with WT, mice. Follow-up analysis revealed decreases in claudin 5 and occludin mRNA expression in CD200^{-/-} mice, perhaps as a result of an increase in basal levels of pro-inflammatory cytokines which have been shown to disrupt expression of the tight junction proteins.

BBB disruption could also lead to the passage of amyloid-beta (A β) from areas of high concentration in the brain, to areas of lower concentration in the blood. However, the increase in BBB permeability induced by small interfering ribonucleic acid (siRNA) targeting suppression of claudin 5 and occludin was not sufficient to propagate a movement in soluble amyloid peptides down the concentration gradient in the APP/PS1 model of Alzheimer's disease (AD).

Overall, this study highlights the fact that MRI can be used in the assessment of astrocyte function and BBB integrity in several models of neuroinflammation.

IV. Table of Contents

I	Declaration of authorship	i
II	Acknowledgements	ii
III	Abstract	iv
IV	Contents Page	vi
V	List of Figures	xi
VI	List of Tables	xviii
VII	Abbreviations	xix

Chapter 1. Introduction

1.1 The Central Nervous System	1
<i>1.1.1 The brain</i>	1
<i>1.1.2 Ageing in the CNS</i>	2
<i>1.1.3 The membrane hypothesis</i>	3
<i>1.1.4 Free radical theory of ageing</i>	4
1.2 Barriers of the Brain	4
<i>1.2.1 Structure of the BBB</i>	5
<i>1.2.2 Tight junctions</i>	6
<i>1.2.3 Function of the BBB</i>	8
<i>1.2.5 Measuring and modulating BBB integrity</i>	9
1.3 The CNS defence system	10
<i>1.3.1 Microglial cells</i>	11
<i>1.3.2 Astrocytic cells</i>	12
<i>1.3.3 Cytokines in the CNS</i>	13
1.4 Pro-inflammatory cytokines	15

1.4.1	<i>Interleukin-1β</i>	15
1.4.2	<i>TNF-α</i>	16
1.4.3	<i>Interleukin-6</i>	17
1.5	Markers of glial activation	18
1.5.1	<i>CD11b</i>	18
1.5.2	<i>CD40</i>	19
1.5.3	<i>GFAP</i>	20
1.6	CD200	21
1.6.1	<i>Expression of CD200 and CD200 receptor</i>	21
1.6.2	<i>CD200 signalling</i>	22
1.6.3	<i>Function of CD200</i>	22
1.7	Alzheimer's Disease	24
1.7.1	<i>Neurofibrillary tangles</i>	25
1.7.2	<i>Amyloid precursor protein</i>	26
1.7.3	<i>Amyloid precursor protein processing</i>	26
1.7.4	<i>Senile plaques</i>	27
1.7.5	<i>Amyloid-beta</i>	27
1.7.6	<i>Non-transgenic models of AD</i>	29
1.7.7	<i>Transgenic mouse models of AD</i>	30
1.8	Magnetic Resonance Imaging	31
1.8.1	<i>Introduction</i>	31
1.8.2	<i>T₁ and T₂ relaxometry</i>	32
1.8.3	<i>Relaxometry and neuroinflammation</i>	33
1.8.4	<i>High-resolution anatomic imaging</i>	34
1.8.5	<i>Arterial spin labelling</i>	35
1.8.6	<i>Contrast-enhanced MRI</i>	36
1.9	Aims of study	36

Chapter 2. Materials and Methods

2.1 Magnetic resonance imaging	39
2.1.1 <i>Animal acclimatisation</i>	39
2.1.2 <i>Induction of anaesthesia</i>	39
2.1.3 <i>Tail vein cannulation</i>	40
2.1.4 <i>Data acquisition and scanner preparation</i>	41
2.1.5 <i>T₁-weighted imaging</i>	41
2.1.6 <i>T₂-weighted imaging</i>	42
2.1.7 <i>High-resolution anatomic imaging</i>	42
2.1.8 <i>Arterial spin labelling</i>	43
2.1.9 <i>Gadolinium-enhanced contrast imaging</i>	43
2.2 Data Analysis	45
2.2.1 <i>Relaxometry</i>	45
2.2.2 <i>Voxel-Based Morphometry</i>	45
2.2.3 <i>ASL image analysis</i>	46
2.2.4 <i>Contrast enhanced image analysis</i>	47
2.3 Animals	50
2.3.1 <i>Groups and maintenance of animals</i>	50
2.4 Animal experiments	51
2.4.1 <i>Analysis of the age-related changes in CD200^{-/-} mice</i>	51
2.4.2 <i>Analysis of the effects of LPS treatment in WT and CD200^{-/-} mice</i>	52
2.4.3 <i>Analysis of the effect of inducing BBB permeability in WT and APP/PS1 mice</i>	53
2.5 Preparation of tissue	53
2.5.1 <i>Dissections and preparation of tissue</i>	53
2.6 Analysis of mRNA by qPCR	54
2.6.1 <i>Preparation of tissue for mRNA isolation</i>	54

2.6.2 Protocol for RNA isolation	54
2.6.3 Reverse Transcriptase for complimentary DNA (cDNA) synthesis	55
2.6.4 cDNA amplification by Q-PCR	55
2.6.5 PCR Quantification	56
2.7 Immunohistochemical analysis	58
2.7.1 Preparation of slides	58
2.7.2 Preparation of slices and slicing	58
2.7.3 Immunohistochemical analysis of CD11b	58
2.7.4 Immunohistochemical analysis of GFAP	59
2.7.5 Quantification of DAB-enhanced staining	60
2.7.6 Immunohistochemical staining of A β by Congo red	60
2.7.7 Quantification of A β plaques	61
2.7.8 Extraction of soluble and insoluble A β from brain tissue	61
2.7.9 Detection of soluble and insoluble A β concentrations in cortical tissue by multi-spot ELISA	62
2.7.10 Detection of A β concentrations in serum samples by multi-spot ELISA	62
2.8 Statistical Analysis	63
<u>Chapter 3. Analysis of the age-related changes in CD200^{-/-} mice</u>	64
3.1 Introduction	64
3.2 Methods	66
3.3 Results	67
3.4 Discussion	99

<u>Chapter 4. Analysis of the effects of LPS treatment in WT and CD200^{-/-} mice</u>	107
4.1 Introduction	107
4.2 Methods	108
4.3 Results	110
4.4 Discussion	166
<u>Chapter 5. Analysis of the effect of inducing BBB permeability in WT and APP/PS1 mice</u>	175
5.1 Introduction	175
5.2 Methods	176
5.3 Results	178
5.4 Discussion	227
<u>Chapter 6. General Discussion</u>	238
<u>References</u>	246
Appendix I: Animal Weights	302
Appendix II: Mean Data	303
Appendix III: Mean Data	305
Appendix IV: Company Addresses	307

V. List of Figures

- Figure 1.1** Schematic of MR signal generation
- Figure 2.1** Sample T_1 - (A) and T_2 - (B) weighted images from an APP/PS1 transgenic mouse, approximately 2.54mm posterior to Bregma.
- Figure 2.2** Pipeline of VBM methodology, indicating the brain extraction and spatial registration steps
- Figure 2.3** Sample data set displaying pre- and post-contrast images following injection of the gadolinium-based contrast agent, Magnevist
- Figure 3.1** Animal weights at experimental timepoints.
- Figure 3.2** T_1 relaxation times in the cortex of WT and CD200^{-/-} mice.
- Figure 3.3** T_1 relaxation times in the hippocampus of WT and CD200^{-/-} mice.
- Figure 3.4** T_1 relaxation times in the corpus callosum of WT and CD200^{-/-} mice.
- Figure 3.5** T_1 relaxation times in the thalamus of WT and CD200^{-/-} mice.
- Figure 3.6** T_1 relaxation times in a representative WT and CD200^{-/-} mouse at 4 months.
- Figure 3.7** T_2 relaxation times in the cortex of WT and CD200^{-/-} mice.
- Figure 3.8** T_2 relaxation times in the motor cortex of WT and CD200^{-/-} mice.
- Figure 3.9** T_2 relaxation times in the entorhinal cortex of WT and CD200^{-/-} mice.
- Figure 3.10** T_2 relaxation times in the hippocampus of WT and CD200^{-/-} mice.
- Figure 3.11** T_2 relaxation times in the corpus callosum of WT and CD200^{-/-} mice.
- Figure 3.12** T_2 relaxation times in the thalamus of WT and CD200^{-/-} mice.
- Figure 3.13** Representative coronal images displaying T_2 relaxation times in CD200^{-/-} mice with associated colour reference bar.
- Figure 3.14** GFAP immunoreactivity in cortical sections prepared from WT and CD200^{-/-} mice at 4, 13 and 17 months.

- Figure 3.15** GFAP immunoreactivity in hippocampal sections prepared from WT and CD200^{-/-} mice at 4, 13 and 17 months.
- Figure 3.16** CD11b immunoreactivity in cortical sections prepared from WT and CD200^{-/-} mice at 4, 13 and 17 months.
- Figure 3.17** CD11b immunoreactivity in hippocampal sections prepared from WT and CD200^{-/-} mice at 4, 13 and 17 months.
- Figure 3.18** Significant volumetric decreases in CD200^{-/-} mice at 9 months.
- Figure 3.19** Significant volumetric increases in CD200^{-/-} mice at 13 months.
- Figure 3.20** Significant volumetric decreases in CD200^{-/-} mice at 17 months.
- Figure 3.21** Cortical MTT and CTT values in WT and CD200^{-/-} mice at 4, 9, 13 and 17 months.
- Figure 3.22** Hippocampal MTT and CTT values in WT and CD200^{-/-} mice at 4, 9, 13 and 17 months.
- Figure 3.23** Whole brain MTT and CTT values in WT and CD200^{-/-} mice at 4, 9, 13 and 17 months.
- Figure 4.1** The effect of LPS on cortical CD40 mRNA expression in WT and CD200^{-/-} mice.
- Figure 4.2** The effect of LPS on hippocampal CD40 mRNA expression in WT and CD200^{-/-} mice.
- Figure 4.3** The effect of LPS on cortical CD11b mRNA expression in WT and CD200^{-/-} mice.
- Figure 4.4** The effect of LPS on hippocampal CD11b mRNA expression in WT and CD200^{-/-} mice.
- Figure 4.5** The effect of LPS on cortical CD11b expression in WT and CD200^{-/-} mice.
- Figure 4.6** The effect of LPS on hippocampal CD11b expression in WT and CD200^{-/-} mice.
- Figure 4.7** The effect of LPS on cortical IL-1 β mRNA expression in WT and CD200^{-/-} mice.
- Figure 4.8** The effect of LPS on hippocampal IL-1 β mRNA expression in WT and CD200^{-/-} mice.
- Figure 4.9** The effect of LPS on cortical TNF- α mRNA expression in WT and CD200^{-/-} mice.

- Figure 4.10** The effect of LPS on hippocampal TNF- α mRNA expression in WT and CD200^{-/-} mice.
- Figure 4.11** The effect of LPS on cortical IL-6 mRNA expression in WT and CD200^{-/-} mice.
- Figure 4.12** The effect of LPS on hippocampal IL-6 mRNA expression in WT and CD200^{-/-} mice.
- Figure 4.13** The effect of LPS on cortical GFAP mRNA expression in WT and CD200^{-/-} mice.
- Figure 4.14** The effect of LPS on hippocampal GFAP mRNA expression in WT and CD200^{-/-} mice.
- Figure 4.15** The effect of LPS on cortical GFAP expression in WT and CD200^{-/-} mice.
- Figure 4.16** The effect of LPS on hippocampal GFAP expression in WT and CD200^{-/-} mice.
- Figure 4.17** The effect of LPS on T₁ relaxation times in the whole cortex of WT and CD200^{-/-} mice at 3.5 hours.
- Figure 4.18** The effect of LPS on T₁ relaxation times in the motor cortex of WT and CD200^{-/-} mice at 3.5 hours.
- Figure 4.19** The effect of LPS on T₁ relaxation times in the entorhinal cortex of WT and CD200^{-/-} mice at 3.5 hours.
- Figure 4.20** The effect of LPS on hippocampal T₁ relaxation times of WT and CD200^{-/-} mice at 3.5 hours.
- Figure 4.21** The effect of LPS on T₁ relaxation times in the thalamus of WT and CD200^{-/-} mice at 3.5 hours.
- Figure 4.22** The effect of LPS on T₁ relaxation times in the corpus callosum of WT and CD200^{-/-} mice at 3.5 hours.
- Figure 4.23** The relationship between GFAP mRNA and T₁ relaxation times.
- Figure 4.24** The effect of LPS on T₂ relaxation times in the whole cortex of WT and CD200^{-/-} mice at 3.5 hours.
- Figure 4.25** The effect of LPS on T₂ relaxation times in the motor cortex of WT and CD200^{-/-} mice at 3.5 hours.
- Figure 4.26** The effect of LPS on T₂ relaxation times in the entorhinal cortex of WT and CD200^{-/-} mice at 3.5 hours.

- Figure 4.27** The effect of LPS on hippocampal T₂ relaxation times in WT and CD200^{-/-} mice at 3.5 hours.
- Figure 4.28** The effect of LPS on T₂ relaxation times in the thalamus of WT and CD200^{-/-} mice at 3.5 hours.
- Figure 4.29** The effect of LPS on T₂ relaxation times in the corpus callosum of WT and CD200^{-/-} mice at 3.5 hours.
- Figure 4.30** The effect of LPS on cortical claudin 5 mRNA expression in WT and CD200^{-/-} mice.
- Figure 4.31** The effect of LPS on hippocampal claudin 5 mRNA expression in WT and CD200^{-/-} mice.
- Figure 4.32** The effect of LPS on cortical occludin mRNA expression in WT and CD200^{-/-} mice.
- Figure 4.33** The effect of LPS on hippocampal occludin mRNA expression in WT and CD200^{-/-} mice.
- Figure 4.34** The effect of LPS on cortical claudin 12 mRNA expression in WT and CD200^{-/-} mice.
- Figure 4.35** The effect of LPS on hippocampal claudin 12 mRNA expression in WT and CD200^{-/-} mice.
- Figure 4.36** Representative contrast MRI data sets from control- and LPS-treated WT and CD200^{-/-} mice injected with gadolinium.
- Figure 4.37** Contrast-enhanced SI changes in the right motor cortex of control- and LPS-treated WT and CD200^{-/-} mice.
- Figure 4.38** Contrast-enhanced SI changes in the right somatosensory cortex of control- and LPS-treated WT and CD200^{-/-} mice.
- Figure 4.39** Contrast-enhanced SI changes in the right entorhinal cortex of control- and LPS-treated WT and CD200^{-/-} mice.
- Figure 4.40** Contrast-enhanced SI changes in the right dentate gyrus of control- and LPS-treated WT and CD200^{-/-} mice.
- Figure 4.41** Contrast-enhanced SI changes in right ventrolateral thalamus of control- and LPS-treated WT and CD200^{-/-} mice.
- Figure 4.42** Contrast-enhanced SI changes in the right frontal association cortex of control- and LPS-treated WT and CD200^{-/-} mice.

- Figure 4.43** Contrast-enhanced SI changes in the right lateral cerebellar nucleus of control- and LPS-treated WT and CD200^{-/-} mice.
- Figure 4.44** Relationship between SI values and claudins 5, 12 and occludin mRNA expression.
- Figure 5.1** Cortical CD11b mRNA expression in WT and APP/PS1 transgenic mice.
- Figure 5.2** CD11b immunoreactivity in cortical sections prepared from WT and APP/PS1 mice.
- Figure 5.3** CD11b immunoreactivity in hippocampal sections prepared from WT and APP/PS1 mice.
- Figure 5.4** Cortical CD40 mRNA expression in WT and APP/PS1 transgenic mice.
- Figure 5.5** Cortical GFAP mRNA expression in WT and APP/PS1 transgenic mice.
- Figure 5.6** GFAP immunoreactivity in cortical sections prepared from WT and APP/PS1 mice.
- Figure 5.7** GFAP immunoreactivity in hippocampal sections prepared from WT and APP/PS1 mice.
- Figure 5.8** Cortical IL-1 β mRNA expression in WT and APP/PS1 transgenic mice.
- Figure 5.9** Cortical TNF- α mRNA expression in WT and APP/PS1 transgenic mice.
- Figure 5.10** Cortical IL-6 mRNA expression in WT and APP/PS1 transgenic mice.
- Figure 5.11** T₂ relaxation times in the whole cortex of WT and APP/PS1 mice.
- Figure 5.12** T₂ relaxation times in the motor and entorhinal cortex of WT and APP/PS1 mice.
- Figure 5.13** T₂ relaxation times in the hippocampus of WT and APP/PS1 mice.
- Figure 5.14** T₂ relaxation times in the corpus callosum of WT and APP/PS1 mice.
- Figure 5.15** T₂ relaxation times in the thalamus of WT and APP/PS1 mice.

- Figure 5.16** T_1 relaxation times in the whole cortex of WT and APP/PS1 mice.
- Figure 5.17** T_1 relaxation times in the motor and entorhinal cortex of WT and APP/PS1 transgenic mice.
- Figure 5.18** T_1 relaxation times in the hippocampus of WT and APP/PS1 mice.
- Figure 5.19** T_1 relaxation times in the corpus callosum of WT and APP/PS1 transgenic mice.
- Figure 5.20** T_1 relaxation times in the thalamus of WT and APP/PS1 transgenic mice.
- Figure 5.21** The effect of genotype on VBM output
- Figure 5.22** The effect of siRNA treatment on cortical claudin 5 mRNA expression in WT and APP/PS1 transgenic mice.
- Figure 5.23** The effect of siRNA treatment on cortical occludin mRNA expression in WT and APP/PS1 transgenic mice.
- Figure 5.24** The effect of siRNA treatment on cortical claudin 12 mRNA expression in WT and APP/PS1 transgenic mice.
- Figure 5.25** Representative contrast MRI data sets from control- and siRNA-treated WT and APP/PS1 mice injected with gadolinium.
- Figure 5.26** Contrast-enhanced SI changes in the left motor cortex of control and siRNA-treated WT and APP/PS1 mice.
- Figure 5.27** Contrast-enhanced SI changes in the left somatosensory cortex of control and siRNA-treated WT and APP/PS1 mice.
- Figure 5.28** Contrast-enhanced SI changes in the left entorhinal cortex of control and siRNA-treated WT and APP/PS1 mice.
- Figure 5.29** Contrast-enhanced SI changes in the left dentate gyrus of control and siRNA-treated WT and APP/PS1 mice.
- Figure 5.30** Contrast-enhanced SI changes in the left ventrolateral thalamus of control- and siRNA-treated WT and APP/PS1 mice.
- Figure 5.31** Contrast-enhanced SI changes in the left cerebellar nucleus of control- and siRNA-treated WT and APP/PS1 mice.
- Figure 5.32** Contrast-enhanced SI changes in the left frontal association cortex of control- and siRNA-treated WT and APP/PS1 mice.

- Figure 5.33** Tight junction expression and contrast MRI SI levels.
- Figure 5.34** Congo Red staining confirms the presence of A β plaques in the brains of APP/PS1 mice.
- Figure 5.35** Plaque count in siRNA-treated APP/PS1 mice.
- Figure 5.36** Soluble and insoluble A β_{40} expression in control- and siRNA-treated WT and APP/PS1 mice.
- Figure 5.37** Soluble and insoluble A β_{42} expression in control- and siRNA-treated WT and APP/PS1 mice.
- Figure 5.38** A β_{40} and A β_{42} expression in blood serum of control- and siRNA-treated WT and APP/PS1 mice.

VI. List of Tables

Table 2.1	MR scanning protocols
Table 2.2	Mouse PCR primer assay numbers
Table 7.1	Average weights of WT and CD200 ^{-/-} mice throughout longitudinal study.
Table 7.2	Average WT and APP/PS1 weights in siRNA study.
Table 7.3	Average T ₁ relaxation times from control- and LPS-treated WT and CD200 ^{-/-} mice 2.5 hours after treatment.
Table 7.4	Average T ₁ relaxation times from control- and LPS-treated WT and CD200 ^{-/-} mice 3.5 hours after treatment.
Table 7.5	Average T ₂ relaxation times from control- and LPS-treated WT and CD200 ^{-/-} mice 2.5 hours after treatment.
Table 7.6	Average T ₂ relaxation times from control- and LPS-treated WT and CD200 ^{-/-} mice 3.5 hours after treatment.
Table 7.7	Average SI values post-gadolinium injection in control- and LPS-treated WT and CD200 ^{-/-} mice.
Table 7.8	Average SI values post-gadolinium injection in control- and siRNA-treated WT and APP/PS1 ^{-/-} mice.

VII. Abbreviations

The following abbreviations have been used in this report:

-/-	knock out
$\alpha_M\beta_2$	Alpha-M beta-2
A2	Secondary auditory cortex
A β	Amyloid-beta
AD	Alzheimer's disease
AMPA	α -amino-3-hydroxy-5-methyl-4 isoxazolepropionic acid receptor
ANOVA	Analysis of variance
APC	Antigen-presenting cell
APP	Amyloid precursor protein
ASL	Arterial spin labelling
BBB	Blood brain barrier
BSA	Bovine serum albumin
CA1	Cornu ammonis 1
C57BL/6	C57 Black 6
CD	Cluster of differentiation molecule
cDNA	Complimentary deoxyribonucleic acid
CIA	Collagen-induced arthritis
CNS	Central nervous system
CSF	Cerebrospinal fluid
CT	Computed tomography
CTT	Capillary transit time
Da	Dalton
dH ₂ O	Distilled water
DOK	Docking protein
EAE	Experimental autoimmune encephalomyelitis
EPA	Eicosapentaenoic acid

EAU	Experimental autoimmune uveoretinitis
FAD	Familial AD
FAST	FMRIB Automated segmentation tool
FLASH	Fast low angle shot
FLIRT	FMRIB linear image registration tool
FNIRT	FMRIB non-linear image registration tool
FSL	FMRIB software library
Gd-DTPA	Gadopentetate dimeglumine
GFAP	Glial fibrillary acidic protein
GLM	General linear model
HD	Huntington's disease
H ₂ O	Water
ICAM-1	Intercellular adhesion molecule-1
ICE	IL-1 β -converting enzyme
IFN	Interferon
IDL	Interactive data language
IgSf	Immunoglobulin superfamily
IL	Interleukin
IP	Intraperitoneal
ISA	Image sequence analysis
IV	Intravenous
JAK	Janus kinase
JNK	Jun N-terminal kinase
KO	Knock out
LBP	LPS binding protein
LPS	Lipopolysaccharide
LRP	Lipoprotein receptor-related protein
LTP	Long-term potentiation
M1	Primary motor cortex
M2	Secondary motor cortex
MCAO	Middle cerebral artery occlusion
MAPK	Mitogen-activated protein kinase
MHC II	Major histocompatibility complex class II

MIPAV	Medical Image process, analysis and visualization
MOG	Myelin oligodendrocyte glycoprotein
MRI	Magnetic resonance imaging
mRNA	Messenger ribonucleic acid
MS	Multiple sclerosis
Ms	milliseconds
MSME	Multi spin multi echo
MTT	Mean transit time
MyD88	Myeloid differentiation primary response gene (88)
MWM	Morris water maze
NaCl	Sodium chloride
NaOH	Sodium hydroxide
NF- κ B	nuclear factor kappa-light-chain-enhancer of activated B cells
NFT	Neurofibrillary tangle
NK	Natural killer
NO	Nitric oxide
OCT	Optimum cooling temperature
PAMPs	Pathogen-associated molecular patterns
PBS	Phosphate buffer saline
PCR	Polymerase chain reaction
PD	Parkinson's disease
PET	Positron emission tomography
PNS	Peripheral nervous system
PPAR γ	Perioxisome proliferator-activated receptor gamma
PS	Presenilin
qPCR	Quantitative polymerase chain reaction
RARE	Rapid acquisition with relaxation enhancement
RARE-VTR	RARE with variable repetition time
RasGap	Ras GTPase-activating protein
RF	Radio frequency
RNA	Ribonucleic acid

ROI	Region of interest
RQ	Relative quantities
RT	Room temperature
RT	Reverse transcriptase
S1	Primary somatosensory cortex
SEM	Standard error of the mean
siRNA	Small interfering ribonucleic acid
SI	Signal intensity
SPF	Specific pathogen free
SPM	Statistical parametric mapping
STAT	Signal transducers and activators of transcription
T ₁	Time 1
T ₂	Time 2
TBS	Tris-buffered saline
TE	Echo time
TEER	Transendothelial electrical resistance
TLE	Temporal lobe epilepsy
TLR	Toll-like receptor
TNF- α	Tumour necrosis factor- α
TR	Repetition time
USPIO	Ultra-small particles of iron oxide
V2	Secondary visual cortex
VBM	Voxel-based morphometry
WT	Wildtype

Chapter 1

Introduction

1.1 The Central Nervous System

The central nervous system (CNS) is derived from the walls of a fluid-filled tube that is formed at an early stage of embryonic development, the components of which are crucial for life and enable us to sense, move and think. Historically, even our ancestors appreciated that the brain was vital to life. As early as 7000 years ago, people were boring holes in each other's skulls, evidently not with the aim to kill, but to cure.

The CNS is predominantly composed of 2 two types of cells, neurons and neuroglial cells. It was Ramon y Cajal in the 19th century who proposed that neurons are distinct membrane-bound entities; that the neurites or projections of a neuron are not continuous with one another, and must communicate by contact, not continuity. While the neuroglia: neuron ratio varies in individual brain areas, the overall ratio in the human brain as a whole has been reported to be approximately 1:1 (Azevedo *et al.*, 2009). Neuroglia can be subdivided into macroglia (including astrocytes and oligodendrocytes) and microglia, the resident macrophages of the brain and spinal cord. While the function of neurons is information processing and communication through electrical pulses (Kennedy, 1989), the role of neuroglia was traditionally considered to be a supportive one, involved in maintaining homeostasis in the CNS.

1.1.1 The brain

The cerebral cortex is the key neural structure subserving higher brain function and intellect. It occupies approximately 70% of the brain mass and plays key roles in memory, language and consciousness. The cerebrum is noteworthy for its convoluted structure; the folded nature of the cerebral cortex into sulci and gyri means that up to two thirds of the human cortex is buried in folds (Bear *et al.*, 1996). By convention, the cerebral cortex is divided into lobes named after the bones of the skull that lie over them; the central sulcus divides the frontal lobe from the parietal lobe. The temporal lobe lies immediately ventral to the deep lateral fissure. The occipital lobe lies at the back of the cerebrum, bordering both parietal and temporal lobes. The neocortex, the outer layer of the cerebral hemispheres, is composed of six different layers. The outermost layer consists of grey matter and neuronal cell bodies, surrounding the deeper white matter of myelinated axons.

The hippocampus is a structure of the limbic system that was initially described by Aranzi (1587) who likened the curved formation to a seahorse. The hippocampal formation consists of the *cornu Ammonis* fields (CA1-CA4), the *area dentate* (dentate gyrus) and the subicular region. Like the cerebral cortex, it is a paired structure, with mirror-image halves in the medial temporal lobe of the two hemispheres. Historically, it was originally believed to be involved primarily in olfaction and follow-up studies revealed projections between the olfactory bulb and the CA1 field of the hippocampus (Biella & de Curtis, 2000).

However it is in the study of memory formation and consolidation that hippocampal function has received the most attention amongst researchers. The idea that the hippocampus is involved in memory is derived from a case study involving the patient H.M. (Milner *et al.*, 1968) who underwent surgical destruction of the hippocampus to reduce epileptic seizures. Following the surgery H.M. suffered anterograde and retrograde amnesia, but his ability to recall distant memories was unimpaired. This case study resulted in H.M. becoming one of the most intensively-studied medical subjects in history. There is now consensus that the hippocampus plays a major role in memory; however the exact nature of this remains fiercely debated.

1.1.2 Ageing in the CNS

Ageing has been described as a series of detrimental changes that occur over time ultimately leading to impairments in function, including loss of cognitive abilities (Peters, 2002). Ageing is the biggest risk factor in Alzheimer's disease (AD) and Parkinson's disease (PD). Neurodegenerative disorders, particular AD, are accompanied by loss of neurons. However, age-related loss of neurons may not be as extensive as once thought. Indeed, it has been reported that the overall numbers of cortical neurons only declines by approximately 10% with ageing, although some brain regions show more loss than others (Morrison & Hof, 1997).

A reduced ability to cope with stressors has been associated with ageing. Behavioural stress is accompanied by secretion of hormones brain cells, including corticosteroids (Karten *et al.*, 2005), which negatively impact on memory function (McEwen *et al.*, 1999), and inhibit long-term potentiation (LTP), a putative model for cellular learning and memory (Murray & Lynch, 1998b).

It has been proposed that ageing could result from the accumulation of age-specific and deleterious genetic mutations (Partridge & Gems, 2006). Factors which contribute to the deterioration in function of the CNS with age include increases in mitochondrial insufficiency, reactive oxygen species (ROS) production and aberrant deposition of transition metals including iron and zinc, for example in AD (Bush & Tanzi, 2008). While the exact means by which ageing might contribute to deficits in plasticity have yet to be fully understood, there are two main theories of ageing. These are the membrane hypothesis, and the free radical theory.

1.1.3 The membrane hypothesis

Membrane fluidity refers to the viscosity of the lipid bilayer of a cell membrane. Reduced fluidity of brain cell membranes represents an important mechanism that could explain many functional age-related alterations in the brain (Muller *et al.*, 1997). An age-related reduction in membrane fluidity has been shown in many species, and is usually explained by increased cholesterol to phospholipid ratios of brain membranes, and by enhanced lipid peroxidation (Zs-Nagy, 2001). Lipid peroxidation leads to higher concentrations of saturated fatty acids (Muller *et al.*, 1997) and a decrease in polyunsaturated fatty acids (Murray & Lynch, 1998a). For example, the polyunsaturated fatty acid content of phospholipids in the brains of aged compared with young rats (Little *et al.*, 2007) and also in the brains of individuals with AD (Edlund *et al.*, 1992).

Nervous tissue has relatively high concentrations of unsaturated fatty acids, compared with other organs (Bourre, 2004). These fatty acids participate directly in the structure and in the functioning of cell membranes. Lipid composition of the membrane is critical for the optimal functioning of membrane proteins; for example in ligand binding, enzyme activation, receptor activity, and for signal transduction (Uauy & Dangour, 2006). Interestingly, a reduction in arachidonic acid incorporation is observed with ageing and this has been predictably correlated with decreased membrane fluidity (Bourre, 2004). Furthermore, the reduction in arachidonic acid is correlated with an impairment in LTP in the aged rat, and can be partially restored with dietary supplementation of ω -6 (McGahon *et al.*, 1999b) or ω -3 fatty acids (McGahon *et al.*, 1999a).

1.1.4 Free radical theory of ageing

Of the many theories of ageing put forward over the last several decades, the free radical theory remains among the most plausible. The free radical theory of ageing was proposed by Harman in 1957 who postulated that the main driving force behind the ageing process is an accumulation of damage to proteins and other cell components as a result of free radical attacks (Biesalski, 2002). Mitochondria produce most of the energy of the cell and therefore need the majority of oxygen. Consequently, with increasing metabolic rate, more ROS are produced. However, the ROS-induced mutations of mitochondrial DNA and the role of antioxidants are not fully understood. Nevertheless, ROS can cause harm by random oxidation of proteins, which can result in degradation by associated proteases (Berlett & Stadtman, 1997). This in turn causes progressive tissue ageing, and suggests that any disease that exacerbates mitochondrial ROS production could accelerate senescence of the affected tissue or organ. Antioxidant mechanisms to counteract this effect include reversing the age-related decline in free radical scavengers such as glutathione, and vitamins C and E (Lynch, 1998),

1.2 Barriers of the CNS

The CNS is subject to two opposing requirements: the need to change in response to experience and the need for stability. Neurons are highly sensitive to changes in their microenvironment; for example, neural signalling requires precise regulation of the local ionic microenvironment around axons and synapses. Of the three barriers formed, the blood-brain barrier (BBB) is perhaps the most important in regulating the immediate microenvironment of neuronal cells. In the brain and spinal cord of mammals including humans, the BBB is created at the level of the cerebral capillary endothelial cells by tight junction formation (Wolburg & Lippoldt, 2002). Several pathologies that result in neural damage are associated with an early phase typified by disruption of the BBB; thus, early treatment of BBB disruption could reduce the severity of neuropathological symptoms and facilitate recovery.

A second interface, the blood-cerebrospinal fluid barrier (BCSFB), is formed by the epithelial cells of the choroid plexus facing the cerebrospinal fluid of the lateral,

third and fourth ventricles of the brain. Here, tight junctions are formed between the epithelial cells at the CSF-facing surface of the epithelium. The CSF is secreted across the choroid plexus epithelial cells into the brain's ventricular system (Brown *et al.*, 2004), while the remainder of the brain's extracellular fluid is derived in part by secretion across the capillary endothelium of the BBB (Abbott *et al.*, 2006). Some drugs and solutes can enter the brain across the choroid plexuses into the CSF, while others can enter via the BBB and BCSFB.

The final interface, the arachnoid barrier, is formed by the avascular arachnoid epithelium, underlying the dura and completely enclosing the CNS. It is a multi-layered epithelium with tight junctions between cells of the inner layer that form an effective seal between the extracellular fluids of the CNS and that of the rest of the body (Vandenabeele *et al.*, 1996). Although the arachnoid also forms a barrier layer, its avascular nature and relatively small surface area signifies that it does not represent a significant surface for exchange between the blood and the CNS (Abbott *et al.*, 2010).

1.2.1 Structure of the BBB

The BBB is formed by endothelial cells that line cerebral microvessels (Risau & Wolburg, 1990) together with astrocytes and pericytes. It acts as a physical barrier because tight junctions, '*zonulae occludentes*', between adjacent endothelial cells force most molecular traffic to take a transcellular route, rather than moving paracellularly through the junctions (Wolburg & Lippoldt, 2002). The BBB, along with the blood-cerebrospinal fluid barrier (BCSFB) and avascular arachnoid epithelium, results from the combination of physical barrier (tight junctions reducing flux via intercellular cleft or paracellular pathway), transport barrier (mediating solute flux) and metabolic barrier (enzymes metabolising molecules in transit). The combined surface area of cerebral microvessels constitutes by far the largest interface for blood-brain exchange, and in the adult human brain is between 12 and 18m² in surface area (Abbott *et al.*, 2010). It is clear from the earliest histological studies that brain capillary cells are surrounded by, or closely associated with, several other cell types including the perivascular endfeet of astrocytes, microglia and neuronal process. Astrocytes provide the cellular connection to neurons (Abbott *et al.*, 2006).

Cerebral perivascular macrophages are key cells by virtue of their location at the BBB. They are situated between the endothelial basement membrane and the *glia limitans*. They are the first cells to respond to inflammation within the brain in various experimental settings, including experimental autoimmune encephalomyelitis, neuronal damage and intracerebroventricular injection of interferon- γ (Galea *et al.*, 2005). They also respond to peripheral immune activation after systemic lipopolysaccharide (LPS) injection (Schiltz & Sawchenko, 2002). Moreover, they display constitutive phagocytic potential as well as effective antigen presentation, including up-regulation of immunophenotypical markers of activation, for example major histocompatibility complex class II (Williams *et al.*, 2001). Thus, they are ideally suited to respond to pro-inflammatory stimuli arising from both within the brain and from the periphery.

1.2.2 Tight junctions

Tight junctions are domains of occluded intercellular clefts (Farquhar & Palade, 1963) which are a critical determinant of the permeability properties of the BBB; in addition to the protection offered by preventing the passage of potentially harmful agents into the brain, they also prevent the entry of many potentially beneficial drugs (Matter & Balda, 2003). Therefore much effort has been directed toward the understanding the factors which maintain the integrity of tight junctions of brain endothelial cells.

Two of the most abundant tight junction proteins are occludin and the claudins. In the discovery of occludin, Furuse and colleagues (1993) reported that it was a 504-amino acid polypeptide of 65 kDa with no significant homology with other tight junction-associated proteins (Furuse *et al.*, 1993). Occludin spans the plasma membrane four times, forming two extracellular loops. These extracellular loops are thought to play a role in the regulation of paracellular permeability (Balda *et al.*, 2000) and cell adhesion (Kubota *et al.*, 1999).

The tight junctions of six week-old occludin-deficient mice developed by Saitou and colleagues (2000) were not affected morphologically. A striking neuropathological finding in occludin^{-/-} mice is the progressive accumulation of mineral deposits in the cerebellum and basal ganglia; these deposits were revealed by electron microscopy to be calcium deposits that were localized along small vessels and capillaries (Saitou *et al.*,

2000). These changes were accompanied by chronic inflammation and postnatal growth retardation. However, the study indicated that occludin was not required for the formation of tight junctions *per se*.

The claudins, which have a molecular weight of approximately 23kDa (Nitta *et al.*, 2003), are the tight junction molecules which seem to fulfil the task of establishing barrier properties, contributing to the high transendothelial electrical resistance (TEER) (Wolburg & Lippoldt, 2002) and thus may mediate paracellular ion permeability. There are some 20 isoforms of claudin (Abbott *et al.*, 2010); these also bear four transmembrane domains similar to occludin, but do not contain any sequence homology to occludin. Most cell types express more than two claudin species in various combinations to form the tight junction strands (Tsukita *et al.*, 2001).

Functional studies support the view that the composition of the claudins species directly determines barrier function. Blood vessels of newborn claudin 5-deficient mice generated by Nitta and colleagues (2003) do not exhibit overt morphological differences compared with wildtype (WT) mice, and were largely intact. Inspection of tight junctions in claudin 5^{-/-} mice revealed that endothelial cell-cell contacts appeared normal. This indicates that tight junction strands of WT mice are not only composed of claudin 5, but also the other claudins species, including claudin 12 (Nitta *et al.*, 2003). Interestingly, expression of claudin 12 was similar in WT and claudin 5-deficient mice.

Tracer experiments revealed that BBB permeability was induced in claudin 5^{-/-} mice, in a size-selective manner. Magnetic resonance imaging (MRI) studies revealed the presence and diffusion of gadolinium-based contrast agent (molecular weight: 742Da), but not larger molecules, in the brain and spinal cord of claudin 5-deficient mice, and extravasation or leakage of gadolinium occurred in a dose-dependent manner, with approximately 15% of the injected solution leaking across the BBB. Gadolinium was retained within the blood vessels of WT mice (approximately 1% of total volume). Thus, the authors conclude, when tight junctions are composed of more than one distinct claudin species, the removal of one claudin markedly changes the barrier function of tight junctions, while keeping their continuous structural integrity (Nitta *et al.*, 2003).

1.2.3 Function of the BBB

The BBB has several roles; it has low passive permeability to many essential water-soluble nutrients and metabolites required by nervous tissue, as well as mediating the efflux of many waste products (Abbott *et al.*, 2006). This indicates that the BBB is a mostly hydrophobic, rigid and highly restrictive membrane with low polarity (Di *et al.*, 2009). Specific transport systems are therefore present in the BBB. It also provides a stable environment for neural function by a combination of specific ion channels and transporters, thereby keeping ionic composition optimal for synaptic signalling function (Abbott *et al.*, 2010). For example, the concentration of potassium in mammalian plasma is approximately 4.5mM, but in brain and CSF interstitial fluid is maintained at 2.5-2.9mM, despite changes that can occur in plasma following exercise or induced experimentally (Bradbury *et al.*, 1963). Calcium and magnesium are actively regulated at the BBB and BCSFB.

Blood plasma contains high levels of the neuroexcitatory amino acid glutamate. If glutamate is released into the brain interstitial fluid in an uncontrolled manner, this would lead to considerable neurotoxic damage to neural tissue. Since the central and peripheral nervous systems use many of the same neurotransmitters, the BBB also helps to keep the peripheral and central neurotransmitter pools separate, thus minimizing 'crosstalk' (Abbott *et al.*, 2006).

The BBB acts as a protective barrier which shields the CNS against neurotoxic substances circulating in the blood. These neurotoxins include endogenous metabolites or proteins, or xenobiotics ingested from food or through the environment. A number of energy-dependent efflux transporters actively pump these agents out of the brain (Loscher & Potschka, 2005). Maintaining the integrity of the BBB is important because the CNS does not have a significant regenerative capacity, and fully differentiated neurons are not able to divide and replace themselves under normal circumstances (Ming & Song, 2005). However it is recognised that there is a steady rate of neuronal cell death from birth throughout life in the healthy human brain, with relatively low levels of neurogenesis (Lim *et al.*, 2007). Any acceleration in the natural rate of cell death resulting from an increased access of neurotoxins into the brain would become prematurely debilitating.

The BBB has low passive permeability to many water-soluble nutrients and metabolites that are required by nervous tissue. Specific transport systems are therefore present in the BBB to ensure an adequate supply of these substances. The differentiation of the barrier layer begins at embryonic angiogenesis, and is maintained in adulthood by a close association with several cell types, including the endfeet of astrocytes. This association promotes the up-regulation of tight junction proteins (Wolburg & Lippoldt, 2002), as well as the polarity in the endothelial cells arising from the differential expression of specific transporter proteins in the luminal and abluminal membranes (Beck *et al.*, 1984). Pericytes, microglia and nerve terminals are also closely associated with the endothelium, and all play supporting roles in maintaining barrier function. The barrier function is not fixed, however, and can be modulated and regulated, both in pathology and in physiology (Abbott *et al.*, 2006).

1.2.4 Measuring and modulating BBB integrity

The BBB was originally identified in 1904 by Paul Ehrlich, who noticed that injection of a water-soluble dye stained all organs except for the brain and spinal cord. Further evidence of a BBB was provided by Ehrlich's student Edwin Goldmann, who injected trypan blue directly into the CSF and found that only cells in the brain were stained (Goldmann, 1913). Today, extravasation of tracer dyes such as horseradish peroxidase (molecular weight: 40kDa) and Evans blue (980Da) is routinely used to measure BBB disruption and integrity (Westergaard, 1977; Belayev *et al.*, 1996) in the rodent brain. However, non-invasive measurement of BBB integrity can be carried out using contrast-enhanced MRI (cMRI) using intravenously-administered contrast agent, for example meglumine gadopentate (Gd-DTPA) (Larsson *et al.*, 1990). Gadolinium-based contrast agents exceed the 180 Dalton threshold for paracellular transport in the healthy BBB (Sakaeda *et al.*, 2001) and thus are sufficiently large enough to detect alterations in the compromised BBB, when injected intravenously. Application of this methodology has revealed BBB defects in animal models of a range of disorders, including multiple sclerosis (MS) (McCandless *et al.*, 2009) and AD (Ramakrishnan *et al.*, 2008).

It has been shown that BBB permeability to the slowly penetrant tracer Mannitol (182 Dalton) is between 0.19-0.22 $\mu\text{l g}^{-1} \text{min}^{-1}$ in the brains of 1 week-old rats, and this

permeability is the similar in adult rats (Preston *et al.*, 1995). The high electrical resistance, characteristic of low paracellular permeability, is exhibited by rats by E21, indicating firstly that functional tight junctions are formed prenatally, and also that they already form an effective barrier to the movement of ions (Butt, 1995). Several reports have shown that the human BBB is as well formed at birth as in the adult. Expression of occludin and claudin 5 has been detected in the capillary endothelium of the human brain in the 14 week-old foetus, and shows the same distribution at cell margins compared to that seen in the adult (Virgintino *et al.*, 2004). Furthermore, post-mortem studies have revealed that a BBB impermeable to trypan blue (960 Dalton) is present from at least the start of the second trimester, which is comparable to that of an adult human

Novel mechanisms have recently emerged that attempt to investigate the transient opening of the BBB by suppressing expression of proteins involved in endothelial cell tight junctions. Small interfering ribonucleic acid (siRNA) can induce a temporary opening of the BBB by silencing claudin 5 expression (Campbell *et al.*, 2010) for periods up to 36 hours. Claudin knockdown allows the formation of pores in the paracellular pathway of the cells, similar to that seen in claudin 5-deficient mice, allowing the passive diffusion of molecules from the blood to the brain (Campbell *et al.*, 2010). This technique renders neuronal areas permeable to compounds up to a molecular weight of at least 742 Da, and the use of this barrier modulation has been extended to increase drug delivery to prevent retinal degeneration in mice (Campbell *et al.*, 2011).

1.3 The CNS defence system

Although it was suggested at one time that the CNS may be an immune privileged site, this is now known to be incorrect and it is accepted that cells of the CNS can control the delicate balance between CNS function and self-defence (Carson & Sutcliffe, 1999). Microglia and astrocytes acting together constitute a resident innate immune system, serving as both sentinel cells and the first line of defence by responding to nonspecific 'danger' signals (Carson & Sutcliffe, 1999). Both microglia and astrocytes express Toll-like receptors (TLRs), which recognise structurally

conserved molecules derived from microbes, as well as endogenous damage-associated molecular-patterns (DAMPs) like high mobility box 1 (HMGB1) which is released from damaged cells (Rubartelli & Lotze, 2007). The interaction between a TLR and its ligand results in the secretion of anti-bacterial peptides and pro-inflammatory cytokines including tumour-necrosis factor (TNF)- α and interleukin (IL)-6. These initiate an inflammatory response to clear the invading organism (Renshaw *et al.*, 2002).

1.3.1 Microglial cells

Microglia were first described in 1920 by del Rio-Hortega (Kitamura, 1973), a student of Ramon Y Cajal, who characterized the microglial response to brain lesions. In 1988, it was confirmed that microglial cells are bone marrow-derived cells and can express high levels of major histocompatibility complex (MHC) II proteins for antigen presentation following stimulation (Hickey & Kimura, 1988). Microglia represent about 10% of the total brain cell population (Alliot *et al.*, 1999); under normal, and especially under pathological, conditions neuronal well-being and proper functioning are highly dependent on the large numbers of glial cells that sustain several neuron functions (Streit, 2002). The unique fact about microglia is that they are both supportive glia, immunocompetent cells and antigen-presenting cells (APCs) (Perry *et al.*, 1993). Microglia express many of the common macrophage antigens, including F4/80 and macrophage (Mac)-1, which consists of cluster of differentiation (CD)11b. In contrast to macrophages, microglia express MHC I and II at very low levels in their quiescent state (Bauer *et al.*, 1995).

Microglia are extremely plastic and can undergo an array of structural changes depending on their location and function. This level of plasticity is crucial for the wide variety of immunological functions that microglia perform, as well as maintaining homeostasis in the CNS. Ramified microglial cells remain as surveying, quiescent cells in the nervous parenchyma (Vela *et al.*, 1995; Nakamura *et al.*, 1999), until they are confronted by a stressor, for example pathologically- or experimentally-induced changes in conditions that compromise the integrity of the CNS (Banati & Graeber, 1994). A typical ramified morphology is characterized by elongated processes extending from both poles of the cell. A variable number of secondary processes emanate from these primary processes (Ling & Wong, 1993). Under pathological

conditions, activation and reactivity of microglia can include transformation in their distribution and shape, including a change into an amoeboid morphology (Milner & Campbell, 2003). Microglia are the phagocytic cells of the brain (DeWitt *et al.*, 1998) which is a critical event in the resolution of an inflammatory attack (Chan *et al.*, 2001).

In addition to the transformation in shape, activated microglia release pro-inflammatory cytokines, including IL-1 β (Sanz & Di Virgilio, 2000), and TNF- α (Hide *et al.*, 2000), a major pro-inflammatory cytokine which promotes infiltration of cells to the CNS. Activated microglia also release anti-inflammatory cytokines, including IL-10. IL-10 has a number of immunomodulatory roles, for example *in vitro* studies have shown that pre-treatment of microglia with IL-10 is effective in blocking the lipopolysaccharide (LPS)-induced production of TNF- α , thereby attenuating the inflammatory response (Kim *et al.*, 2002).

However, it is possible that overexpression of pro-inflammatory cytokines released from activated glial cells contributes to the onset or progression of neurodegenerative consequences. Normal ageing raises the threshold of inflammatory cytokine expression in the brain without the need for a secondary insult (Ogata *et al.*, 2003), and evidence from the study of neurodegenerative conditions, for example AD, suggests that the release of pro-inflammatory cytokines by activated glia have deleterious effects on neurons.

1.3.2 Astrocytic cells

Astrocytes are the most abundant glial cells in the brain and play a vital role in homeostasis of the CNS (Dong & Benveniste, 2001). Astrocytes are characterized by their star-shaped morphology. They are closely associated with synapses where they play a major role in regulating synaptic concentration of glutamate and ions. The evidence suggests that they also participate in synaptic network formation and neurogenesis (Ransom *et al.*, 2003). Astrocyte foot processes are in close proximity to the abluminal surface of the microvasculature endothelium of the BBB. Furthermore, several studies have suggested that astrocytes promote endothelial cell maturation *in vitro* (Abbott, 2002).

Astrocytes are frequently referred to as ‘supportive cells’ of the CNS, for their role in supporting neurons and microglia, and the repair of the brain and spinal cord

after traumatic injury or assault. Within a few hours of virtually any brain injury, astrocytes proliferate and begin to exhibit hypertrophy (Chen & Swanson, 2003), a process that has been termed *reactive astrogliosis* (Ridet et al., 1997).

Astrocytes share some properties with microglia. A study investigating the effects of stab injury to the rat cerebral cortex revealed that astrocytes, like microglia, participate in phagocytosis (al-Ali & al-Hussain, 1996) and endocytosis (Megias *et al.*, 2000). Evidence from *in vivo* studies designed to investigate the effects of ageing suggests that astrocytes, like microglia, increase production of pro-inflammatory cytokines, including including IL-1 β , IL-6 and TNF- α (Dong & Benveniste, 2001) as well as S100 calcium binding protein β . Interestingly, tissue levels of biologically active S100 β are elevated in the AD brain (Marshak *et al.*, 1992) and S100 β levels also correlate with neuritic plaques in AD (Sheng *et al.*, 1994).

It is well-established that age-related increases in levels of glial fibrillary acidic protein (GFAP)-expressing astrocytes occurs in the healthy human brain (Hansen *et al.*, 1987), and ageing rats show progressively increased levels of S100 β with age (Linnemann & Skarsfelt, 1994). These increases are further exacerbated when the animals are subjected to experimental head injury, which is a risk factor for AD (Kato *et al.*, 1990).

In vitro studies have shown that astrocytes, like microglia, also express a number of TLRs, including TLR4 (Bowman *et al.*, 2003) and are therefore able to respond to LPS. Following LPS treatment, astrocytes up-regulate their expression of IL-6, increasing rapidly 1-2 hours after exposure (Krasowska-Zoladek *et al.*, 2007). As a potent source of immunologically-relevant cytokines, astrocytes play a pivotal role in the type and extent of CNS immune and inflammatory responses.

1.3.3 Cytokines in the CNS

The study of actions of cytokines in the CNS is in its infancy, but has already revealed direct effects of these molecules on many aspects of neuronal function. Available data indicate a complex picture, with many cytokines exerting opposing actions depending on their concentration, site and duration of action. Microglia and astrocytes are thought to govern the survival of neurons after damage to the CNS. Bacterial endotoxins and cytokines such as IL-1, TNF- α , interferon (IFN)- γ stimulate

the production of both themselves and other cytokines released by microglia and astrocytes (Benveniste, 1992). Sustained or excessive production of pro-inflammatory cytokines can have deleterious results. For example, excessive production of TNF- α can result in demyelination and axonal degeneration (Stoll *et al.*, 1993), while IL-6 treatment enhances N-methyl D-aspartate (NMDA)-induced neurotoxicity (Grulic & Nelson, 1997). In addition, TNF- α is toxic to oligodendrocytes, and has been associated with demyelination (Louis *et al.*, 1993). Therefore, TNF- α might contribute to the neuropathies that are associated with diseases like leprosy (Rothwell & Hopkins, 1995).

Several cytokines have been reported to affect neuronal differentiation and growth, and modify synaptic plasticity in brain slice preparations. IL-1 β , IL-2, TNF- α , IFN- α and β all inhibit LTP (Rothwell & Hopkins, 1995), although these effects probably do not share common mechanisms, since the timecourse and nature of inhibition differs for each cytokine (Kent *et al.*, 1992).

A variety of measures have been developed for suppressing cytokine synthesis or actions. For example, supplementation of rats with ω -3 fatty acids inhibits both central and peripheral effects of IL-1 on fever and reduces neuronal damage caused by focal ischemia (Relton *et al.*, 1993). Evidence from this laboratory has shown that the age-related increase in IL-1 β expression is attenuated following treatment with dexamethasone and vitamin D₃ for a period of two weeks. Similarly, the age-related increase in activation of the stress-activated protein kinase, c-Jun N-terminal kinase (JNK), as well as caspase-3, are all attenuated in hippocampal tissue prepared from rats that received dexamethasone and vitamin D₃ (Moore *et al.*, 2007). In addition, treatment with the anti-inflammatory cytokine IL-10 reverses the LPS-induced inhibitory effect on LTP. Treatment with IL-10 also inhibits the LPS-induced increase in IL-1 β and enhanced phosphorylation of JNK (Lynch *et al.*, 2004). Furthermore, treatment with IL-4 attenuates the A β -induced inhibition of LTP and the associated increase in MHCII, JNK phosphorylation and IL-1 β concentration in the rat hippocampus (Lyons *et al.*, 2007). Central to these studies is the discovery of the naturally-occurring IL-1 receptor antagonist (IL-1Ra) which endogenously inhibits the action of IL-1 and is present in the normal brain. Central injection of IL-1Ra inhibits endotoxin-induced cytokine release in rodents (Bluthe *et al.*, 1992).

It is now clear that cytokines have several distinct actions on the nervous system: as communicators to the brain of systemic injury, infection and inflammation,

and as neuromodulators of the CNS control of systemic host defence responses to diseases and injury, and as molecules that inhibit or mediate neurodegeneration and repair.

1.4 Pro-inflammatory cytokines

1.4.1 Interleukin-1 β

IL-1 β is a member of the IL-1 cytokine family and was discovered in 1972. IL-1 plays a crucial role in the development of the inflammatory response, in part by mediating its own production and by stimulating the synthesis of other pro-inflammatory cytokines such as IL-6, IL-8 and TNF- α . IL-1 β also has a role in actions modulating cell growth (Dinarello, 1992). The biological activity of IL-1 is mediated by two different gene products, IL-1 α and IL-1 β . These two proteins share only 25% amino acid identity but have similar three-dimensional structures, use the same receptor (IL-1R) for signalling and share the same biological activities. IL-1 α remains intracellular or membrane-bound while IL-1 β is processed by a specific enzyme called IL-1 β -converting enzyme (ICE) or caspase-1 and is usually secreted as a mature molecule (Rachal Pugh *et al.*, 2001). The presence of IL-1 β in the CNS is believed to reflect synthesis by diverse cells such as endothelium, microglia, astrocytes and neurons (Liu *et al.*, 1993).

IL-1 β works via specific brain receptors that demonstrate significant spatial distribution. As in peripheral tissues, the pro-inflammatory actions of IL-1 β in excessive levels will promote acute neuropathological changes in the brain by an activation of IL-1R1 (Dinarello, 1992).

Evidence from pharmacological studies has indicated that systemic or central administration of IL-1 β to both rats and mice induces the full spectrum of behavioural signs of sickness, including staying in the corner of their home cage and showing little or no interest in their social environment, in a dose and time dependent manner (Biella & de Curtis, 2000). However, the effect of IL-1 β goes beyond its role in organizing the behavioural adaptations to infection (the sickness syndrome). Work by Pugh and colleagues (2001) has shown that its activation also significantly impairs memory

consolidation in the hippocampal-dependent contextual fear conditioning task (Rachal Pugh *et al.*, 2001). This correlates with other work showing memory deficits in IL-1 β -treated rats in the Morris water maze (Oitzl *et al.*, 1993). Interestingly, there is an age-related increase in IL-1 β expression in the hippocampus of the aged rat (Lynch, 2010), and this is positively correlated with the age-related deficit in LTP (Minogue *et al.*, 2007). Interestingly, this age-related increase in IL-1 β can be reversed with treatment of the polyunsaturated fatty acid eicosapentaenoic acid (EPA) (Martin *et al.*, 2002). It is important to note that systemic administration of LPS induces the expression of IL-1 β in the brain (Dantzer *et al.*, 2008). The primary role of IL-1 β in LPS-induced changes are confirmed from IL-1 receptor blockade studies, that have shown IL-1 β to be one of the principal mediators of LPS-induced neurotoxicity (Fantuzzi *et al.*, 1996).

1.4.2 TNF- α

Hints of the existence of a biological factor mediating tumour necrotic activity date back to the 18th century. In 1975, it was reported that TNF was released into the circulation of animals subsequent to LPS challenge (Carswell *et al.*, 1975). This protein has been demonstrated to cause rapid necrotic regression of certain forms of tumours. TNF- α and TNF- β are two structurally- and functionally-related proteins, with a 30% homology in their encoded amino acid residues (Idriss & Naismith, 2000). There are two TNF-receptors (TNF-Rs) of 55 and 75 kDa which are members of the TNF-R superfamily that also includes CD40 and CD27, and which exhibit specific and high-affinity binding to either TNF- α and TNF- β (Benveniste & Benos, 1995). TNF-R1 is responsible for mediating most of the actions of TNF, including its antiviral activity, as well as its ability to induce apoptosis and cytokine production (Chen & Goeddel, 2002).

TNF- α has a molecular weight of 17kDa and is released by activated microglia and endothelial cells (Suzuki *et al.*, 2004) as well as astrocytes (Molina-Holgado *et al.*, 1997) although activated microglia are probably the primary cellular source of TNF- α . The biological functions of TNF- α are varied and the mechanism of action is somewhat complex. It modulates immune responses by affecting the expression of MHC I and II molecules, and it can stimulate different cell types to produce other cytokines, including IL-1, IL-6 and TNF- α itself. It has been shown that mice deficient in the TNF-R displayed a suppressed inflammatory response upon challenge with bacterial endotoxins

(Acton *et al.*, 1996). TNF- α therefore plays an important role in the initiation of an inflammatory response.

The ligand-receptor interaction generates downstream signalling via two classes of cytoplasmic adaptor proteins: TNF-R associated factors (TRAFs) and “death domain” (DD) molecules (Inoue *et al.*, 2000). Recruitment of DD or TNFR-associated DD leads to activation of a downstream signalling cascade and activation of caspases and ultimately, apoptosis. Recruitment of TRAF leads to activation of nuclear factor kappa-light-chain-enhancer of activated B cells (NF- κ B) and (JNK) (Micheau & Tschopp, 2003).

TNF- α also plays an important role in the alteration of the BBB due to its effects on the adhesive properties of both astrocytes and brain endothelium. Recent studies have shown that up-regulation of adhesion molecules such as intercellular adhesion molecule-1 (ICAM-1) on brain endothelial cells by exposure to TNF- α mediates leukocyte adhesion to endothelium. The presence of ICAM-1 and other adhesion molecules in the vessel walls may guide inflammatory leukocytes into and through the brain, thereby contributing to impairment of the BBB and promoting inflammatory infiltration into the CNS (Benveniste & Benos, 1995).

Interestingly, there is an age-related increase in TNF- α expression that may be responsible for the increased secondary neuron death after injury in the ageing brain (Sandhir *et al.*, 2004). It can mediate myelin damage and oligodendrocyte death *in vitro*, which may contribute to myelin damage seen in MS (Benveniste & Benos, 1995). In addition, TNF- α -positive astrocytes and microglia have been identified in the brains of MS patients, in particular in the plaque region (Hofman *et al.*, 1989). TNF- α has also been implicated in the pathology underlying AD; increased TNF- α has been reported in serum from AD patients compared with controls (Alvarez *et al.*, 2007) and expression near neuritic plaques in the AD brain has been described (Perry *et al.*, 2001).

1.4.3 Interleukin-6

IL-6 is present on astrocytes and microglia (Sawada *et al.*, 1992) as well as neurons (Gadient & Otten, 1994). Receptors involved in recognition of IL-6 can be subdivided into the non-signalling α -receptor (IL-6R α) and the signal transducing receptor (gp130) (Heinrich *et al.*, 2003). The latter associate with the Janus kinase

(JAK) tyrosine kinase family, leading to the transcription of the signal transducers and activators of transcription (STAT) family. Another major signalling pathway for IL-6 is the mitogen-activated protein kinase (MAPK) cascade (Hideshima *et al.*, 2001). Expression of IL-6 is increased following stimulation by LPS, IL-1 and amyloid-beta (A β) (Spangelo *et al.*, 1991; Deakin *et al.*, 1995; Haas *et al.*, 2002).

IL-6 is a member of a family of cytokines, which includes IL-11, that possess both pro- and anti-inflammatory properties, exerting both neuroprotective and neurotoxic effects. It has multi-functional properties and plays a central role in host defense due to its wide range of immune and hematopoietic activities and its potent ability to activate the acute phase response. The role of IL-6 as an anti-inflammatory cytokine derives from its ability to inhibit some effects of TNF- α and IL-1, and its ability to upregulate IL-1Ra (Steensberg *et al.*, 2003). Thus, pre-treatment of cultured hippocampal neurons with IL-6 protects these cells against glutamate-induced cell death (Yamada & Hatanaka, 1994). *In vivo* studies using IL-6-deficient mice show that while they develop normally, they have impaired immune and acute phase responses (Fattori *et al.*, 1994).

Elevated levels of IL-6 have been observed in the cortex and hippocampus of AD patients, in particular in the early stages of plaque development (Ershler & Keller, 2000). IL-6 is also up-regulated in the brains of patients with PD (Gadient & Otten, 1997) and following brain damage (Penkowa *et al.*, 2003). However, it is unclear whether IL-6 contributes to the neurodegenerative events associated with AD and PD, or is simply reflective of the inflammation caused by progressive neuronal damage (Gadient & Otten, 1997).

1.5 Markers of glial activation

1.5.1 CD11b

CD11b, also known as integrin alpha M (ITGAM), is a surface integrin of cells of the myeloid lineage which includes monocytes, macrophages and microglia. It is one protein subunit that forms the heterodimeric integrin alpha-M beta-2 ($\alpha_M\beta_2$) molecule, also known as macrophage-1 (MAC-1) antigen. The second chain of $\alpha_M\beta_2$ is the

common integrin known as CD18 (Diamond *et al.*, 1993). During activation, microglial cells are not only secretory but they also express several proteins and surface markers of activation. CD11b is perhaps the one with the most biological significance (Roy *et al.*, 2006). It acts as a binding protein for ICAM-1 and inactivated complement component 3b (iC3b), both of which are expressed on endothelial cells.

CD11b is the classical pro-inflammatory activation marker of microglia. It is a sensitive marker of microglial activation since its protein expression is low or negligible in resting microglia. The morphological changes characteristic of activated microglia have been correlated with an increase in expression of CD11b (Rock *et al.*, 2004) and CD11b expression correlates with severity of microglial activation in models of neuroinflammatory disease (Roy *et al.*, 2008). Consistently CD11b expression has been shown to be elevated in the aged rodent brain (Butovsky *et al.*, 2006), as well as in brain tissue prepared from animals following treatment with both LPS and A β (Jana *et al.*, 2008; Lyons *et al.*, 2009), and is up-regulated in the hippocampus and cortex of APP/PS1 and Tg2576 mouse models of AD (van Groen & Kadish, 2005; Rodriguez *et al.*, 2010).

1.5.2 CD40

The CD40 antigen is a 48 kDa molecule that is expressed on a variety of cells, including dendritic cells, B cells and endothelial cells. It is also found on activated microglial cells (Aloisi *et al.*, 1999). Indeed, full microglial activation is dependent on CD40 expression. The protein receptor is a member of the TNF-R superfamily that also includes TNF-R1 and TNF-R2 (Natoli *et al.*, 1997).

The CD40 receptor interacts with its natural ligand CD40L, also known as CD154, which is expressed predominantly on CD4⁺ T cells but also on monocytes, dendritic cells and astrocytes. Using either knockout animals or anti-CD40L antibodies, interference with the CD40-CD40L pathway has been shown to be beneficial in several disease models of autoimmunity and infectious diseases (van Kooten & Banchereau, 2000).

Although CD40 and CD40L are both produced as membrane-bound molecules, they have several characteristics that make them part of the cytokine network. For example, CD40-CD40L interactions play important roles in the production of several

cytokines, including IL-12 (Cella *et al.*, 1996). *In vitro* experiments have shown direct effects of CD40 activation on increased production of IL-6, IL-10 and TNF- α , increased expression of adhesion molecules (ICAM) and increased expression of MHC II (Khanna *et al.*, 1997). Upon ligation of CD40, numerous signalling pathways are activated; these include NF- κ B, MAP kinases and the JAK/STAT pathways (van Kooten & Banchereau, 2000).

Expression of CD40 under resting conditions is minimal but microglial activation is associated with an increase in CD40 expression *in vitro* (Aloisi *et al.*, 2000) and *in vivo* (Townsend *et al.*, 2004). It has been shown that at the peak of experimental autoimmune encephalomyelitis (EAE; a mouse model of MS), full activation and maturation of microglial cells is dependent on CD40, whereas mice deficient in either CD40 or CD154 are resistant to EAE (Becher *et al.*, 2001; Ndhlovu *et al.*, 2001). In addition, insufficient activation of microglial cells by a lack of CD40 was associated with decreased proliferation of T cells and amelioration of disease clinical symptoms (Ponomarev *et al.*, 2006). Similarly, A β initiates microglial activation through the CD40 pathway following administration of a low dose of solubilised A β ; this effect is attenuated in transgenic AD mice deficient in CD40L (Tan *et al.*, 1999). This suggests that A β -induced microglial activation only occurs after ligation of CD40.

1.5.3 Glial fibrillary acidic protein

GFAP was first isolated from white matter plaques of MS patients. Expression of the GFAP gene is intimately linked with astrocyte function and GFAP is commonly used as a marker of normal and reactive astrocytes (de Armond *et al.*, 1980). GFAP is a 50 kDa intracytoplasmic filamentous protein that constitutes a portion of, and is specific for, the cytoskeleton of the astrocyte (Rutka *et al.*, 1997).

GFAP is thought to stabilize the astrocyte's cytoskeleton and to maintain astrocyte cell shape through interactions between GFAP filaments, the nuclear membrane, and the plasma membrane (Fliegner & Liem, 1991). Electron microscopy data has revealed that abundant GFAP filaments are present at sites of contact between astrocytic processes and neurons and endothelia (Rubinstein, 1986). Thus, GFAP forms a structural link between the nucleus and the plasma membrane.

Deletion of the GFAP gene does not affect development or function, and no architectural disturbances of the CNS were found (Gomi *et al.*, 1995). However, it was suggested that GFAP^{-/-} mice may be more prone to the effects of ageing than normal mice. Furthermore, 6-month old GFAP-deficient mice have shorter astrocytic processes leading to reduced contacts between astrocytes and oligodendrocytes, as well as a more permeable BBB (Liedtke *et al.*, 1996).

Following injury to the CNS induced by trauma, genetic disorders or chemical insults, astrocytes become reactive; astrogliosis is defined by astrocyte proliferation and extensive hypertrophy of the cell body and cytoplasmic processes. The hallmark cytopathological feature of astrogliosis is a marked up-regulation of cytoplasmic glial filaments (Rutka *et al.*, 1997). GFAP expression is up-regulated in the AD, PD and ageing brain (Nichols *et al.*, 1993; Otto & Unsicker, 1994; Ingelsson *et al.*, 2004), and this is coupled with an increase in numbers of astrocytes with an activated morphology that occurs with age (Nichols, 1999).

1.6 CD200

1.6.1 Expression of CD200 and CD200 receptor

CD200 (formerly known as OX2) is a cell surface transmembrane glycoprotein that has been shown to deliver an inhibitory signal to cells of the myeloid lineage. Gorczynski and colleagues (2004) reported the existence of four highly related CD200 receptor isoforms (CD200R1-CD200R4) in different tissues. They detected the presence of CD200R1 in the spleen, lung, intestine and bone marrow, with less expression in the brain: expressions of CD200R2, CD200R3 and CD200R4 were negligible in the healthy brain. However, relatively high levels of CD200 ligand expression were found in the brain, as well as in the spleen, lung and bone marrow (Gorczynski *et al.*, 2004b).

Within the CNS, CD200 is widely expressed on a variety of cell types, including neurons (Wright *et al.*, 2001) activated T cells and endothelial cells (Broderick *et al.*, 2002; Jenmalm *et al.*, 2006) and astrocytes (Costello *et al.*, 2011). However, CD200 is not expressed on microglia. CD200R is expressed predominantly on cells of the myeloid lineage (Preston *et al.*, 1997; Wright *et al.*, 2003) which play an important role

in the inflammatory process, and investigations of CD200 and CD200R have indicated that macrophages are restrained from tissue-damaging activation through CD200R-induced signalling (Broderick *et al.*, 2002). The expression of CD200 and CD200R on neurons and microglia, respectively, suggest that the CD200-CD200R interaction provides a cell-cell contact immunoregulatory interaction for myeloid cells (Jenmalm *et al.*, 2006).

1.6.2 CD200 signalling

Structurally, CD200R resembles CD200, with two immunoglobulin superfamily (IgSf) domains, but with a larger cytoplasmic domain (Broderick *et al.*, 2002). Several independent studies analysing the structure of CD200 have revealed that it lacks signalling domains in the cytoplasmic tail or “docking” motifs within membrane-spanning regions (Hoek *et al.*, 2000) that could serve as sites for protein-protein interactions with adaptor signalling molecules. In contrast, CD200R has a longer cytoplasmic domain which includes an NPXY domain that contains 3 tyrosine residues which are phosphorylated upon ligation by CD200 (Wright *et al.*, 2000; Snelgrove *et al.*, 2006). CD200R then recruits docking protein 1 (Dok 1) and Dok 2 which leads to recruitment of Ras GTPase-activating protein (RasGap) and downstream inhibition of the JNK and MAPK pathways (Zhang *et al.*, 2004). The reduced activation of these MAPKs is believed to be responsible for the observed inhibition of cytokine production by CD200R⁺ cells (Gorczyński *et al.*, 2004a).

1.6.3 Function of CD200

The functions of CD200-receptor activation are best described by the study of CD200^{-/-} mice. These mice appear grossly normal in appearance and exhibit a normal lifespan (Hoek *et al.*, 2000). However, differences are in the function of myeloid cells have been consistently described (Barclay *et al.*, 2002; Minas, 2006).

There are increased populations of macrophages in CD200^{-/-} animals (Wright *et al.*, 2003). The CD11b⁺ population is increased in the spleen of CD200^{-/-} mice (Minas, 2006) while microglia of CD200^{-/-} mice spontaneously exhibit many features of activated microglia, including less ramified, shorter glial processes, and increased

CD11b and CD45 expression (Hoek et al., 2000). Recent evidence from this laboratory has indicated that following LPS treatment, glia isolated from CD200-deficient mice show an exaggerated release of pro-inflammatory cytokines by microglia, which was coupled with an increase in TLR4 mRNA expression in CD200^{-/-} mice (Costello *et al.*, 2011). *In vivo* studies have revealed an increased susceptibility of CD200^{-/-} mice to autoimmune disease (Feuer, 2007). Thus, Hoek and colleagues (2000) reported that the symptoms of EAE were more severe, and their onset was more rapid, in CD200^{-/-} mice. Microglial activation, assessed by CD68 immunohistochemistry, was greatly increased in CD200^{-/-} compared with wildtype mice 10 days after immunization. EAE was also found to be more severe in rats treated with an anti-CD200 monoclonal antibody just prior to disease onset, although the disease duration was similar (Wright et al., 2000). Collagen-induced arthritis (CIA) involves the influx of T cells and macrophages into the joint. Whereas WT mice are resistant to CIA after a single immunization with collagen, with an incidence of about 10%, about 50% of CD200^{-/-} mice showed evidence of disease onset about 20 days after injection of collagen (Hoek et al., 2000). There was also evidence of greater inflammation in the joints of CD200^{-/-} mice compared with controls. However, administration of CD200Fc fusion protein suppressed induction of disease in CD200^{-/-} mice when given at the time of collagen injection, and this was associated with a decreased IFN- γ while increasing IL-10 (Gorczyński et al., 2002). CD200Fc also limits symptoms and inflammation when administered to WT mice during the chronic stages of EAE (Liu *et al.*, 2010). This is further evidence that direct and continuous interaction between CD200 and CD200R downregulates macrophage activation. (Hoek *et al.*, 2000; Deckert *et al.*, 2006) and suggests that the ligand may be useful in managing the inflammatory response in a wide range of diseases (Feuer, 2007).

Inducing CD200R signalling through interaction with CD200, which is extensively expressed on neurons in the retina, can also suppress the inflammation associated with experimental autoimmune uveoretinitis (EAU), a model of T cell organ-specific autoimmunity (Copland et al., 2007), which is characterized by tissue destruction mediated by activated macrophages and nitric oxide (NO)-induced damage. Onset and severity of EAU is accelerated in CD200^{-/-} mice with evidence of increased expression of markers of microglial activation on retinal microglia (Broderick et al., 2002). However, systemic administration of a monoclonal antibody which activates

CD200R resulted in suppression of EAU, IFN- γ production and tissue damage in CD200^{-/-} mice, even in the presence of T-cell proliferation. Direct local administration of the antibody before and during peak disease resulted in a 50% reduction of symptoms (Copland et al., 2007). These results indicate that promoting CD200R-mediated signalling can successfully prevent full expression of IFN- γ mediated macrophage activation, and thus protect against tissue damage during autoimmune responses.

As the search for anti-inflammatory therapies for neurodegenerative diseases continues, a potential therapeutic benefit of CD200 glycoprotein has emerged. Recent research by Walker and colleagues (2009) found decreased expression of neuronal expression of CD200 as well as CD200R at mRNA and protein levels in human AD brains. Correlation analysis between plaque scores and CD200 mRNA expression showed a significant inverse relationship, suggesting that as CD200 expression decreases, the pathology worsens (Walker *et al.*, 2009). Microglial activation also plays a critical role in the progression and pathogenesis of PD (Chen et al., 1998) and it has been proposed that CD200-CD200R signalling is closely linked to microglial activation in PD (Wang et al., 2007). Interestingly, the toxicity of rotenone which is used to induce Parkinson's-like symptoms in rodents is enhanced by a CD200R blocking antibody (Wang *et al.*, 2011). These findings have led to the proposal that up-regulation of CD200 expression in the CNS may provide neuroprotection in an array of neuroinflammatory diseases such as AD, MS and PD.

1.7 Alzheimer's Disease

AD is the most common form of dementia. It is characterised by cognitive deterioration and major physiological changes in the brain. It was first named by Alois Alzheimer in 1906 (Maurer *et al.*, 1997) who diagnosed the first case of AD. It is a progressive, neurodegenerative disease characterized by an inability to form new memories. As the disease progresses, symptoms include confusion, irritability and aggression (Deutsch *et al.*, 1991). Age is the biggest risk factor for the disease; it typically affects people over the age of 65. In 2006, there were 26.6 million sufferers of the disease worldwide. By 2050, it is predicted that 1 in 85 people will suffer from AD.

The vast majority of cases are sporadic, although some genes may act as risk factors. On the other hand, approximately 0.1% of all cases are familial AD (FAD), and these usually have an age of onset before 65. While over 400 genes have been tested for association with late-onset sporadic AD, most FAD cases can be attributed to mutations in three genes; amyloid precursor protein (APP), and presenilin (PS) 1 and 2 (Mattila *et al.*, 1998). A strong driving force in AD research is the amyloid cascade hypothesis. It states that improper processing of APP lies at the root of AD, as this generates the neurotoxic and aggregating A β peptide (Mandelkowitz & Mandelkowitz, 1998). Increased production of A β ₁₋₄₂, the main component of senile plaques, results largely from mutations in the APP and PS genes (Scheuner *et al.*, 1996). As of 2010, more than 400 pharmaceutical treatments were in clinical trials. The most common target of these compounds is the reduction of amyloid. However, no effective treatment has been found.

The major pathological hallmarks of the condition are aggregates formed by extracellular deposits of A β , intracellular tau protein as neurofibrillary tangles and extensive neuronal loss (Oddo *et al.*, 2003). A key issue is whether the neuropathological hallmarks can be correlated to progression of the clinical symptoms, and whether they allow a back-extrapolation to pre-clinical stages. This certainly seems possible in the case of tau deposits, where the primary and secondary stages of the spreading of tau are pre-clinical (Mandelkowitz & Mandelkowitz, 1998). Overall, however, there is contradictory evidence describing the exact association between these hallmarks and progression of clinical symptoms. Brains of AD patients and AD transgenic mice are in an enhanced inflammatory state, which includes increased oxidative stress (Markesbery, 1997), but is largely mediated by activated glial cells, resulting in the release of pro-inflammatory cytokines, which lead to a chronic inflammatory environment. This results in significant neuronal loss and synaptic dysfunction, and ultimately, cognitive decline.

1.7.1 Neurofibrillary tangles

NFTs are composed of aggregated conformations of aberrantly phosphorylated forms of the microtubule-associated protein, tau. Tau is one of the microtubule-associated proteins that stabilize neuronal microtubules for their role in the development

of cell processes and intracellular transport (Drewes *et al.*, 1998). However, in the AD brain, the properties of tau change in several ways. AD-tau shows a loss of microtubule binding, which is probably a consequence of the hyperphosphorylation at sites that detach tau from microtubules. This could account for the disappearance of microtubules, causing the breakdown of intracellular traffic, which would result in the deterioration and eventual loss of axons (Mandelkow & Mandelkow, 1998). In addition, there is an increase in tau in the CSF of the AD brain, which has been proposed to be a consequence of dying neurons (Vigo-Pelfrey *et al.*, 1995). This provides the potential of an early diagnostic assay. However, the dementias associated with tau mutations are distinct from AD and affect different regions in the brain. For example, frontotemporal dementia, the second most common cause of dementia in humans under the age of 65, is caused by mutations in tau (Baker *et al.*, 2006).

1.7.2 Amyloid precursor protein

APP has the structural features of a type 1 transmembrane glycoprotein. The gene contains 18 exons; the region encompassing A β comprises parts of exons 16 and 17. Thus, A β cannot be formed solely as an alternatively spliced gene product; alternatively, it seems that A β is formed from the proteolytic processing of APP (Evin *et al.*, 2003). In contrast to the number of studies on the metabolism of APP and neurotoxicity of A β , there has been little work done on the normal function of APP. Several studies have suggested a role for APP for the regulation of neurite outgrowth and synaptogenesis in both the CNS and PNS (Mattson, 2004; Wang *et al.*, 2009). Critically, APP expression increases during ageing (Butterfield & Poon, 2005). Studies describing APP-deficient mice have revealed that APP^{-/-} mice have impaired spatial learning and an impairment in LTP, as well as strongly reduced A β levels in the brain (Ring *et al.*, 2007)

1.7.3 Amyloid precursor protein processing

The proteolytic processing pathways that lead to the formation of A β from APP have been well characterized in a number of cell lines. APP is delivered to the surface membrane where it is subjected to proteolytic processing by α -secretase. APP molecules

that fail to be cleaved by α -secretase can be internalized into endocytic compartments and subsequently cleaved by β -secretase and γ -secretase to form A β (Kamenetz *et al.*, 2003). A β peptides generated in the Golgi and in recycling apparatus can be secreted into the extracellular space (Greenfield *et al.*, 1999). The majority of secreted A β peptides are 40 amino acids in length (A β_{1-40}), although the smaller fraction of longer, 42 amino acid species (A β_{1-42}) have received greater attention due to their greater propensity to drive production of amyloid fibrils (Jarrett *et al.*, 1993) and are most abundant in A β plaques.

1.7.4 Senile plaques

There are two major forms of plaques. One form, the diffuse plaque, contains diffuse forms of amyloid, while the second form, the neuritic plaque, contains amyloid that is surrounded by abnormally shaped neurites (Small, 1998). Both diffuse and neuritic plaques contain the same major constituent, the 4 kDa A β which ranges in length between 39-43 amino acids. The amyloid in neuritic plaques consists of a dense core containing filaments of 7-10 nm in width. The number of neuritic and diffuse plaques increases with age in patients with AD (Price & Morris, 1999) and in transgenic mice overexpressing the APP and PS1 transgenes (Yan *et al.*, 2009). While a small number of plaques can occur with the physiological process of normal ageing, several studies have correlated total levels of A β and general cognitive decline in AD patients (Gandy, 2005).

1.7.5 Amyloid-beta

A β exerts numerous effects in the CNS. At low levels, A β activates kinases and protects against oxidative stress (Gandy, 2005; Nunomura *et al.*, 2006). It is well established that excessive amounts of A β are deleterious to neuronal viability. *In vitro* studies have supported the hypothesis that A β peptides directly contribute to neurodegeneration in AD. In primary neuronal cultures, aggregates of A β peptides induce dystrophic neurite morphology. At higher concentrations, close to 80% of neurons in culture exhibit dystrophic features after 4 days of incubation with A β (Grace *et al.*, 2002). In addition, exposure of neurons to A β induces cell death via an apoptotic

pathway, which includes DNA fragmentation and a dose-dependent loss of cell viability (Peng *et al.*, 2002).

Transgenic mice over-expressing the FAD-linked mutants of APP have an impaired synaptic plasticity and learning (Chapman *et al.*, 1999), and soluble A β has been shown to block LTP *in vivo* (Walsh *et al.*, 2002). It has also been reported that the level of soluble A β is a potent predictor of synapse loss, in particular soluble A β_{1-40} . However, several authors have reported the lack of a correlation between A β deposition and neurodegeneration that occurs in AD dementia, perhaps because total A β rather than the soluble form has generally been evaluated (Lue *et al.*, 1999).

A β_{1-42} increases GFAP immunoreactivity in astrocytes and reorganizes the astrocytic cytoskeleton, typical of a reactive morphology (Hu *et al.*, 1998). Interestingly, it has been shown that cultured adult mouse astrocytes migrate in response to monocytes chemoattractant protein (MCP)-1, a chemokine present in AD lesions, and interact with immobilized A β_{42} (Wyss-Coray *et al.*, 2003). Astrocytes are also capable of binding and degrading A β : astrocytes plated on A β -laden brain sections from a mouse model of AD were shown to associate with the A β deposits and reduce overall A β levels in these sections (O'Barr & Cooper, 2000) indicating a role for astrocytes in the degradation of A β , and suggesting that astrocytes may be involved in clearance of A β in AD. However, microglia are the principal phagocytes in the brain and therefore should play a significant role in A β clearance (Rogers & Lue, 2001).

A β induces secretion of IL-1, IL-6 and TNF- α from microglial cultures and also stimulates the proliferation and morphological transformation of microglia (Araujo & Cotman, 1992; Grammas & Ovase, 2001; Gasic-Milenkovic *et al.*, 2003). Cultured rat microglia exhibit pronounced chemotaxis to pre-aggregated A β_{42} deposits which are virtually carpeted by the cells within 3 weeks (Rogers & Lue, 2001). When plated on post-mortem cortical sections, rodent microglia also migrate to aggregated A β deposits on the section (Ard *et al.*, 1996). In APP transgenic mice, aggregated plaques are associated with hypertrophic microglia, but diffuse plaques are not (Rogers & Lue, 2001). Immunohistochemical studies have shown an increase in markers of microglial activation in the vicinity of A β plaques in sections prepared from APP transgenic mice (Malm *et al.*, 2007). These findings support the hypothesis that accumulation of the A β protein triggers microglia to become reactive and to secrete toxic molecules which contribute to A β -induced neurodegeneration.

1.7.6 Non-transgenic models of AD

Animal models continue to be important in developing an understanding of the mechanisms underlying disease pathogenesis and progression and in identifying targets for therapeutic strategies. However, many models of AD do not closely resemble the pathology of human AD because they do not encompass all pathological features of AD, including both senile plaques and NFTs, and some do not demonstrate neuronal loss (Sultana *et al.*, 2009). The majority of efforts in generating adequate models concentrate on mimicking the increase in A β load seen in disease.

Several studies have attempted to mimic the increase in A β concentrations by intracerebral or intracerebroventricular infusion of A β peptides, and observing the downstream glial activation (Ralay Ranaivo *et al.*, 2006) neurotoxic effects (Butterfield *et al.*, 2002) and memory impairments (Jhoo *et al.*, 2004). The ability of A β infusion to induce neuronal death and glial activation seen in AD is dependent on a number of factors, including surgical procedure, the dose of A β used and the aggregation state of the peptide. Initial reports showed that injection of insoluble amyloid fractions from the AD brain into the rat hippocampus induces dramatic neuronal loss there (Frautschy *et al.*, 1991). However, intraparenchymal injection of A β_{40} into the hippocampus and cortex of adult rats failed to initiate an AD pathology, neuronal death or activation of glial cells (Games *et al.*, 1992). The most likely explanation for this was the use of soluble, rather than the fibrillary, form of A β . Injection of A β_{42} has been shown to induce significant damage to axons, and to increase the numbers of reactive astrocytes and microglia (Jantaratnotai *et al.*, 2003).

Increasing amyloid load by infusion has been shown to induce cognitive deficits. Long-term effects of A β infusion on memory appear to require the aggregated form of A β , which lasts for longer in the CNS as it is not cleared as fast. Intracerebroventricular infusion of A β_{42} produces a dose-dependent impairment in spontaneous alternation performance in the Y-maze task, and place navigation memory in a water maze up to 80 days after treatment. Interestingly, these impairments were significantly more severe 80 days after treatment, compared with the earlier study timepoint at 20 days (Nakamura *et al.*, 2001). Nitta and colleagues (1994) have shown that continuous infusion of A β_{40} into the cerebral ventricle of the rat induced short-term learning and memory deficits in the

standard water maze task (Nitta *et al.*, 1994), as does A β ₄₂ (Yamada *et al.*, 1999). Several studies have indicated that A β negatively impacts on LTP, and continuous intracerebroventricular injection of A β decreased LTP in the CA1 field of hippocampal slices (Itoh *et al.*, 1999).

1.7.7 Transgenic mouse models of AD

The discovery that mutations in genes that encode APP, PS1 and PS2 are linked to FAD has resulted in the generation of genetically-altered mouse models of AD. While no transgenic model completely replicates all of the characteristics of AD, many of the animal models can mimic a number of the pathological hallmarks, including plaque deposition, neuroinflammation as well as cognitive deficits (Eriksen & Janus, 2007). These models have contributed greatly to our understanding of the disease process.

The first model to successfully develop A β plaques and display AD-like pathology was the PD-APP transgenic model generated by Games and colleagues (1995). These mice express high levels of human APP containing the V717F mutation, promoting the expression of A β ₄₂ over A β ₄₀ and leading to extensive plaque deposition, synaptic loss, astrogliosis and microglial activation (Games *et al.*, 1995). Subsequent studies have shown that these mice have significant age-related memory deficits in learning spatial locations in the water maze protocol, and that these deficits are correlated with plaque burden (Chen *et al.*, 2000). Numerous other mouse models have been generated which overexpress human forms of APP, including the Tg2576 model which have a 14-fold increase in A β _{42/43} expression, coupled with deficits in spatial reference learning, compared with controls at 9-10 months of age (Hsiao *et al.*, 1996).

Overexpression of the mutant form of PS1 significantly increases A β ₄₂ in the brain, however mice over-expressing PS1 alone do not develop senile plaques (Duff, 2006). However, crossing this line with the Tg2576 mouse produces double transgenic progeny that develop large numbers of fibrillary A β deposits and substantial neuroinflammation by 6 months of age, far earlier than mice from the Tg2576 line. In addition, double transgenic mice had a 41% increase in A β ₄₂ expression in the months preceding plaque deposition, when compared with single transgenic mice (Holcomb *et*

al., 1998). Therefore, the development of AD pathology is markedly enhanced when a PS1 mutation is introduced into Tg2576-derived mice.

One of the more recent transgenic models used in AD research is the APP^{swe}/PS1^{dE9} double transgenic model, which is the model used in these series of experiments. These mice were generated by injection of both the APP695 isoform containing the Swedish mutation, and exon 9-deleted PS1 into pronuclei. Both genes were driven by a single mouse prion protein (PrP) promoter (Jankowsky *et al.*, 2001). A β deposits are observed in the hippocampus of these mice as early as 4 months of age, and are widespread by 9 months. A β deposits are more abundant in female APP/PS1 mice (Burgess *et al.*, 2006). The concentration of A β ₄₂ is consistently reported as being greater than A β ₄₀, with several studies reporting the ratio of A β peptide 40:42 is 0.5:1 (Garcia-Alloza *et al.*, 2006). Behavioural testing of these mice indicates significant spatial memory deficits at 8 months of age in the standard Morris water maze (Cao *et al.*, 2007), however 6 month-old APP/PS1 mice are indistinguishable from their littermate controls on this task (Savonenko *et al.*, 2005).

1.8 Magnetic Resonance Imaging

1.8.1 Introduction

Magnetic resonance imaging (MRI) technologies have presented a novel set of safe, non-invasive and flexible (Mandeville & Rosen, 2002) tools for describing characteristics of the normal and atypical brain. MRI is a topographic imaging technique, that produces images of internal physical and chemical characteristics of an object (Liang & Lauterbur, 2000). These characteristics are obtained by applying externally-measured nuclear magnetic signals (Roberts & van Bruggen, 2003). At the core of these technologies is quantitative biology (Kennedy *et al.*, 2002). MRI is based predominantly on the sensitivity to the presence and properties of water, which makes up 70-90% of most tissues (McRobbie *et al.*, 2003). At a superficial level, MRI takes advantage of the natural spin and magnetization of water molecules (Hornak, 1996). When hydrogen protons are placed in the magnetic field of an MR scanner, these particles line up in the direction of the externally-applied magnetic field, and the net

alignment of these particles is termed the ‘magnetization vector’. Radio frequency (RF) fields are used to alter the alignment of this magnetization by 90° , causing the hydrogen protons to produce a rotating magnetic field detectable by the scanner. The time constants which describe how the particles relax back to their equilibrium states with the removal of the RF pulse are termed T_1 and T_2 relaxation times, where T_1 refers to the recovery of longitudinal magnetization (i.e. parallel to the magnetic field) and T_2 describes the decay of transverse magnetization (i.e. perpendicular to the main magnetic field) (Weishaupt *et al.*, 2008). Free water and cerebrospinal fluid (CSF) have relatively long T_1 relaxation times.

1.8.2 T_1 and T_2 relaxometry

The magnetic field caused by the motion of nuclei is called the lattice field. The lattice field of a nucleus in a lower energy state can interact with nuclei in a higher energy state. This causes the energy of the higher energy state to distribute itself between the two nuclei (Szczepaniak *et al.*, 1992). Spin-lattice (T_1) relaxation times measure the time for spins to give the energy they obtained from the RF pulse back to the surrounding lattice. T_1 is the decay constant for the recovery of the z component of the nuclear spin magnetization, M_z , towards its equilibrium value, and is quantified using the following formula:

$$M_z(t) = M_{z,eq} (1 - e^{-t/T_1})$$

where t is the time from the removal of the RF pulse. Thus, the magnetization recovers to 63% [$1-(1/e)$] of its equilibrium value, after being flipped into the magnetic transverse plane.

Spin-spin (T_2) relaxometry is the mechanism by the transverse component of the magnetization vector, M_{xy} , exponentially decays to its equilibrium value of zero. It is the time it takes for the MR signal to reach 37% ($1/e$) of its initial value after its generation by tipping the longitudinal magnetization toward the magnetic transverse plane, and is given by:

$$M_{xy}(t) = M_{xy}(0)e^{-t/T_2}$$

where t is the time from the removal of the RF pulse. T_2 relaxation generally precedes T_1 recovery, and different tissue samples have different T_2 relaxation times. For example, water-based tissues are in the 40-200 ms range, while fat-based tissues are in the range 10-100ms (Gatehouse & Bydder, 2003).

1.8.3 Relaxometry and neuroinflammation

Relaxometry is a powerful tool in the analysis of tissue states. T_1 -weighted imaging can be used to investigate hypointense lesions, for example in patients with MS (Anderson et al., 2006), and T_1 lesions have been shown to correlate with disease disability scores (Truyen *et al.*, 1996; Parry *et al.*, 2002), implying that T_1 -weighted imaging could be used as a surrogate marker of disability in MS. As T_1 values have been shown to change in the human brain with age (Cho et al., 1997), the biological significance of increased T_1 values remains unclear. Correlative studies have shown that increased T_1 values are associated with axonal loss (van Walderveen et al., 1998), gliosis (Parry et al., 2002), and increased tissue water (Barnes et al., 1988). T_1 increases were found to accompany increased levels of astrocytic activation in low-flow ischemia and excitotoxicity (Sibson et al., 2008), indicating that early changes in T_1 may provide insight into acute and reversible injury processes in neurological conditions. It has been suggested that this may be a consequence of an increase in free water brought about by localized oedema, associated with the astrocytic activation. Sibson and colleagues (2008) also demonstrated that pre-treatment with kainic acid reversed both the astrocytic excitotoxicity and the T_1 relaxation time. Recent evidence from this laboratory has supported the link between T_1 increases and acute astrocytic activation: pre-treatment with rosiglitazone, a PPAR γ agonist with neuroprotective effects, attenuates both the age-related increase in GFAP expression and T_1 relaxation times (Cowley *et al.*, 2010).

T_2 increases have been found in the hippocampus of patients with temporal lobe epilepsy (TLE) (Pell et al., 2004), which may be as a result of gliosis in the dentate gyrus (Briellmann et al., 2002). T_2 decreases have been observed in the hippocampus and cortex in animal models of AD prior to forming amyloid plaques (El Tayara Nel et

al., 2007; Falangola et al., 2007). The presence of iron in A β plaques is likely to contribute to the reduction in T₂ times, as the accelerated T₂ relaxation in plaques may be attributable to the magnetic susceptibility effect induced by the iron itself (Jack et al., 2005). Furthermore, the presence of iron in activated microglial cells could render T₂ relaxometry a useful biomarker of microglial activation, as has been shown previously in a rat model of ischemic stroke (Justicia *et al.*, 2008).

1.8.4 High-resolution anatomic imaging

Scanners with higher magnetic field strength (7.0 Tesla) have decreased the signal-to-noise ratio in images, resulting in clearer, more precise anatomical imagery that is more reliable for volumetric comparison. MRI, which has a resolution as fine as 10 μ m (Jacobs & Cherry, 2001), has been shown to provide superior contrast resolution than computed tomography (CT) scans (Beets-Tan et al., 2000) and positron emission tomography (PET) (Klein et al., 2002). Anatomic structures can be quantitatively measured and characterized by their anatomic location (Thompson et al., 1997), as well as their surface and volumetric representation (Kennedy et al., 2002). The two primary methodologies that have been developed to analyse between-group volumetric differences are manual volumetric analysis, where the region-of-interest (ROI) is measured on the MR image, and the newer, more reliable technique known as voxel-based morphometry (VBM) (Ashburner & Friston, 2000). As ROI analysis requires manually drawing each individual structure, this method is time-consuming and subject to inter- and intra-experimenter bias. VBM describes deviations in the local concentration of voxel clusters in MR scans from different groups of subjects (Ashburner & Friston, 2000), and has been used to evaluate brain volumetric differences in an aged population (Good et al., 2001), patients with AD (Testa et al., 2004), autism (Boddaert et al., 2004) and PD (Burton et al., 2004).

Volumetric analysis in rodents has, for the most part, had to rely on manual ROI analysis. While there have been few studies comparing volumetric changes in whole brains of young and aged mice and rats, studies have focused instead on the analysis of changes in individual structures, with a particular emphasis on the rat hippocampus. In one ROI study which assessed the hippocampal volume in rats at 3, 12, and 24 months of age, a significant age-related reduction in volume was observed, which correlated

with a reduction in hippocampal neuronal density, and a deficit in performance in the Morris Water Maze (Driscoll et al., 2006).

One significant advantage of VBM is that it offers a whole brain, unbiased approach to describing volumetric differences between groups. No quantitative measurements are taken, instead high-resolution images are skull-stripped from their surrounding tissue, segmented into tissue classes, and spatially-registered to a common stereotactic space generated by a generic reference template (Ashburner & Friston, 2000). Cluster-wise statistics are carried out between groups. The registration step removes the variability induced by normal variation in brain size, and accounts for global, non-linear shape differences. The output from the method is a statistical parametric mapping (SPM) which highlights regions of significant tissue concentration differences between groups.

With the recent introduction of standard reference templates for rat and mouse image registration, VBM has been translated for rodent brain analysis. Using VBM, decreases in the volume of the hippocampus, hypothalamus and cerebellum were found in a mouse model of Huntington's disease (HD) (Sawiak et al., 2009). Interestingly, this correlates with the finding that these areas are also predominantly affected in human HD (Jech *et al.*, 2007).

1.8.5 Arterial spin labelling

Arterial spin labelling (ASL) is an MR technique that can be used to quantitatively describe cerebral perfusion. This relies on the assumption that the signal response is the result of individual labelled water molecules taking a range of times to transverse the system into a volume of interest where they are exchanged between the capillary bed and extravascular water (Dixon et al., 1986). In a recently described ASL protocol (Kelly *et al.*, 2009), boluses of H₂O can be labelled, enabling the measurement of the dispersion of the bolus profile between labelling and imaging locations, thereby providing contrast between perfused and stationary tissue. By simulating an inflowing bolus using inversion pulses of fixed length and of varying delay, a quantitative measure of blood flow and dispersion at the capillary level can be measured (Kelly *et al.*, 2009).

1.8.6 Contrast-enhanced MRI

The ability to alter contrast on MR images has proved a viable avenue for the assessment of diseased tissue, for example altered blood flow in AD (Harris *et al.*, 1996). The majority of contrast agents are based on heavy metals, including gadolinium, and make use of the paramagnetic properties of these agents. Injection of high-sensitivity ultra-small particles of iron oxide (USPIOs) can label phagocytic cells, making correlations between areas of high-contrast on MR images and labelled macrophages possible (Dousset *et al.*, 1999). The inability of gadolinium to cross the BBB in healthy individuals due to the size of the molecule has made the use of this contrast agent an extremely attractive method of measuring changes in BBB permeability *in vivo* in numerous models of disease and inflammation. Thus, gadolinium-based contrast agents such as Gd-DTPA have been used to highlight blood vessels and tumours in the brains of both humans (Kircher *et al.*, 2003) and rodents (Beaumont *et al.*, 2009).

1.9 Aims of study

The aims of these studies were:

To assess microglial and astrocytic activation in WT and CD200^{-/-} mice, to evaluate the relationship between activation of glial cells and MR relaxometry parameters and to measure the age-related changes in mean transit time and capillary transit time.

To assess high-resolution MR images for potential volumetric differences between CD200-deficient and WT mice using the optimized VBM technique.

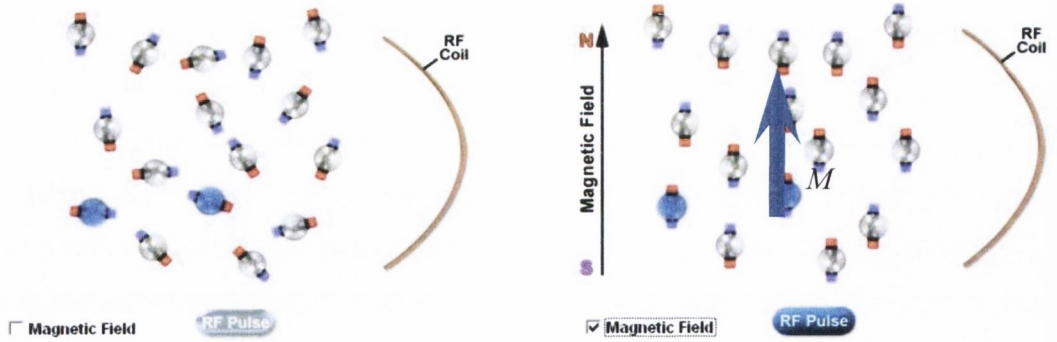
To assess the effect of peripheral LPS challenge on T₁ and T₂ relaxation times in parallel with glial activation in WT and CD200^{-/-} mice.

To assess the effect of LPS treatment on expression of tight junction proteins and BBB integrity, using contrast-enhanced MRI to the gadolinium-based contrast agent gadolinium with a novel tail-vein cannulation method.

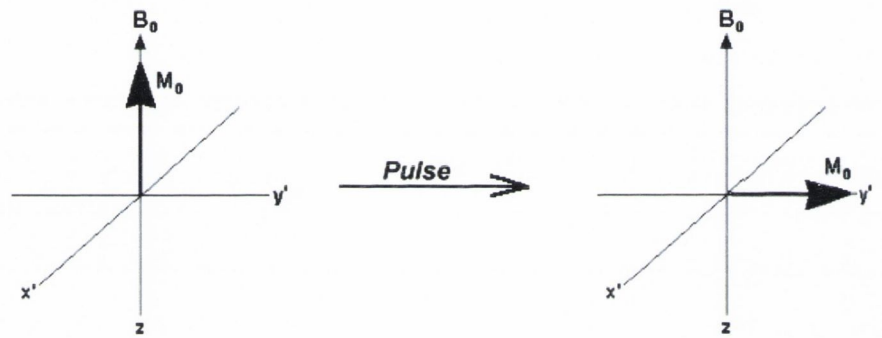
To assess the extent of amyloid deposition, neuroinflammation and relaxation times in 13-14 month-old AD transgenic mice (APP^{swe}/PS1^{dE9} model), and to perform a volumetric analysis on high-resolution images obtained from these mice.

To investigate the effect of siRNA treatment targeting suppression of the claudin 5 and occludin genes on BBB permeability in WT and APP/PS1 mice and to analyse the effect of siRNA treatment on levels of A β in brain tissue and blood serum of APP/PS1 mice.

(A)



(B)



(C)

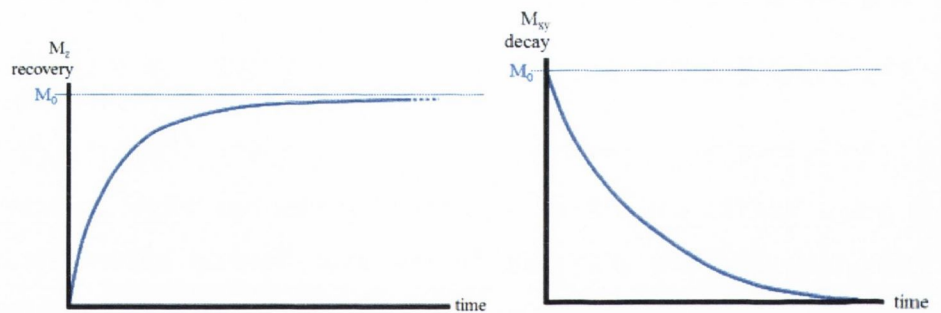


Figure 1.1 Schematic of MR signal generation

Hydrogen protons display in a random manner with no magnetic field. However, with the application of an external magnetic field, a small excess of protons orientate with this field, denoted by the magnetization vector M (Figure A). We can flip M by 90° upon the application of a suitable radiofrequency pulse (Figure B). When the RF is removed, the proton's magnetization returns to equilibrium, emitting T_1 and T_2 signals (Figure C). Adopted from www.mritutor.org

Chapter 2

Materials and Methods

2.1 Magnetic resonance imaging

2.1.1 Animal acclimatisation

Details of the mice used in these experiments are given in section 2.3.1. Prior to MR scanning, all animals spent 24 hours in the scanning control room to habituate to their novel surroundings. A 12 hour light-dark cycle was maintained, consistent with their regular housing environment. This was done to reduce stress induced from the transportation of animals. The weights of all mice were recorded immediately prior to scanning and are provided in Tables 7.1 and 7.2, Appendix 1.

2.1.2 Induction of anaesthesia

All animals were anaesthetized using isoflurane (Isoflo; Abbott Laboratories, UK) mixed with 100% oxygen (5% isoflurane was used for induction of anaesthesia, 1.5% - 2% for maintenance). Animals were placed in a clear plastic chamber which was connected to an anaesthetic scavenging system. This was filled with the gas mixture. Deep anaesthesia was confirmed by the absence of a pedal reflex. Animals were placed in a custom built plastic cradle, and secured safely in position using ear bars to support the head. Anaesthesia was maintained by administration of isoflurane through a facemask in 100% oxygen. A mechanical ventilator (Ugo Basile, Italy) was used to deliver the isoflurane mix to the facemask. The facemask was also attached to an anaesthetic scavenging system to remove waste gas. Movement was minimized by securing the animals on a tooth bar. The body temperature of the animal was controlled by a water-circulating system (S.A. Instruments Inc., US) underneath the mouse, and was maintained at a constant temperature of 37°C-38°C. Each animal was monitored post-scanning for any ill side-effects. Any changes in daily intake of food and water were recorded, as well as any irregular behaviour such as sustained drowsiness. Respiratory rate was obtained using a pressure pad placed under the abdomen and monitored using custom-built software (S.A. Instruments, US). Respiration rate was used to indicate depth of anaesthesia, and, if necessary, this was adjusted by altering isoflurane concentration. Mice were allowed to recover fully on a heated pad following

imaging experiments, breathing normal air, and were only reintroduced to their home cage when they had fully recovered from the effects of anaesthesia.

2.1.3 Tail vein cannulation

A glove filled with water that was heated to approximately 50°C was applied to the tail to induce blood flow. The tail was aseptically prepared with 100% ethanol (Merck, Germany) and the right lateral tail vein was cannulated using a custom-built cannula consisting of a 30 gauge in-dwelling, paediatric intravenous (iv) cannula needle (Introcan, Ireland) connected to an 80cm long polyethylene tubing cannula extension. The cannula was used in experiments to deliver the gadolinium-based contrast agent Magnevist (Bayer, Ireland), in experiments where mice underwent the contrast-enhanced MRI protocol. This cannula set-up negated the need to remove and replace the mouse in the magnet mid scan. The mice remained under isoflurane-induced anaesthesia during the entire cannulation process.

For contrast agent injection, the cannula tubing was connected to a three-way tap, which was connected to one syringe filled with 0.9% w/v sterile saline solution, and one filled with the Magnevist contrast agent solution (Magnevist to saline solution ratio; 1:2). The volume of the equipment was measured at 240µl, and was filled with saline at the beginning of the scanning protocol. A volume of 440µl was used to load the cannula with contrast agent, ensuring that each mouse received 200µl of contrast agent. Injection of the contrast agent solution took place at the commencement of the second repetition of the 10 repetition scan (approximately 2 minutes, 11 seconds into the imaging protocol). The cannulation also allowed for both pre- and post-contrast measurements to be determined within the same contrast scan, without the need to take out and reposition the animal before beginning the post-contrast imaging. This allowed for reliable and accurate localisation of regions of interest (ROIs) between the pre- and post-contrast repetitions in the contrast image analysis, and allowed for the immediate effects of the contrast agent to be investigated with no time delay.

2.1.4 Data acquisition and scanner preparation

All MR scanning experiments were carried out on a dedicated 7 Tesla BioSpec rodent scanner (Bruker Biospin, Germany), Trinity College Institute of Neuroscience. The magnet was set up to a workstation running the ParaVision 4.0 software package (Bruker BioSpin, Germany). This was equipped with a 30cm diameter core, and a 20cm actively-shielded gradient system. A pair of actively decoupled 12cm Helmholtz transmit and 2cm surface quadrature receive coils (Bruker BioSpin, Germany) were used for signal transmission, and reception, respectively. The receive coil was placed directly above the mouse's head and attached to the cradle with adhesive tape. The cradle was placed inside the core of the magnet. Each scanning session began with an initial pilot scan using a fast echo gradient scan. The purpose of this was two-fold; firstly to ensure that the animal was correctly positioned inside the magnet bore, and secondly to ensure that the receive coil was properly positioned above the head of the animal. The isocentre of the magnet was positioned approximately 5.5mm from the central fissure, guaranteeing that the single scan ASL and T_1 images (where appropriate) would be at a position of approximately 2mm posterior to Bregma. This ensured that a representative portion of hippocampal tissue was available for ROI analysis in these scans. When the mouse was in the appropriate position, a 'wobble procedure' was carried out to tune the transmit coil to the resonant frequency. Scans were analysed using the in built ParaVision software, MIPAV (National Institutes of Health, US), FSL (FMRIB Software Library, UK), IDL (ITTVIS, Boulder, CO), Mathematica (Wolfram research, UK) and ImageJ (National Institutes of Health, US), where appropriate.

2.1.5 T_1 -weighted imaging

A rapid acquisition with relaxation enhancement (RARE) with variable repetition time (RARE-VTR) scan was employed to assess T_1 relaxation times; the scan time was 8 minutes, 43 seconds. This was a single slice scan of 128 x 128 voxels, located approximately 2mm posterior to Bregma, thus encompassing sufficient amounts of cortical and hippocampal tissue to ascertain relaxometry times from these brain structures as a whole. T_1 relaxometry data were acquired by varying the repetition times (TR) using values ranging from 300ms to 8000ms (TR values: 300, 589.116, 942.255,

1396.084, 2031.981, 3103.081, and 8000.000ms) with an echo time (TE) of 25.27ms and RARE factor = 4. From this range of repetition times, a quantitative T_1 map was constructed from these images, using a built-in macro in the ParaVision software package (Schmitt et al., 2004). ROIs were measured using this quantitative map in the ImageJ software platform.

2.1.6 T_2 -weighted imaging

A 9 slice, 8 echo multi slice multi echo (MSME) scan was used to quantify T_2 relaxometry times in a scan time of 8 minutes, 32 seconds. These images had the same position as that of the T_1 measurements and a shared geometry of 128 x 128 voxels per slice. The scan parameters were; effective TEs: 12.64, 25.27, 37.91, 50.55, 63.19, 75.82, 88.46, 101.1ms; TR: 2000ms. This allowed for co-localisation of data between the two types of relaxometry assessed in this study. Only the middle 5 echo times were used to assess T_2 relaxation times in these data, after a quantitative mapping had been produced using a scripting procedure completed with IDL. ImageJ was employed to analyse structures in the quantitative mappings using a ROI approach. Sample T_1 - and T_2 -weighted images are presented in Figure 2.5.

2.1.7 High-resolution anatomic imaging

High resolution MR imaging was completed on all animals using a RARE scanning sequence. This scanning sequence offers good anatomical contrast between grey and white matter as well as excellent resolution. A single repetition scan was first carried out to ensure optimum animal positioning (scanning time: 2 minutes, 45 seconds). Five repetitions were then carried out in a total time of 13 minutes, 48 seconds. Data from the 6 repetitions were averaged to produce a high-resolution full brain image in the coronal view, with the following image dimensions: 54 slices x 196 x 256 voxels. These high-resolution scans were used for volumetric analysis using the voxel-based morphometry analysis technique, where each data set was spatially registered to a standard C57BL/6 mouse grey matter template image.

2.1.8 Arterial spin labelling

Quantitative blood flow and volume measurements were investigated using a bolus-ASL methodology (Kelly et al., 2009). This method uses a bolus-tracking ASL sequence to provide groups of 11 one slice images on a single time curve following the passage of a 3 second bolus through the imaging slice. Using a series of scripts in IDL, control and labelled images were created for each animal. Corresponding pairs of labelled and control images were subtracted to provide perfusion-weighted maps. Using a high resolution slice with the same geometry and position as that of the blood flow mappings, it was possible to fit the data to the formula described (Kelly et al., 2009) for several user-defined ROIs. Typically this scan was repeated 4 times to achieve optimum signal to noise ratio (1 repetition scan time: 2 minutes, 34 seconds). From this, the MTT and CTT were calculated.

2.1.9 Gadolinium-enhanced contrast imaging

BBB permeability to the contrast agent gadopentate dimeglumine (Magnevist; Clissmann, Ireland) was assessed in some experiments. Contrast imaging was carried out using a 10 repetition T_1 -weighted fast low angle shot (FLASH) sequence (1 repetition time: 2 minutes, 11 seconds, total scan time: 21 minutes, 50 seconds). The 15 slice protocol had dimensions 128 x 128 voxels per slice. Prior to commencing the scan, the tail vein was checked for patency by flushing with saline, and the cannula and tubing with the pre-filled contrast agent were loaded. Pre-contrast measurements were acquired on the first repetition of the scan to provide a contrast-free baseline. At the beginning of the second repetition of the scan, a bolus of contrast agent (200 μ l) was injected via the tail vein into the mouse, and the following 9 scan repetitions recorded the passage of the bolus throughout the brain over the remaining 18 minutes, 49 seconds. The scan parameters for the relaxometry, high-resolution, ASL and contrast scans are provided in Table 2.1.

Scan purpose	Scan type	No. repetitions	Matrix	Field of View	Num. slices	Resolution (μm)	Scan Duration
High-resolution	RARE	6	196 x 256	1.8cm x 1.8cm	54	91.8367 x 70.3125	16 min, 33 sec
T1-weighted	RARE-VTR	1	128 x 128	1.8cm x 1.8cm	1	141 x 141	8 min, 43 sec
T2-weighted	MSME	1	128 x 128	1.8cm x 1.8cm	9	141 x 141	8 min, 32 sec
Arterial Spln Labelling	FLASH	4	128 x 64	2cm x 2cm	1	156 x 312	10 min, 16 sec
Contrast enhancement	FLASH	10	128 x 128	1.8cm x 1.8cm	15	141 x 141	21 min, 50 sec

Table 2.1: MR scanning protocols

2.2 Data Analysis

2.2.1 Relaxometry

T_1 relaxation times were calculated using the ISA (Image Sequence Analysis) software within the Bruker software package. T_1 relaxation times were fitted to a mono-exponential rise function, exported and analysed in the ImageJ software program. All ROIs were drawn with reference to a standardised mouse brain atlas (Paxinos and Franklin, 1995). The cortex, hippocampus, corpus callosum and thalamus were drawn and calculated for each mouse data set. ROIs were calculated bilaterally in each hemisphere for all regions except for the corpus callosum, and averaged for each animal.

The raw data from the T_2 MSME scan were exported to Interactive Data Language (IDL) and analysed using an in-house scripting procedure, producing a voxelwise linear fitting to the logarithm of the data on the entire data set. The middle 5 echo times were used to create a parametric, quantitative T_2 map that was exported to ImageJ. Once again, ROIs within the cortex, hippocampus, corpus callosum and thalamus were manually drawn, and T_2 relaxation times calculated bilaterally for each hemisphere in 2 adjacent slices, and averaged for each mouse.

2.2.2 Voxel-Based Morphometry

High-resolution, structural T_2 -weighted scans from WT and $CD200^{-/-}$, WT and APP/PS1 mice were analysed for differences in anatomic grey matter volume using an in-house, optimized voxel-based morphometry (VBM) protocol (Good *et al.*, 2001). All 10 repetitions of the anatomic scan were averaged to produce 1 high-resolution image. Where there was animal movement throughout the course of the repetitions, the later repetition(s) were removed from the data set and the remaining repetitions averaged. Raw Bruker data were converted into analyze image format using the `pvconv.pl` conversion script (see <http://pvconv.sourceforge.net>). Brain extraction was performed to separate the brain from extraneous tissue surrounding it, using the brain extraction tool within the MIPAV software package. Where the extraction tool produced inadequate brain removal, the MIPAV paint tool was employed to complete the brain extraction

step. Image orientation was changed to mirror that of human image VBM analysis, and voxel size enlarged by a factor of 10 in MIPAV. These adjustments enabled the images to be analysed in the FSL software program, which is normally reserved for human image analysis (Smith *et al.*, 2004). Grey matter segmentation was carried out using FMRIB Automated Segmentation Tool (FAST) within FSL (Zhang *et al.*, 2001). The grey matter partitions were non-linearly, spatially registered to a generic C57BL/6 mouse grey matter brain atlas (Ma *et al.*, 2005) using the FSLREG utility. A study-specific grey matter template was produced by averaging the registered images from each experimental group. Registered images were then non-linearly registered to the study-specific template using FMRIB's Non-Linear Image Registration Tool (FNIRT), following an initial registration estimate by FMRIB's Linear Image Registration Tool (FLIRT). This was carried out to compensate for the areas of enlargement or contraction that are introduced due to the non-linear element of the initial spatial transformation to the stereotactic space. Each voxel within each registered image was divided by the Jacobian of the warp field for the image. A general linear model (GLM) was set up and fitted to the data, and this was used to investigate group volumetric differences in the specific studies. FSL Randomise, a permutation based utility, was used to enable modelling and inference using the standard GLM approach, producing voxel-wise based comparisons. FSL Randomise also offers variance smoothing as an option (Nichols & Holmes, 2002), and images were smoothed with a 1mm kernel prior to analysis. The results produced by Randomise were overlaid on the generic C57BL/6 grey matter template atlas to indicate areas of significant volumetric difference between groups. Results maps were thresholded at $p < 0.05$ to indicate statistical significance for all comparisons. A pipeline of the VBM procedure is presented in Figure 2.2.

2.2.3 ASL image analysis

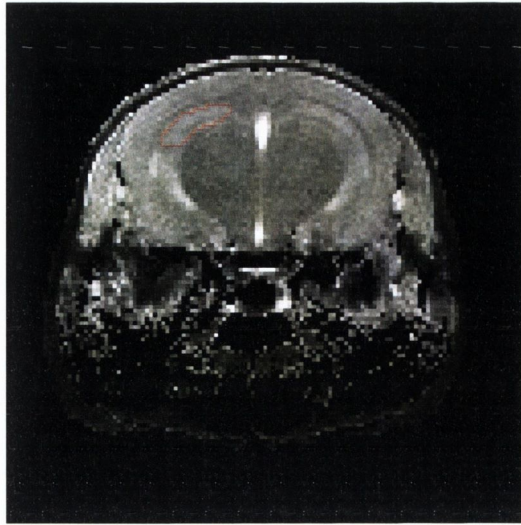
Qualitative ASL images were analysed in Mathematica, and cortical, hippocampal, and whole brain ROIs manually drawn on perfusion-weighted images. The average for each ROI was plotted against the acquisition timepoint in the bolus tracking ASL sequence. The curve was fitted to the solution of the non-compartmental cerebral perfusion ASL model (Kelly *et al.*, 2009), allowing the measurement of MTT and CTT. The curve-fitting utility in Mathematica was used to find the least squares fit

to the experimental curves. The MTT and CTT were calculated from the first and second statistical moments of the signal-time curves, respectively.

2.2.4 Contrast-enhanced image analysis

Gadolinium-enhanced contrast images acquired from the BBB permeability studies were analysed in the MIPAV software package. The average signal intensity changes in each treatment group were plotted against repetition. The first repetition was used as a contrast-free, baseline measurement. Anatomically-distinct ROIs viewed in the first repetition were overlaid with a 2 x 2 voxel square, and average pre-contrast intensity measured. The ROI squares were copied into the same locations in the remaining 9 repetitions for each mouse brain, measuring the contrast change following injection of the gadolinium-based contrast agent at the commencement of the second repetition. Regions of the cortex, hippocampus, thalamus, cerebellum and olfactory bulb were measured and compared. Values for each data set were normalised to the pre-contrast measurement, and expressed as a proportion of the pre-contrast value. For statistical analysis, values from the final 4 repetitions of the scan were averaged and compared across groups by 2-way ANOVA.

A



B



Figure 2.1: Sample T_1 - (A) and T_2 - (B) weighted images from an APP/PS1 transgenic mouse, approximately 2.54mm posterior to Bregma. The left hippocampus has been selected for ROI analysis.

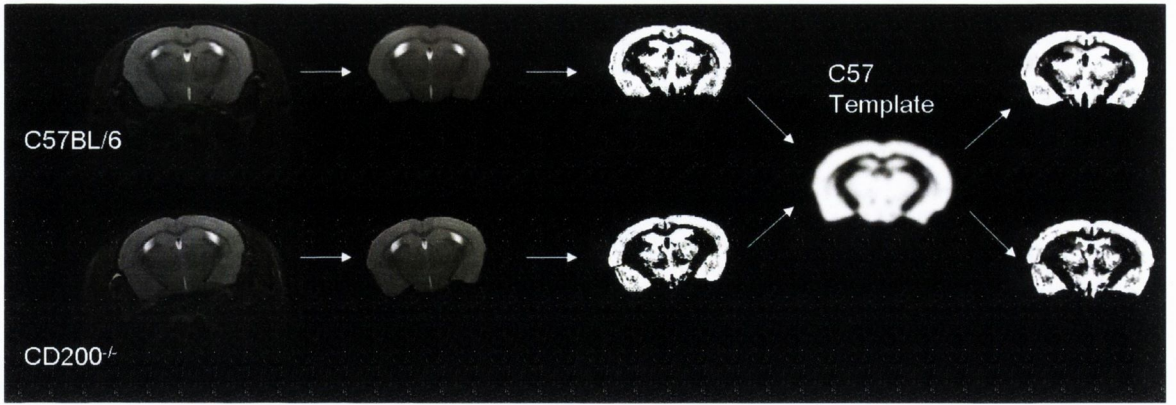


Figure 2.2: Pipeline of VBM methodology, indicating the brain extraction and spatial registration steps

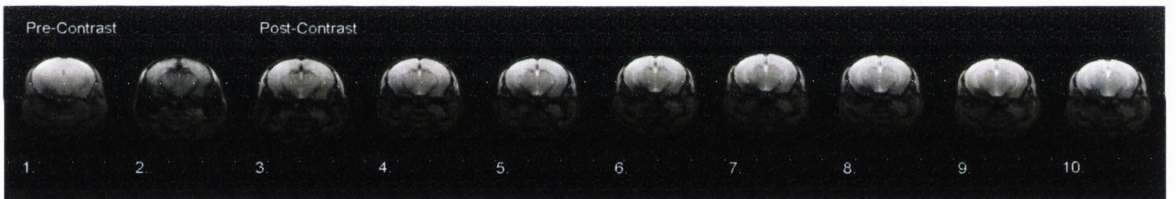


Figure 2.3: Sample data set displaying pre- (repetition 1) and post- (repetitions 3-10) contrast images following injection of the gadolinium-based contrast agent, Magnevist (repetition 2)

2.3 Animals

2.3.1 Groups and maintenance of animals

Specific pathogen-free (SPF) groups of 4 month-old (weighing 19g-29g), 6-9 month-old (21g-33g), C57BL/6 (WT) and CD200^{-/-} mice used in this study were supplied by the Bio-resources Unit, Trinity College. CD200^{-/-} mice were generated by recombination of the CD200 gene as previously described (Hoek *et al.*, 2000) and backcrossed to the C57BL/6 strain. Groups of age-matched C57BL/6 mice were purchased from Harlan UK Ltd. (Bicester, UK).

Groups of 13-14 month-old (weighing 31g-56g) APP^{swe}/PS1^{dE9} mice were also used in this study. Transgenic mice from a colony of APP/PS1 mice, purchased from the Jackson Laboratory (US), were used to form breeding pairs with C57BL/6 mice. Groups of 13-14 month-old wildtype (WT) littermates (weighing 31g-54g) were used as age-matched controls in these experiments. These were supplied from a breeding colony in an SPF housing facility in the Bio-resources Unit (Trinity College Institute of Neuroscience). A mixture of male and female mice was used in these studies; the exact numbers are detailed in the relevant methods sections.

Animals were housed in a controlled environment under a 12-hour light-dark cycle at an ambient temperature of 22°C-23°C; animals were maintained under veterinary supervision in the animal housing centre (Trinity College Institute of Neuroscience, Trinity College Dublin, Dublin 2, Ireland). throughout the study and housed in groups of either 2 or 3 per cage. All animals used in these studies had access to normal laboratory chow and water on an *ad libitum* basis. All experiments were carried out under a license obtained from the Department of Health and Children (Ireland) under the Cruelty to Animals Act 1876 and the European Community Directive, 86/609/EEC, and in agreement with experimental procedures laid down by the local ethics committee. Every effort was made to minimise stress to the animals at all stages of the study.

2.4 Animal experiments

2.4.1 Analysis of the age-related changes in $CD200^{-/-}$ mice

To investigate the effect of age and genotype on T_1 and T_2 relaxometry, anatomical volumetry and blood flow and volume, WT and $CD200^{-/-}$ mice were scanned at 9, 13 and 17 months of age. At 13 months ('middle-age'), half of each group were sacrificed for immunohistochemical analysis, while the remaining mice were re-scanned at 17 months. Groups of young (4 months old) WT mice ($N = 8$) and $CD200^{-/-}$ mice ($N = 8$) were scanned to provide a young, baseline measurement. Mice were scanned as outlined below (Figure 2.4) and allowed to recover and were monitored for any possible ill side-effects of the anaesthesia or scanning procedure. The magnet control room and facilities were converted to 'clean room' status for mice undergoing the longitudinal study by disinfecting bench surfaces, cleaning floors and the wearing of tyvek suits throughout the duration of the scanning period, at the end of which the mice were returned to their housing facilities.

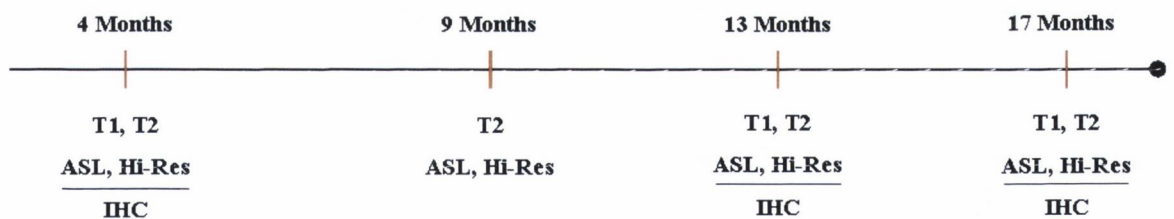


Figure 2.4: Timeline of longitudinal $CD200^{-/-}$ study

2.4.2 Analysis of the effects of LPS treatment in WT and CD200^{-/-} mice

The effects of LPS treatment on 6-8 month-old WT and CD200^{-/-} mice were investigated. Mice were randomly divided into control and experimental groups (N = 6-8/group). The control groups received an intraperitoneal (ip) injection of sterile saline (200µl). One experimental group received an ip injection of LPS (200µl; 10µg/mouse diluted in sterile saline) and the second experimental group received an ip injection of LPS (200µl; 50µg/mouse diluted in sterile saline). LPS was prepared from *Escherichia coli* (E. coli) serotype EH 100 (Ra) (Alexis Biochemicals, Switzerland). All injections were carried out in the MRI control room.

Mice were anaesthetized (see section 2.1.2) and T₁- and T₂-weighted relaxometry scans were acquired 2.5 and 3.5 hours post LPS administration to assess the effect of LPS administration throughout the 4 hour timepoint. Tail-vein cannulations were carried out in these mice (see section 2.1.3) and BBB permeability to the gadolinium-based contrast agent gadopentetate dimeglumine was assessed using contrast enhanced MRI in mice that received the 50µg LPS treatment. Animals were sacrificed following scanning, 4 hours after LPS injection. Brains were rapidly removed, hemisected, and prepared for immunohistochemistry (right hemisphere) and mRNA analysis by quantitative polymerase chain reaction (qPCR; left hemisphere). In the case of qPCR, one hemisphere per animal was carefully dissected into hippocampal and cortical tissue. A timeline of this study is presented in Figure 2.5.



Figure 2.5: Timeline of LPS study

2.4.3 Analysis of the effect of inducing BBB permeability in WT and APP/PS1 mice

Groups of middle-aged (13-14 month-old, N = 7-9/group) APP/PS1 and WT littermates were randomly assigned to control and experimental groups. The control groups received an iv injection of a non-target control siRNA solution (20µg/mouse; Applied Biosystems, Germany) diluted in nuclease-free H₂O (400µl; Applied Biosystems, Germany), while the treatment groups received an iv injection of siRNA solution targeting both claudin 5 (20µg/mouse; Applied Biosystems, Germany) and occludin (20µg/mouse; Applied Biosystems, Germany) diluted in nuclease-free H₂O (400µl; Applied Biosystems, Germany). Mice were individually placed in a custom-built 60ml volume plastic tube that was open ended at one end, but filled with a rubber stopper at the opposite end. The mouse's body was placed head first inside this tube, with the mouse's head positioned under the rubber stopper. This rubber stopper had an air hole drilled through it to provide a continuous supply of air. The protruding tail was warmed for 5 minutes prior to injection. Injections were rapidly carried out using a 30 gauge needle (Introcan, Ireland) with a 1ml syringe. T₁- and T₂-weighted imaging was carried out 48 hours after injection, and following this, mice were assessed for BBB permeability (see section 2.1.3). Following scanning, tissue was prepared for immunohistochemical staining of glial activation, and PCR analysis of pro-inflammatory cytokines and BBB proteins.

2.5 Preparation of tissue

2.5.1 Dissections and preparation of tissue

Following MR scanning, brain tissue was harvested from all mice. In all studies, mice were sacrificed by cervical dislocation and decapitation whilst still under anaesthesia. The scalp tissue was carefully removed using curved forceps and fine surgical scissors. The brain was rapidly removed and placed on a chilled Petri dish placed on ice. The cerebellum was removed and the remaining brain was hemisected. The left hemisphere was coated in optimal cooling temperature (OCT) compound (Tissue-Tek, US) and placed cutting surface down onto a pre-labelled cork disc (R.A.

Lamb, UK). This was slowly submerged and snap-frozen in a bath of isopentane (Methylbutane; Sigma-Aldrich, UK) in liquid nitrogen (Cryoproducts, Ireland), placed in aluminium foil and stored at -80°C , and subsequently sectioned for light microscopy. The thalamus of the right hemisphere was quickly removed using a curved forceps and discarded, and the hippocampus was carefully extracted. The remaining cerebral cortical tissue was halved into anterior and posterior sections with a surgical scalpel. This tissue was placed in Eppendorf tubes, snap-frozen in liquid nitrogen and stored at -80°C for subsequent isolation and analysis of mRNA. Unless otherwise noted, mRNA analysis is taken from the anterior portion of the cortex.

2.6 Analysis of mRNA by qPCR

2.6.1 Preparation of tissue for mRNA isolation

mRNA was extracted from snap-frozen cortical and hippocampal tissue from WT and $\text{CD200}^{-/-}$, control and LPS-treated, mice and from cortical tissue of siRNA-treated WT and APP/PS1 transgenic mice. In all cases, samples were thawed on ice and cell lysis mastermix (353.5 μl ; RA1 buffer containing 1% β -mercaptoethanol; Nucleospin RNA II, Macherey-Nagel; Germany) was added to each sample in RNase-free tubes. These samples and cell lysis mastermix were homogenised for extraction of RNA with a Polytron homogeniser (2 x 5 second pulses; PT 1200E; Kmematica, Switzerland) at high speed.

2.6.2 Protocol for RNA isolation

To remove any insoluble tissue and to reduce viscosity, the lysate of each sample was added to a NucleoSpin Filter placed in an Eppendorf collecting tube and centrifuged at 11,000g for 1 minute. The NucleoSpin Filter column was discarded and ethanol (350 μl ; 70%; Sigma, UK) was added to the lysate. The ethanol and lysate were mixed and loaded onto NucleoSpin RNA II columns. The new column and lysate were added to new collecting tubes and centrifuged at 8,000g for 30 seconds, allowing the RNA to bind to the column (the addition of ethanol improves this binding). The column

was removed and added to a new collecting tube. The silica membrane was desalted by adding membrane desalting buffer (350 μ l) and centrifuged at 11,000g for 1 minute to dry the membrane. To digest the DNA, DNase reaction mixture (95 μ l) was added to the column, and samples were incubated at room temperature for 15 minutes. The silica membrane was washed with RA2 buffer (200 μ l), deactivating the DNAses, and centrifuged at 11,000g for 30s to dry, and added to a new collecting tube. The silica membrane was washed with RA3 buffer (600 μ l), centrifuged at 11,000g for 30 seconds, and added to a new collecting tube. The silica membrane was once again washed with RA3 buffer (250 μ l), centrifuged at 11,000g for 2 minutes to completely dry the membrane, and placed into nuclease-free 1.5ml collecting Eppendorf tubes. The RNA was eluted in RNase-free H₂O (60 μ l) and centrifuged at 11,000g for 1 minute. RNA concentration was quantified using a NanoDrop-spectrophotometer (ND-1000 v3.5; Nanodrop Technologies Inc., US).

2.6.3 Reverse Transcriptase for complimentary DNA (cDNA) synthesis

Total mRNA (1 μ g) was reverse-transcribed into complimentary DNA (cDNA) using a high-capacity cDNA archive kit (Applied Biosystems, Germany) according to the protocol supplied by the manufacturer. RNA (1 μ g) was added to fresh tubes containing the appropriate amount of nuclease-free H₂O to make a final volume of 30 μ l. A 3x mastermix was prepared containing 10x RT buffer (6 μ l), 25x dNTPs (2.4 μ l), 10x random primers (6 μ l), multiscribe reverse transcriptase (3 μ l) and nuclease-free water (12.6 μ l). The mastermix (30 μ l) was added to the RNA and nuclease-free H₂O, and tubes were spun and incubated at 25°C, followed by 2 hours at 37°C in a thermocycler (PTC-200, Peltier Thermal Cycler; MJ Research, Ireland).

2.6.4 cDNA amplification by Q-PCR

The expression of CD11b, CD40, GFAP, Il-1 β , IL-6, TNF- α , claudin 5, claudin 12, and occludin mRNA was assessed in cortical and hippocampal tissue. Primers and probes were delivered as “TaqMan ® Gene Expression Assays” (Applied Biosystems, Germany). For each analysis, a PCR mastermix, composed of Taqman Universal PCR Mastermix (12.5 μ l/ sample), mouse β -actin RNA (1.25 μ l/ sample) as the endogenous

control and the specific primer (1.25 μ l) for each target gene was prepared (see Table 2.8 for primer assay numbers). In all cases, cDNA was diluted at a ratio of 1:4 (2.5 μ l cDNA and 7.5 μ l RNA-free H₂O) and added to a 96-well reaction plate (Applied Biosystems, US). Mastermix for each target gene (15 μ l) was added to each well, giving a total reaction volume of 25 μ l/well. Samples were centrifuged at 2,000g for 3 minutes, and real-time PCR was carried out on an Applied Biosystems ABI Prism 7300 real-time Sequence Detection System v1.3.1 (Applied Biosystems, US). The PCR consisted of 60 cycles, with 2 minutes at 50°C, 10 minutes at 95°C, 15 seconds per cycle at 95°C for denaturation and 1 minute at 60°C to ensure complete extension of the PCR product.

2.6.5 PCR Quantification

Analysis of gene expression values was performed using the efficiency-corrected comparative $\Delta\Delta$ CT method. Target genes from different samples were compared with the expression of β -actin, which acted as an endogenous control. These values were normalized to the control sample, and differences between samples were expressed as a ratio. Values are expressed as relative quantities of specific genes (7300 real-time PCR Software; Applied Biosystems, US).

Gene Name	Gene Description	TaqMan Gene Expression Assay Number
CD11b	Integrin alpha M	Mm00434455_m1
CD40	Cluster of differentiation 40	Mm00441891_m1
GFAP	Glial Fibrillary Acidic Protein	Mm01253033_m1
TNF- α	Tumor necrosis factor- α	Mm00443258_m1
IL-1 β	Interleuken 1- β	Mm00434228_m1
Il-6	Interleuken 6	Mm00446190_m1
Cldn5	Claudin 5	Mm00727012_s1
Cldn12	Claudin 12	Mm01316311_m1
Ocln	Occludin	Mm00500912_m1

Table 2.2: Mouse PCR primer assay numbers

2.7 Immunohistochemical analysis

2.7.1 Preparation of slides

Prior to slicing of tissue and immunohistochemical analysis, all slides were covered in a subbing solution to improve adhesion between the tissue and slide. Gelatine (2.5g; Fluka, Switzerland) was dissolved in 500ml dH₂O that had been heated to a low temperature. Chromium potassium sulphate (0.25g; Sigma Aldrich, UK) was added to the solution, and the solution was heated to a temperature of 60°C. The subbing solution was filtered into a staining tank using filter paper (Whatman International, UK) and clean slides were immersed briefly into this solution (30-60 seconds). The slides were drained of surplus solution and were laid out to dry overnight.

2.7.2 Preparation of slices and slicing

Samples which were mounted on cork discs were placed inside the cryostat (Leica CM 1900; Leica Microsystems, Ireland), and allowed to equilibrate to -20°C for 30 minutes, the temperature at which the slicing was carried out. Tissue sections were sliced at a thickness of 10µm, and anatomical position was assessed using Toluidine-Blue staining viewed under a light microscope. When the hippocampus became visible, 30 sections (3 per slide) were cut and placed on 10 gelatine-coated, twin-frosted, premium microscope slides (76 x 26mm; Ramboldi, Cyprus). The slices were cut in the coronal view to match with the MR scanning protocols. Following slicing, slides were laid to dry for 20 minutes at room temperature before being stored at -20°C.

2.7.3 Immunohistochemical analysis of CD11b

Frozen brain sections were brought to room temperature for approximately 30 minutes. Hydrophobic wells were created around the 3 slices with a cytomation pen (Dako, UK). All sections were fixed in an ice-cold methanol and acetone solution (1:1; Sigma-Aldrich, US) for 5-10 minutes. Endogenous peroxidases were blocked with 0.3% H₂O₂ in phosphate buffer saline (PBS) for 5 minutes (200µl/ slice). Sections were washed with PBS (2 x 10 minutes) and blocked with 10% rabbit serum (Vector

Laboratories, UK). Sections were incubated overnight at room temperature with rat anti mouse CD11b primary antibody (200µl/ slice; 1:100 dilution in 5% rabbit serum in PBS; AbD Serotec, UK). Negative controls were incubated in 5% rabbit serum in PBS alone. The following day, sections were washed in PBS (2 x 10 minutes) and incubated for 2 hours in biotinylated rabbit anti-rat secondary antibody (200µl/ slice; 1/200 in 5% rabbit serum in PBS; Vector, UK) at room temperature. Sections were rinsed (2 x 10 minutes) and incubated for 30 minutes in Vectastain Elite ABC reagent (2 drops of A/B in 5ml PBS; Vector Laboratories, US) and washed in PBS (2 x 10 minutes) to rinse off excess ABC. Sections were developed using the substrate 3, 3 diaminobenzidine (DAB) enhanced liquid substrate system tetrahydrochloride (1 drop solution B in 1ml solution A; Aldrich, UK) for 10 minutes. The development of the DAB reaction was monitored throughout this incubation period. Sections were counterstained with methyl green (1% in distilled water; Sigma Aldrich, UK) for 10 minutes. Distilled water was used to stop this reaction. The sections were dehydrated through a succession of graded alcohols (75% ethanol in distilled water (5 seconds), 95% ethanol in distilled water (5 seconds), 100% ethanol (30 seconds), 100% ethanol (1 minute); Sigma, UK). Finally, the slides were immersed in 100% xylene (2 x 2 minutes; VWR International, UK). Coverslips (60mm; VWR International, UK) were mounted onto the slides using dinbutyl phthalate in xylene (DPX; RA Lamb, UK) and left to set in a fume hood overnight. Stained slices were viewed on an Olympus IX51 light microscope with a built-in camera (Olympus, Japan).

2.7.4 Immunohistochemical analysis of GFAP

Frozen brain sections were fixed and prepared for staining as described in section 2.7.3, and permeabilised with 0.1% Triton X-100 surfactant (Sigma, UK) for 15 minutes and washed (3 x 5 minutes). Sections were blocked with 10% goat serum (Vector Laboratories, UK) in PBS for 30 minutes. Sections were incubated for 90 minutes at room temperature with rabbit anti mouse GFAP primary antibody (200µl/ slice; 1:2000 dilution in 1% bovine serum albumin (BSA) in PBS; Dako, UK). Negative controls were incubated in 1% BSA in PBS alone. Sections were rinsed in PBS (3 x 5 minutes) and incubated for 40 minutes in biotinylated goat anti rabbit secondary antibody (200µl/ slice; 1/200 in 1% BSA in PBS; Vector, UK) at room temperature.

Sections were rinsed again (3 x 5 minutes) and incubated for 30 minutes in Vectastain Elite ABC reagent (1 drops of A/B in 5ml PBS; Vector Laboratories, US) and washed again in PBS (3 x 5 minutes) to rinse off excess ABC. Sections were developed using the DAB substrate system as described in section 2.7.3.

2.7.5 *Quantification of DAB-enhanced staining*

Representative pictures of DAB-enhanced CD11b and GFAP positive staining from the three studies were analysed using the Immunoratio plugin (<http://imtmicroscope.uta.fi/immunoratio/>) available for the ImageJ software package (Tuominen *et al.*, 2010). Firstly, the images were uploaded for image segmentation. The automated program then segments the image into DAB and nuclear-stained regions, and calculates the percentage of DAB-stained nuclear area over the total nuclear area (labelling index) in the uploaded image. The program also generates a pseudo-coloured result image matching the area segmentation.

The advanced mode of analysis was used for the analysis in these studies. Briefly, the settings used were; Image scale for detection of nuclei: 9.3pixels/ μm , Brown threshold adjustment: -50, Blue threshold adjustment: +15. The percentage DAB-enhancement/ total nuclear area was calculated for cortical and hippocampal regions for the study groups, and averaged for statistical analysis. Unless otherwise indicated, representative cortical images are taken from the motor cortex, and from the dentate gyrus of the hippocampus.

2.7.6 *Immunohistochemical staining of A β by Congo red*

Frozen brain sections from APP/PS1 and WT littermates were stained for the presence of A β plaques using the Congo red staining method. Sections were allowed equilibrate to room temperature for 30 minutes. Hydrophobic wells were created around the 3 slices with a cytostation pen (Dako, UK). Sections were fixed in ice-cold methanol for 5 minutes, and washed in PBS (2 x 5 minutes). During these washes, 1 M NaOH (2ml) was added to saturated NaCl (200ml; 80% ethanol in dH₂O) to produce an alkaline solution. Slices were incubated in this alkaline solution at room temperature for 20 minutes. During this incubation, Congo red solution (0.2% Congo red dye in

saturated NaCl; Sigma Aldrich, UK) was filtered through a syringe using a cellulose acetate membrane filter (0.2 μ M Supor membrane Acrodisc syringe filters; Pall Corporation, US) and 200ml of this filtered solution was added to NaOH (2ml) to create an alkaline solution. Brain slices were incubated in this solution at room temperature for 30 minutes. Slides were rinsed in dH₂O (2 dips) to remove excess dye and slices were incubated in methyl green solution (1% in dH₂O; Sigma Aldrich, UK) for 10 minutes to counterstain the chromatin. The slices were washed in dH₂O (1 dip) to remove surplus methyl green solution, and were dehydrated by dipping 6 times in a succession of graded alcohols (95% ethanol, 100% ethanol, 100% ethanol; Sigma, UK). Sections were briefly left to dry, before being incubated in 100% xylene (3 x 5 minutes; VWR International, UK). Coverslips (60mm; VWR International; UK) were mounted onto the slides using dibutyl phthalate in xylene (DPX; RA Lamb, UK) and allowed to set and dry in a fume hood overnight.

2.7.7 Quantification of A β plaques

Congo red positive-A β plaques were counted in 6 half hemisphere sections per mouse. The examiner was blind as to which treatment group the mouse belonged. Sections were viewed and plaques counted under the same light settings, and results were expressed as average number of plaques per section per animal.

2.7.8 Extraction of soluble and insoluble A β from brain tissue

Snap-frozen cortical tissue from control and siRNA-treated WT and APP/PS1 mice was homogenised in 5 volumes (w/v) of homogenising buffer (SDS/NaCl in dH₂O with proteases). The samples were centrifuged at 15,000 rpm for 40 minutes at 4°C. The supernatant samples were removed to extract SDS-soluble A β and the pellets were kept for extraction of insoluble A β .

Supernatants were equalised (3 mg/ml) with homogenising buffer using a bicinchoninic acid protein assay. Equalised supernatant samples were neutralised by the addition of 10 % (w/v) 0.5 M Tris-HCl (pH 6.8). Samples were stored at -20 °C for later detection of soluble A β .

Pellets were incubated in guanidine buffer (50 μ l; 5 M guanidine-HCl/50 mM Tris-HCl, pH 8, Sigma-Aldrich, UK) for 4 hours on ice, and centrifuged at 15,000 rpm for 30 minutes at 4 °C. Supernatant samples were equalised (0.3 mg/ml) with guanidine buffer and stored at -20 °C for later detection of insoluble A β .

2.7.9 Detection of soluble and insoluble A β concentrations in cortical tissue by multi-spot ELISA

Concentrations of soluble and insoluble A β were determined using “MSD® 96-well multi-spot 4G8 A β triple ultra-sensitive assay” kits (Meso Scale Discovery, USA). All solutions and reagents used were supplied by Meso Scale Discovery. Multi-spot A β 3-plex plates were blocked with 1% Blocker A (150 μ l/well; 50 ml 1 X Tris wash buffer: 0.5 g Blocker A) for 1 hour at RT with vigorous shaking (300-1000 rpm). Plates were washed 3 times in 1 X Tris wash buffer (TWB) and detection antibody solution (25 μ l/well; 60 μ l 50 X SULFO-TAG 4G8 detection antibody, 30 μ l 100 X Blocker G in 2910 μ l 1% Blocker A solution) was added. SDS-solubilised samples were diluted in Blocker A (200 μ g/ml) plus protease inhibitors (1:100) and guanidine-treated samples were diluted in Blocker A (0.3 μ g/ml) solution. Standards were prepared by serial dilutions of recombinant human A β ₁₋₃₈ (0-3,000 pg/ml), A β ₁₋₄₀ (0-10,000 pg/ml) and A β ₁₋₄₂ (0-3,000 pg/ml) in 1% Blocker A. Samples and standards (25 μ l/well) were added in duplicate to the appropriate wells of the 96-well plates which were incubated for 2 hours at RT with vigorous shaking (300-1000 rpm). Plates were washed in wash buffer and 2 X MSD read buffer (150 μ l/well; 10 ml dH₂O: 10 ml 4 X MSD read buffer) was added. Plates were read immediately using a Sector Imager plate reader (Meso Scale Discovery, US) and A β concentrations in test samples were evaluated with reference to the standard curve prepared using A β ₁₋₃₈ (0-3,000 pg/ml), A β ₁₋₄₀ (0-10,000 pg/ml) and A β ₁₋₄₂ (0-3,000 pg/ml).

2.7.10 Detection of A β concentrations in serum samples by multi-spot ELISA

Concentrations of A β in serum were determined using “MSD® 96-well multi-spot 4G8 A β triple ultra-sensitive assay” kits (Meso Scale Discovery, US). Plates were prepared as per section 2.7.8 with the exception that Blocker G was omitted from the

detection antibody solution. Plates were read immediately using a Sector Imager plate reader (Meso Scale Discovery, US) and A β concentrations in serum samples were evaluated with reference to the standard curve prepared using A β ₁₋₃₈ (0-3,000 pg/ml), A β ₁₋₄₀ (0-10,000 pg/ml) and A β ₁₋₄₂ (0-3,000 pg/ml).

2.8 Statistical Analysis

Data are expressed as means \pm standard error of the mean (SEM). A one-tailed or two-tailed Student's t-test for unpaired means, or a two-way analysis of variance (ANOVA) was performed, where appropriate, to determine whether significant differences existed between means. When a two-way ANOVA indicated significance (* $p < 0.05$), a Bonferroni post-hoc test was employed to determine which conditions were significantly different from each other. Statistical analyses were carried out using the Prism software (Graphpad Prism, v 4.0; US).

Chapter 3

Analysis of the age-related changes in CD200^{-/-} mice

3.1 Introduction

Microglial cells are the resident antigen presenting cells of the CNS, and as such, form the interface between the neural parenchyma and the immune system. Resting microglia show a downregulated immunophenotype adapted to the specialised microenvironment of the CNS (Kreutzberg, 1996). One mechanism that has been shown to regulate and control microglial activation is through ligation of the CD200 receptor, which is expressed on microglia. It has been shown that mice lacking CD200, which is expressed on neurons and microvascular endothelium (Taylor *et al.*, 2005), spontaneously exhibit many features of activated microglia, including shorter, more ramified processes, and increased expression of CD11b and CD45 (Neumann, 2001). The regulatory role of CD200-CD200R signalling can be seen in the profound effect on neuronal tissues, where CD200-deficient mice have a significantly accelerated onset of inflammation in experimental models of autoimmunity, including EAE (Hoek *et al.*, 2000; Chitnis *et al.*, 2007) and EAU (Broderick *et al.*, 2002).

Several studies have shown that ageing is associated with an impairment in memory (Long *et al.*, 1998), LTP function (Murray & Lynch, 1998) and these impairments are accompanied by a spontaneous increase in pro-inflammatory cytokines (O'Donnell *et al.*, 2000) and astrocytic activation (Cotrina & Nedergaard, 2002). It has also been shown that activation of microglia induces the release of iron from ferritin (Kondo *et al.*, 1995; Yoshida *et al.*, 1995). Both iron and ferritin are present in activated microglia, in particular in the aged compared with young, rat brain (Benkovic & Connor, 1993) and in the brains of PD patients (Jellinger *et al.*, 1990). While the microglial response is enhanced in the brain of aged rats (Ogura *et al.*, 1994) and mice (Lyons *et al.*, 2007), the first aim of this study was to determine whether aged mice lacking CD200 would show an enhanced microglial and astrocytic phenotype compared with WT mice.

MRI takes advantage of the natural spin and magnetization properties of water molecules in brain tissue. Once placed inside the magnetic field of a MR scanner, protons line up in the direction of the externally applied magnetic field. Radio frequency pulses flip the orientation of the protons' magnetization. The time constants that describe how the particles 'relax' or return to equilibrium are termed T_1 and T_2 times, referring to the recovery parallel and perpendicular to the magnetic field,

respectively. These parameters are effected by the type of tissue in which the protons reside, including the proportion of free water (Barnes *et al.*, 1988), and the presence of magnetic substances, for example iron-laden amyloid plaques in AD (Jack *et al.*, 2005).

Several studies have shown an association between MR parameters and changes that are linked with neuroinflammation in the brain. These include an increase in the T_1 signal following axonal loss (van Walderveen *et al.*, 1998) and gliosis (Parry *et al.*, 2002). T_1 increases have also been found to occur following increased astrocytic activation in low flow ischemia and excitotoxicity (Sibson *et al.*, 2008). It has been shown that the aged-related increase in GFAP mRNA and protein levels in the rat brain are associated with a concomitant increase in T_1 relaxation values and, importantly, that treatment with rosiglitazone, a PPAR γ agonist, reversed both the age-related increased in astrocytosis and T_1 relaxometry (Cowley *et al.*, 2010). T_2 decreases have been principally associated with iron deposits in the brains of ageing mice (El Tannir El Tayara *et al.*, 2006). The second aim of this study was to describe the age-related changes in T_1 and T_2 parameters in WT and CD200-deficient mice.

The final aim of this study was to utilise the power of MRI to assess the changes in brain volume and blood flow. VBM of the rodent brain, though common in human brain volumetric analysis, is a relatively new technique. Several studies have shown significant volumetric deficits in mouse models of neurodegenerative conditions, including models of Huntington's disease (Sawiak *et al.*, 2009) and AD (Yang *et al.*). ASL provides a non-invasive measurement of cerebral blood flow, where labelled water molecules are delivered to a volume of interest in the brain, where they are exchanged between the capillary bed and extravascular water (Kelly *et al.*, 2009). The MTT is defined as measuring the time taken for a bolus to reach a ROI, while the MTT described the dispersion of the bolus at the ROI (Weisskoff & Rosen, 1995). It was hypothesized here that volume, as well as MTT and CTT, may vary under the neuroinflammatory changes that occur with age and in the absence of CD200.

The following analyses were therefore undertaken in this study:

- (i) T_1 and T_2 relaxometry parameters in WT and CD200^{-/-} mice.
- (ii) Immunohistochemical analysis of microglial and astrocytic phenotype in WT and CD200^{-/-} mice

- (iii) Volumetric differences between CD200^{-/-} and WT mice.
- (iv) MTT and CTT assessment in perfusion-weighted ASL maps.

3.2 Methods

Groups of 4 month-old (19g-29g) and 9 month-old (21g-40g) WT and CD200^{-/-} mice were anaesthetized with isoflurane (see section 2.1.2) and underwent MRI scanning in this study. The 4 month-old WT mice consisted of 6 males and 2 females, and the CD200^{-/-} mice consisted of 5 males and 3 females. At 9 months, the WT mice consisted of 7 males and 9 females, and the CD200^{-/-} mice consisted of 6 males and 10 females. The MR protocol in this study was comprised of relaxometry, anatomic and perfusion-weighted imaging (see sections 2.1.4, 2.1.5, 2.1.6 and 2.1.7 for specific scan details). T₁ relaxometry was not performed in 9 month-old mice. The young mice (n=8/group) used in this study were sacrificed by cervical dislocation after their single scan and brain tissue was taken for analysis. The 9 month-old mice (n=16/group) were scanned again at 13 months, at which point half of each group were sacrificed for immunohistochemical analysis. The remaining mice in each group were scanned again at 17 months, sacrificed, and brain tissue was prepared for staining. The tissue obtained from the 3 timepoints provided a platform for the longitudinal assessment of microglial and astrocytic activation (CD11b and GFAP, respectively; see sections 2.7.3 and 2.7.4) in the cortex and hippocampus of these mice. The immunohistochemical results from the aged mice were taken as positive controls. The CD11b and GFAP staining was quantified using the Immunoratio plugin for ImageJ (see section 2.7.5).

T₁ and T₂ relaxation times and MTT and CTT values were calculated using the ImageJ software platform, while a volumetric analysis was carried out using the FSL software package (see sections 2.2.1, 2.2.2 and 2.2.3 for specific details). Data are presented as means ± SEM, and a 2-way ANOVA was performed to determine whether significant differences existed in the data. Bonferroni post-hoc analyses were carried out to determine where individual differences lay (see section 2.8 for specific details). VBM results are presented as a SPM overlaid on a study-specific grey matter template in the coronal view, indicating specific volumetric differences between groups using voxel-

wise statistics (maps are thresholded at $p < 0.05$ to indicate significance; see section 2.2.2).

3.3 Results

3.3.1 Body weights

Body weights from WT and CD200^{-/-} mice at 4, 9, 13 and 17 months are presented in Figure 3.1. Mean body weights of WT mice increased with age and the values at 9, 13 and 17 months of age were significantly increased compared with 4 months (^{***} $p < 0.001$; ANOVA). Mean body weights of CD200^{-/-} mice were significantly increased at 13, compared with 4 months (⁺⁺ $p < 0.01$; ANOVA). There was no significant genotype-related change.

3.3.2 Effect of genotype and age on T_1 relaxation times

To investigate the effect of genotype and age on T_1 relaxometry, CD200^{-/-} and WT mice were scanned at 4, 13 and 17 months. Analysis of T_1 relaxation times in the ROIs investigated in the RARE-VTR scans revealed significant increases in T_1 values in CD200^{-/-}, compared with WT, mice. Figure 3.2 shows that at 4 months, T_1 relaxation times were significantly increased in the cortex of CD200^{-/-} mice (1830 ± 22.67 ms; $n=8$) compared with WT mice (1746.25 ± 14.38 ms; $n=8$; ^{**} $p < 0.01$; ANOVA). This trend continued throughout the remaining timepoints of the study but these comparisons failed to reach statistical significance. At 13 and 17 months, cortical T_1 values in CD200^{-/-} mice were 1823.33 ± 11.08 ms ($n=6$) and 1811.66 ± 11.08 ms ($n=6$) respectively, and in WT mice were 1761.42 ± 12.98 ms ($n=6$) and 1774.28 ± 22.02 ms ($n=7$) respectively. There were no significant changes in cortical T_1 values with age.

T_1 relaxation times were also assessed in the hippocampus of these animals. Figure 3.3 shows that at 4 months, hippocampal T_1 values were significantly increased in CD200^{-/-} mice (1823.12 ± 22.57 ms; $n=8$) compared with WT mice (1711.87 ± 22.59 ms; $n=8$; ^{**} $p < 0.01$; ANOVA). This trend continued in the latter timepoints of the study but these comparisons failed to reach statistical significance. At 13 and 17 months,

hippocampal T_1 values in WT mice were 1724.23 ± 8.67 (n=13) and 1722.85 ± 22.93 (n=7) respectively, and in CD200^{-/-} mice were 1793.57 ± 20.69 (n=14) and 1762.50 ± 15.20 (n=6) respectively. As in the cortex, there were no significant changes in hippocampal T_1 values with age.

Longitudinal T_1 changes in the white matter regions of the corpus callosum and thalamus were also assessed. Figure 3.4 shows that mean T_1 values were similar in the corpus callosum of CD200^{-/-} mice and WT mice at all 3 timepoints. At 4 months, mean T_1 values of the corpus callosum in CD200^{-/-} mice were 1640.0 ± 18.70 ms (n=8) and in WT mice were 1622.5 ± 22.72 ms (n=8). At 13 months, T_1 values in CD200^{-/-} mice were 1596.42 ± 9.29 ms (n=14) and in WT mice were 1566.42 ± 12.90 ms (n=14) and at 17 months, T_1 relaxation times in CD200^{-/-} mice were 1606.66 ± 16.05 ms (n=6) and in WT mice were 1565.71 ± 15.56 ms (n=6). Figure 3.5 shows that mean T_1 values were also similar in the thalamus of CD200^{-/-} mice compared with WT mice at all 3 timepoints. At 4 months, thalamic T_1 values in CD200^{-/-} mice were 1516.87 ± 25.61 ms (n=8) and in WT mice were 1440.62 ± 14.18 ms (n=8). There was a trend towards statistical significance at this timepoint. At 13 months, mean thalamic T_1 values in CD200^{-/-} mice were 1486.78 ± 15.60 ms (n=14) and in WT mice were 1457.14 ± 13.38 ms (n=14). At the 17 month timepoint, T_1 values in CD200^{-/-} mice were 1467.5 ± 14.24 ms (n=6) and in WT mice were 1434.28 ± 12.02 ms (n=6).

Figure 3.6 presents a pictorial representation of these changes. There was a significant increase in voxel colour intensities in the grey matter regions of the cortex and hippocampus of the 4 month-old CD200^{-/-}, compared with the WT, mouse. No genotype-related difference was observed in the thalamus of corpus callosum. A coloured reference bar is also presented in this figure to display voxel colour intensities and their associated T_1 values.

3.3.3 *The effect of genotype and age on T_2 relaxometry*

To determine the effects of age and genotype on T_2 relaxometry, WT and CD200^{-/-} mice were scanned at 4, 9, 13 and 17 months of age. As with the T_1 assessment, analysis was carried out on the MSME scans using an ROI approach. Evaluation of T_2 relaxation times was first examined in the grey matter regions of the cortex and hippocampus. Figure 3.7 illustrates that T_2 relaxation times were

significantly decreased in the whole cortex of both genotypes with age. In WT mice, there was a significant decrease in cortical T_2 values at 9 months (50.82 ± 0.16 ms; $n=16$), compared with 4 months (51.61 ± 0.12 ms; $n=8$; $***p<0.001$; ANOVA). T_2 values were also significantly decreased at 13 months (50.80 ± 0.11 ms; $n=15$; $***p<0.001$; ANOVA) compared with 4 months, and at 17 months (50.57 ± 0.18 ms; $n=7$; $***p<0.001$; ANOVA) compared with 4 months. Likewise, in $CD200^{-/-}$ mice, there was an age-related decrease in cortical T_2 relaxation times. Cortical T_2 values were decreased in $CD200^{-/-}$ mice at 9 months (51.25 ± 0.12 ms; $n=16$) compared with 4 months (52.24 ± 0.19 ms; $n=7$; $+++p<0.001$; ANOVA). Cortical T_2 values in $CD200^{-/-}$ mice were also decreased at 13 months (51.25 ± 0.12 ms; $n=13$; $+++p<0.001$; ANOVA) compared with 4 months, and at 17 months (50.86 ± 0.14 ms; $n=6$; $+++p<0.001$; ANOVA) compared with 4 months of age. Although there was a significant genotype effect ($***p<0.001$; ANOVA) in the overall data, comparisons between WT and $CD200^{-/-}$ mice at the individual timepoints failed to reach statistical significance.

Figure 3.8 illustrates the age-related changes in T_2 relaxometry in the motor cortex of WT and $CD200^{-/-}$ mice. In WT mice, there was a significant decrease in T_2 values at 9 months (50.39 ± 0.18 ms; $n=16$) compared with 4 months (52.70 ± 0.27 ms; $n=8$; $***p<0.001$; ANOVA). T_2 values were also significantly decreased at 13 months (50.26 ± 0.22 ms; $n=15$; $***p<0.001$; ANOVA) compared with 4 months of age, and also at 17 months (50.16 ± 0.19 ms; $n=7$; $***p<0.001$; ANOVA) compared with 4 months of age. Similarly, T_2 values in motor cortex of $CD200^{-/-}$ mice were significantly decreased at the 3 later timepoints. There was a significant decrease in T_2 relaxation times in the motor cortex of $CD200^{-/-}$ mice at 9 months (50.94 ± 0.19 ms; $n=16$) compared with 4 months of age (52.59 ± 0.38 ms; $n=7$; $+++p<0.001$; ANOVA). T_2 values were also decreased at 13 months (50.49 ± 0.23 ms; $n=13$; $+++p<0.001$; ANOVA) and 17 months (50.14 ± 0.09 ms; $n=6$; $+++p<0.001$; ANOVA) compared with 4 months of age. There was no genotype-associated difference in WT and $CD200^{-/-}$ mice at any of the 4 timepoints.

T_2 relaxation times were also measured in the entorhinal cortex of the MSME scan of WT and $CD200^{-/-}$ mice. Figure 3.9 illustrates the age-related changes in T_2 values of the entorhinal cortex of WT and $CD200^{-/-}$ mice at all 4 experimental timepoints of the study. There was no change in T_2 values of the entorhinal cortex in WT mice at 9 months (52.95 ± 0.13 ms; $n=16$) compared with 4 months of age ($53.13 \pm$

0.24 ms; n=8). However, there was a significant decrease in T₂ relaxometry in the entorhinal cortex of WT mice at 13 months (51.92 ± 0.14 ms; n=15; ***p<0.001; ANOVA) compared with 4 months. There was also a significant age-related decrease at 13, compared with 9, months (§§§p<0.001; ANOVA). There was no age-related change between 4 and 17 months (52.72 ± 0.25 ms; n=7). However, there was an increase in T₂ values of the entorhinal cortex of WT mice between 17 and 13 months (δp<0.05; ANOVA). A similar age-related change in T₂ values of the entorhinal cortex of CD200^{-/-} mice was noted. There was no change in T₂ values of the entorhinal cortex of CD200^{-/-} mice at 9 months (53.45 ± 0.18 ms; n=16) compared with 4 months (53.50 ± 0.18 ms; n=8) of age. There was a significant decrease in T₂ values in the entorhinal cortex CD200^{-/-} mice at 13 months (52.29 ± 0.20 ms; n=13; +++p<0.001; ANOVA) compared with 4 months, and compared with 9 months (°°°p<0.001; ANOVA). There was an age-related increase in T₂ values noted at 17 months (53.33 ± 0.32 ms; n=6; ##p<0.01; ANOVA) compared with 13 months. Genotype was a significant factor in the data (**p<0.01; ANOVA), however comparisons at the individual experimental timepoints failed to reach statistical significance.

The age- and genotype-related changes in T₂ relaxation times in the hippocampus of WT and CD200^{-/-} mice are presented in Figure 3.10. There was a significant age-related decrease noted in T₂ values in WT and CD200^{-/-} mice. In WT mice, there was a significant decrease in T₂ values at 9 months (50.60 ± 0.16 ms; n=16) compared with 4 months (51.35 ± 0.16 ms; n=8; **p<0.01; ANOVA). This significant decrease in T₂ relaxometry was also evident at 13 months (49.99 ± 0.14; n=15; ***p<0.001; ANOVA) and at 17 months (49.74 ± 0.48 ms; n=7; ***p<0.001; ANOVA) compared with 4 months of age. A similar age-related change in T₂ relaxometry was observed in the hippocampus of CD200^{-/-} mice. There was a significant decrease in hippocampal T₂ values at 9 months (50.84 ± 0.16 ms; n=16) compared with 4 months (52.03 ± 0.20 ms; n=7; +++p<0.001; ANOVA). This significant decrease was also observed at 13 months (50.37 ± 0.14 ms; n=13; +++p<0.001; ANOVA) and at 17 months (49.85 ± 0.09 ms; n=6; +++p<0.001; ANOVA) compared with 4 months of age. There was a significant decrease also noted in hippocampal T₂ values of CD200^{-/-} mice at 17, compared with 9, months (°°°p<0.001; ANOVA). As with the T₂ values recorded in the cortex, there was no genotype difference observed at any of the 4 timepoints in the

experiment, although genotype is a significant factor throughout the data overall (** $p < 0.01$; ANOVA).

T_2 relaxation times in the white matter regions of the corpus callosum and thalamus were also assessed at all 4 experimental timepoints. Figure 3.11 illustrates that in WT mice, there was a significant decrease in T_2 relaxometry at 9 months (41.00 ± 0.36 ms; $n=16$) compared with 4 months (44.41 ± 0.37782 ms; $n=8$; *** $p < 0.001$; ANOVA). There was also an age-related decrease in T_2 values of the corpus callosum at 13 months (40.32 ± 0.37 ms; $n=15$; *** $p < 0.001$; ANOVA) and at 17 months (41.40 ± 0.27 ms; $n=7$; *** $p < 0.001$; ANOVA) compared with values recorded at 4 months. A similar age-related decrease was observed in CD200^{-/-} mice. There was a significant decrease in corpus callosum T_2 values in CD200^{-/-} mice at 9 months (41.85 ± 0.42 ms; $n=16$) compared with 4 months (45.76 ± 0.40 ms; $n=7$; +++ $p < 0.001$; ANOVA). This age-related decrease was also observed at 13 months (41.59 ± 0.32 ms; $n=13$; +++ $p < 0.001$) and at 17 months (42.72 ± 0.35 ms; $n=6$; +++ $p < 0.001$; ANOVA) compared with values measured at 4 months. Although genotype was a significant factor in the data (** $p < 0.001$; ANOVA), no genotype difference in T_2 values of the corpus callosum was observed between WT and CD200^{-/-} mice at any of the 4 experimental timepoints.

Figure 3.12 illustrates the age-related changes in T_2 relaxometry in the thalamus of WT and CD200^{-/-} mice. There was an age related decrease in T_2 relaxation times in the thalamus of WT mice at 9 months (43.56 ± 0.14 ms; $n=16$) compared with 4 months (44.69 ± 0.17 ms; $n=8$; *** $p < 0.001$; ANOVA). This significant age-related decrease in thalamic T_2 values was also present at 13 months (43.51 ± 0.16 ; $n=15$) and at 17 months (43.30 ± 0.18 ms; $n=7$; *** $p < 0.001$; ANOVA) compared with 4 months. Additionally, there was an age-related decrease in T_2 values in the thalamus of CD200^{-/-} mice. There was a significant decrease in thalamic T_2 relaxation times in CD200^{-/-} mice at 9 months (44.02 ± 0.13 ms; $n=16$) compared with 4 months (45.01 ± 0.30 ms; $n=8$; +++ $p < 0.001$; ANOVA). This decrease was also evident at 13 months (44.30 ± 0.14 ms; $n=13$; + $p < 0.05$; ANOVA) and at 17 months (43.33 ± 0.16 ms; $n=6$; +++ $p < 0.001$; ANOVA) compared with values acquired at 4 months. There was also a significant decrease in thalamic T_2 values in CD200^{-/-} mice at 17 months compared with 9 months ($\delta p < 0.05$; ANOVA) and compared with 13 months ($\epsilon p < 0.01$; ANOVA). Genotype was a significant factor in these data (** $p < 0.01$; ANOVA), and at 13 months, T_2 values were significantly increased in CD200^{-/-}, compared with WT, mice ($\#p < 0.05$; ANOVA).

The age-related T_2 signal decreases in $CD200^{-/-}$ mice are illustrated visually in Figure 3.13, which presents parametric maps obtained from the MSME scans at all 4 experimental timepoints. These images suggest cortical and hippocampal voxels display decreased relaxation times in aged, compared with young, mice. A colour reference bar is included in this figure, which displays voxel colour intensities and their associated T_2 values.

3.3.4 The effect of age and genotype on GFAP immunoreactivity

Brain tissue from 4, 13 and 17 month old WT and $CD200^{-/-}$ mice was stained for GFAP and representative micrographs from the cortex and hippocampus of both genotypes are presented in Figures 3.14 and 3.15, respectively. Positive immunoreactivity is denoted by brown positive staining, while methyl green was used to counterstain the chromatin of the cells. Positive GFAP staining was low in sections prepared from 4 month old WT mice. There was an age-related increase in GFAP positive immunoreactivity in cortical sections prepared from WT mice at 13 and 17, compared with 4, months. There was also an age-related increase in GFAP positive staining in cortical sections prepared from $CD200^{-/-}$ mice, however, this increase was more pronounced in $CD200^{-/-}$ mice at each of the 3 timepoints. Figure 3.14 illustrates the age and genotype associated changes in GFAP expression in hippocampal sections prepared from WT and $CD200^{-/-}$ mice. Positive staining was low in hippocampal sections prepared from 4 month-old WT mice. There was no marked change in GFAP positive staining in hippocampal tissue prepared from WT mice throughout the remaining timepoints of the study. GFAP positive staining was more pronounced in hippocampal sections prepared from $CD200^{-/-}$, compared with WT, mice at 4 and 13, but not 17, months. There was an age-related decrease in GFAP positive immunoreactivity in hippocampal sections prepared from $CD200^{-/-}$ mice.

3.3.5 The effect of age and genotype on CD11b immunoreactivity

Figure 3.16 illustrates the changes in CD11b immunoreactivity in cortical tissue prepared from WT and $CD200^{-/-}$ mice. CD11b positive staining was low in cortical tissue prepared from 4 month old WT mice. There was an age-related increase in

CD11b immunoreactivity with more pronounced staining in cortical sections prepared from 13 and 17, compared with 4, month-old WT mice. There was also an age-related increase in positive staining for CD11b in cortical tissue prepared from CD200^{-/-} mice. However, there was a marked increase in CD11b staining in cortical tissue prepared from CD200^{-/-}, compared with WT, mice, in particular at 4 months and 17 months. The most marked staining for CD11b was seen in 17 month-old CD200^{-/-} mice.

Similar to the increase seen in the cortex, CD11b immunoreactivity was greater in sections prepared from the hippocampus of WT mice at 13 and 17 months, compared with 4 months (Figure 3.17). There was also an age-related increase in CD11b expression in hippocampal tissue prepared from CD200^{-/-} mice. Additionally, CD11b expression was markedly increased in hippocampal tissue prepared from CD200^{-/-}, compared with WT, mice at each of the 3 timepoints.

3.3.6 *The effect of genotype on anatomic volumetry*

One of the aims of this study was to perform a volumetric analysis of high-resolution T₂-weighted MR images of WT and CD200^{-/-} mice using the VBM methodology. Grey matter segmentations from WT and CD200^{-/-} mice were spatially aligned to a generic C57 template atlas and voxel-wise statistics were carried out for group comparisons. Figures 3.18, 3.19 and 3.20 illustrate the significant changes in the distribution of grey matter in CD200^{-/-}, compared with WT, mice at 9, 13 and 17 months, respectively. Statistical maps were thresholded at $p < 0.05$ to indicate significance. No significant differences were noted between groups at 4 months of age. At 9 months (Figure 3.18), there were significant grey matter deficits in CD200^{-/-}, compared with WT, mice ($n=16$ /group). The areas of significant volumetric difference at this timepoint include auditory and visual cortices, the ventral nucleus, the motor cortex, the primary somatosensory cortex and frontal association cortex. There were no significant volumetric increases observed in CD200^{-/-}, compared with WT, mice at 9 months.

At 13 months, the VBM output in Figure 3.19 illustrates significant grey matter increases in CD200^{-/-}, compared with WT, mice ($n=16$ /group). The areas of significant grey matter change were the cerebellum, the CA3 field of the hippocampus and the retrosplenial cortex. At 17 months, significant grey matter decreases were noted in

CD200^{-/-}, compared with WT, mice (n=7/group). These are illustrated in Figure 3.20. Significant grey matter deficits were observed in the primary and secondary motor cortices. There were no significant volumetric increases observed in CD200^{-/-}, compared with WT, mice at 17 months.

3.3.7 Effect of age and genotype on ASL parameters; MTT and CTT

MTT and CTT measurements were assessed in the cortex, hippocampus and whole brain in WT and CD200^{-/-} mice at all 4 timepoints in the study. Figure 3.21 illustrates that MTT and CTT values in the cortex (Figures A and B, respectively) were similar in WT and CD200^{-/-} mice at 4, 9, 13 and 17 months. MTT values in WT mice were 2.319409 ± 0.07816 s (n=8), 2.2746 ± 0.0608 s (n=16), 2.276 ± 0.0495 s (n=13) and 2.241 ± 0.0724 s (n=7) respectively, and in CD200^{-/-} mice were 2.1756 ± 0.0589 s (n=8), 2.25998 ± 0.0505 s (n=16), 2.15589 ± 0.0945 s (n=12) and 2.2183 ± 0.13227 s (n=6). CTT values in WT mice through the 4 timepoints were 2.0386 ± 0.717 s (n=8), 2.107 ± 0.0608 s (n=16), 2.1075 ± 0.0573 s (n=13) and 1.8947 ± 0.1169 s (n=7) and in CD200^{-/-} mice were 1.8319 ± 0.0957 s (n=8), 2.0304 ± 0.0583 s (n=16), 1.8223 ± 0.1255 s (n=12) and 1.7304 ± 0.1102 s (n=6). Both age (*p<0.05; ANOVA) and genotype (**p<0.01; ANOVA) were significant factors in predicting cortical CTT values, although individual comparisons by Bonferroni post-hoc tests did not reach statistical significance.

Figure 3.22 illustrates that MTT and CTT values in the hippocampus (Figures A and B, respectively) were similar in WT and CD200^{-/-} mice at all 4 experimental timepoints. MTT values in WT mice were 2.102 ± 0.0877 s (n=8), 2.1614 ± 0.0531 s (n=16), 2.0943 ± 0.04104 s (n=13) and 2.0206 ± 0.032 s (n=7) and in CD200^{-/-} mice were 2.288 ± 0.0394 s (n=8), 2.1497 ± 0.0398 s (n=16), 2.11808 ± 0.0364 s (n=12) and 2.111 ± 0.0628 s (n=6). CTT values in WT mice were 2.0755 ± 0.9206 s; (n=8), 2.0166 ± 0.053 s (n=16), 1.9255 ± 0.08104 s (n=13) and 2.0275 ± 0.079 s (n=7), while CTT values in CD200^{-/-} mice were 1.9938 ± 0.0708 s (n=8), 1.9356 ± 0.0471 s (n=16), 1.9889 ± 0.06602 s (n=12) and 1.9618 ± 0.0567 s (n=6).

Figure 3.23 illustrates that MTT and CTT values in the whole brain (Figures A and B, respectively) were similar in WT, compared with CD200^{-/-}, mice at all timepoints. MTT times in WT mice were 2.0891 ± 0.05508 s (n=8), 2.143 ± 0.0442 s

(n=16), 2.066 ± 0.0287 s; (n=13) and 2.047 ± 0.05106 s; (n=7) and in CD200^{-/-} mice were 2.294 ± 0.084 s (n=8), 2.1545 ± 0.0517 s (n=16), 2.018 ± 0.0616 s (n=12) and 2.127 ± 0.0779 s (n=6) at 4, 9, 13 and 17 months, respectively. CTT values in WT mice were (2.01715 ± 0.0464 s; n=8), (2.1187 ± 0.0445 s; n=16), (1.9838 ± 0.04307 s; n=13) and (1.9066 ± 0.0808 s; n=7), and in CD200^{-/-} mice were (2.1313 ± 0.04355 s; n=8), (2.0129 ± 0.0767 s; n=16), (1.9695 ± 0.0731 s; n=12) and (1.9435 ± 0.0776 s; n=6).

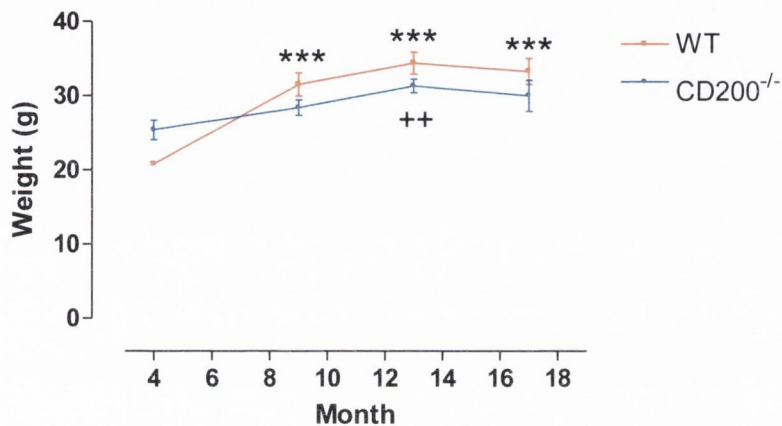


Figure 3.1 Animal weights at experimental timepoints.

There was a significant increase in body weight of WT mice at the 9, 13 and 17, compared with 4, months (** $p < 0.001$; ANOVA). There was a significant increase in the weight of CD200^{-/-} mice at 13, compared with 4, months ($^{++}p < 0.01$; ANOVA) alone. Data are presented as means \pm SEM.

2-way ANOVA: Genotype effect $F(1, 68) = 1.400$; $p = 0.2408$, Age effect $F(3, 68) = 18.69$; $p < 0.0001$, Interaction effect $F(3, 68) = 3.515$; $p = 0.0197$

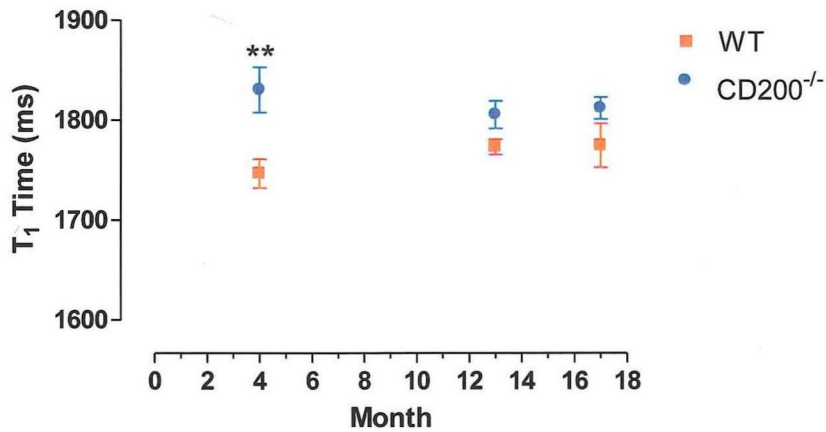


Figure 3.2 T₁ relaxation times in the whole cortex of WT and CD200^{-/-} mice.

Groups of WT and CD200^{-/-} mice underwent MR scanning at 4, 13 and 17 months. Quantitative T₁ relaxometry analysis was carried out on the RARE-VTR scans on an ROI approach. There was a significant increase in cortical T₁ relaxation times in CD200^{-/-}, compared with WT, mice at 4 months (**p<0.01; ANOVA) but no age-related change in WT or CD200^{-/-} mice was observed. Data are presented as means ± SEM.

2-way ANOVA: Genotype effect F (1, 51) = 15.67; p=0.0002, **Age effect** F (2, 51) = 0.04560; p=0.9555, **Interaction effect** F (2, 51) = 1.695; p=0.1938

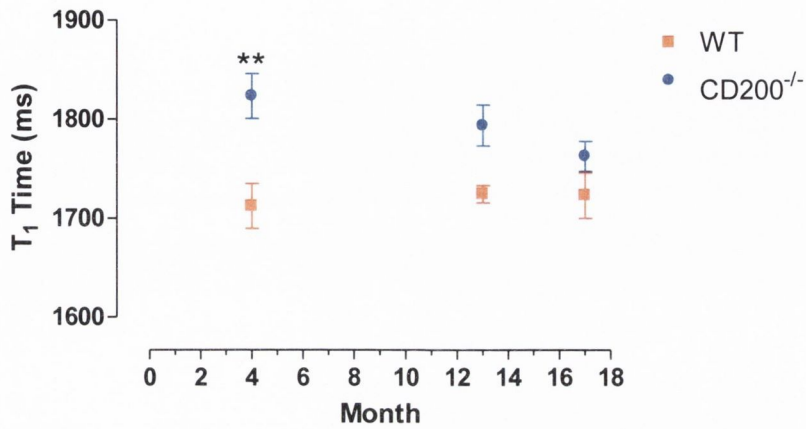


Figure 3.3 T₁ relaxation times in the hippocampus of WT and CD200^{-/-} mice.

Groups of WT and CD200^{-/-} mice underwent MR scanning at 4, 13 and 17 months. T₁ relaxation times of the hippocampus were measured bilaterally on the RARE-VTR scans. There was a significant increase in hippocampal T₁ relaxation times in CD200^{-/-}, compared with WT, mice at 4 months (**p<0.01; ANOVA) but no age-related change in WT or CD200^{-/-} mice was observed. Data are presented as means ± SEM.

2-way ANOVA: Genotype effect F (1, 50) = 19.48; p<0.0001, Age effect F (2, 50) = 0.6383; p=0.5324, Interaction effect F (2, 50) = 1.351; p=0.2682

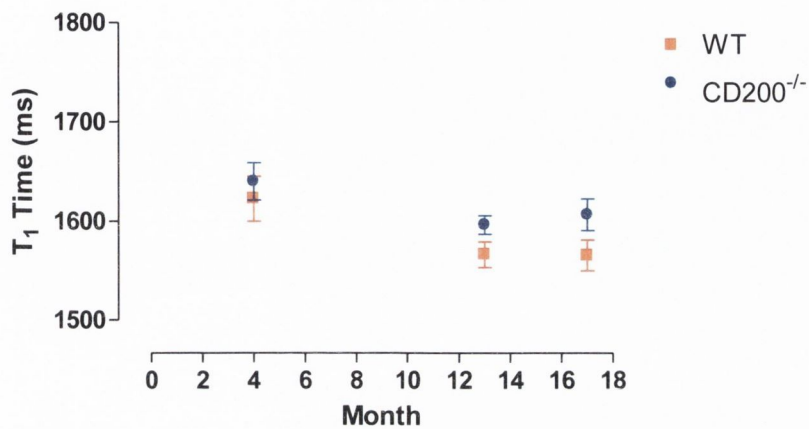


Figure 3.4 T₁ relaxation times in the corpus callosum of WT and CD200^{-/-} mice.

Groups of WT and CD200^{-/-} mice underwent MR scanning at 4, 13 and 17 months. T₁ relaxation times of the corpus callosum were measured bilaterally on the RARE-VTR scans. Mean T₁ values were similar in CD200^{-/-}, compared with WT, mice at all 3 timepoints. Data are presented as means ± SEM.

2-way ANOVA: Genotype effect $F(1, 51) = 5.059$; $p=0.0288$, **Age effect** $F(2, 51) = 5.865$; $p=0.0051$, **Interaction effect** $F(2, 51) = 0.2671$; $p=0.7666$

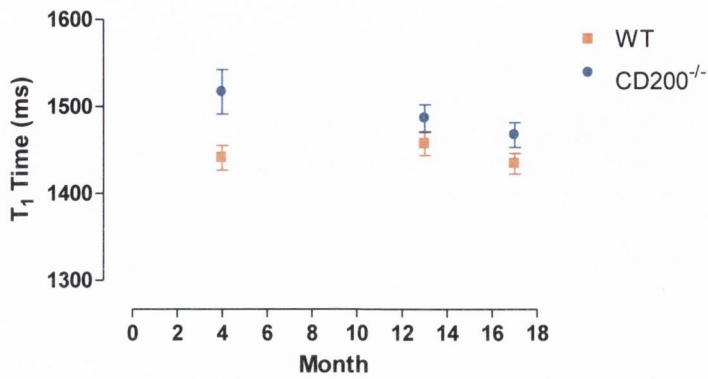


Figure 3.5 T₁ relaxation times in the thalamus of WT and CD200^{-/-} mice.

Groups of WT and CD200^{-/-} mice underwent MR scanning at 4, 13 and 17 months. T₁ relaxation times of the thalamus were measured bilaterally on the RARE-VTR scans. Mean T₁ values were similar in CD200^{-/-}, compared with WT, mice, at all 3 timepoints. Data are presented as means ± SEM.

2-way ANOVA: Genotype effect $F(1, 51) = 10.25$; $p=0.0024$, **Age effect** $F(2, 51) = 1.341$; $p=0.2706$, **Interaction effect** $F(2, 51) = 1.069$; $p=0.3509$

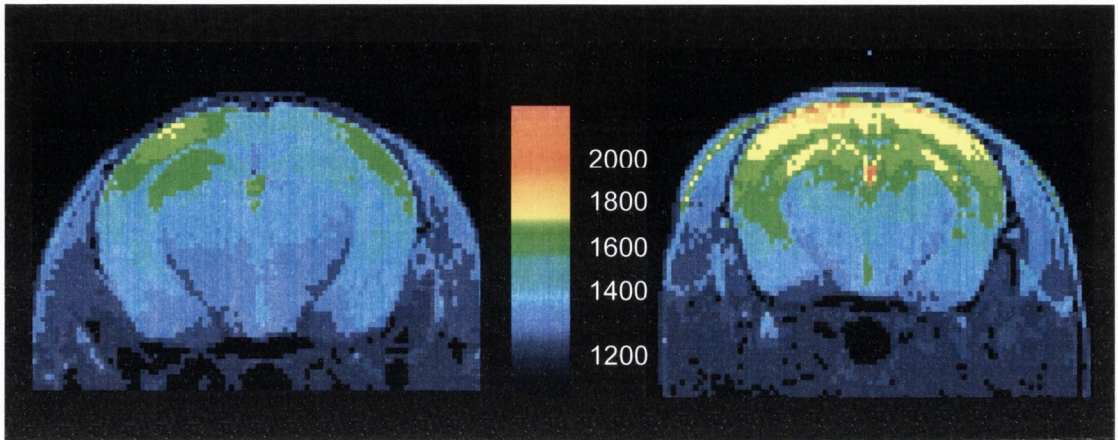


Figure 3.6 T₁ relaxation times in a representative WT and CD200^{-/-} mouse at 4 months.

Groups of WT and CD200^{-/-} mice underwent MR scanning at 4, 13 and 17 months. Quantitative parametric T₁ maps from a 4 month-old WT and CD200^{-/-} mouse are presented above. These maps show increased T₁ relaxation times, denoted by increased pixel colour intensities, in the CD200^{-/-} mouse (Figure C), compared with the WT mouse (Figure A), particularly in the hippocampus and cortex. A coloured scale bar (Figure B) is presented correlating pixel colour intensities and T₁ values (ms).

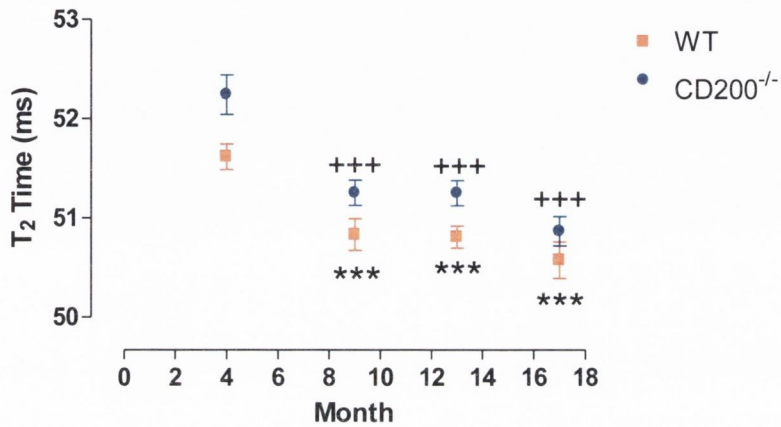


Figure 3.7 T₂ relaxation times in the whole cortex of WT and CD200^{-/-} mice.

Groups of WT and CD200^{-/-} mice underwent MR scanning at 4, 9, 13 and 17 months. T₂ relaxation times of the whole cortex were measured in 2 adjacent slices of the MSME scan. There was a significant decrease in cortical T₂ values in WT and CD200^{-/-} mice at 9, compared with 4, months (**p<0.001; ANOVA); (+++p<0.001; ANOVA), at 13, compared with 4, months (**p<0.001; ANOVA); (+++p<0.001; ANOVA) and at 17, compared with 4, months (**p<0.001; ANOVA); (+++p<0.001; ANOVA). Mean cortical T₂ values were similar in CD200^{-/-}, compared with WT, mice at all 4 timepoints. Data are presented as means ± SEM.

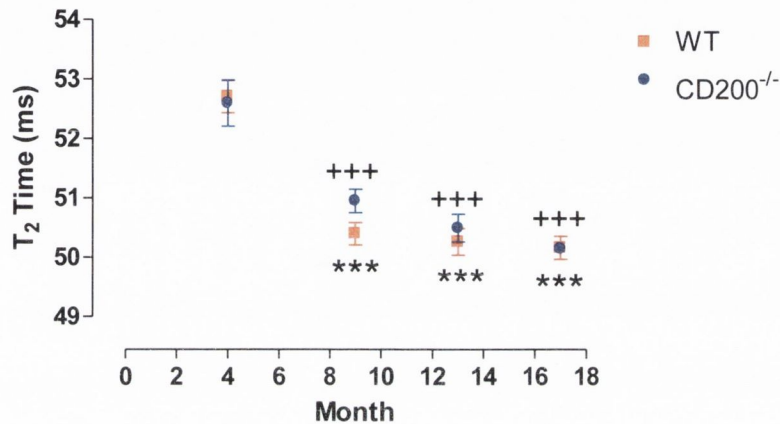


Figure 3.8 T₂ relaxation times in the motor cortex of WT and CD200^{-/-} mice.

Groups of WT and CD200^{-/-} mice underwent MR scanning at 4, 9, 13 and 17 months. T₂ relaxation times were measured in the motor cortex bilaterally in 2 adjacent slices of the MSME scan. There was a significant decrease in cortical T₂ values in WT and CD200^{-/-} mice at 9, compared with 4, months (**p<0.001; ANOVA); (+++p<0.001; ANOVA), at 13, compared with 4, months (**p<0.001; ANOVA); (+++p<0.001; ANOVA) and at 17, compared with 4, months (**p<0.001; ANOVA); (+++p<0.001; ANOVA). Mean motor cortex T₂ values were similar in CD200^{-/-}, compared with WT, mice at all 4 timepoints. Data are presented as means ± SEM.

2-way ANOVA: Genotype effect F (1, 80) = 0.8488; p=0.3597, Age effect F (3, 80) = 40.32; p<0.0001, Interaction effect F (3, 80) = 0.6710; p=0.5723

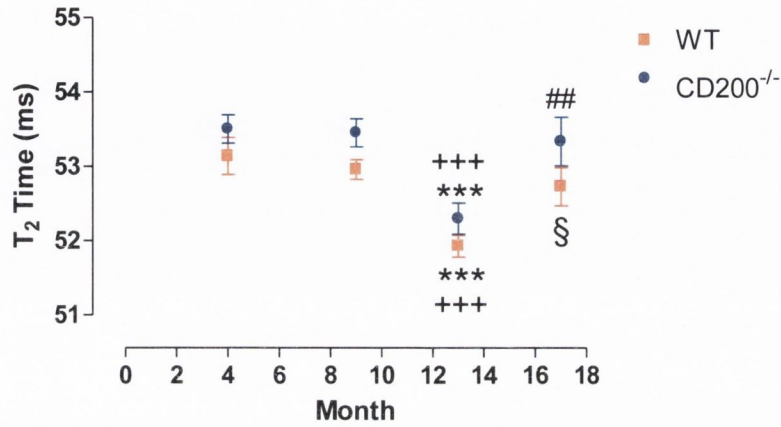


Figure 3.9 T₂ relaxation times in the entorhinal cortex of WT and CD200^{-/-} mice.

Groups of WT and CD200^{-/-} mice underwent MR scanning at 4, 9, 13 and 17 months. T₂ relaxation times were measured in the entorhinal cortex bilaterally in 2 adjacent slices of the MSME scan. There was a significant decrease in T₂ values in WT and CD200^{-/-} mice at 13, compared with 4, months (**p<0.001; ANOVA); (**p<0.001; ANOVA), at 13, compared with 9, months (+++p<0.001; ANOVA); (+++p<0.001; ANOVA) and a significant increase in values at 17, compared with 13, months (§p<0.05; ANOVA); (§#p<0.01; ANOVA). There was no difference in T₂ values between WT and CD200^{-/-} mice at any timepoint. Data are presented as means ± SEM.

2-way ANOVA: Genotype effect F (1, 81) = 9.394; p=0.0030, Age effect F (3, 81) = 13.32; p<0.0001, Interaction effect F (3, 81) = 0.1468; p=0.9315

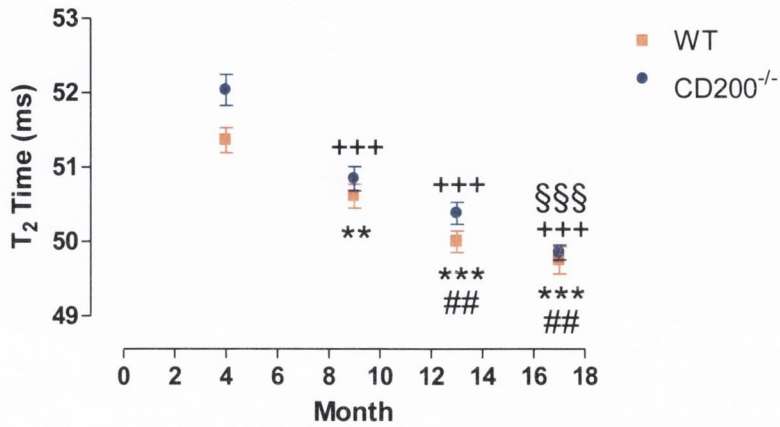


Figure 3.10 T₂ relaxation times in the hippocampus of WT and CD200^{-/-} mice.

Groups of WT and CD200^{-/-} mice underwent MR scanning at 4, 9, 13 and 17 months. T₂ relaxation times were measured in the hippocampus bilaterally in 2 adjacent slices of the MSME scan. There was a significant decrease in cortical T₂ values in WT and CD200^{-/-} mice at 9, compared with 4, months (** p<0.01; ANOVA); (+++ p<0.001; ANOVA), at 13, compared with 4, months (*** p<0.001; ANOVA); (+++ p<0.001; ANOVA) and at 17, compared with 4, months (*** p<0.001; ANOVA); (+++ p<0.001; ANOVA). Mean T₂ values were decreased in the hippocampus of WT mice at 13, compared with 9, months (## p<0.01; ANOVA) and at 17, compared with 9, months (## p<0.01; ANOVA) and in CD200^{-/-} mice at 17, compared with 9, months (SSS p<0.001; ANOVA). Mean hippocampal T₂ values were similar in CD200^{-/-}, compared with WT, mice at all 4 timepoints. Data are presented as means ± SEM.

2-way ANOVA: Genotype effect F (1, 80) = 7.226; p=0.0087, Age effect F (3, 80) = 40.10; p<0.0001, Interaction effect F (3, 80) = 0.8941; p=0.4480

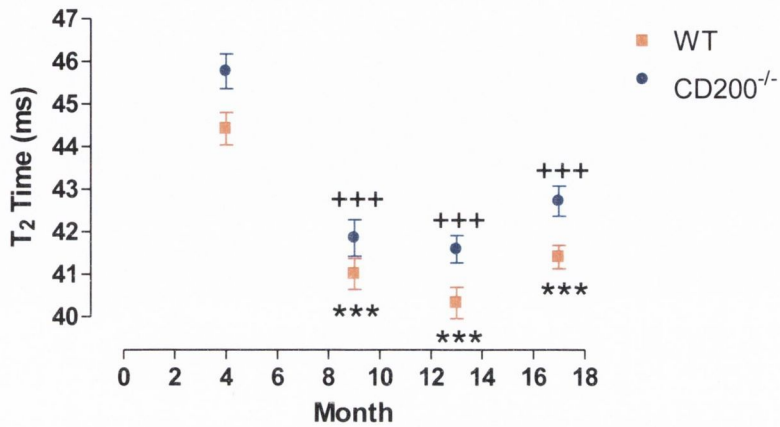


Figure 3.11 T₂ relaxation times in the corpus callosum of WT and CD200^{-/-} mice.

Groups of WT and CD200^{-/-} mice underwent MR scanning at 4, 9, 13 and 17 months. T₂ relaxation times were measured in the corpus callosum in 2 adjacent slices of the MSME scan. There was a significant decrease in cortical T₂ values in WT and CD200^{-/-} mice at 9, compared with 4, months (**p<0.001; ANOVA); (+++p<0.001; ANOVA), at 13, compared with 4, months (**p<0.001; ANOVA); (+++p<0.001; ANOVA) and at 17, compared with 4, months (**p<0.001; ANOVA); (+++p<0.001; ANOVA). Mean T₂ values were similar in CD200^{-/-}, compared with WT, mice at all 4 timepoints. Data are presented as means ± SEM.

2-way ANOVA: Genotype effect F (1, 80) = 15.12; p=0.0002, Age effect F (3, 80) = 36.51; p<0.0001, Interaction effect F (3, 80) = 0.1442; p=0.9331

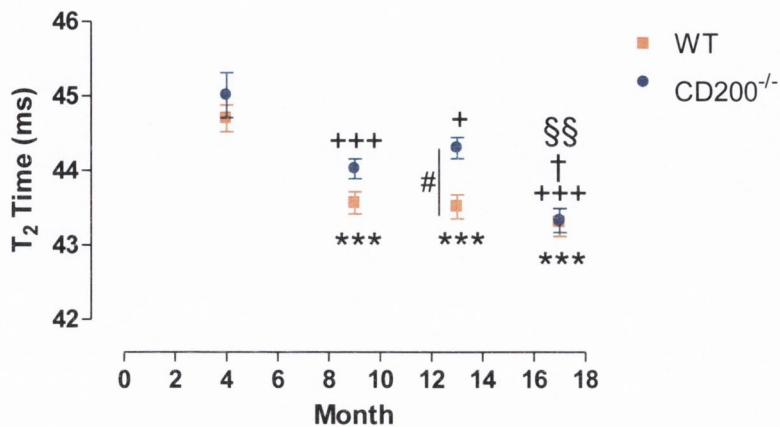


Figure 3.12 T₂ relaxation times in the thalamus of WT and CD200^{-/-} mice.

Groups of WT and CD200^{-/-} mice underwent MR scanning at 4, 9, 13 and 17 months. T₂ relaxation times were measured in the thalamus in 2 adjacent slices of the MSME scan. There was a significant decrease in thalamic T₂ values in WT and CD200^{-/-} mice at 9, compared with 4, months (**p<0.001; ANOVA); (+++p<0.001; ANOVA), at 13, compared with 4, months (**p<0.001; ANOVA); (+p<0.05; ANOVA), and at 17, compared with 4, months (**p<0.001; ANOVA); (+++p<0.001; ANOVA) and in CD200^{-/-} mice at 17, compared with 9, months (†p<0.05; ANOVA) and at 17, compared with 13, months (§§p<0.01; ANOVA). Mean thalamic T₂ values were increased in CD200^{-/-}, compared with WT, mice at 13 months (#p<0.05; ANOVA). Data are presented as means ± SEM.

2-way ANOVA: Genotype effect F (1, 81) = 8.991; p=0.0036, **Age effect** F (3, 81) = 23.67; p<0.0001, **Interaction effect** F (3, 81) = 1.435; p=0.2387

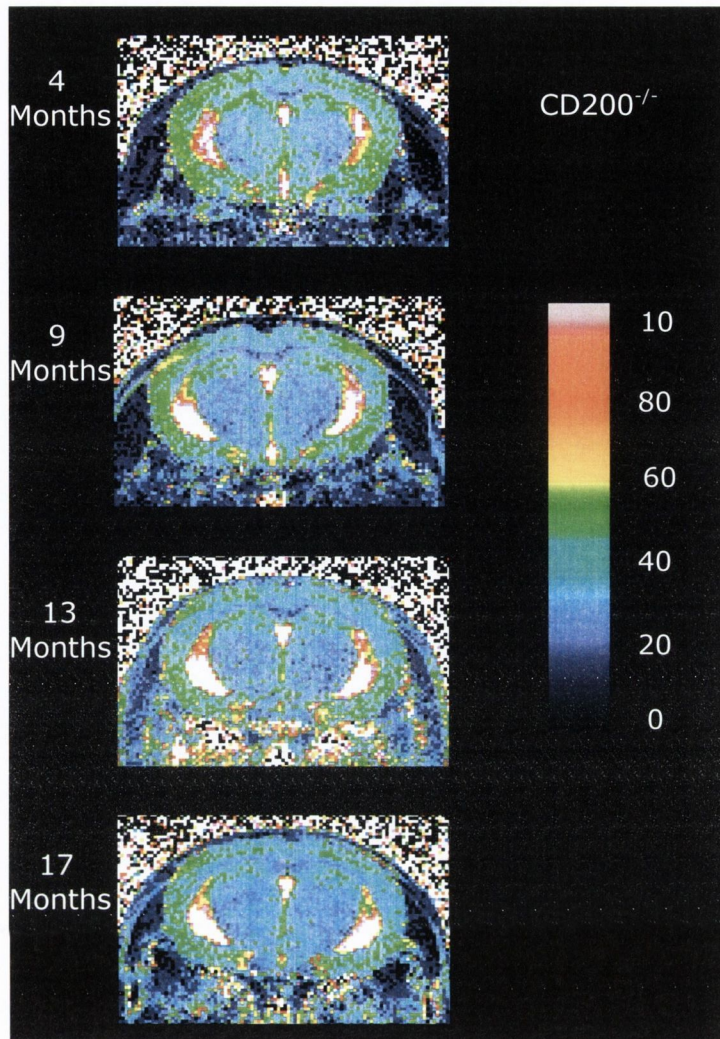


Figure 3.13 Representative coronal images displaying T₂ relaxation times in CD200^{-/-} mice with associated colour reference bar.

Groups of WT and CD200^{-/-} mice underwent MR scanning at 4, 9, 13 and 17 months. Sample parametric T₂ maps from CD200^{-/-} mice at all 4 timepoints are presented. There was a significant decrease in T₂ values in all brain regions at 9 months (Figure B), 13 months (Figure C) and 17 months (Figure D) compared with 4 months (Figure A). Coronal images are approximately 2.3mm posterior to Bregma. A coloured scale bar (Figure E) is presented correlating pixel colour intensities and T₂ values (ms).

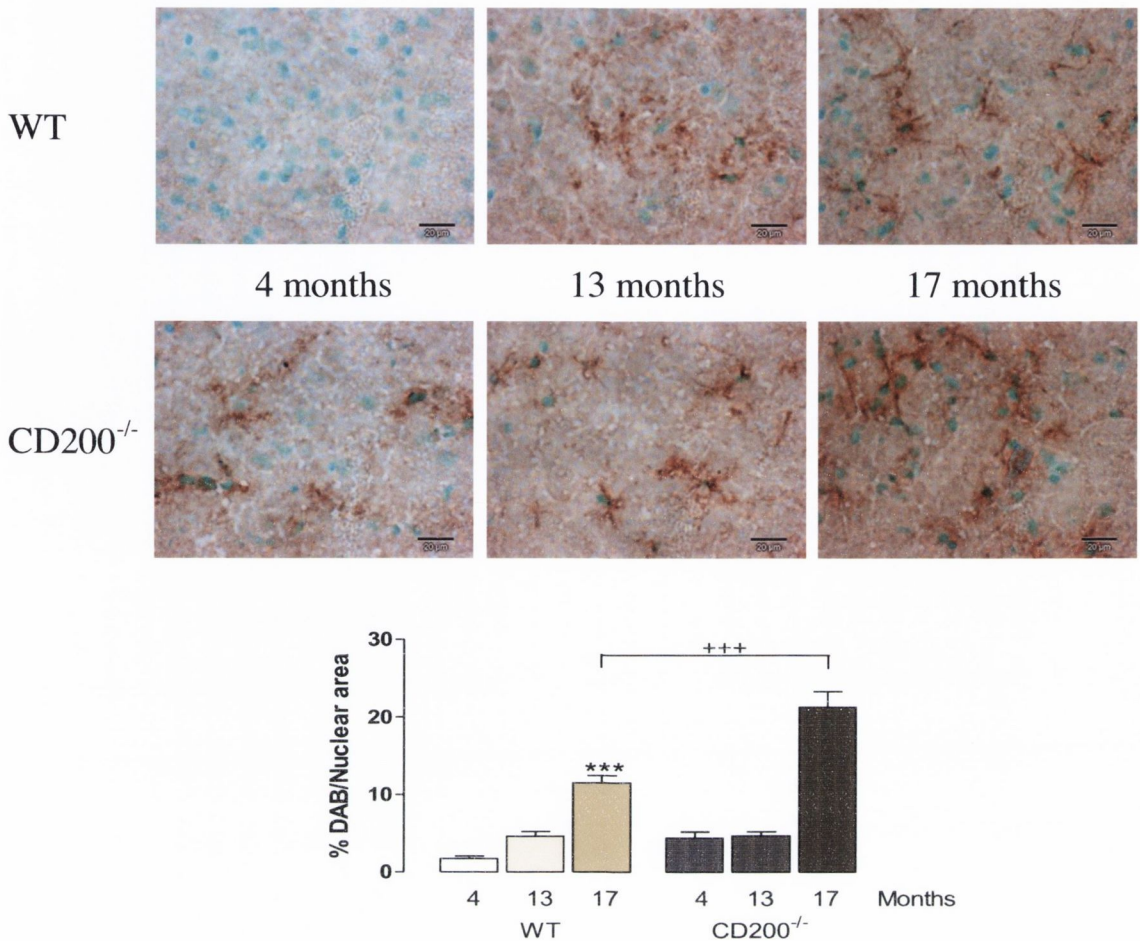


Figure 3.14 GFAP immunoreactivity in cortical sections prepared from WT and CD200^{-/-} mice at 4, 13 and 17 months.

Sections of cortical tissue prepared from groups of WT and CD200^{-/-} mice were assessed for immunohistochemical staining of GFAP at 4, 13 and 17 months. There was an age-related increase in immunoreactivity in cortical sections prepared from 13 and 17 month-old WT mice. This age-related increase in staining was more pronounced in CD200^{-/-}, compared with WT, mice. (Magnification 40x, scale bar 20 μm).

There was a significant age-related increase in the ratio of DAB/nuclear area in the cortex of WT mice (** $p < 0.001$; ANOVA). DAB/nuclear area was significantly enhanced in the cortex of CD200^{-/-} mice at 17 months (+++ $p < 0.001$; ANOVA).

2-way ANOVA: Age effect $F(2, 30) = 101.2$; $p < 0.0001$, Genotype effect $F(1, 30) = 25.15$; $p < 0.0001$, Interaction effect $F(2, 26) = 11.93$; $p = 0.0002$

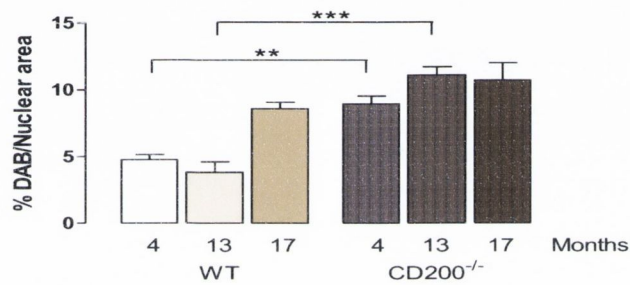
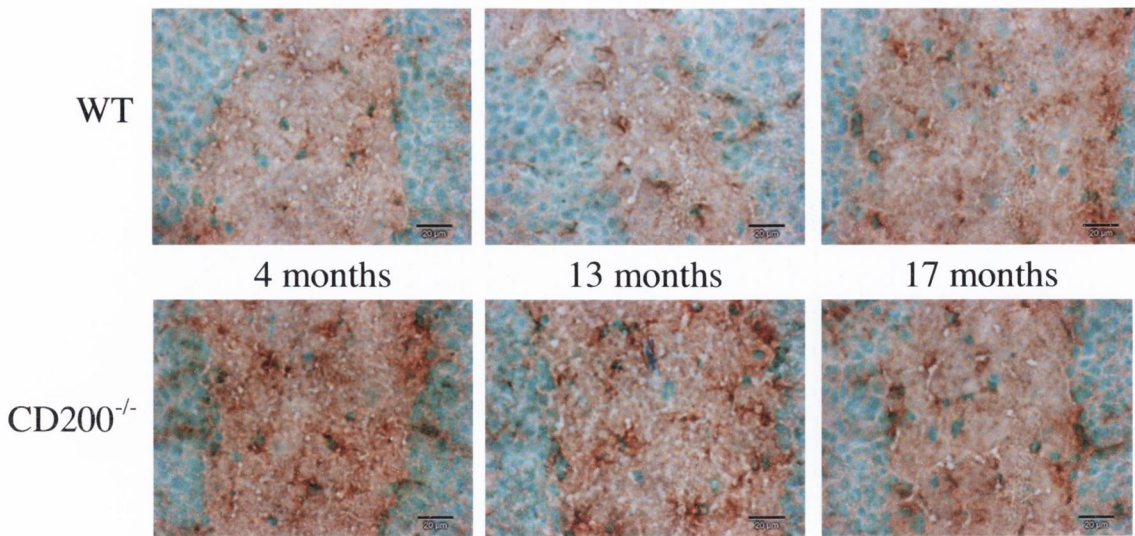


Figure 3.15 GFAP immunoreactivity in dentate gyrus of WT and CD200^{-/-} mice at 4, 13 and 17 months.

Sections of hippocampal tissue prepared from groups of WT and CD200^{-/-} mice were assessed for immunohistochemical staining of GFAP at 4, 13 and 17 months. There was an increase in GFAP staining in hippocampal sections prepared from CD200^{-/-}, compared with WT, mice at 4 and 13 months. (Magnification 40x, scale bar 20 μ m).

There was a significant age-related increase in the ratio of DAB/nuclear area in the hippocampus of CD200^{-/-} mice, compared with WT, mice at 4 months (** p<0.01; ANOVA) and 13 months (***) p<0.001; ANOVA).

2-way ANOVA: Age effect F (2, 30) = 7.783; p=0.0019, Genotype effect F (1, 30) = 55.45; p<0.0001, Interaction effect F (2, 26) = 6.026; p=0.0063

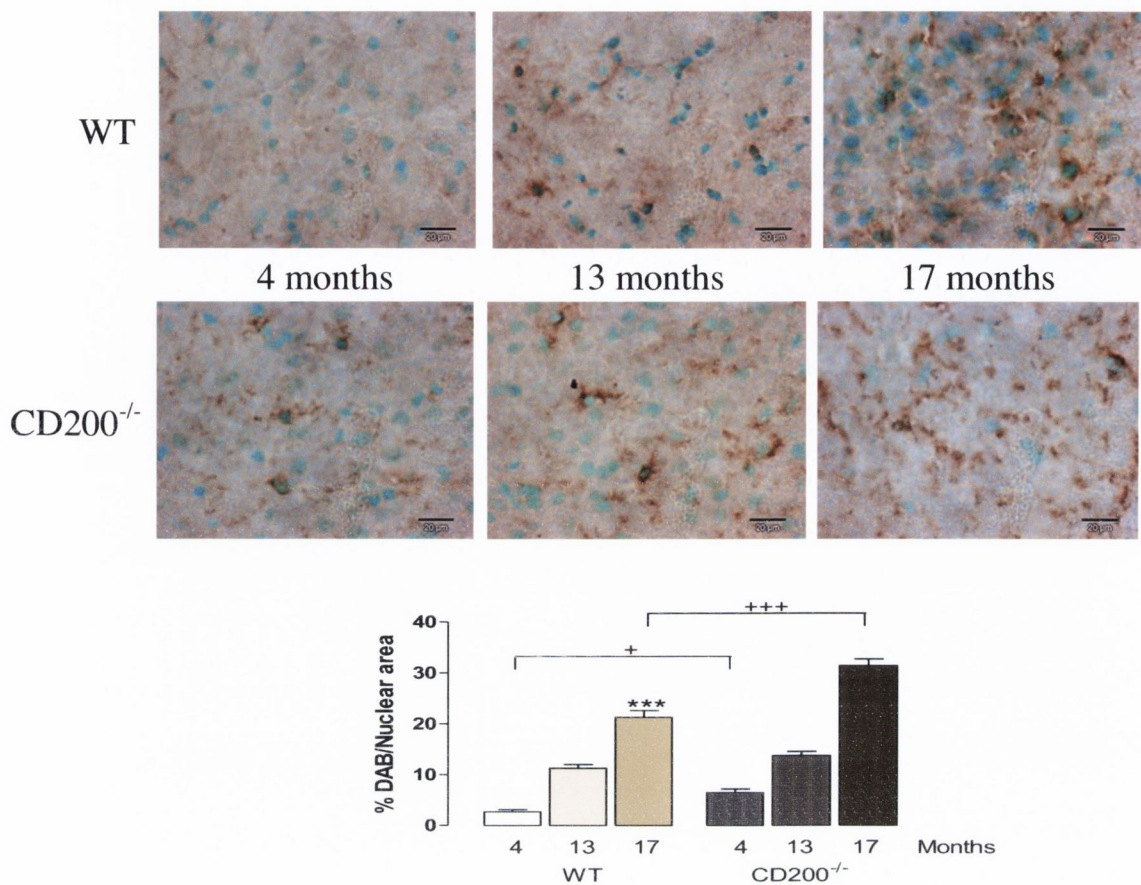


Figure 3.16 CD11b immunoreactivity in cortical sections prepared from WT and CD200^{-/-} mice at 4, 13 and 17 months.

Sections of cortical tissue prepared from groups of WT and CD200^{-/-} mice were assessed for immunohistochemical staining of CD11b at 4, 13 and 17 months. There was an aged-related increase in CD11b positive staining in cortical sections prepared from WT and CD200^{-/-} mice at 13 and 17 months. There was a marked increase in CD11b positive immunoreactivity in CD200^{-/-}, compared with WT, mice, in particular at 4 and 17 months (40x magnification, magnification bar 20 μ m).

There was a significant age-related increase in the ratio of DAB/nuclear area in the cortex of WT mice (** $p < 0.001$; ANOVA). DAB/nuclear area was significantly enhanced in the cortex of CD200^{-/-} mice at 4 months (⁺ $p < 0.05$; ANOVA) and 17 months (⁺⁺⁺ $p < 0.001$; ANOVA).

2-way ANOVA: Age effect $F(2, 30) = 280.1$; $p < 0.0001$, Genotype effect $F(1, 30) = 51.46$; $p < 0.0001$, Interaction effect $F(2, 26) = 9.531$; $p = 0.0006$

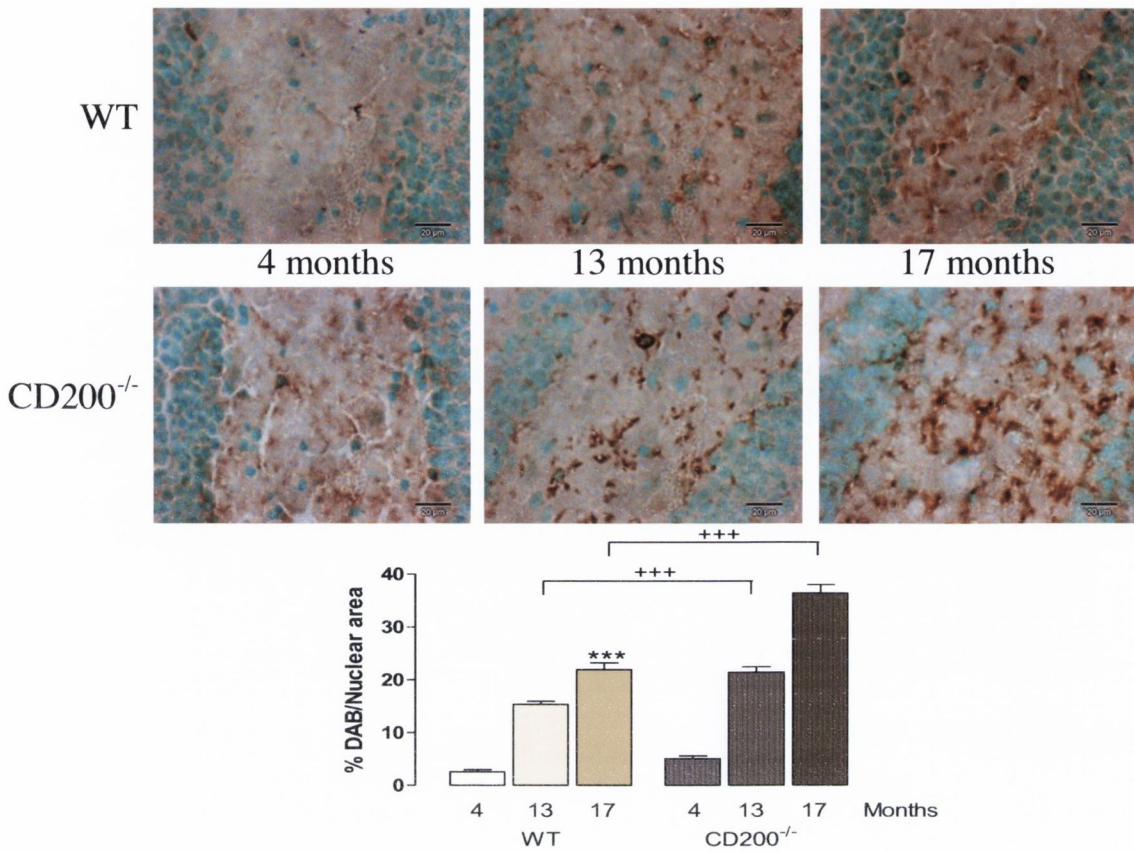


Figure 3.17 CD11b immunoreactivity in the dentate gyrus of WT and CD200^{-/-} mice at 4, 13 and 17 months.

Sections of hippocampal tissue from groups of WT and CD200^{-/-} mice were assessed for immunohistochemical staining of CD11b at 4, 13 and 17 months. There was an age-related increase in CD11b positive staining in the dentate gyrus of WT and CD200^{-/-} mice at 13 and 17 months. There was a marked increase in CD11b positive immunoreactivity in CD200^{-/-}, compared with WT, mice, in particular at 13 and 17 months. (40x magnification, magnification bar 20 μ m).

There was a significant age-related increase in the ratio of DAB/nuclear area in the cortex of WT mice (** $p < 0.001$; ANOVA). DAB/nuclear area was significantly enhanced in the cortex of CD200^{-/-} mice at 4 months (++ $p < 0.001$; ANOVA) and 17 months (++ $p < 0.001$; ANOVA).

2-way ANOVA: Age effect $F(2, 30) = 309.3$; $p < 0.0001$, Genotype effect $F(1, 30) = 84.06$; $p < 0.0001$, Interaction effect $F(2, 26) = 17.9$; $p < 0.0001$

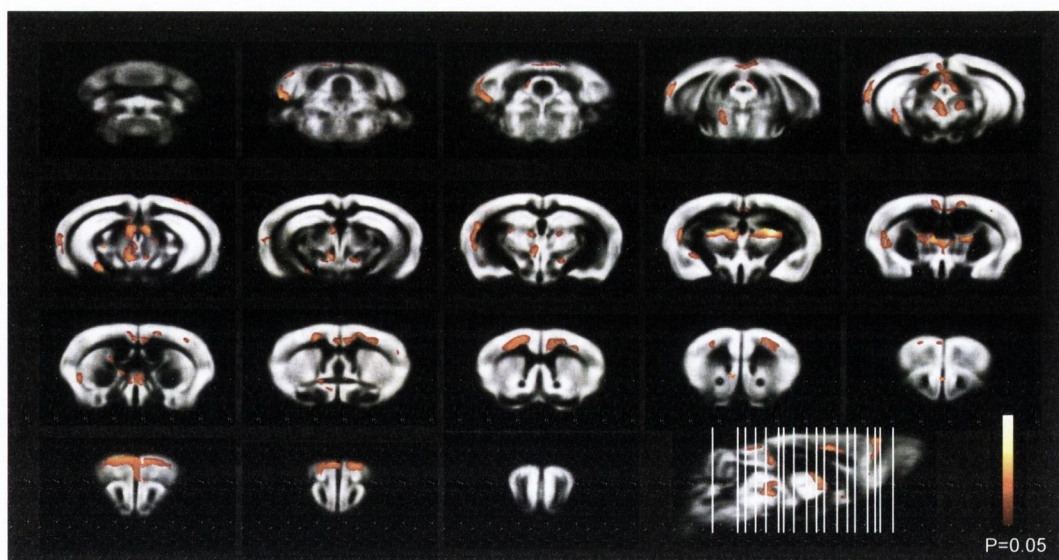


Figure 3.18 Areas of significant volumetric decreases in CD200^{-/-} mice at 9 months.

Groups of WT and CD200^{-/-} mice underwent high-resolution MR scanning at 9 months. Anatomic scans were prepared for volumetric analysis by the optimized VBM protocol. Images were spatially registered to a generic C57 template and voxel-wise group comparisons were carried out. The 18 coronal images displayed above display areas of significant volume decreases in 9 month-old CD200^{-/-}, compared with WT, mice. Areas of greatest grey matter volume loss are indicated by higher colour intensities. Areas of significant volumetric difference include the cerebellum, auditory and visual cortices, the ventral thalamic nucleus, the motor cortex, the primary somatosensory cortex and frontal association cortex. No significant volumetric increases were noted in 9 month-old CD200^{-/-}, compared with WT, mice.

A sagittal slice with the position of the coronal slices is provided, as well as a colour bar correlating greater colour intensity and decreased statistical significance. (n=16 per group, p<0.05; voxel-wise statistics)

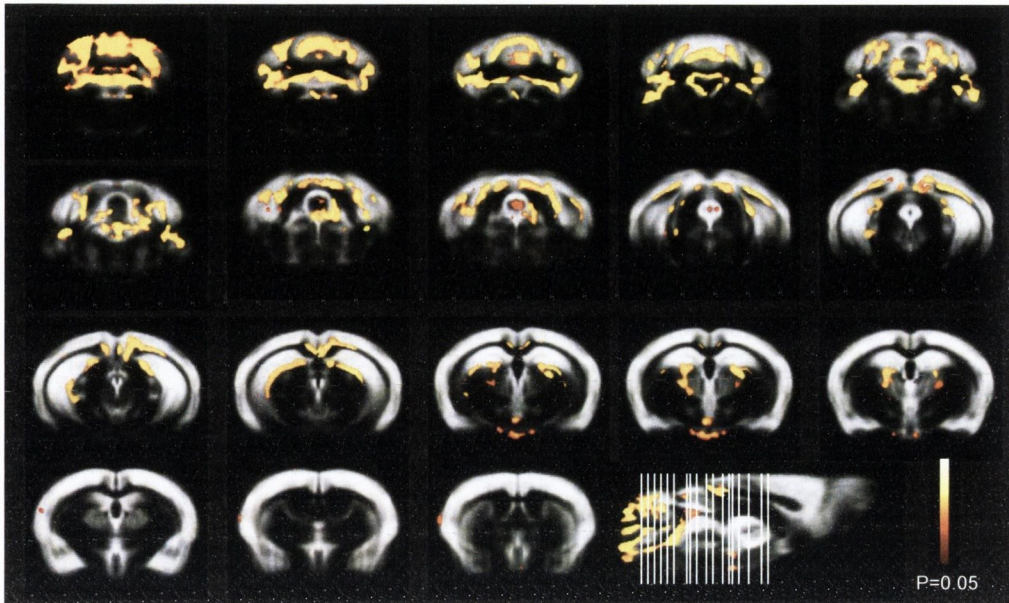


Figure 3.19 Areas of significant volumetric increases in CD200^{-/-} mice at 13 months.

Groups of WT and CD200^{-/-} mice underwent high-resolution MR scanning at 13 months. Anatomic scans were prepared for volumetric analysis by the optimized VBM protocol. Images were spatially registered to a generic C57 template and voxel-wise group comparisons were carried out. The 18 coronal images displayed above display areas of significant volume increases in 13 month-old CD200^{-/-}, compared with WT, mice. Areas of greatest grey matter volume increase are indicated by higher colour intensities. Areas of significant volumetric difference include the cerebellum, and the CA3 field of the hippocampus. No significant volumetric decreases were noted in 13 month-old CD200^{-/-}, compared with WT, mice.

A sagittal slice with the position of the coronal slices is provided, as well as a colour bar correlating greater colour intensity and decreased statistical significance. (n=16 per group, p<0.05; voxel-wise statistics)

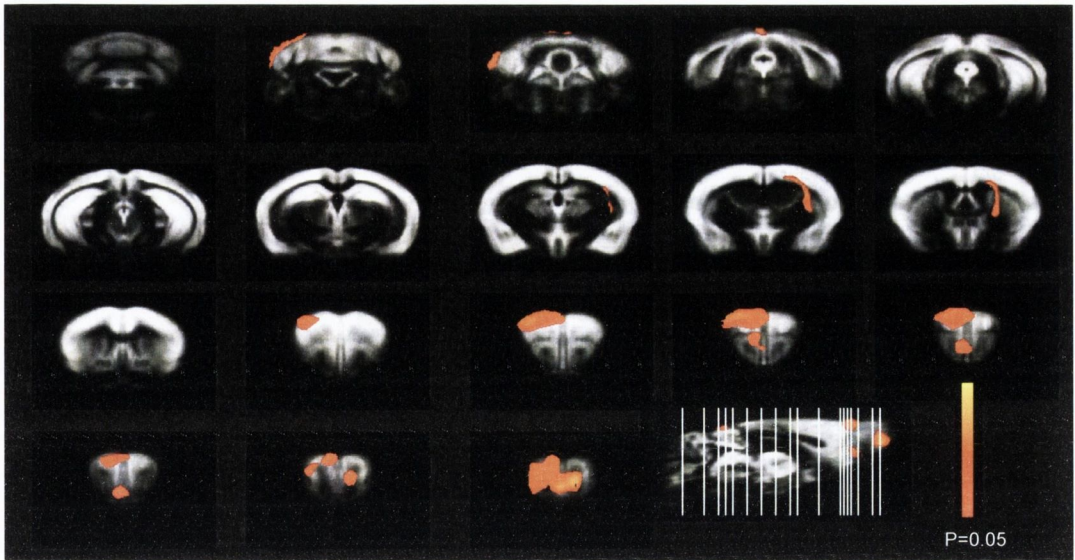


Figure 3.20 Areas of significant volumetric decreases in $CD200^{-/-}$ mice at 17 months.

Groups of WT and $CD200^{-/-}$ mice underwent high-resolution MR scanning at 17 months. Anatomic scans were prepared for volumetric analysis by the optimized VBM protocol. Images were spatially registered to a generic C57 template and voxel-wise group comparisons were carried out. The 18 coronal images displayed above display areas of significant volume decreases in 17 month-old $CD200^{-/-}$, compared with WT, mice. Areas of greatest grey matter volume loss are indicated by higher colour intensities. Areas of significant volumetric difference include the primary and secondary motor cortices. No significant volumetric increases were noted in 17 month-old $CD200^{-/-}$, compared with WT, mice.

A sagittal slice with the position of the coronal slices is provided, as well as a colour bar correlating greater colour intensity and decreased statistical significance. (n=7 per group, $p < 0.05$; voxel-wise statistics)

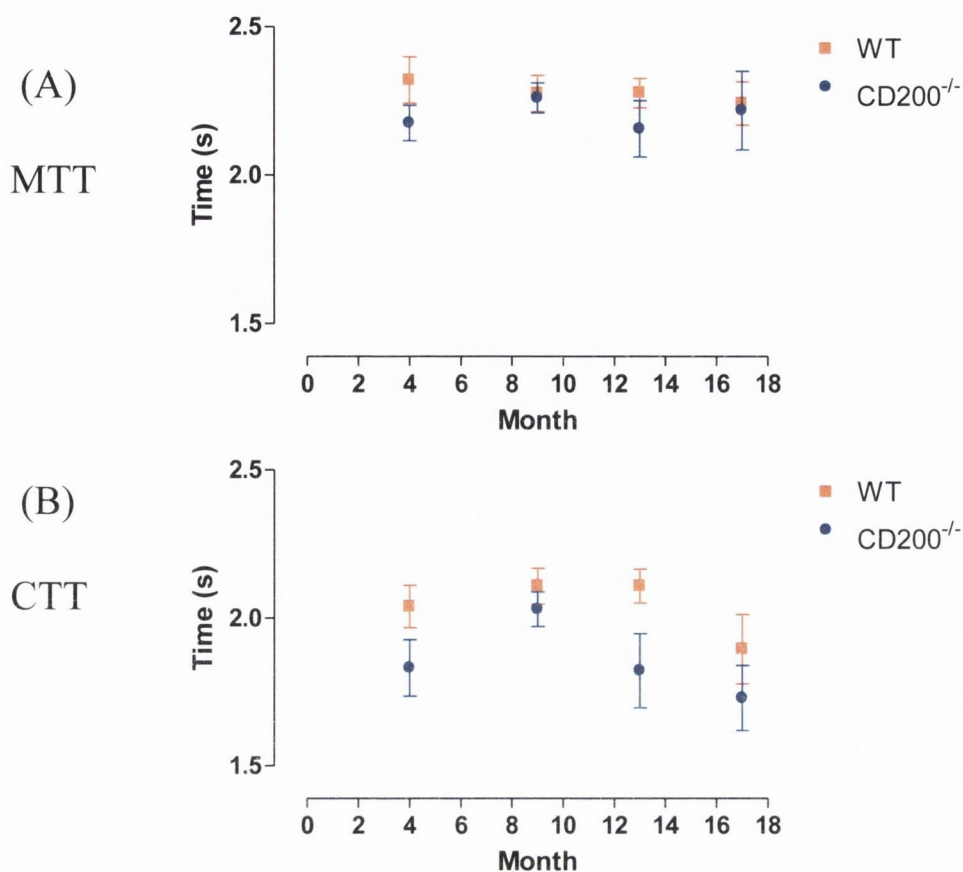


Figure 3.21 Cortical MTT and CTT values in WT and CD200^{-/-} mice at 4, 9, 13 and 17 months.

Groups of WT and CD200^{-/-} mice underwent MR scanning at 4, 9, 13 and 17 months. Cortical ROI were drawn on perfusion weighted images and the average was plotted against acquisition timepoint in the ASL sequence. The MTT and CTT were calculated from the ASL theoretical model. Mean MTT (A) and CTT (B) values were similar in WT and CD200^{-/-} mice at all timepoints. Data are presented as means \pm SEM.

(A) 2-way ANOVA: Genotype effect $F(1, 78) = 1.937$; $p=0.1680$, Age effect $F(3, 78) = 0.1674$; $p=0.9181$, Interaction effect $F(3, 78) = 0.3712$; $p=0.7740$

(B) 2-way ANOVA: Genotype effect $F(1, 78) = 8.224$; $p=0.0053$, Age effect $F(3, 78) = 2.725$ $p=0.0498$, Interaction effect $F(3, 78) = 0.4597$; $p=0.7112$

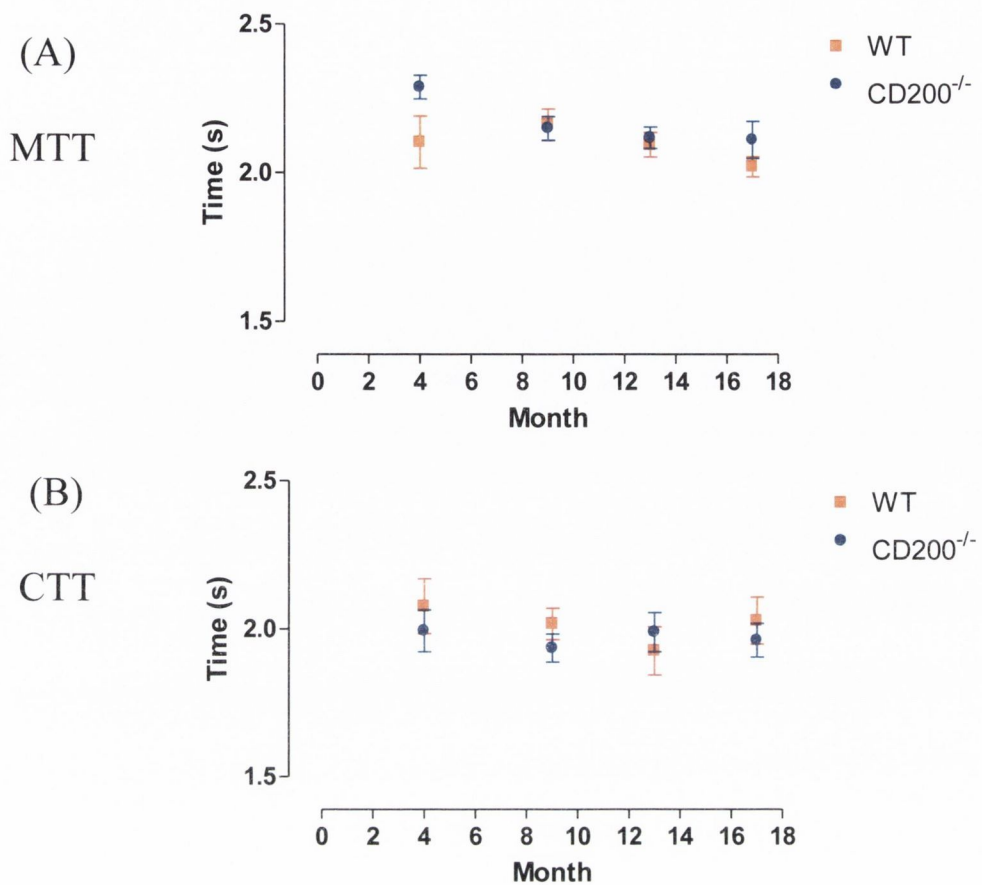


Figure 3.22 Hippocampal MTT and CTT values in WT and CD200^{-/-} mice at 4, 9, 13 and 17 months.

Groups of WT and CD200^{-/-} mice underwent MR scanning at 4, 9, 13 and 17 months. Hippocampal ROI were drawn on perfusion weighted images and the average was plotted against acquisition timepoint in the ASL sequence. The MTT and CTT were calculated from the ASL theoretical model. Mean MTT (A) and CTT (B) values were similar in WT and CD200^{-/-} mice at all timepoints. Data are presented as means \pm SEM.

(A) 2-way ANOVA: Genotype effect $F(1, 78) = 3.531$; $p=0.0640$, Age effect $F(3, 78) = 2.164$; $p=0.0989$, Interaction effect $F(3, 78) = 1.284$; $p=0.2859$

(B) 2-way ANOVA: Genotype effect $F(1, 78) = 0.6390$; $p=0.4265$, Age effect $F(3, 78) = 0.4115$; $p=0.7452$, Interaction effect $F(3, 78) = 0.4630$; $p=0.7089$

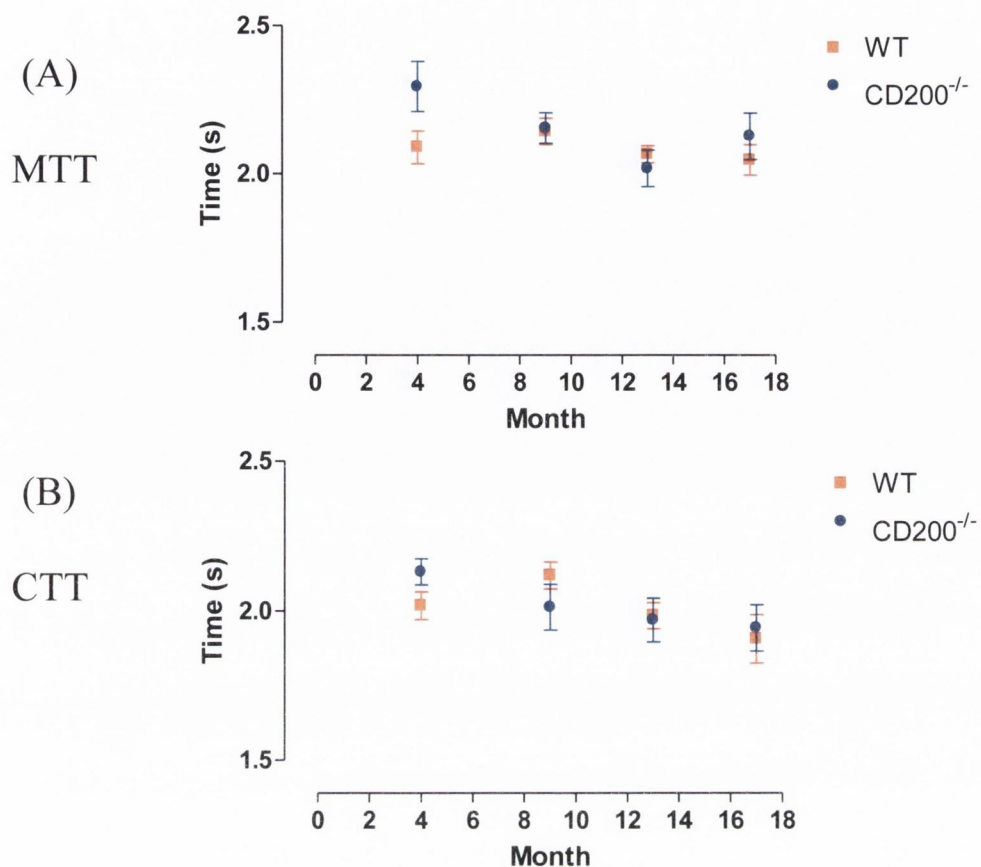


Figure 3.23 Whole brain MTT and CTT values in WT and CD200^{-/-} mice at 4, 9, 13 and 17 months.

Groups of WT and CD200^{-/-} mice underwent MR scanning at 4, 9, 13 and 17 months. Whole brain ROI were drawn on perfusion weighted images and the average was plotted against acquisition timepoint in the ASL sequence. The MTT and CTT were calculated from the ASL theoretical model. Mean MTT (A) and CTT (B) values were similar in WT and CD200^{-/-} mice at all timepoints. Data are presented as means \pm SEM.

(A) 2-way ANOVA: Genotype effect $F(1, 78) = 2.192$; $p=0.1427$, **Age effect** $F(3, 78) = 2.467$; $p=0.0683$, **Interaction effect** $F(3, 78) = 1.668$; $p=0.1807$

(B) 2-way ANOVA: Genotype effect $F(1, 78) = 0.02489$; $p=0.875$, **Age effect** $F(3, 78) = 2.144$; $p=0.1013$, **Interaction effect** $F(3, 78) = 0.8805$; $p=0.4550$

3.4 Discussion

One of the central aims of this study was to assess the age-related changes in glial activity in WT mice and in mice lacking CD200. The foundations for this study were based on the fact that CD200-deficient mice show an enhanced microglial response both in resting conditions (Hoek *et al.*, 2000) and under inflammatory stress (Chitnis *et al.*, 2007) and that changes including microglial activation have been observed with age (Griffin *et al.*, 2006). The hypothesis was that deficiency in CD200 would exacerbate the age-related changes in microglial activation.

The first significant finding of this study is that ageing in CD200-deficient mice was associated with an enhanced microglial response, compared with the response seen in ageing WT mice. Microglial activation in this study was assessed by CD11b immunostaining. This age-related increase in cortical and hippocampal CD11b expression was markedly exacerbated in CD200^{-/-} mice, in particular at 17 months, at which point the most profound immunoreactivity was noted. CD11b, also known as complement receptor 3 (CR3), is a cell surface marker of microglia, and has been shown to be upregulated under conditions of inflammatory stress (Sugama *et al.*, 2003; Kim & de Vellis, 2005), for example in response to LPS challenge (Zhou *et al.*, 2005). Microglial activation, as characterized by CD11b expression, has been shown to be a hallmark of several neurodegenerative disorders, and is up-regulated in culture in response to treatment of neurotoxic molecules including A β peptides and HIV-1 gp120 (a glycoprotein expressed on the surface of the HIV envelope) (Roy *et al.*, 2008). Age-related increases in CD11b positive immunoreactivity were observed in both cortical and hippocampal sections and a marked increase was evident in sections prepared from 13 and 17 month old WT mice compared with 4 month-old mice where staining was negligible. This results is consistent with other reports in the literature that suggest that CD11b expression is up-regulated with ageing (Mouton *et al.*, 2002).

CD11a, CD11b and CD11c are readily detectable in resting microglia in both grey and white matter; however their expression is markedly increased in activated microglia in AD affected tissue (Gonzalez-Scarano & Baltuch, 1999; Kim & de Vellis, 2005). Activated microglia in neuroinflammatory conditions and also in ageing express increased levels of MHC antigens (I and II) and increased expression of the cell surface receptor CD40 in the rat (Minogue *et al.*, 2007) which leads to the induction of pro-

inflammatory cytokines, and other co-stimulatory molecules (Stout & Suttles, 1996). Among all the surface markers and neurotoxic molecules expressed by activated microglia, CD11b is perhaps the one with the most biological significance. Critically, expression of CD11b has been shown to correspond to the severity of microglial activation (Roy *et al.*, 2008).

The present findings show that CD11b immunoreactivity was increased in CD200^{-/-} mice, which is consistent with a previous report which indicated an exacerbated microglial response at resting state in the CNS of CD200-deficient mice. A study by Hoek and colleagues (2000) showed spontaneous, heightened microglial activation in the spinal cord of CD200-deficient mice, identified by increased CD11b and CD45 expression. A change in microglial morphology to less ramified, shorter glial processes was observed. Moreover, microglial aggregation, another morphological feature of activated microglia, was observed in the spinal cord of CD200-deficient mice. Microglial aggregation does not occur in the normal, healthy CNS, and is generally a reflection of old age; the presence of microglial aggregates suggests that the microglia have lost their contact inhibition and begun to bind to each other (Streit, 2006).

The present finding that changes in microglial activation are CD200 dependent correlates with previous findings from the laboratory. It has been previously reported that the addition of neurons to LPS-induced glial activation decreased glial activity, significantly attenuating the increases in IL-1 β , TNF- α and IL-6 production (Lyons *et al.*, 2009). Furthermore, it has been shown that the A β -induced glial cell activation is inhibited by the addition of neurons. Moreover, the age-related increase in MHC II mRNA expression was accompanied by a decrease in CD200 immunostaining in the rat brain (Lyons *et al.*, 2007). Expression of CD200 has been found to be significantly decreased in patients with AD, and this correlated negatively with plaque count and disease progression (Walker *et al.*, 2009). This finding, coupled with the results presented here, strengthens the claim that engagement of CD200R by CD200 down-regulates the inflammatory response, and helps in maintaining microglia in a quiescent state.

To investigate T₂ relaxation times throughout the entire brain, the following anatomically distinct regions were assessed for T₂ times at all 4 experimental timepoints: whole, motor and entorhinal cortex, hippocampus, corpus callosum and thalamus. The results indicated that T₂ values of both grey and white matter regions

were significantly decreased with age in both genotypes. It was previously reported that T_2 relaxation times were unchanged in 12, compared with 3 month-old, rats (Heiland *et al.*, 2002) whereas the present findings revealed changes at 9 months of age. One possible explanation for the apparent difference in findings is that the rats used in this study were scanned at 2.35 Tesla, a significantly lower field strength than what was used in the present study. The greater field strength allowed for a thinner slice thickness to be used, thus reducing partial volume effects which can lead to CSF contamination of grey matter. This in turn would lead to overestimation of T_2 values, which has been reported to occur in grey matter in humans (Rugg-Gunn *et al.*, 2005).

It is well known that iron accumulates in most, if not all, A β plaques (LeVine, 1997). Non-transgenic WT littermate control mice assessed in studies of mouse models of AD do not show age-related reductions in cortical or hippocampal T_2 relaxometry, unlike transgenic mice over-expressing one or both of the APP or PS1 transgenes (Braakman *et al.*, 2006; El Tannir El Tayara *et al.*, 2006; Falangola *et al.*, 2007). The finding that single transgenic PS1 mice show reduced T_2 times with age is somewhat surprising, since mice expressing the PS1 transgene alone do not develop amyloid plaques, and thus do not possess the elevated levels of iron accumulation within A β plaques that acts as intrinsic contrast in hypointense T_2 lesions (Falangola *et al.*, 2005). Furthermore, it has been shown that 2.5 month old APP/PS1 transgenic mice that develop A β plaque load in the subiculum but do not present histologically detectable amyloid associated iron accumulation, retain a negative correlation between T_2 values and amyloid load (El Tayara Nel *et al.*, 2007). These findings suggest that mechanisms other than an increase in focal iron accumulation could be responsible for shortening the T_2 signal in the pathology of AD, for example neuronal loss or increased tissue water content (Sadowski *et al.*, 2003).

Several attempts have been made to describe T_2 changes in terms of underlying alterations in the physiological properties of the tissue which they describe. The spin-spin lattice time T_2 is a specific property of spins that depends on their surroundings; interaction between spins destroys the phase coherence, and therefore the T_2 value can be a sensitive indicator of impaired cell physiology or oedema (Braakman *et al.*, 2006). In a study involving human subjects ranging from 3 weeks to 39 years of age, T_2 relaxation times were reported to decrease continuously with increasing age. This was best modelled by a biexponential function, and was suggested to reflect the maturation

of myelination through adolescence and adulthood (Ding *et al.*, 2004). Hippocampal T₂ signal increases have been observed in patients with temporal lobe epilepsy (Pell *et al.*, 2004), and this was reported to reflect gliosis of the dentate gyrus (Briellmann *et al.*, 2002).

The ability to monitor the progression of EAE lesions in the rat brain has provided us with much information about the biophysical changes underlying changes in T₂ relaxometry. Acute hyperintense lesions on T₂-weighted images have been shown to correspond to contrast enhanced lesions (McFarland, 1998; Lee *et al.*, 1999), and have been extended for use as an index to monitor disease progression. These T₂ lesions have been found to be indicative of a range of pathological changes, including macrophage recruitment, demyelination, and axonal loss (Bruck *et al.*, 1997). T₂ hypointense lesions, manifest as dark holes, are said to occur in the grey matter at a distance from the main MS lesions, and have been reported to occur as a result of significant iron deposition (LeVine, 1997). Moreover, in a study conducted by Broom and colleagues (2005), the area of T₂ hypointensity was found to be significantly correlated with numbers of recruited macrophages, either as a result of significant iron deposition, or axonal loss (Broom *et al.*, 2005).

Microglia are considered to play a role in iron homeostasis by expressing ferritin proteins, while astrocytes contain negligible amounts (Lopes *et al.*, 2008). Superoxide, which is promoted and released by activated microglia, acts as a reducing agent and can release iron from ferritin (Biemond *et al.*, 1984), which in turn can lead to oxidative damage (Yoshida *et al.*, 1995). Furthermore, research has shown that aged rats that received a striatal injection of LPS show enhanced ferritin expression and total striatal iron concentration, in addition to the increased microglial activation (Hunter *et al.*, 2008). In the present study, it was considered that iron accumulation may occur in microglia with age and, if this was the case, a shortening of the T₂ signal would occur. It was further suggested that the decrease would be enhanced in CD200-deficient mice, because of the previously-reported increased activated microglia phenotype.

While immunohistochemical analysis suggested an enhanced microglial activity in the cortex and hippocampus of aged CD200^{-/-}, compared with WT, mice, the predicted decrease in T₂ relaxation times was not observed. T₂ reductions were evident in all ROIs assessed in both genotypes; however, this reduction in T₂ signal was not enhanced in CD200^{-/-} mice in any ROI assessed. These data suggest that a reduction in

T_2 measurement does not reflect an increase in microglial activity, and that use of this MR parameter as a biomarker of changes in microglial activation is inappropriate. It is possible that the degree of additional microglial activation manifest in the CD200^{-/-} mice was not sufficient to impact on T_2 relaxation time. Future work should include the staining for iron deposition in WT and CD200^{-/-} tissue. Overall, the relationship between microglial activation and T_2 relaxometry remains unclear, and is worthy of further analysis.

In this study, T_1 relaxation times were significantly increased in the grey matter areas of the cortex and hippocampus of 4 month-old CD200^{-/-}, compared with WT, mice. These changes were not observed in the ROIs of the corpus callosum and thalamus, although there was a genotype difference was observed. Interestingly, GFAP positive staining was markedly increased in the cortex and hippocampus of 4 month-old CD200^{-/-}, compared with WT, mice. When quantified, there was a significant age-related increase in GFAP positive staining in cortical sections prepared from WT mice, and this age-related increase was exacerbated in CD200^{-/-} mice. GFAP positive staining was unchanged in hippocampal sections prepared from WT mice, while representative images show an age-related decrease in GFAP positive staining in CD200^{-/-} mice. These results suggest an age-induced increase in astrocytic activation in cortical sections of both genotypes, while hippocampal immunoreactivity showed no change in WT mice and a decrease in CD200^{-/-} mice with age.

Astrocytes have been reported to display elevated levels of GFAP mRNA and immunostaining (Kohama *et al.*, 1995), and the calcium binding protein S100 β (Nichols, 1999) as an animal ages. Several studies have shown an increase of approximately 20% in total astrocyte number in the aged mouse cortex (Pilegaard & Ladefoged, 1996; Mouton *et al.*, 2002). Conversely, studies have shown no age-related change in total astrocyte number in the hippocampus of aged mice (Long *et al.*, 1998) or rats (Hattiangady & Shetty, 2008). It has been shown that normal ageing is associated with an inflammatory response (Lee *et al.*, 2000; Swift *et al.*, 2001) and oxidative stress (Sohal & Weindruch, 1996) and the evidence suggests that activated astrocytes contribute to these changes. Astrocytes, in conjunction with microglia, undergo a series of metabolic and morphological changes following neuronal injury. These are collectively known as *reactive gliosis*. These changes include astrocytic hypertrophy characterized by elongated process, and a significant variation in the expression of the

major cytoplasmic antigens GFAP (Cotrina & Nedergaard, 2002) and vimentin (Alonso, 2001). These changes in astrocytic activation are also observed under a variety of conditions, including the AD brain (Porchet *et al.*, 2003), and in cultured rat astrocytes following treatment with β -amyloid peptides (Pike *et al.*, 1994).

The data indicated that T_1 relaxation times were unaffected by age. However, the increase in T_1 signal and GFAP immunoreactivity observed in 4 month-old CD200^{-/-}, compared with WT, mice is of particular interest. This finding is consistent with studies that have demonstrated a positive correlation between acute astrocytosis and enhanced T_1 signal (Sibson *et al.*, 2008). It has been shown that treatment with arundic acid, an astrocytic inhibitor with known neuroprotective effects, significantly reduces the extent of the T_1 signal hypointensity seen in a model of low-flow ischemia induced by endothelin-1 injection (Sibson *et al.*, 2008). Similarly, recent evidence from this laboratory has shown that treatment with rosiglitazone, a PPAR γ agonist that has potential anti-inflammatory actions, reverses both the age-related increase in astrocytic activation denoted by GFAP expression and T_1 relaxometry, while T_2 relaxometry was unaffected (Cowley *et al.*, 2010).

Taken together, these findings suggest that acute astrocytosis may be reflected in an enhancement of the spin-lattice T_1 relaxation time. Several reasons have been put forward relating to the nature of this relationship. T_1 increases have been noted following increases in tissue water content (Barbier *et al.*, 2005), and it has been suggested that astrocytic hypertrophy, or changes in tissue structure following acute astrocytic activation may underlie these changes in T_1 signal (Sibson *et al.*, 2008). Manganese, a paramagnetic metal that is bound to the glutamine synthetase enzyme which is expressed primarily on astrocytes, can also cause a delayed T_1 after ischemia. A study by Fujioka and colleagues (2003) found that manganese concentrations were significantly increased in the rat striatum following a 15 minute period of middle cerebral artery occlusion. Subsequent T_1 intensity increases, observed up to 4 weeks after treatment, were temporally correlated with increased glutamate synthetase and manganese concentrations, as well as GFAP immunoreactivity in reactive astrocytes in the dorsolateral striatum of treated rats (Fujioka *et al.*, 2003). Together, these data suggest T_1 signal enhancement in MR images may be a proxy marker for astrocytosis.

The VBM technique is capable of comparing local differences in grey matter volume in different groups of animals, while ignoring differences in whole brain size

and shape. At 4 months of age, no significant difference in grey matter volumetry was observed in CD200-deficient mice, indicating that anatomical brain volume was unchanged at this early stage of development. It is important to note that CD200^{-/-} mice are bred against a C57BL/6 background.

A major finding in our present study was that grey matter volume was decreased in CD200^{-/-}, compared with WT, mice at 9 and 17 months of age. At 9 months of age, areas of significant decreases were found in cerebellar and cortical regions with the auditory, visual and motor cortices displaying the greatest change. These data may infer a loss of function in auditory and visual function in the CD200-deficient mouse. However, day-to-day observations and inspection provided no evidence of loss of function. The loss of grey matter found in the motor cortex and cerebellum may suggest a loss of motor coordination (Dar, 1997; Allin *et al.*, 2001) but no gross differences in gait were observed. At 17 months of age, significant grey matter loss in CD200^{-/-} mice was restricted to regions in the olfactory bulbs of the frontal lobes. Several reports have identified body weight as a significant factor in predicting brain size (Williams, 2000) and, interestingly, body mass in CD200^{-/-} mice was consistently reduced by approximately 10% compared with WT mice.

Several studies have shown a decrease in rodent brain volume with age (Geinisman *et al.*, 1995). There are several causes of this reduction, including cell death and reduced neurogenesis. Indeed, Driscoll and colleagues (2006) reported an age-related decrease in hippocampal volume in the rat brain. This was marginally associated with decreased neuronal density in the hippocampus of the aged, compared with young, rat, but strongly correlated with a decrease in neurogenesis in the 24 month-old rat (Driscoll *et al.*, 2006). Atrophy has been reported to result from axonal damage in models of MS (Owens, 2003). Interestingly, treatment with steroids (Fisher *et al.*, 2002) or an IFN- β remedy (Gasparini *et al.*, 2002) has been shown to reduce atrophy in relapsing MS patients. The primary target for these treatments is the inflammatory response, and their ability to reduce atrophy suggests a role for inflammation in axonal loss.

Activated microglia release substantial amounts of glutamate (Bruck & Stadelmann, 2003) and activate AMPA receptors present on neurons. It has been shown that blockade of these receptors ameliorates EAE, and clinical relapses, and protects axons from immune-mediated damage (Steinman, 2001). While enhanced microglial

activation is the hallmark of CD200^{-/-} mice, at this stage it is unknown whether neuronal or axonal stress is a feature of these mice.

At 13 months of age, increases in grey matter volume were observed in the cerebellum and the CA3 area of the hippocampus in CD200^{-/-}, compared with WT, mice. This result is somewhat surprising, as these same mice underwent the same anatomic analysis 4 months earlier, and differences were observed in the opposite direction, as already described. At this point it is unclear whether a change in ventricle size, which has been shown to affect hippocampal atrophy (Thompson *et al.*, 2004), was a feature of CD200-deficient mice, and thus could explain the changes in hippocampal volume seen in CD200^{-/-} mice at this timepoint.

The ASL technique has one significant advantage over the traditional BOLD fMRI approach: the ASL signal is primarily related to blood flow, and not blood oxygenation, and therefore perfusion of active brain regions can be quantified. Using this technique, no age- or genotype-related changes in MTT and CTT values were observed over the course of the experiment. The bolus tracking ASL approach identified a significant increase in both the MTT and CTT in aged, compared to both young and middle-aged, rats (Kelly *et al.*, 2009b). This contrasts with the lack of an age-related change observed here. However, it is prudent to point out that the rats used in the earlier study were 22-24 months of age, while the oldest mice used in the present study were just 17 months of age. Variation in vascular dynamics due to ageing associated with reduced vascular reactivity are known to affect cerebral perfusion (D'Esposito *et al.*, 2003).

The results presented in this study indicate that CD200-deficient mice show increased CD11b expression with age and this age-related change was greater than that seen in WT mice. T₂ MR relaxometry, which we hypothesized may reflect an activated microglial profile, was significantly decreased with age in the cortex and hippocampus of both WT and CD200^{-/-} mice, however there was no further enhancement in CD200^{-/-} mice. T₁ relaxometry, a parameter defining water content of tissue, and GFAP immunostaining, were both significantly increased in the cortex and hippocampus of 4 month-old CD200^{-/-}, compared with WT, mice, and this result correlates with reports linking an increase in spin-lattice relaxation time and acute astrocytic activation.

Chapter 4

Analysis of the effects of LPS treatment in WT and CD200^{-/-} mice

4.1 Introduction

Several studies have shown that ligation of the CD200R by its endogenous ligand helps preserve microglia in a quiescent state, for example Lyons and colleagues (2009). Consistent with this is the finding that models of inflammatory diseases are exaggerated in CD200-deficient mice (Hoek *et al.*, 2000) and that treatment with a CD200 fusion protein can alleviate the development of arthritis in a model of CIA (Gorczyński *et al.*, 2002). Recent evidence from this laboratory has shown an enhanced response to both LPS and Pam₃Cysk₄ administration in glial cells prepared from CD200^{-/-}, compared with WT, mice (Costello *et al.*, 2011) which was characterized by an increase in the production of the pro-inflammatory cytokines IL-1 β , IL-6 and TNF- α . These changes were associated with a concomitant increase in TLR4 mRNA expression in CD200^{-/-}, compared with WT, mice. It has also been previously shown that ip injection with LPS induces glial activation, characterized by an increase in the production of IL-1 β in the hippocampus of the rat brain (Vereker *et al.*, 2000) and that this effect is enhanced in aged mice (Henry *et al.*, 2009). Thus, the first aim of this study was to investigate the effect of LPS treatment on markers of glial activation in 6-8 month-old WT and CD200^{-/-} mice.

The ability of MRI to detect subtle changes in tissue water properties has allowed for its use as a clinical tool in a variety of neurodegenerative and inflammatory conditions, including the detection of MS lesions (Truyen *et al.*, 1996) and A β -laden plaques in AD (Vanhoutte *et al.*, 2005). Moreover, several studies have implicated changes in the spin-lattice T₁ and spin-spin lattice T₂ times with changes in reactive astrocytosis (Sibson *et al.*, 2008) and the cellular distribution of iron or ferritin (Imon *et al.*, 1998), respectively. Evidence from the previous chapter indicated that both T₁ values and astrocytosis, which was denoted by GFAP immunoreactivity, were increased in the cortex and hippocampus of CD200-deficient mice. In addition, T₂ relaxation times were significantly decreased with age in WT and CD200^{-/-} mice. This may have been reflective of enhanced microglial activation in the aged WT and CD200^{-/-} mouse, although the exaggerated increase in CD11b expression in CD200^{-/-} mice was not reflected in an enhanced T₂ signal decrease. Therefore, the second aim was to use an acute model of inflammation to further explore the relationship between T₁ and T₂ relaxation times, and acute astrocytosis and microglial activation, respectively.

The functionality of the BBB in separating components of the circulating blood from neuronal tissue depends on surrounding cells (pericytes, microglia, astrocytes) (Zlokovic, 2008). This remains connected through the presence of tight junctions, which limit the entry of plasma components, red blood cells and leukocytes. Breakdown of BBB integrity, due to tight junction disruption, has been shown to occur in conditions of the CNS in which inflammatory changes have been described, including normal ageing, MS, PD and bacterial meningitis (Weiss *et al.*, 2009).

Several studies have shown increase BBB disruption following LPS treatment (Banks *et al.*, 1999; Xaio *et al.*, 2001), however the degree to which LPS causes BBB permeability has not been quantified. BBB breakdown is commonly assessed following intravenous delivery of the contrast-agent gadolinium, a magnetic compound with a molecular weight of 742 Daltons. Due to its relative size, gadolinium-based agents are unable to passively diffuse across microvessels in homeostatic circumstances (Campbell *et al.*, 2009). By virtue of its ability to shorten the relaxation time of surrounding hydrogen nuclei (Hashimoto *et al.*, 1988), post-gadolinium image enhancement manifests as an increase in T₁ signal intensity (Blamire *et al.*, 2000) in cases where BBB leakage and gadolinium extravasation has occurred. Therefore, the third and final aim in this study was to quantify BBB permeability to gadolinium in WT and CD200^{-/-} mice following a 4 hour treatment with 50µg LPS, using a tail-vein cannulation procedure in mice residing inside the scanner.

4.2 Methods

Groups of 6-8 month-old WT and CD200^{-/-} mice (weighing 21g-40g) were used in this study. The WT mice consisted of 8 males and 13 females, and the CD200^{-/-} mice consisted of 12 males and 19 females. Mice were randomly divided into control and experimental groups (n=6-9/group). The control groups received an ip injection of sterile saline (200µl). The first experimental group received an ip injection of LPS (200µl; 10µg/mouse diluted in sterile saline) and the second experimental group received an ip injection of LPS (200µl; 50µg/mouse diluted in sterile saline). LPS was prepared from *Escherichia coli* (*E. coli*) serotype EH 100 (Ra) (Alexis Biochemicals, Switzerland).

Mice were anaesthetized with isoflurane (see section 2.1.2), and MR scanning was carried out 2.5 and 3.5 hours post treatment. The mice remained in the scanner between these two scans. T₁- and T₂-weighted imaging (see sections 2.1.5 and 2.1.6, respectively) were obtained in the first part of this study. Data suggested that there was no significant effect 2.5 hours after LPS treatment and these data are summarised in Tables 7.3 and 7.5 in Appendix II.

BBB permeability to the gadolinium-based contrast agent gadopentate dimeglumine was investigated using contrast enhanced MRI. The mouse cradle was removed from the magnet, and a heated glove was applied to the mouse tails to induce blood flow. The mice remained under anaesthetic during the cannulation process. The right lateral tail veins were cannulated with a custom-built cannula consisting of a 30 gauge in-dwelling, paediatric iv cannula needle (Introcan, Ireland) which was connected to an 80cm long polyethylene tubing cannula extension. This tubing was filled with sterile saline, and connected to a three-way tap, which was connected to two syringes. One of these was filled with saline; the other was filled with the Magnevist contrast agent solution (Bayer, Ireland; Magnevist to saline ratio; 1:2).

Mice were injected with the contrast agent solution (200µl) at the commencement of the second repetition of the 10 repetition T₁-weighted FLASH contrast scan (approximately 2 minutes, 11 seconds into the imaging scan), allowing both pre- and post-contrast image analysis of the same contrast scan, without the need to remove and reposition the mouse. This permitted the accurate placement of ROIs from pre-contrast images into the identical voxels in subsequent repetitions, and allowed for the immediate effects of the contrast agent to be analysed. The contrast enhanced imaging was performed on the control-treated and 50µg LPS-treated WT and CD200^{-/-} mice.

Following scanning and 4 hours after LPS treatment, mice were sacrificed by cervical dislocation and brain tissue was prepared for analysis of inflammatory markers. Brains were rapidly removed, and placed on a Petri dish that had been filled with ice. Brains were hemisected and prepared for immunohistochemical analysis of CD11b and GFAP (right hemisphere) which was later quantified (see section 2.7.5), and mRNA analysis of microglial and astrocytic markers and tight junction proteins by qPCR (left hemisphere). For PCR, each hemisphere was divided into hippocampal and cortical tissue (see section 2.5.1 for specific details).

Data are presented as means \pm standard error of the mean. For the contrast analysis, ROIs consisting of a 2x2 voxel square were manually placed in each anatomically distinct region; contrast analysis was performed in the cortex, hippocampus, thalamus, cerebellum and frontal lobes. These data are expressed as a ratio by dividing post-contrast images by the pre-contrast measurement. The last four repetitions of the contrast scan from each mouse were used for statistical analysis. The contrast MRI results presented here are from ROI analysis in the right cortex; the tissue from which was later analysed by PCR. The data from the left cortex are presented in Table 7.7 in Appendix III.

A two-way ANOVA was performed to ascertain whether significant differences existed in all the data. Where significance was found, Bonferroni post-hoc tests were used to determine where significant differences lay in the data (see section 2.8 for details). Where appropriate, a two-tailed Student's t-test of independent means was performed to determine whether statistical difference existed between conditions.

4.3 Results

4.3.1 *The effect of LPS on cortical and hippocampal CD40 mRNA expression*

The effect of 10 μ g and 50 μ g LPS treatment on glial activation was investigated on WT and CD200^{-/-} mice, and the subsequent effects on relaxometry parameters. Treatment of mice with LPS increased expression of CD40 mRNA in cortical and hippocampal tissue in a dose-dependent manner. Figure 4.1 shows that CD40 mRNA expression was significantly increased in snap-frozen cortical tissue prepared from WT mice treated with 50 μ g LPS (149.0 ± 52.67 RQ; n=6) compared with control-treated WT mice (1.24 ± 0.24 RQ; n=12; *p<0.05; ANOVA). CD40 mRNA expression was significantly increased in cortical tissue prepared from CD200^{-/-} mice treated with 50 μ g LPS (301.9 ± 103.3 RQ; n=7) compared with control-treated CD200^{-/-} mice (0.66 ± 0.1274 ; n=15; ***p<0.001; ANOVA). LPS (50 μ g) induced a significant increase in CD40 mRNA expression in CD200^{-/-} mice (301.9 ± 103.3 RQ; n=7) compared with WT mice (149.0 ± 52.67 RQ; n=6; #p<0.05; ANOVA) while 10 μ g LPS had no significant

effect on cortical CD40 mRNA expression in WT (35.43 ± 12.54 RQ; n=6) or CD200^{-/-} (5.123 ± 1.707 RQ; n=9) mice.

Figure 4.2 illustrates that CD40 mRNA expression was significantly increased in hippocampal tissue prepared from WT mice treated with 50µg LPS (465.0 ± 150.7 RQ; n=6) compared with control-treated WT mice (1.52 ± 0.27 RQ; n=13; ***p<0.001; ANOVA). CD40 mRNA expression in hippocampal tissue prepared from CD200^{-/-} mice treated with 50µg LPS (783.9 ± 229.5 RQ; n=5) compared with control-treated CD200^{-/-} mice (0.81 ± 0.12 RQ; n=15; ***p<0.001; ANOVA). LPS (50µg) induced a significant increase in CD40 mRNA expression in hippocampal tissue prepared from CD200^{-/-} mice (783.9 ± 229.5 RQ; n=5) compared with WT mice (465.0 ± 150.7 RQ; n=6; #p<0.05; ANOVA) while 10µg LPS had no significant effect on hippocampal CD40 mRNA expression in either WT mice (34.20 ± 10.80 RQ; n=6) or CD200^{-/-} mice (2.01 ± 0.69 RQ; n=8).

4.3.2 The effect of LPS treatment on CD11b expression

It has been shown in several studies that CD200 helps maintain microglia in a quiescent state (Copland *et al.*, 2007). The results from the previous chapter suggested that CD200^{-/-} mice have an inflammatory phenotype at rest as indicated by an increase in CD11b immunoreactivity. Thus, it was hypothesized that ip treatment of LPS would initiate an exaggerated response in CD200^{-/-}, compared with WT, mice.

In contrast with the effects of LPS on CD40 mRNA, neither dose affected cortical expression of CD11b mRNA in tissue prepared from either WT, or CD200^{-/-}, mice (Figure 4.3). Mean CD11b mRNA values were similar in cortical tissue prepared from WT mice treated with 50µg LPS (0.99 ± 0.07 RQ; n=8) compared with WT mice treated with 10µg LPS (1.13 ± 0.05 RQ; n=6) or control-treated WT mice (1.01 ± 0.05 RQ; n=13). Mean CD11b mRNA values were similar in cortical tissue prepared from CD200^{-/-} mice treated with 50µg LPS (0.86 ± 0.12 RQ; n=7) compared with control-treated CD200^{-/-} mice (1.02 ± 0.05 RQ; n=15) and compared with CD200^{-/-} mice treated with 10µg LPS (1.11 ± 0.13 RQ; n=9). There was no significant difference in cortical CD11b mRNA values between WT and CD200^{-/-} mice.

Expression of CD11b mRNA was also unchanged in hippocampal tissue prepared from WT mice treated with 50µg LPS (1.39 ± 0.14 RQ; n=7; Figure 4.4)

compared with control-treated WT mice (1.04 ± 0.14 RQ; $n=6$) and compared with WT mice treated with $10\mu\text{g}$ LPS (1.14 ± 0.19 RQ; $n=6$). However, $50\mu\text{g}$ LPS significantly increased CD11b mRNA in CD200^{-/-} mice (2.12 ± 0.37 RQ; $n=8$) compared with control-treated CD200^{-/-} mice (1.14 ± 0.17 RQ; $n=15$; * $p<0.05$; ANOVA) and $10\mu\text{g}$ LPS-treated CD200^{-/-} mice (1.32 ± 0.15 RQ; $n=7$; + $p<0.05$; ANOVA). Treatment with $50\mu\text{g}$ LPS exerted a significantly greater increase in CD11b mRNA in CD200^{-/-} mice (2.12 ± 0.37 RQ; $n=8$) compared with WT mice (1.39 ± 0.14 RQ; $n=7$; # $p<0.05$; ANOVA).

Figure 4.5 illustrates the effect of LPS on CD11b immunoreactivity in cortical sections prepared from the right hemisphere of control-treated and LPS-treated WT and CD200^{-/-} mice. Positive staining was low in sections prepared from control-treated WT mice. There was a moderate increase in positive staining in cortical sections prepared from WT mice treated with LPS with indication of a dose-dependent response. A similar trend was identified in sections prepared from CD200^{-/-} mice. Positive staining was low in cortical sections prepared from control-treated CD200^{-/-} mice. There was a dose-dependent increase in CD11b immunoreactivity in sections prepared from LPS-treated CD200^{-/-}, compared with control-treated, mice. There was no difference in CD11b immunoreactivity due to genotype. There was a significant LPS-related increase in the ratio of DAB/nuclear area in the cortex of WT mice (** $p<0.001$; ANOVA) and CD200^{-/-} mice (** $p<0.001$; ANOVA).

The effect of LPS treatment on hippocampal CD11b immunostaining is presented in Figure 4.6. Positive staining was low in hippocampal sections prepared from control-treated and WT mice treated with $10\mu\text{g}$ LPS. There was an increase in immunoreactivity in hippocampal sections prepared from WT mice treated with $50\mu\text{g}$ LPS. CD11b immunoreactivity was also low in hippocampal sections from control-treated CD200^{-/-} mice. There was a dose-dependent increase in CD11b staining in hippocampal sections prepared from LPS-treated CD200^{-/-} mice. There was a significant LPS-related increase in the ratio of DAB/nuclear area in the dentate gyrus of WT mice (** $p<0.001$; ANOVA) and CD200^{-/-} mice (** $p<0.001$; ANOVA).

4.3.3 The effect of LPS treatment on mRNA expression of pro-inflammatory cytokines

Given that aged CD200^{-/-} mice exhibited a heightened microglial response compared with young mice, and that LPS treatment exerted a more profound effect in CD200^{-/-}, compared with WT, mice, it was hypothesized that LPS treatment would exert a more exaggerated response in the release of the pro-inflammatory cytokines IL-1 β , TNF- α and IL-6 in 6-8 month old CD200^{-/-}, compared with WT, mice. Figure 4.7 illustrates that there was a significant increase in IL-1 β mRNA expression in snap-frozen cortical tissue prepared from WT mice treated with 50 μ g LPS (382500 ± 227909 RQ; n=4) compared with control-treated WT mice (1.11 ± 0.21 RQ; n=12; *** p<0.001; ANOVA) and compared with WT mice treated with 10 μ g LPS (8.99 ± 0.67 RQ; n=6; ++ p<0.01; ANOVA). The changes in tissue prepared from CD200^{-/-} were similar; thus 10 μ g LPS exerted no significant effect over control-treated WT mice (6.41 ± 2.39 RQ; n=8 vs 0.98 ± 0.14 RQ; n=14). There was a significant increase in IL-1 β mRNA expression in cortical tissue prepared from CD200^{-/-} mice treated with 50 μ g LPS (460346 ± 353901 ; n=5) compared with control-treated CD200^{-/-} mice (0.98 ± 0.14 RQ; n=14; ** p<0.01; ANOVA) and compared with CD200^{-/-} mice treated with 10 μ g LPS (6.41 ± 2.39 RQ; n=8; ++ p<0.01; ANOVA). There was no significant effect of genotype.

The effect of LPS on hippocampal IL-1 β mRNA is presented in Figure 4.8. Mean hippocampal IL-1 β mRNA was increased in WT mice treated with 50 μ g LPS (2446225 ± 1799393 RQ; n=5) compared with control-treated WT mice (0.97 ± 0.11 RQ; n=12; * p<0.05; ANOVA), but similar with WT mice treated with 10 μ g LPS (39.69 ± 13.65 RQ; n=6). The changes in tissue prepared from CD200^{-/-} mice were similar; thus 10 μ g LPS exerted no significant effect over controls (5.43 ± 0.43 RQ; n=14 vs 1.22 ± 0.22 RQ; n=4). There was a significant increase in IL-1 β mRNA in hippocampal tissue prepared from CD200^{-/-} mice treated with 50 μ g LPS (2591800 ± 1798900 RQ; n=6) compared with control-treated CD200^{-/-} mice (1.22 ± 0.22 RQ; n=4; * p<0.05; ANOVA) and CD200^{-/-} mice treated with 10 μ g LPS (5.43 ± 0.43 RQ; n=14; + p<0.05; ANOVA). Genotype was not a factor in predicting IL-1 β .

Figure 4.9 illustrates the LPS effect on TNF- α mRNA on snap-frozen cortical tissue prepared from WT and CD200^{-/-} mice. There was a significant increase in TNF- α mRNA in cortical tissue prepared from WT mice treated with 50 μ g LPS (41249 ± 19542 RQ; n=7) compared with control-treated WT mice (1.84 ± 0.55 RQ; n=12;

p<0.01; ANOVA) and WT mice treated with 10µg LPS (57.83 ± 11.25 RQ; n=6; ⁺p<0.05; ANOVA). Likewise, there was a significant increase in TNF-α mRNA expression in cortical tissue prepared from CD200^{-/-} mice treated with 50µg LPS (44482 ± 19656 RQ; n=7) compared with control-treated CD200^{-/-} mice (2.62 ± 0.57 RQ; n=15; *p<0.001; ANOVA) and CD200^{-/-} mice treated with 10µg LPS (30.10 ± 7.49 RQ; n=8; ⁺⁺p<0.01; ANOVA). Individual comparisons yielded no significant genotype differences in the data.

The effect of LPS treatment on hippocampal TNF-α mRNA expression in WT and CD200^{-/-} mice is presented in Figure 4.10. There was a significant increase in TNF-α mRNA expression in hippocampal tissue prepared from WT mice treated with 50µg LPS (130410 ± 64167 RQ; n=7) compared with control-treated WT mice (1.32 ± 0.27 RQ; n=13; **p<0.01; ANOVA) and WT mice treated with 10µg LPS (23.79 ± 3.14 RQ; n=6; ⁺p<0.05; ANOVA). In addition, there was a significant increase in TNF-α mRNA expression in CD200^{-/-} mice treated with 50µg LPS (104242 ± 65018 RQ; n=6) compared with control-treated CD200^{-/-} mice (1.21 ± 0.24 RQ; n=14; *p<0.05; ANOVA) and compared with CD200^{-/-} mice treated with 10µg LPS (9.57 ± 2.32 RQ; n=7; ⁺p<0.05; ANOVA). Genotype was not a factor in predicting TNF-α values.

Figure 4.11 illustrates the LPS-induced changes in IL-6 mRNA expression in snap-frozen cortical tissue prepared from WT and CD200^{-/-} mice. There was a significant increase in cortical IL-6 mRNA expression in WT mice treated with 50µg LPS (19281 ± 7644 RQ; n=8) compared with control-treated WT mice (1.78 ± 0.60 RQ; n=12; ***p<0.001; ANOVA) and WT mice treated with 10µg LPS (23.73 ± 8.08 RQ; n=5; ⁺⁺p<0.01; ANOVA). The changes in tissue prepared from CD200^{-/-} mice were similar; thus 10µg LPS exerted no significant effect over controls (16.67 ± 6.62 RQ vs 0.87 ± 0.21 RQ; n=14) whereas there was a significant increase in expression of IL-6 mRNA in cortical tissue prepared from CD200^{-/-} mice treated with 50µg LPS (19962 ± 4687 RQ; n=7) compared with control-treated CD200^{-/-} mice (0.87 ± 0.21 RQ; n=14; ***p<0.001; ANOVA) and CD200^{-/-} mice treated with 10µg LPS (16.67 ± 6.62 RQ; ⁺⁺⁺p<0.001; ANOVA).

A similar effect on hippocampal IL-6 mRNA expression was observed in LPS-treated mice in this study, which is presented in Figure 4.12. There was a significant increase in IL-6 mRNA in WT mice treated with 50µg LPS (48514 ± 15476 RQ; n=7) compared with control-treated WT mice (1.41 ± 0.32 RQ; n=13; ***p<0.001; ANOVA)

and WT mice treated with 10 μ g LPS (34.46 ± 13.21 RQ; n=5; ⁺⁺⁺p<0.001; ANOVA). The changes in tissue prepared from CD200^{-/-} mice were similar; thus, 10 μ g LPS exerted no significant effect over controls (4.27 ± 1.46 RQ; n=7 vs 0.90 ± 0.22 RQ; n=14) whereas there was a significant increase in IL-6 mRNA expression in hippocampal tissue prepared from CD200^{-/-} mice treated with 50 μ g LPS (32579 ± 14678 RQ; n=7) compared with control-treated CD200^{-/-} mice (0.90 ± 0.22 RQ; n=14; ⁺⁺p<0.01; ANOVA) and CD200^{-/-} mice treated with 10 μ g LPS (4.27 ± 1.46 RQ; n=7; ⁺⁺p<0.01; ANOVA). There was no effect of genotype on determining IL-6 mRNA values in these data.

4.3.4 The effect of LPS treatment on GFAP expression

Given that LPS-treated astrocytes exhibit a heightened response compared with control-treated astrocytes (Lieberman *et al.*, 1989; Brahmachari *et al.*, 2006) and that LPS induces astroglial activation *in vivo* (Iravani *et al.*, 2005), the effect of LPS treatment on GFAP mRNA expression in WT and CD200^{-/-} mice was investigated.

GFAP mRNA was significantly increased in cortical tissue prepared from WT and CD200^{-/-} mice treated with 50 μ g LPS compared with controls (1.40 ± 0.09 RQ; n=7 vs 0.95 ± 0.07 RQ; n=12; ^{**}p<0.01; ANOVA and 1.26 ± 0.11 RQ; n=7 vs 0.91 ± 0.08 RQ; n=14; ^{*}p<0.05; Figure 4.13) and compared with tissue obtained from WT and CD200^{-/-} mice treated with 10 μ g LPS compared with controls (1.40 ± 0.09 RQ; n=7 vs 0.93 ± 0.12 RQ; n=6; ⁺p<0.05; ANOVA and 1.26 ± 0.11 RQ; n=7 vs 0.81 ± 0.05 RQ; n=8; ⁺p<0.05; ANOVA). The changes in the hippocampus were similar with no evidence of a change in tissue prepared from WT and CD200^{-/-} mice treated with 10 μ g LPS compared with controls (1.34 ± 0.07 RQ; n=6 vs 1.10 ± 0.10 RQ; n=13 and 1.24 ± 0.10 RQ; n=7 vs 0.97 ± 0.05 RQ; n=15; Figure 4.14) whereas 50 μ g LPS significantly increased hippocampal GFAP mRNA in WT and CD200^{-/-} mice compared with controls (1.75 ± 0.11 RQ; n=8 vs 1.10 ± 0.10 RQ; n=13; ^{*}p<0.05; ANOVA and 2.26 ± 0.44 RQ; n=8 vs 0.97 ± 0.05 RQ; n=15; ^{***}p<0.001; ANOVA) and compared with CD200^{-/-} mice treated with 10 μ g LPS (2.26 ± 0.44 RQ; n=8 vs 1.24 ± 0.10 RQ; n=7; ⁺⁺p<0.01; ANOVA).

Figure 4.15 illustrates the effect of LPS treatment on GFAP immunostaining in cortical sections in the right hemisphere of WT and CD200^{-/-} mice. Positive staining

was low in cortical sections prepared from control-treated and WT and CD200^{-/-} mice and in mice treated with 10µg LPS. There was an increase in positive staining for GFAP in sections prepared from mice treated with 50µg LPS compared with control-treated mice. There was a significant LPS-related increase in the ratio of DAB/nuclear area in the cortex of WT mice (***p*<0.001; ANOVA) and CD200^{-/-} mice (***p*<0.001; ANOVA).

Positive staining for GFAP was also low in hippocampal sections prepared from control-treated WT mice (Figure 4.16). There was a moderate increase in GFAP immunoreactivity in hippocampal sections from WT mice treated with 10µg LPS and a further increase following treatment with 50µg LPS. There was no effect of 10µg LPS treatment on hippocampal GFAP immunoreactivity in CD200^{-/-} mice. However, there was a marked increase in GFAP positive staining in hippocampal sections prepared from CD200^{-/-} mice treated with 50µg LPS. There was a significant LPS-related increase in the ratio of DAB/nuclear area in the dentate gyrus of WT mice (***p*<0.001; ANOVA) and CD200^{-/-} mice (***p*<0.001; ANOVA).

4.3.5 The effect of LPS treatment on T₁ relaxometry

To determine if the astrocytic activation induced by the LPS treatment was reflected in changes in T₁ relaxometry as previously reported (Sibson *et al.*, 2008), control and LPS-treated WT and CD200^{-/-} mice were scanned at two timepoints following treatment. These timepoints were 2.5 and 3.5 hours after LPS administration. ROI analysis was carried out bilaterally on the RARE-VTR images. There were no changes observed at the first timepoint and therefore the data from the 2.5 hours timepoint are included in Table 7.3 in Appendix II. There was a significant increase in T₁ values in the whole cortex of WT mice treated with 50µg LPS (1671 ± 25.67 ms; n=8) compared with control-treated WT mice (1576 ± 23.90 ms; n=6; ***p*<0.01; ANOVA) and compared with WT mice treated with 10µg LPS (1537 ± 23.65 ms; n=6; +++*p*<0.001; ANOVA). In addition, there was a significant increase in T₁ values in the whole cortex of CD200^{-/-} mice treated with 50g LPS (1707 ± 19.96 ms; n=7) compared with control-treated CD200^{-/-} mice (1633 ± 13.01 ms; n=9; **p*<0.05; ANOVA) and CD200^{-/-} mice treated with 10µg LPS (1626 ± 10.07 ms; n=9; +*p*<0.05; ANOVA). Furthermore, there was a significant increase in cortical T₁ values of CD200^{-/-} mice

treated with 10 μ g LPS (1626 \pm 10.07 ms; n=9) compared with WT mice treated with 10 μ g LPS (1537 \pm 23.65 ms; n=6; §p<0.05; ANOVA).

T₁ relaxation times were also assessed in the motor cortex, entorhinal cortex, hippocampus, thalamus and corpus callosum. The lower concentration of LPS exerted no effect in any of the brain areas examined in either WT or CD200^{-/-} mice. Interestingly, 50 μ g LPS significantly increased T₁ relaxation times in all brain areas except corpus callosum in WT mice (*p<0.05; ***p<0.001; **p<0.01; +p<0.05; ANOVA; Figures 4.18-4.22). T₁ relaxation times were also significantly increased in the entorhinal cortex, hippocampus, thalamus and corpus callosum, but not motor cortex, of CD200^{-/-} mice treated with 50 μ g LPS compared with controls (**p<0.001; ***p<0.001; *p<0.05; p<0.05; ANOVA). Interestingly, the LPS-induced change was significantly greater in the hippocampus of CD200^{-/-}, compared with WT, mice (§§§p<0.001; ANOVA). The values for T₁ relaxation times are presented in Table 7.4, Appendix II.

The relationship between T₁ relaxation times of the cortex and hippocampus, and GFAP mRNA in these regions is presented in Figure 4.23. There was a moderate relationship between T₁ values and the associated GFAP mRNA expression in these areas (Pearson r = 0.5613; ***p<0.001; n=82).

4.3.6 The effect of LPS treatment on T₂ relaxometry

Control- and LPS-treated mice were scanned at two timepoints following treatment to determine if the enhanced microglial activation was reflected in changes in the T₂ relaxometry parameter. There were no changes observed at the first timepoint and therefore the data from the 2.5 hour timepoint is presented in Table 7.5 in Appendix II. The LPS-induced changes in T₂ values in the whole cortex of WT and CD200^{-/-} mice are presented in Figure 4.24. Mean cortical T₂ values were similar in control-treated WT mice (49.78 \pm 0.23 ms; n=6), compared with WT mice treated with 10 μ g LPS (49.78 \pm 0.33 ms; n=6) and WT mice treated with 50 μ g LPS (50.58 \pm 0.36 ms; n=8). Mean cortical T₂ values were similar in control-treated CD200^{-/-} mice (50.31 \pm 0.21 ms; n=9) compared with CD200^{-/-} mice 10 μ g LPS (50.36 \pm 0.28 ms; n=9). There was a significant increase in T₂ values in the cortex of CD200^{-/-} mice treated with 50 μ g LPS (51.47 \pm 0.19 ms; n=7) compared with control-treated mice (50.31 \pm 0.21 ms; n=9;

**p<0.01; ANOVA) and CD200^{-/-} mice treated with 10µg LPS (50.36 ± 0.28 ms; n=9; ⁺p<0.05).

T₂ relaxation times were also assessed in the motor cortex, entorhinal cortex, hippocampus, thalamus and corpus callosum. The lower concentration of LPS exerted no significant effect on T₂ values in any of these brain regions of WT or CD200^{-/-} mice. There was a decrease in T₂ values in the motor cortex of WT mice treated with 50µg LPS compared with controls (**p<0.001; ANOVA) and in WT and CD200^{-/-} mice treated with 50µg LPS compared with mice treated with 10µg LPS (**p<0.001; ⁺p<0.05; ANOVA; Figure 4.25). However, there was an increase in T₂ values in the entorhinal cortex of WT and CD200^{-/-} mice treated with 50µg LPS compared with controls (**p<0.001; **p<0.001; ANOVA) and compared with mice treated with 10µg LPS (⁺⁺⁺p<0.001; ⁺⁺⁺p<0.001; ANOVA; Figure 4.26). There was a significant increase in T₂ values in CD200^{-/-} mice treated with 50µg LPS compared with controls (*p<0.05; ANOVA; Figure 4.27) but there was no effect of LPS treatment on T₂ values in the thalamus of either WT or CD200^{-/-} mice (Figure 4.28). There was a significant decrease in T₂ values in the corpus callosum of WT mice treated with 50µg LPS compared with controls (**p<0.001; ANOVA) and compared with WT mice treated with 10µg LPS (⁺⁺⁺p<0.001; ANOVA; Figure 4.29). The T₂ values are presented in Table 7.6 in Appendix II.

4.3.7 *The effect of LPS treatment on tight junction proteins*

Claudin 5 mRNA and occludin mRNA was investigated in cortical and hippocampal samples prepared from control-treated mice and mice treated with 50µg LPS. There was a significant decrease in claudin 5 mRNA expression in the cortex of LPS-treated WT mice (0.24 ± 0.11 RQ; n=8) compared with control-treated WT mice (1.01 ± 0.08 RQ; n=7; **p<0.001; ANOVA; Figure 4.30). There was also a significant decrease in cortical expression of claudin 5 mRNA in LPS-treated CD200^{-/-} mice (0.15 ± 0.01 RQ; n=6) compared with control-treated CD200^{-/-} mice (0.60 ± 0.06 RQ; n=8; **p<0.001; ANOVA). Moreover, there was a significant decrease in claudin 5 mRNA expression in cortical tissue prepared from control-treated CD200^{-/-} mice (0.60 ± 0.06 RQ) compared with control-treated WT mice (1.01 ± 0.08 RQ; n=7; ⁺⁺⁺p<0.001; ANOVA).

Similar data were obtained in the hippocampus (Figure 4.31). Claudin 5 mRNA was significantly decreased in tissue prepared from LPS-treated WT mice (0.17 ± 0.02 RQ; n=7) compared with control-treated WT mice (1.03 ± 0.77 RQ; n=7; ***p<0.001; ANOVA) and in LPS-treated CD200^{-/-} mice (0.14 ± 0.01 RQ; n=7) compared with control-treated CD200^{-/-} mice (0.57 ± 0.08 RQ; n=7; ***p<0.001; ANOVA). In addition, expression of claudin 5 mRNA was significantly reduced in hippocampal tissue prepared from control-treated CD200^{-/-} mice (0.57 ± 0.08 RQ; n=7) compared with control-treated WT mice (1.03 ± 0.77 RQ; n=7; +++p<0.001; ANOVA).

In parallel, occludin mRNA was decreased in cortical tissue prepared from LPS-treated WT and CD200^{-/-} compared with controls (0.10 ± 0.03 RQ; n=5 and 0.12 ± 0.02 RQ; n=7 vs 0.82 ± 0.09 RQ; n=5; ***p<0.001; ANOVA and 0.41 ± 0.07 RQ; n=7; **p<0.01; ANOVA; Figure 4.32) and a genotype-related change was observed (0.41 ± 0.07 RQ; n=7 vs 0.82 ± 0.09 RQ; n=5; +++p<0.001; ANOVA). A similar pattern of change was observed in hippocampal tissue (Figure 4.33) but in this case a significant effect of LPS was observed in LPS-treated compared with control-treated WT mice (0.32 ± 0.11 RQ; n=7 vs 1.14 ± 0.46 RQ; n=5; *p<0.05; ANOVA) but not CD200^{-/-} mice (0.12 ± 0.03 RQ; n=6 vs 0.72 ± 0.23 RQ; n=6).

In addition, claudin 12 mRNA was decreased in cortical tissue prepared from LPS-treated WT and CD200^{-/-} mice compared with controls (0.78 ± 0.04 RQ; n=8 and 0.73 ± 0.07 RQ; n=7 vs 1.01 ± 0.06 RQ; n=7; *p<0.05; ANOVA and 0.97 ± 0.07 RQ; n=7; *p<0.05; ANOVA; Figure 4.34). A similar trend was observed in hippocampal tissue prepared from control-treated and LPS-treated WT and CD200^{-/-} mice (0.52 ± 0.01 RQ; n=5 and 0.47 ± 0.05 RQ; n=7 vs 0.79 ± 0.19 RQ; n=5 and 0.70 ± 0.06 RQ; n=9; Figure 4.35); however, individual comparisons did not reach statistical significance.

4.3.8 The effect of LPS treatment on BBB permeability to gadolinium

The BBB is a highly specialized, structural and functional barrier that is formed by the tight cohesion of the fully differentiated brain microvascular endothelium. Several studies have shown that LPS induces BBB disruption in mice, for example in the uptake of insulin which has a molecular weight of 5808 Da (Xaio *et al.*, 2001), however BBB permeability in CD200^{-/-} mice has not been studied to date. In this study,

BBB permeability to the gadolinium-based contrast agent, Magnevist, was assessed in control- and LPS (50 μ g)-treated WT and CD200^{-/-} mice. ROI analysis was carried out bilaterally on groups of voxels in the cortex, dentate gyrus, thalamus, cerebellum and olfactory bulb. The data from the right hemisphere is presented in Figures 4.37-4.43 and the data from the left hemisphere is presented in Table 7.7 in Appendix II.

Sample data sets showing pre- and post-contrast contrast enhancement from a control- and LPS-treated, WT and CD200^{-/-} mouse, are presented (Figure 4.36). The pre-contrast scans (first repetitions) from the four data sets have been set at equivalent signal values to enable comparisons. SI in the control-treated WT mouse did not change post-contrast whereas SI was increased in the brain of the LPS-treated WT mouse following contrast injection, which is denoted by a change in voxel colours from yellow to red. A similar increase in SI was evident in the control-treated CD200^{-/-} mouse and the greatest change in contrast between pre- and post-gadolinium injection was in the LPS-treated CD200^{-/-} mouse.

SI values in the right motor cortex of WT mice were unchanged following gadolinium injection compared with the pre-contrast value (Figure 4.37) but there was a significant increase in SI in the motor cortex of WT mice treated with LPS (1.06 ± 0.01 RQ; n=7) compared with control-treated WT mice (1.01 ± 0.01 RQ; n=5; ***p<0.001; ANOVA). In addition, there was a significant increase in SI in the motor cortex of control-treated CD200^{-/-} mice (1.05 ± 0.01 RQ; n=5) compared with control-treated WT mice (1.01 ± 0.01 RQ; n=5; ***p<0.001; ANOVA) although treatment with LPS had no significant effect on SI values in CD200^{-/-} mice (1.08 ± 0.01 RQ; n=5) compared with control-treated CD200^{-/-} mice (1.05 ± 0.01 RQ; n=5).

SI values were also assessed in the right somatosensory cortex, entorhinal cortex, dentate gyrus, ventrolateral thalamus, frontal association cortex and cerebellar nucleus. SI values in these areas were unchanged following gadolinium injection compared with the pre-contrast values. However, there were significant increases in SI in the somatosensory and entorhinal cortices, and dentate gyrus of WT mice treated with 50 μ g LPS compared with control-treated WT mice (***p<0.001; ***p<0.001; ***p<0.001; ANOVA; Figures 4.37-4.42). However, SI values were unchanged in the thalamus, frontal association cortex and cerebellum of LPS-treated WT mice compared with control-treated WT mice. In addition, there was a significant increase in SI in the somatosensory and entorhinal cortices, dentate gyrus, thalamus of CD200^{-/-} mice

(* p<0.01; *** p<0.001; ** p<0.001; * p<0.01; ANOVA) but not in the frontal association cortex or cerebellum. Interestingly, the LPS-induced change in SI was significantly greater in the somatosensory and entorhinal cortices and thalamus of CD200^{-/-} mice compared with LPS-treated WT mice (* p<0.01; * p<0.05; * p<0.05; ANOVA). The SI values are presented in Table 7.7 in Appendix III.

4.3.9 Correlation between SI and tight junction mRNA

The relationship between post-contrast SI values and mRNA expression of tight junction proteins is presented in Figure 4.44. SI values from cortical and hippocampal ROIs were pooled and paired with the associated expression of tight junction proteins claudins 5, 12 and occludin. There was a strong inverse correlation between SI and claudin 5 mRNA expression (Figure A: Pearson r = -0.79; *** p<0.0001; n=44). There were moderate and significant inverse correlations between SI and claudin 12 mRNA expression (Figure B: Pearson r = -0.54; *** p=0.0002; n=44) and between post-contrast SI values and occludin mRNA expression (Figure C: Pearson r = -0.62; *** p<0.0001; n=44).

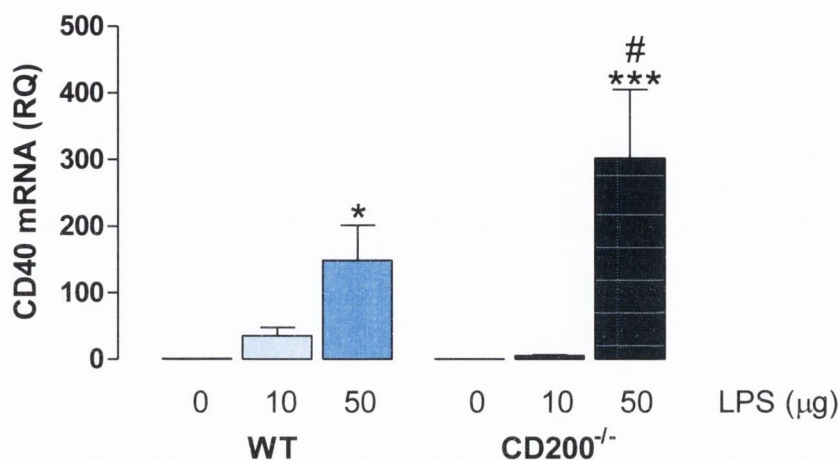


Figure 4.1 The effect of LPS on cortical CD40 mRNA expression in WT and CD200^{-/-} mice.

Groups of WT and CD200^{-/-} mice were injected ip with sterile saline (200µl) or LPS (10µg or 50µg/mouse; 200µl). After 4 hours, mice were sacrificed by decapitation, right cortex dissected free, homogenized and CD40 mRNA expression determined by qPCR. Mean CD40 mRNA expression was increased in cortical tissue prepared from 50µg LPS-treated WT mice compared with control-treated mice (*p<0.05; ANOVA) and in cortical tissue prepared from 50µg LPS-treated CD200^{-/-} mice compared with control-treated CD200^{-/-} mice (**p<0.001; ANOVA). Treatment with 50µg LPS induced a significantly greater effect in CD200^{-/-} mice compared with WT mice (#p<0.05; ANOVA). Values are expressed as relative quantities (RQ) obtained from calculating the ratio of CD40 mRNA to an endogenous control and are means ± SEM.

2-way ANOVA: LPS effect F (2, 49) = 21.47; p<0.0001, Genotype effect F (1, 49) = 1.846; p=0.1805, Interaction effect F (2, 49) = 3.112; p=0.0534

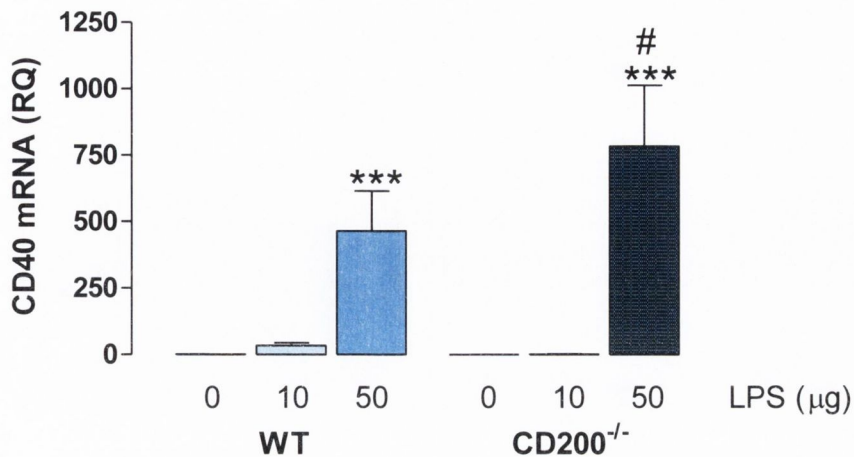


Figure 4.2 The effect of LPS on hippocampal CD40 mRNA expression in WT and CD200^{-/-} mice.

Groups of WT and CD200^{-/-} mice were injected ip with sterile saline (200µl) or LPS (10µg or 50µg/mouse; 200µl). After 4 hours, mice were sacrificed by decapitation, right hippocampus dissected free, homogenized and CD40 mRNA expression determined by qPCR. Mean CD40 mRNA expression was increased in hippocampal tissue prepared from 50µg LPS-treated WT mice compared with control mice (***p*<0.001; ANOVA) and in 50µg LPS-treated CD200^{-/-} mice compared with control-treated CD200^{-/-} mice (***p*<0.001; ANOVA). Treatment with 50µg LPS induced a significantly greater effect in CD200^{-/-} mice compared with WT mice ([#]*p*<0.05; ANOVA). Values are expressed as relative quantities (RQ) obtained from calculating the ratio of CD40 mRNA to an endogenous control and are means ± SEM.

2-way ANOVA: LPS effect $F(2, 47) = 44.61$; $p < 0.0001$, **Genotype effect** $F(1, 47) = 2.758$; $p = 0.1034$, **Interaction effect** $F(2, 47) = 3.112$; $p = 0.0493$

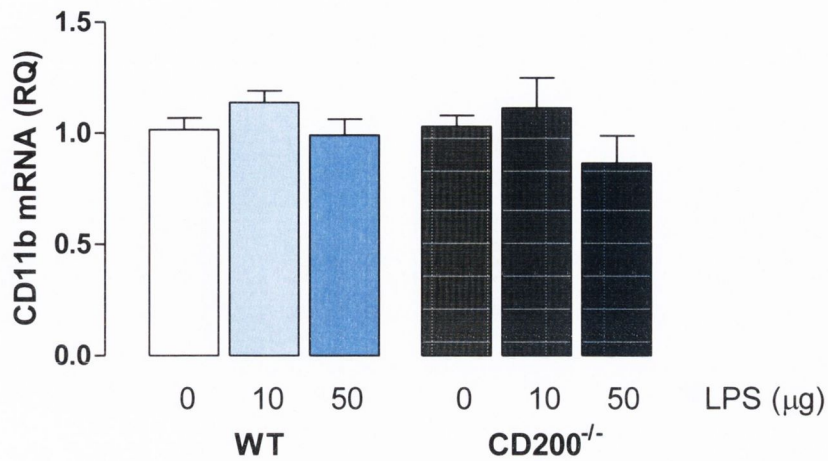


Figure 4.3 The effect of LPS on cortical CD11b mRNA expression in WT and CD200^{-/-} mice.

Groups of WT and CD200^{-/-} mice were injected ip with sterile saline (200µl) or LPS (10µg or 50µg/mouse; 200µl). After 4 hours, mice were sacrificed by decapitation, right cortex dissected free, homogenized and CD11b mRNA expression determined by qPCR. Mean CD11b mRNA expression was similar in cortical tissue prepared from 50µg LPS-treated WT mice, compared with 10µg LPS and control-treated WT mice, and in 50µg LPS-treated CD200^{-/-} mice, compared with 10µg LPS-treated and control-treated CD200^{-/-} mice. Values are expressed as relative quantities (RQ) obtained from calculating the ratio of CD11b mRNA to an endogenous control and are means ± SEM.

2-way ANOVA: LPS effect F (2, 52) = 2.264; p=0.1141, Genotype effect F (1, 52) = 0.4363; p=0.5118, Interaction effect F (2, 52) = 0.3766.; p=0.6881

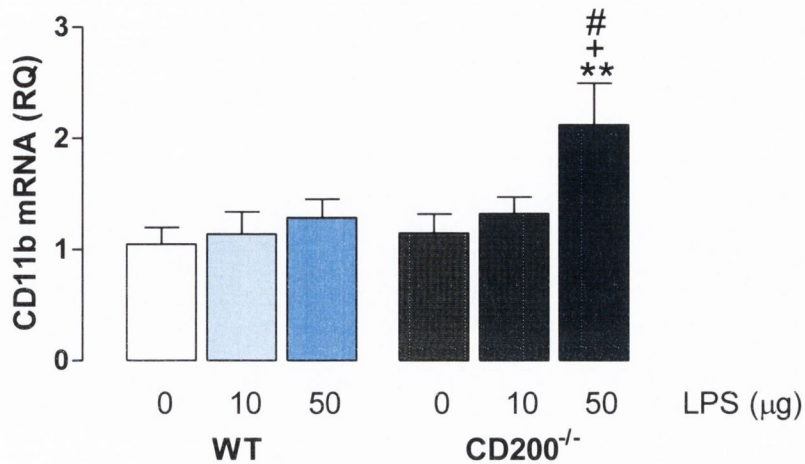


Figure 4.4 The effect of LPS on hippocampal CD11b mRNA expression in WT and CD200^{-/-} mice.

Groups of WT and CD200^{-/-} mice were injected ip with sterile saline (200µl) or LPS (10µg or 50µg/mouse; 200µl). After 4 hours, mice were sacrificed by decapitation, right hippocampus dissected free, homogenized and CD11b mRNA expression determined by qPCR. Mean CD11b mRNA expression was increased in hippocampal tissue prepared from 50µg LPS-treated CD200^{-/-} mice compared with control-treated mice (**p<0.01; ANOVA) and compared with 10µg LPS-treated mice (+p<0.05; ANOVA). Treatment with 50µg LPS induced a significantly greater effect in CD200^{-/-} mice compared with WT mice (#p<0.05; ANOVA). Values are expressed as relative quantities (RQ) obtained from calculating the ratio of CD11b mRNA to an endogenous control and are means ± SEM.

2-way ANOVA: LPS effect F (2, 43) = 4.599; p=0.0155, Genotype effect F (1, 43) = 3.234; p=0.0792, Interaction effect F (2, 43) = 1.085.; p=0.3471

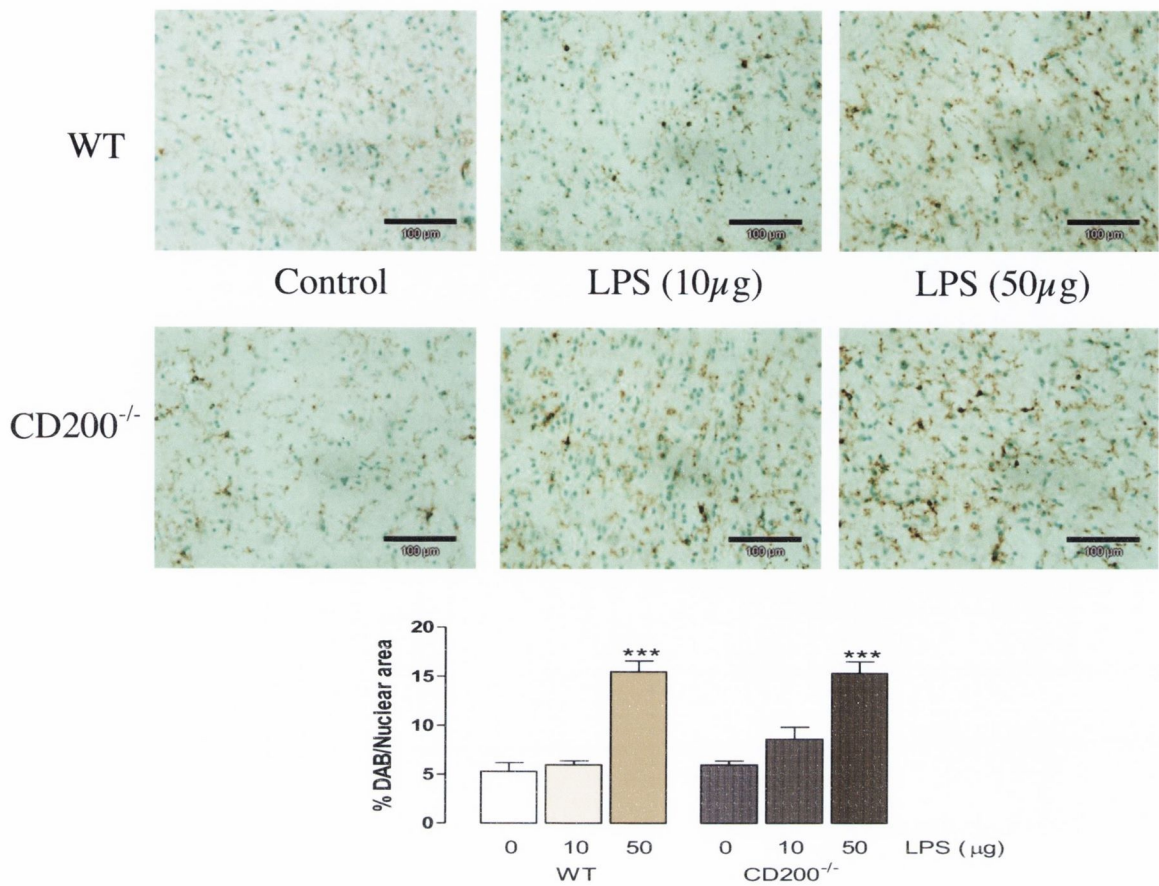


Figure 4.5 The effect of LPS on cortical CD11b expression in WT and CD200^{-/-} mice.

Groups of WT and CD200^{-/-} mice received an ip injection of sterile saline (200µl) or LPS (10µg or 50µg/mouse; 200µl). There was an increase in CD11b positive staining in cortical sections prepared from 10µg and 50µg LPS-treated WT and CD200^{-/-} mice, compared with control-treated mice (Magnification 40x, scale bar 100µm).

There was a significant LPS-related increase in the ratio of DAB/nuclear area in the cortex of WT mice (***p*<0.001; ANOVA) and CD200^{-/-} mice (***p*<0.001; ANOVA).

2-way ANOVA: Treatment effect $F(2, 30) = 62.09$; $p < 0.0001$, **Genotype effect** $F(1, 30) = 1.86$; $p = 0.1828$, **Interaction effect** $F(2, 26) = 1.183$; $p = 0.3203$

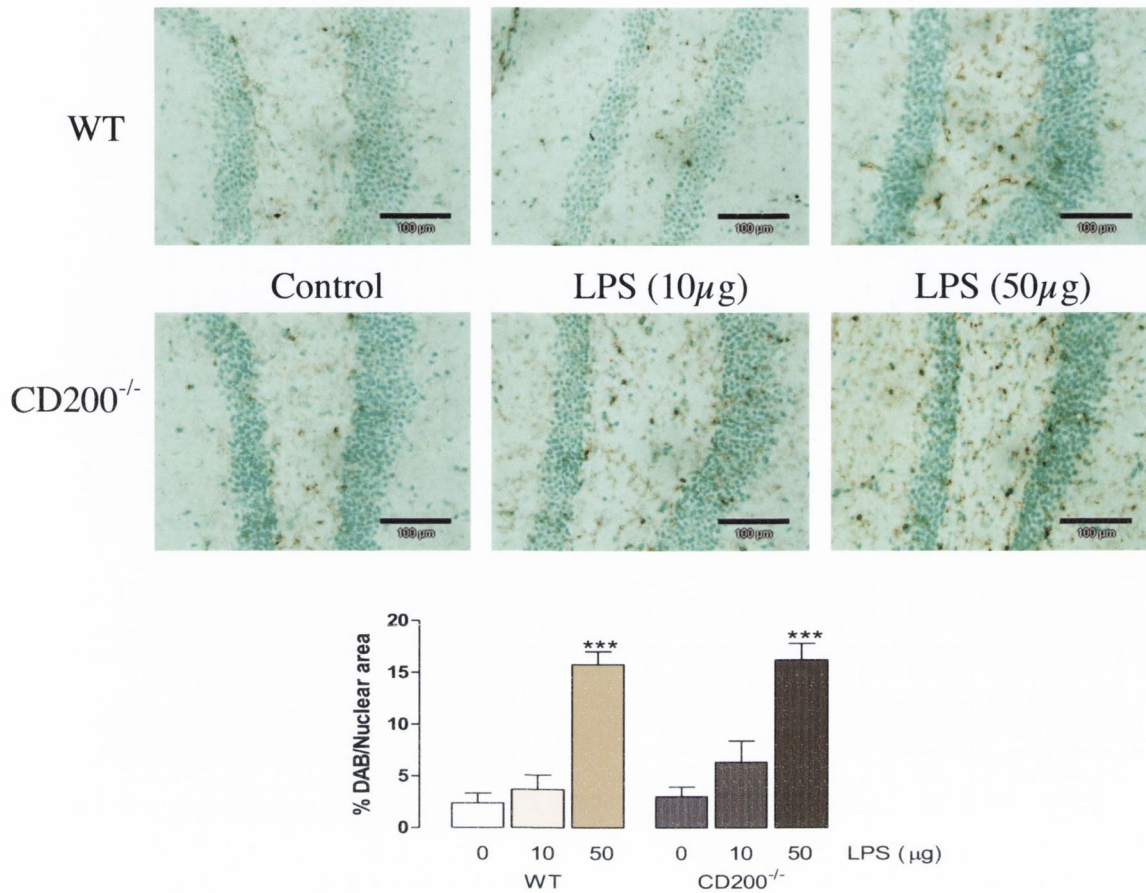


Figure 4.6 The effect of LPS on hippocampal CD11b expression in WT and CD200^{-/-} mice.

Groups of WT and CD200^{-/-} mice received an ip injection of sterile saline (200µl) or LPS (10µg or 50µg/mouse; 200µl). There was a dose dependent increase in CD11b positive staining in hippocampal sections prepared from LPS-treated WT mice, compared with control-treated mice, and in 10µg and 50µg LPS-treated CD200^{-/-}, compared with control-treated CD200^{-/-}, mice. (Magnification 40x, scale bar 100µm).

There was a significant LPS-related increase in the ratio of DAB/nuclear area in the dentate gyrus of WT mice (***) p<0.001; ANOVA) and CD200^{-/-} mice (***) p<0.001; ANOVA).

2-way ANOVA: Treatment effect F (2, 30) = 50.21; p<0.0001, Genotype effect F (1, 30) = 1.148; p=0.2926, Interaction effect F (2, 26) = 0.3656; p=0.6968

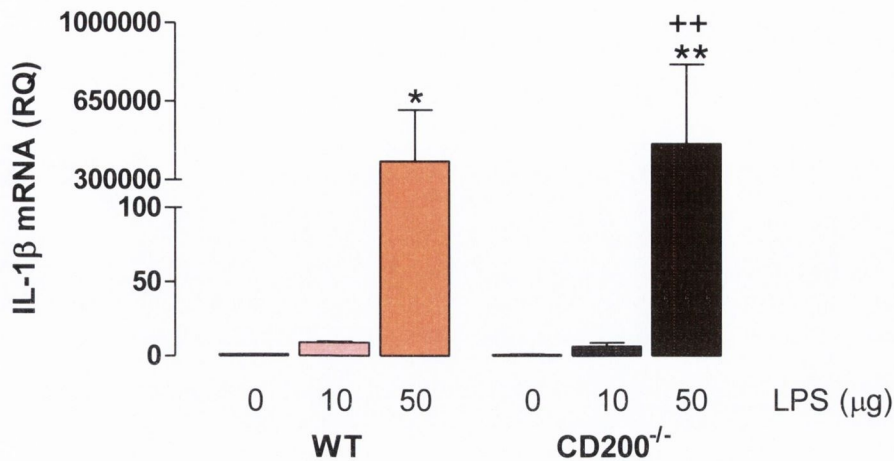


Figure 4.7 The effect of LPS on cortical IL-1 β mRNA expression in WT and CD200^{-/-} mice.

Groups of WT and CD200^{-/-} mice were injected ip with sterile saline (200 μ l) or LPS (10 μ g or 50 μ g/mouse; 200 μ l). After 4 hours, mice were sacrificed by decapitation, right cortex dissected free, homogenized and IL-1 β mRNA expression determined by qPCR. Mean IL-1 β mRNA expression was increased in cortical tissue prepared from 50 μ g LPS-treated WT mice compared with control-treated mice (* p <0.05; ANOVA) and 50 μ g LPS-treated CD200^{-/-} mice compared with control-treated mice (** p <0.01; ANOVA) and compared with 10 μ g LPS-treated mice (++) p <0.01; ANOVA). Values are expressed as relative quantities (RQ) obtained from calculating the ratio of IL-1 β mRNA to an endogenous control and are means \pm SEM.

2-way ANOVA: LPS effect $F(2, 43) = 8.859$; $p=0.0006$, **Genotype effect** $F(1, 43) = 0.0929$; $p=0.762$, **Interaction effect** $F(2, 43) = 0.0755$; $p=0.9273$

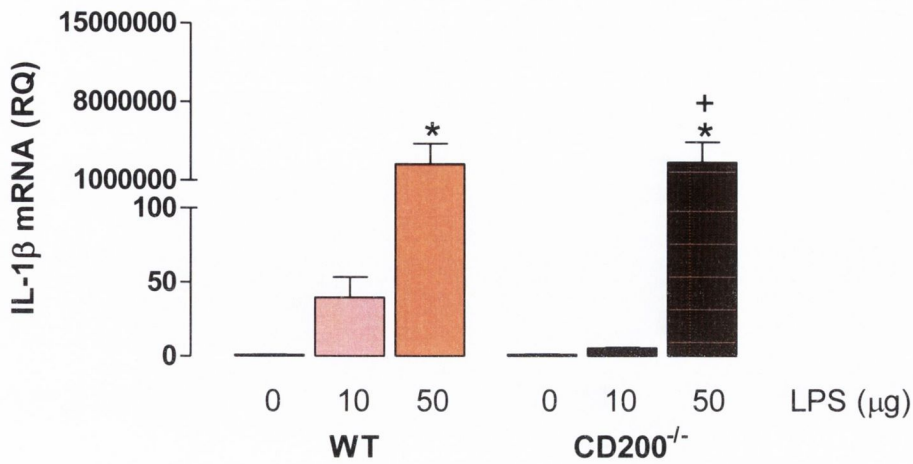


Figure 4.8 The effect of LPS on hippocampal IL-1 β mRNA expression in WT and CD200^{-/-} mice.

Groups of WT and CD200^{-/-} mice were injected ip with sterile saline (200 μ l) or LPS (10 μ g or 50 μ g/mouse; 200 μ l). After 4 hours, mice were sacrificed by decapitation, right hippocampus dissected free, homogenized and IL-1 β mRNA expression determined by qPCR. Mean IL-1 β mRNA expression was increased in hippocampal tissue prepared from 50 μ g LPS-treated WT mice compared with control-treated WT mice (* p <0.05; ANOVA) and in 50 μ g LPS-treated CD200^{-/-} mice compared with control-treated mice (* p <0.05; ANOVA) and compared with 10 μ g LPS-treated mice (⁺ p <0.05; ANOVA). Values are expressed as relative quantities (RQ) obtained from calculating the ratio of IL-1 β mRNA to an endogenous control and are means \pm SEM.

2-way ANOVA: LPS effect $F(2, 44) = 7.344$; $p = 0.0018$, **Genotype effect** $F(1, 44) = 0.0069$; $p = 0.934$, **Interaction effect** $F(2, 44) = 0.0061$; $p = 0.9939$

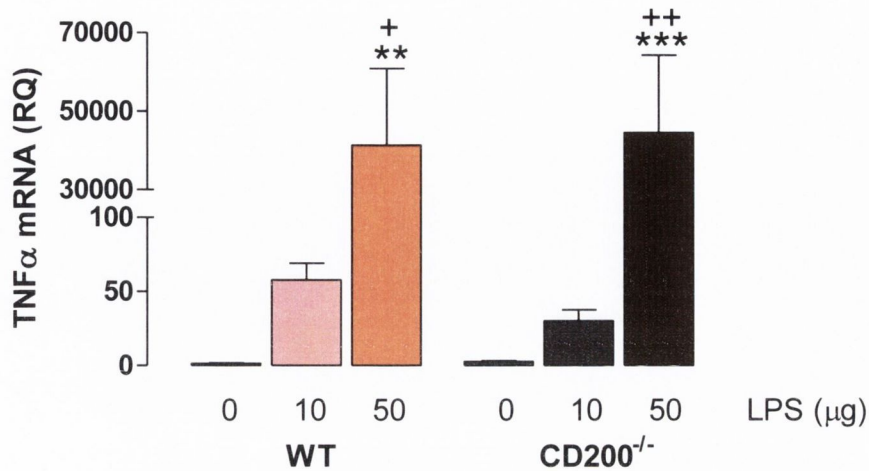


Figure 4.9 The effect of LPS on cortical TNF- α mRNA expression in WT and CD200^{-/-} mice.

Groups of WT and CD200^{-/-} mice were injected ip with sterile saline (200μl) or LPS (10μg or 50μg/mouse; 200μl). After 4 hours, mice were sacrificed by decapitation, right cortex dissected free, homogenized and TNF- α mRNA expression determined by qPCR. Mean TNF- α mRNA expression was increased in cortical tissue prepared from 50μg LPS-treated WT mice compared with control-treated mice (**p<0.01; ANOVA) and compared with 10μg LPS-treated WT mice (+p<0.05; ANOVA). TNF- α mRNA was significantly increased in cortical tissue prepared from 50μg LPS-treated CD200^{-/-} mice compared with control-treated CD200^{-/-} mice (**p<0.001; ANOVA) and compared with 10μg LPS-treated mice (++)p<0.01; ANOVA). Values are expressed as relative quantities (RQ) obtained from calculating the ratio of TNF- α mRNA to an endogenous control and are means \pm SEM.

2-way ANOVA: LPS effect F (2, 49) = 14.49; p<0.0001, Genotype effect F (1, 49) = 0.0214; p=0.8841, Interaction effect F (2, 49) = 0.0207.; p=0.9795

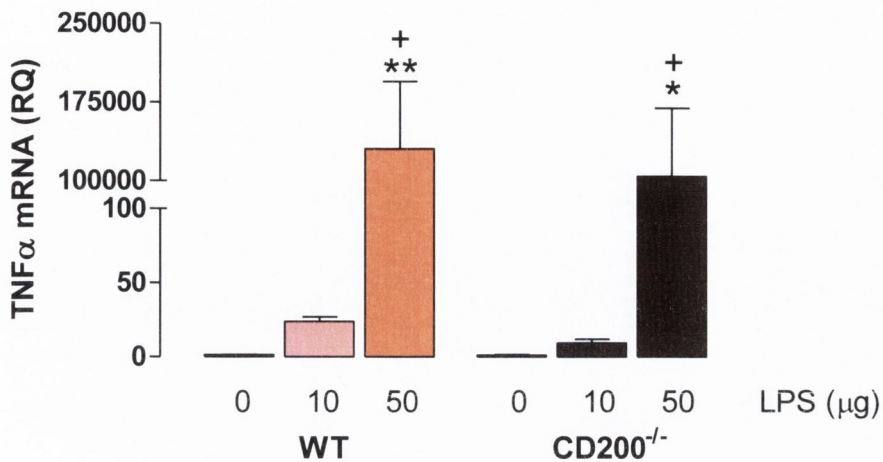


Figure 4.10 The effect of LPS on hippocampal TNF- α mRNA expression in WT and CD200^{-/-} mice.

Groups of WT and CD200^{-/-} mice were injected ip with sterile saline (200 μ l) or LPS (10 μ g or 50 μ g/mouse; 200 μ l). After 4 hours, mice were sacrificed by decapitation, right hippocampus dissected free, homogenized and TNF- α mRNA expression determined by qPCR. Mean TNF- α mRNA expression was increased in hippocampal tissue prepared from 50 μ g LPS-treated WT mice compared with control-treated mice (** p <0.01; ANOVA) and compared with 10 μ g LPS-treated mice (+ p <0.05; ANOVA). TNF- α mRNA was significantly increased in hippocampal tissue prepared from 50 μ g LPS-treated CD200^{-/-} mice compared with control-treated CD200^{-/-} mice (* p <0.05; ANOVA) and compared with 10 μ g LPS-treated CD200^{-/-} mice (+ p <0.05; ANOVA). Values are expressed as relative quantities (RQ) obtained from calculating the ratio of TNF- α mRNA to an endogenous control and are means \pm SEM.

2-way ANOVA: LPS effect $F(2, 47) = 10.53$; $p=0.0002$, **Genotype effect** $F(1, 47) = 0.1401$; $p=0.7099$, **Interaction effect** $F(2, 47) = 0.1310$.; $p=0.8776$

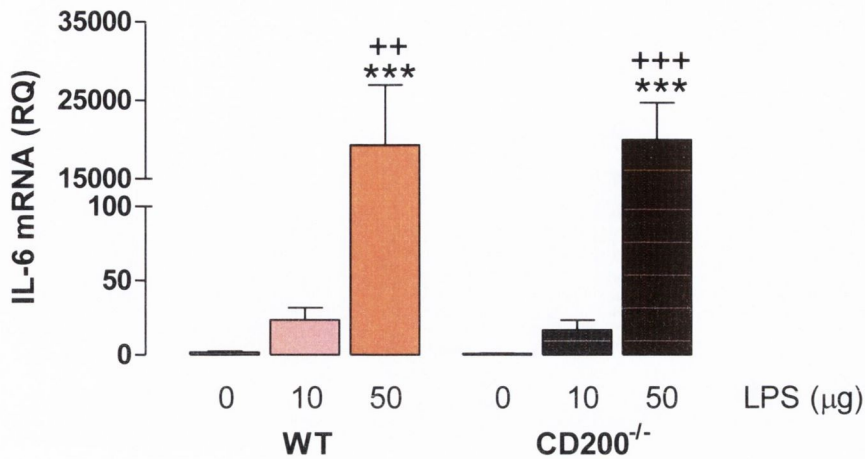


Figure 4.11 The effect of LPS on cortical IL-6 mRNA expression in WT and CD200^{-/-} mice.

Groups of WT and CD200^{-/-} mice were injected ip with sterile saline (200µl) or LPS (10µg or 50µg/mouse; 200µl). After 4 hours, mice were sacrificed by decapitation, right cortex dissected free, homogenized and IL-6 mRNA expression determined by qPCR. Mean IL-6 mRNA expression was increased in cortical tissue prepared from 50µg LPS-treated WT mice compared with control-treated WT mice (**p<0.001; ANOVA) and compared with 10µg LPS-treated WT mice (††p<0.01; ANOVA). IL-6 mRNA was significantly increased in cortical tissue prepared 50µg LPS-treated CD200^{-/-} mice compared with control-treated mice (**p<0.001; ANOVA) and compared with 10µg LPS-treated mice (†††p<0.001; ANOVA). Values are expressed as relative quantities (RQ) obtained from calculating the ratio of IL-6 mRNA to an endogenous control and are means ± SEM.

2-way ANOVA: LPS effect F (2, 49) = 24.21; p<0.0001, Genotype effect F (1, 49) = 0.0072; p=0.9327, Interaction effect F (2, 49) = 0.0073.; p=0.9927

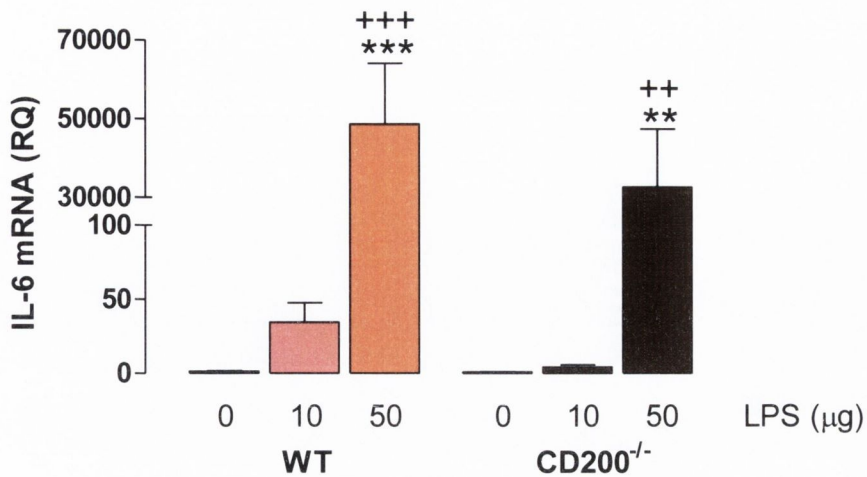


Figure 4.12 The effect of LPS on hippocampal IL-6 mRNA expression in WT and CD200^{-/-} mice.

Groups of WT and CD200^{-/-} mice were injected ip with sterile saline (200µl) or LPS (10µg or 50µg/mouse; 200µl). After 4 hours, mice were sacrificed by decapitation, right hippocampus dissected free, homogenized and IL-6 mRNA expression determined by qPCR. Mean IL-6 mRNA expression was increased in hippocampal tissue prepared from 50µg LPS-treated WT mice compared with control-treated WT mice (**p<0.001; ANOVA) and compared with 10µg LPS-treated WT mice (***p<0.001; ANOVA). IL-6 mRNA was increased in 50µg LPS-treated CD200^{-/-} mice compared with control-treated mice (**p<0.01; ANOVA) and compared with 10µg LPS-treated mice (††p<0.01; ANOVA). Values are expressed as relative quantities (RQ) obtained from calculating the ratio of IL-6 mRNA to an endogenous control and are means ± SEM.

2-way ANOVA: LPS effect F (2, 47) = 20.77; p<0.0001, Genotype effect F (1, 47) = 0.807; p=0.3736, Interaction effect F (2, 47) = 0.8013.; p=0.4548

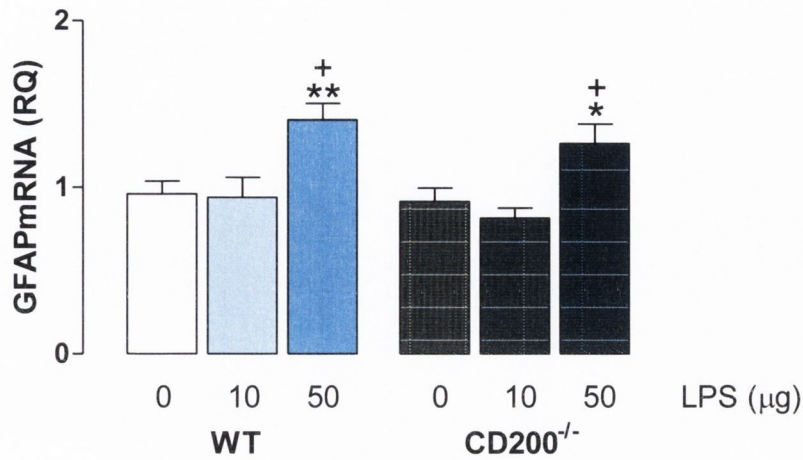


Figure 4.13 The effect of LPS on cortical GFAP mRNA expression in WT and CD200^{-/-} mice.

Groups of WT and CD200^{-/-} mice were injected ip with sterile saline (200µl) or LPS (10µg or 50µg/mouse; 200µl). After 4 hours, mice were sacrificed by decapitation, right cortex dissected free, homogenized and GFAP mRNA expression determined by qPCR. Mean GFAP mRNA expression was increased in cortical tissue prepared from 50µg LPS-treated WT mice compared with control-treated WT mice (**p<0.01; ANOVA) and compared with the 10µg LPS-treated WT mice (+p<0.05; ANOVA), and in 50µg LPS-treated CD200^{-/-} mice compared with control-treated CD200^{-/-} mice (*p<0.05; ANOVA) and compared with 10µg LPS-treated CD200^{-/-} mice (+p<0.05; ANOVA). Values are expressed as relative quantities (RQ) obtained from calculating the ratio of GFAP mRNA to an endogenous control and are means ± SEM.

2-way ANOVA: LPS effect F (2, 48) = 12.05; p<0.0001, Genotype effect F (1, 48) = 1.72; p=0.1959, Interaction effect F (2, 48) = 0.1748; p=0.8372

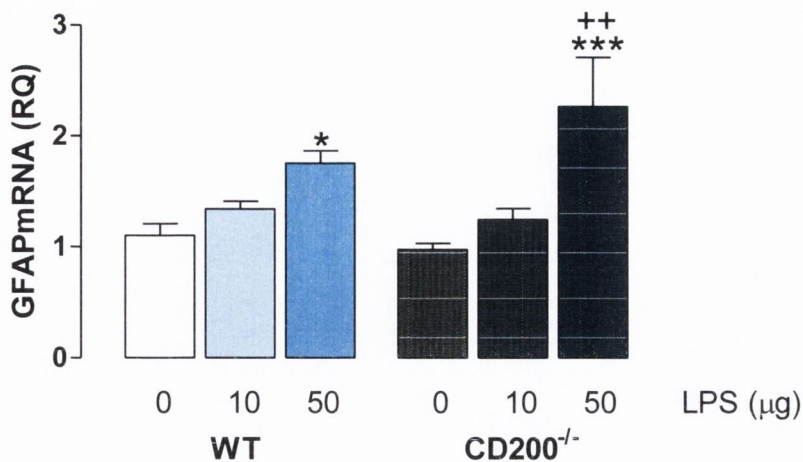


Figure 4.14 The effect of LPS on hippocampal GFAP mRNA expression in WT and CD200^{-/-} mice.

Groups of WT and CD200^{-/-} mice were injected ip with sterile saline (200µl) or LPS (10µg or 50µg/mouse; 200µl). After 4 hours, mice were sacrificed by decapitation, right hippocampus dissected free, homogenized and GFAP mRNA expression determined by qPCR. Mean GFAP mRNA expression was similar in hippocampal tissue prepared from control-treated and 10µg LPS-treated WT and CD200^{-/-} mice. Mean GFAP mRNA expression was increased in hippocampal tissue prepared from 50µg LPS-treated WT mice compared with control-treated WT mice (*p<0.05; ANOVA) and tissue prepared from 50µg LPS-treated CD200^{-/-} mice compared with control-treated mice (**p<0.001; ANOVA) and compared with 10µg LPS-treated CD200^{-/-} mice (**p<0.01; ANOVA). There was no effect of genotype on the RQ values. Values are expressed as relative quantities (RQ) obtained from calculating the ratio of GFAP mRNA to an endogenous control and are means ± SEM.

2-way ANOVA: LPS effect F (2, 51) = 16.76; p<0.0001, Genotype effect F (1, 51) = 0.4272; p=0.5163, Interaction effect F (2, 51) = 1.946.; p=0.1533

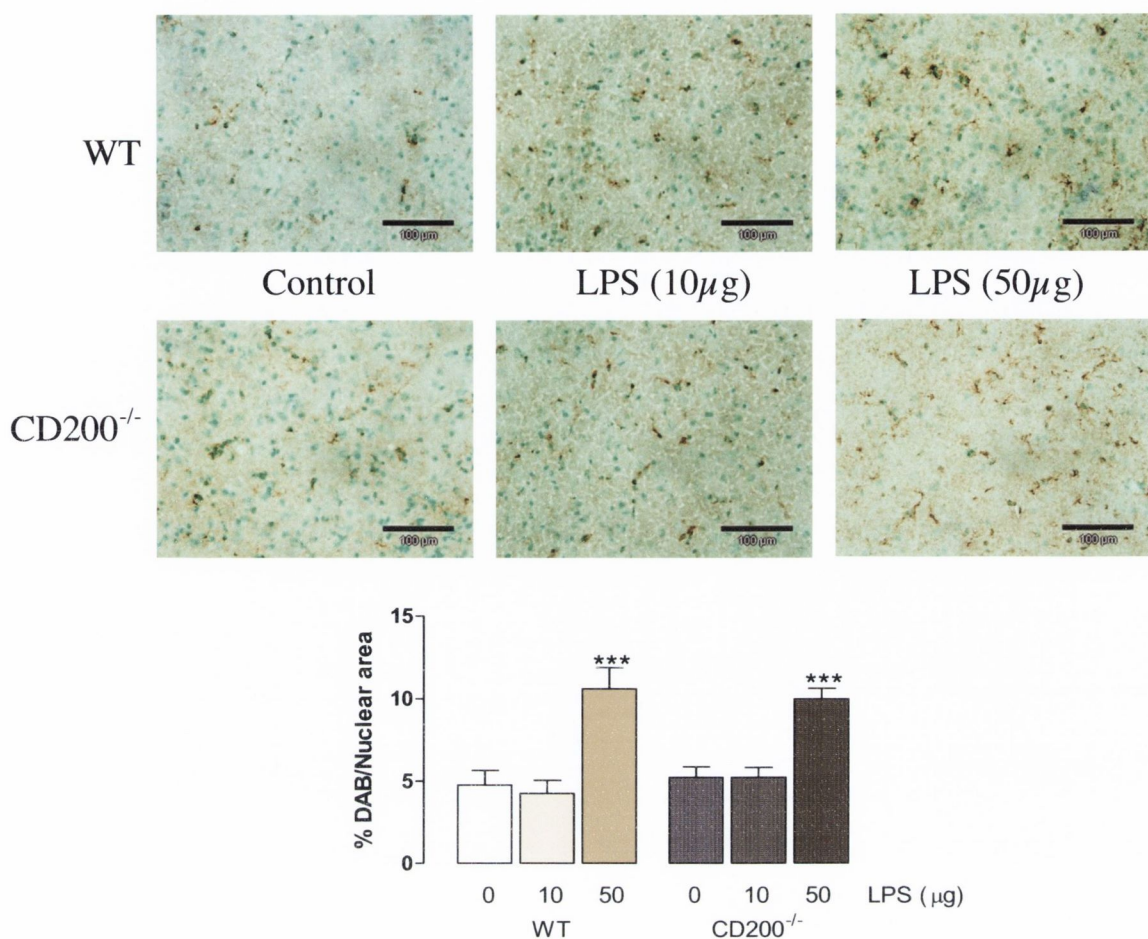


Figure 4.15 The effect of LPS on cortical GFAP expression in WT and CD200^{-/-} mice.

Groups of WT and CD200^{-/-} mice received an ip injection of sterile saline (200µl) or LPS (10µg or 50µg/mouse; 200µl). There was an increase in GFAP positive immunoreactivity in cortical sections prepared from 50µg LPS-treated WT and CD200^{-/-} mice, compared with control and 10µg LPS-treated mice (Magnification 40x, scale bar 100µm). There was a significant LPS-related increase in the ratio of DAB/nuclear area in the cortex of WT mice (**p<0.001; ANOVA) and CD200^{-/-} mice (**p<0.001; ANOVA).

2-way ANOVA: LPS effect F (2, 30) = 27.68; p<0.0001, Genotype effect F (1, 30) = 0.1633; p=0.689, Interaction effect F (2, 26) = 0.4703; p=0.6294

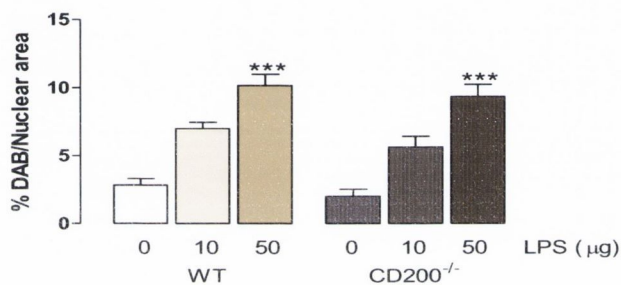
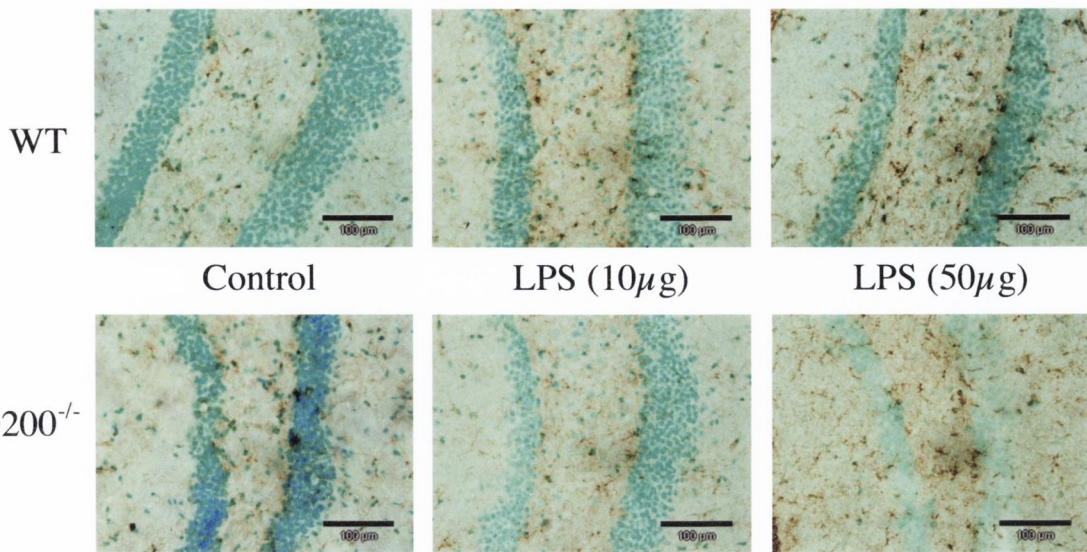


Figure 4.16 The effect of LPS on GFAP expression in the dentate gyrus of WT and CD200^{-/-} mice.

Groups of WT and CD200^{-/-} mice received an ip injection of sterile saline (200µl) or LPS (10µg or 50µg/mouse; 200µl). There was a dose-dependent increase in GFAP positive staining in hippocampal sections prepared from 10µg and 50µg LPS-treated WT, and CD200^{-/-} mice, compared with control-treated WT mice (Magnification 40x, scale bar 100µm).

There was a significant LPS-related increase in the ratio of DAB/nuclear area in the dentate gyrus of WT mice (**p<0.001; ANOVA) and CD200^{-/-} mice (**p<0.001; ANOVA).

2-way ANOVA: LPS effect F (2, 30) = 58.05; p<0.0001, Genotype effect F (1, 30) = 3.198; p=0.0838, Interaction effect F (2, 26) = 0.1022; p=0.9031

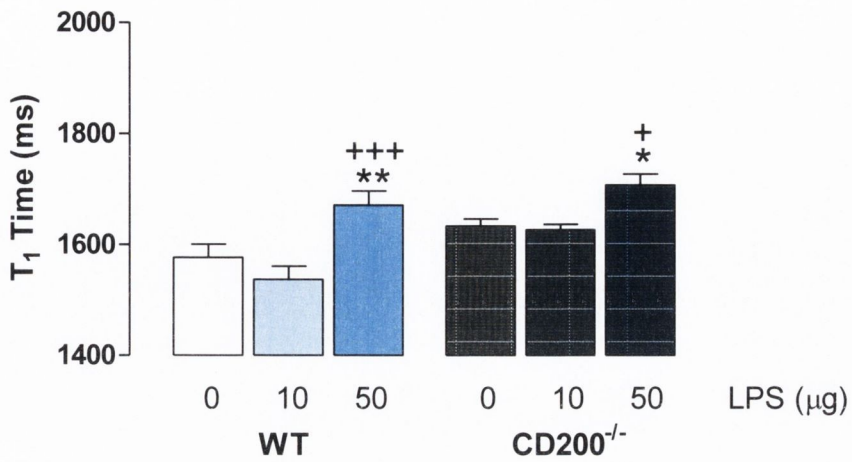


Figure 4.17 The effect of LPS on T₁ relaxation times in the whole cortex of WT and CD200^{-/-} mice at 3.5 hours.

Groups of WT and CD200^{-/-} mice were injected ip with sterile saline (200µl) or LPS (10µg or 50µg/mouse; 200µl). After 3.5 hours, mice were prepared for MR scanning. T₁ relaxation times of the whole cortex were measured on the RARE-VTR scans. Mean T₁ times were increased in the whole cortex of 50µg LPS-treated WT mice compared with control-treated WT mice (**p<0.01; ANOVA) and compared with 10µg LPS-treated WT mice (+++p<0.001; ANOVA), and in the whole cortex of 50µg LPS-treated CD200^{-/-} mice compared with control-treated mice (*p<0.05; ANOVA) and 10µg LPS-treated mice (+p<0.05; ANOVA). Data are presented as means ± SEM.

2-way ANOVA: LPS effect F (2, 39) = 17.21; p<0.0001, Genotype effect F (1, 39) = 14.64; p=0.0005, Interaction effect F (2, 39) = 0.9463; p=0.3969

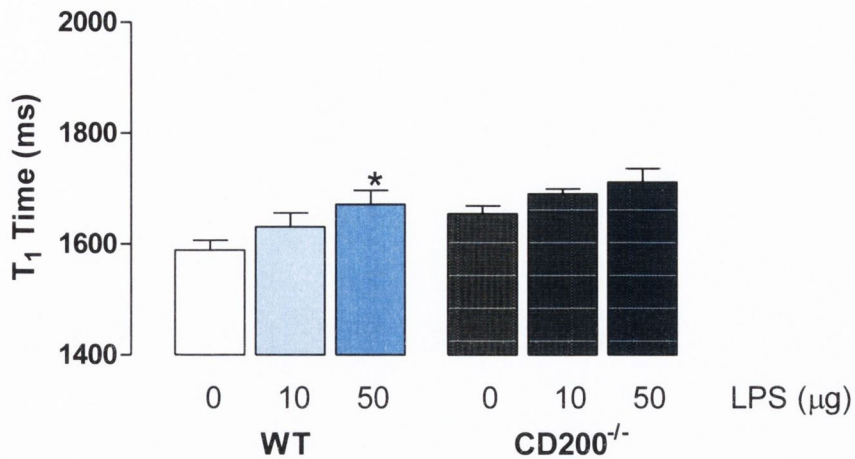


Figure 4.18 The effect of LPS on T₁ relaxation times in the motor cortex of WT and CD200^{-/-} mice at 3.5 hours.

Groups of WT and CD200^{-/-} mice were injected ip with sterile saline (200µl) or LPS (10µg or 50µg/mouse; 200µl). After 3.5 hours, mice were prepared for MR scanning. T₁ relaxation times of the motor cortex were measured bilaterally on the RARE-VTR scans. T₁ relaxation times were significantly increased in the motor cortex of 50µg LPS-treated WT mice compared with control-treated mice (*p<0.05; ANOVA). Data are presented as means ± SEM.

2-way ANOVA: LPS effect F (2, 37) = 11.07; p=0.0020, Genotype effect F (1, 37) = 5.871; p=0.0061, Interaction effect F (2, 37) = 0.2232; p=0.8010

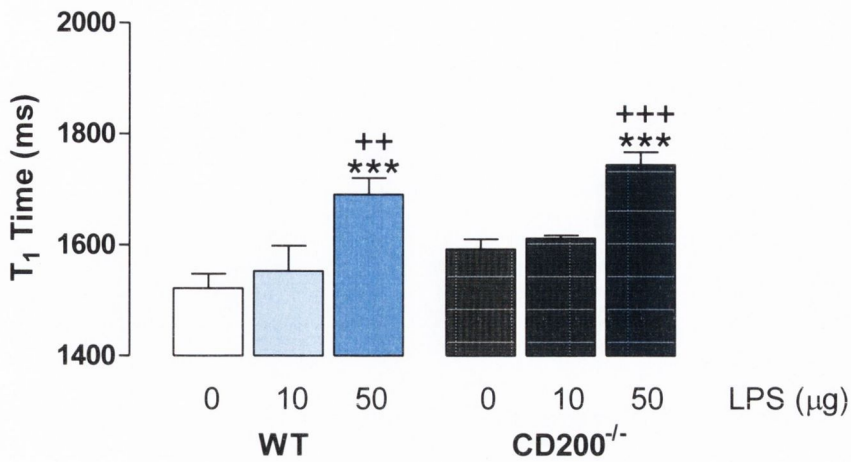


Figure 4.19 The effect of LPS on T₁ relaxation times in the entorhinal cortex of WT and CD200^{-/-} mice at 3.5 hours.

Groups of WT and CD200^{-/-} mice were injected ip with sterile saline (200µl) or LPS (10µg or 50µg/mouse; 200µl). After 3.5 hours, mice were prepared for MR scanning. T₁ relaxation times of the entorhinal cortex were measured bilaterally on the RARE-VTR scans. Mean T₁ times were increased in the entorhinal cortex of 50µg LPS-treated WT mice compared with control-treated mice (**p<0.001; ANOVA) and compared with 10µg LPS-treated WT mice (††p<0.01; ANOVA). There was also a significant increase in T₁ values in the entorhinal cortex of 50µg LPS-treated CD200^{-/-} mice compared with control-treated mice (**p<0.001; ANOVA) and compared with 10µg LPS-treated CD200^{-/-} mice (†††p<0.001; ANOVA). Data are presented as means ± SEM.

2-way ANOVA: LPS effect $F(2, 39) = 23.92$; $p < 0.0001$, **Genotype effect** $F(1, 39) = 8.806$; $p = 0.0051$, **Interaction effect** $F(2, 39) = 0.0608$; $p = 0.9410$

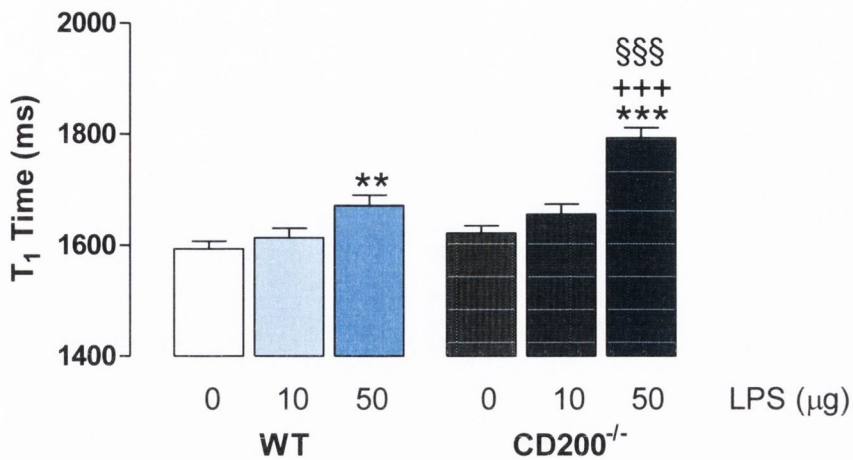


Figure 4.20 The effect of LPS on hippocampal T₁ relaxation times of WT and CD200^{-/-} mice at 3.5 hours.

Groups of WT and CD200^{-/-} mice were injected ip with sterile saline (200µl) or LPS (10µg or 50µg/mouse; 200µl). After 3.5 hours, mice were prepared for MR scanning. T₁ relaxation times of the hippocampus were measured bilaterally on the RARE-VTR scans and averaged. Mean T₁ times were increased in the hippocampus of 50µg LPS-treated WT mice, compared with control-treated mice (**p<0.01; ANOVA) and in the hippocampus of 50µg LPS-treated CD200^{-/-}, compared with control-treated, mice (**p<0.001; ANOVA) and compared with 10µg LPS-treated mice (+++p<0.001; ANOVA). Treatment with 50µg LPS exerted a significantly greater increase in hippocampal T₁ values in CD200^{-/-}, compared with WT, mice (§§§p<0.001; ANOVA). Data are presented as means ± SEM.

2-way ANOVA: LPS effect F (2, 37) = 28.62; p<0.0001, Genotype effect F (1, 37) = 21.09; p<0.0001, Interaction effect F (2, 37) = 4.30; p=0.0209

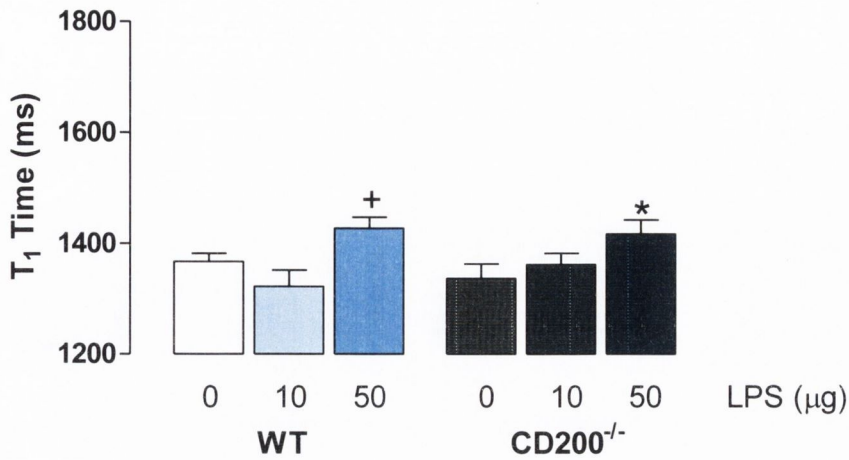


Figure 4.21 The effect of LPS on T₁ relaxation times in the thalamus of WT and CD200^{-/-} mice at 3.5 hours.

Groups of WT and CD200^{-/-} mice were injected ip with sterile saline (200µl) or LPS (10µg or 50µg/mouse; 200µl). After 3.5 hours, mice were prepared for MR scanning. T₁ relaxation times of the thalamus were measured on the RARE-VTR scans. There was an increase in thalamic T₁ values in 50µg LPS-treated WT mice compared with 10µg LPS-treated WT mice (⁺p<0.05; ANOVA) and in 50µg LPS-treated CD200^{-/-} mice compared with control-treated mice (^{*}p<0.05; ANOVA). Data are presented as means ± SEM.

2-way ANOVA: LPS effect F (2, 37) = 6.661; p=0.0034, Genotype effect F (1, 37) = 0.0009; p=0.9758, Interaction effect F (2, 37) = 0.9911; p=0.3808

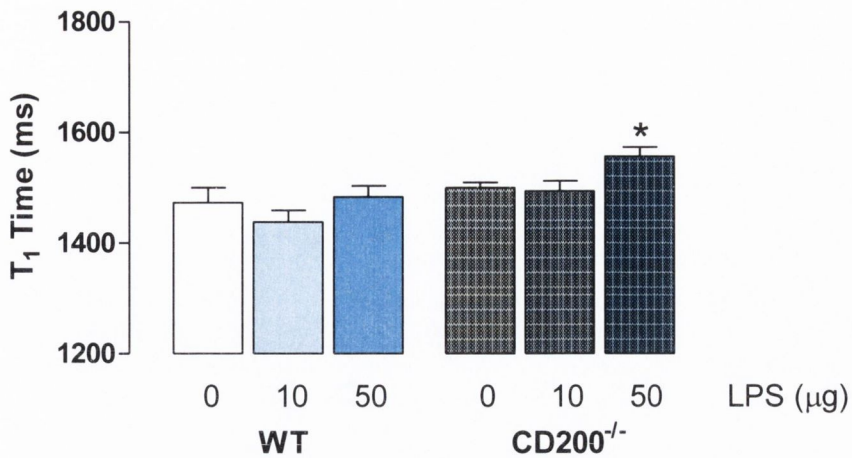


Figure 4.22 The effect of LPS on T₁ relaxation times in the corpus callosum of WT and CD200^{-/-} mice at 3.5 hours.

Groups of WT and CD200^{-/-} mice were injected ip with sterile saline (200µl) or LPS (10µg or 50µg/mouse; 200µl). After 3.5 hours, mice were prepared for MR scanning. T₁ relaxation times of the corpus callosum were measured on the RARE-VTR scans. There was an increase in T₁ values in 50µg LPS-treated CD200^{-/-} mice compared with control-treated mice (*p<0.05; ANOVA). Data are presented as means ± SEM.

2-way ANOVA: LPS effect F (2, 39) = 4.233; p=0.0217, Genotype effect F (1, 39) = 11.53; p=0.0016, Interaction effect F (2, 39) = 0.7598; p=0.4746

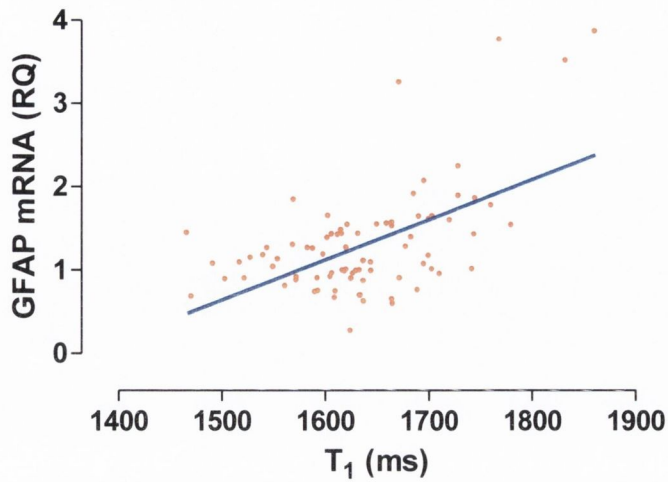


Figure 4.23 The relationship between GFAP mRNA and T₁ relaxation times

Groups of WT and CD200^{-/-} mice were injected ip with sterile saline (200μl) or LPS (10μg or 50μg/mouse; 200μl). After 3.5 hours, mice were prepared for MR scanning, and T₁ values were assessed in the cortex and hippocampus. Mice were sacrificed by decapitation after 4 hours, right cortex and hippocampus dissected free, homogenized and GFAP mRNA expression determined by qPCR. There was a moderate correlation between T₁ relaxation times and GFAP mRNA in these regions.

T₁ and GFAP mRNA: Pearson $r = 0.5613$, $p < 0.0001$; $n = 82$

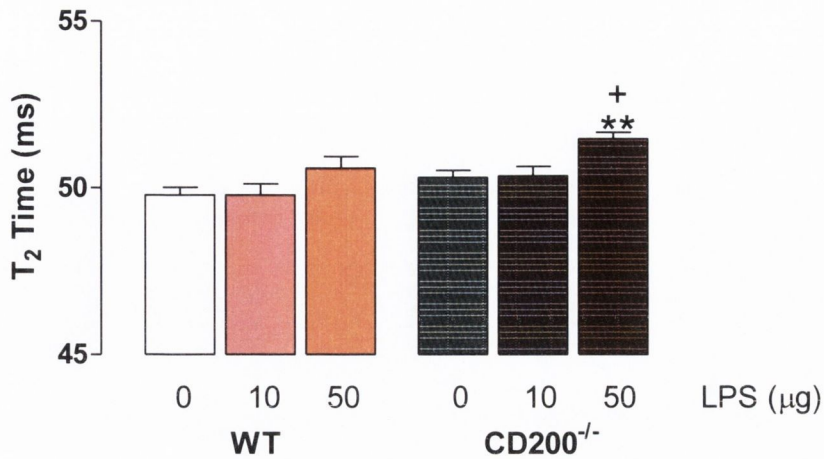


Figure 4.24 The effect of LPS on T₂ relaxation times in the whole cortex of WT and CD200^{-/-} mice at 3.5 hours.

Groups of WT and CD200^{-/-} mice were injected ip with sterile saline (200µl) or LPS (10µg or 50µg/mouse; 200µl). After 3.5 hours, mice were prepared for MR scanning. T₂ relaxation times of the whole cortex were measured on 2 adjacent slices of the MSME scan. There was a significant increase in T₂ values in the whole cortex of 50µg LPS-treated CD200^{-/-} mice compared with control-treated mice (**p<0.01; ANOVA) and 10µg LPS-treated mice (+p<0.05; ANOVA). Data are presented as means ± SEM.

2-way ANOVA: LPS effect F (2, 39) = 7.725; p=0.0015, Genotype effect F (1, 39) = 8.025; p=0.0073, Interaction effect F (2, 39) = 0.2339; p=0.7925

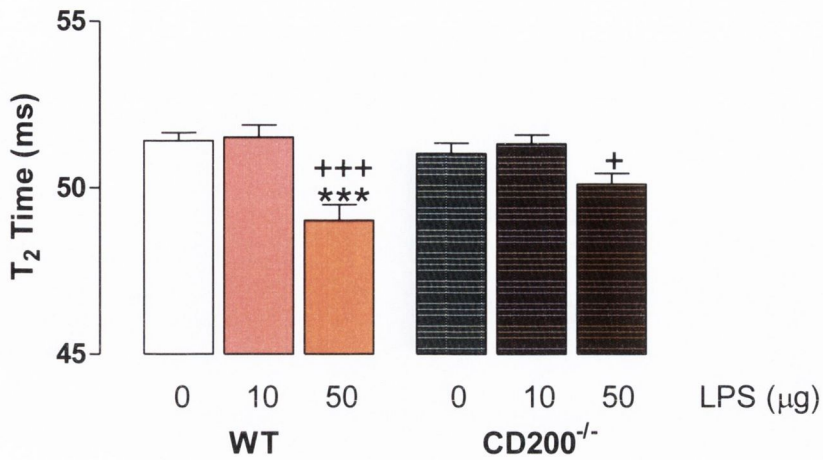


Figure 4.25 The effect of LPS on T₂ relaxation times in the motor cortex of WT and CD200^{-/-} mice at 3.5 hours.

Groups of WT and CD200^{-/-} mice were injected ip with sterile saline (200µl) or LPS (10µg or 50µg/mouse; 200µl). After 3.5 hours, mice were prepared for MR scanning. T₂ relaxation times of the motor cortex were measured bilaterally on 2 adjacent slices of the MSME scan. There was a significant decrease in T₂ values in the motor cortex of 50µg LPS-treated WT mice compared with control-treated mice (***p*<0.001; ANOVA) and 10µg LPS-treated mice (****p*<0.001; ANOVA), and in 50µg LPS-treated CD200^{-/-} mice compared with 10µg LPS-treated mice (+*p*<0.05; ANOVA). Data are presented as means ± SEM.

2-way ANOVA: LPS effect F (2, 39) = 16.81; *p*<0.0001, Genotype effect F (1, 39) = 0.3387; *p*=0.5640, Interaction effect F (2, 39) = 2.601; *p*=0.0870

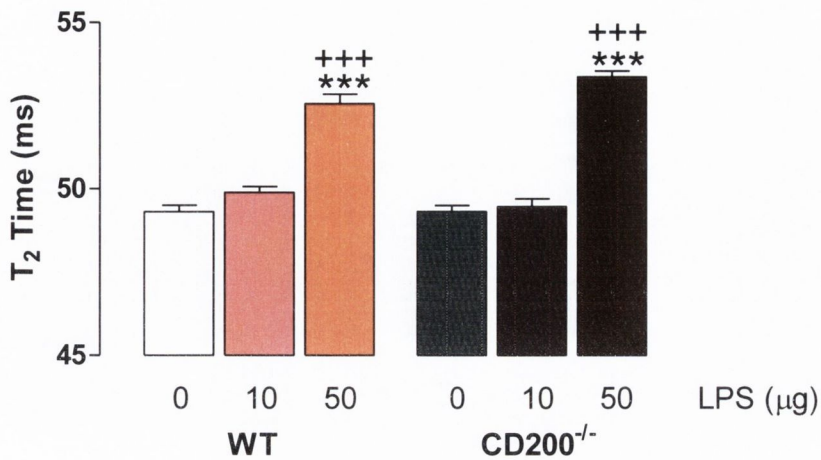


Figure 4.26 The effect of LPS on T₂ relaxation times in the entorhinal cortex of WT and CD200^{-/-} mice at 3.5 hours.

Groups of WT and CD200^{-/-} mice were injected ip with sterile saline (200µl) or LPS (10µg or 50µg/mouse; 200µl). After 3.5 hours, mice were prepared for MR scanning. T₂ relaxation times of the entorhinal cortex were measured bilaterally on 2 adjacent slices of the MSME scan. There was a significant increase in T₂ values in the entorhinal cortex of 50µg LPS-treated WT mice compared with control-treated mice (**p<0.001; ANOVA) and compared with 10µg LPS-treated WT mice (+++p<0.001; ANOVA). Mean T₂ values were significantly increased in the entorhinal cortex of 50µg LPS-treated CD200^{-/-} mice compared with control-treated mice (**p<0.001; ANOVA) and compared with 10µg LPS-treated mice (+++p<0.001; ANOVA). Data are presented as means ± SEM.

2-way ANOVA: LPS effect F (2, 39) = 159.4; p<0.0001, Genotype effect F (1, 39) = 0.4986; p=0.4843, Interaction effect F (2, 39) = 3.851; p=0.0298

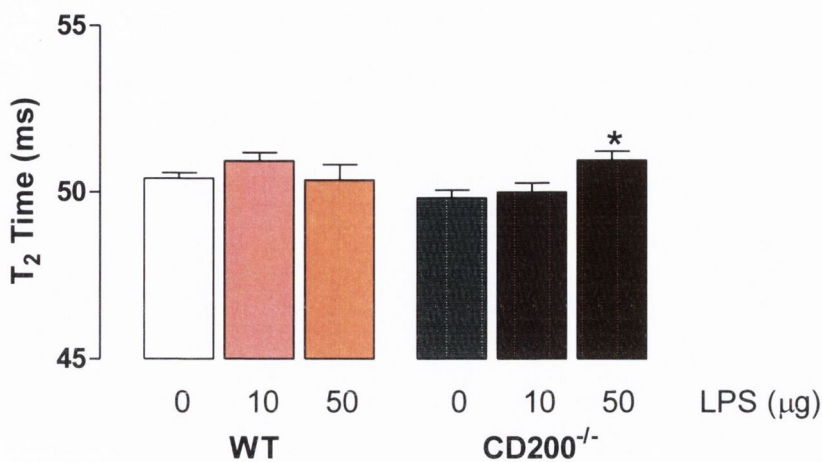


Figure 4.27 The effect of LPS on hippocampal T₂ relaxation times in WT and CD200^{-/-} mice at 3.5 hours.

Groups of WT and CD200^{-/-} mice were injected ip with sterile saline (200µl) or LPS (10µg or 50µg/mouse; 200µl). After 3.5 hours, mice were prepared for MR scanning. T₂ relaxation times of the hippocampus were measured bilaterally on 2 adjacent slices of the MSME scan. There was a significant increase in T₂ values in the hippocampus of 50µg LPS-treated CD200^{-/-} mice compared with control-treated mice (*p<0.05; ANOVA). Data are presented as means ± SEM.

2-way ANOVA: LPS effect F (2, 39) = 1.477; p=0.2409, Genotype effect F (1, 39) = 1.487; p=0.2299, Interaction effect F (2, 39) = 3.294; p=0.0476

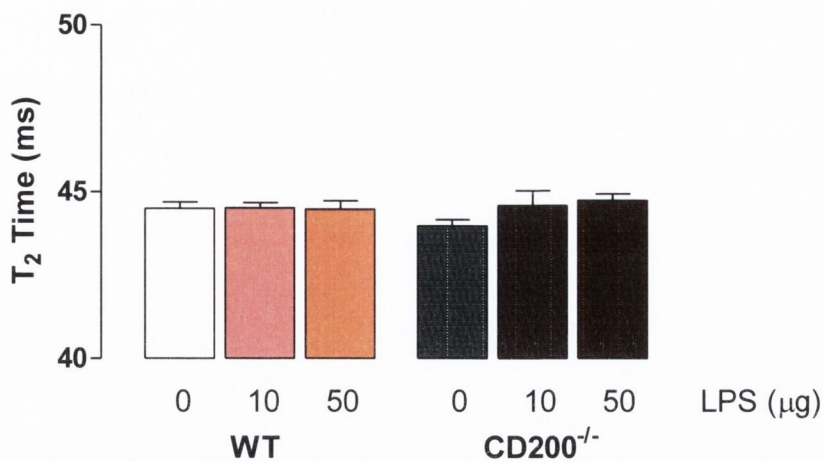


Figure 4.28 The effect of LPS on T₂ relaxation times in the thalamus of WT and CD200^{-/-} mice at 3.5 hours.

Groups of WT and CD200^{-/-} mice were injected ip with sterile saline (200µl) or LPS (10µg or 50µg/mouse; 200µl). After 3.5 hours, mice were prepared for MR scanning. T₂ relaxation times of the thalamus were measured bilaterally on 2 adjacent slices of the MSME scan. Mean T₂ values were similar in control-treated, and 10µg and 50µg LPS-treated WT and CD200^{-/-} mice. Data are presented as means ± SEM.

2-way ANOVA: LPS effect F (2, 39) = 0.9595; p=0.3919, Genotype effect F (1, 39) = 0.0643; p=0.8010, Interaction effect F (2, 39) = 1.015; p=0.3716

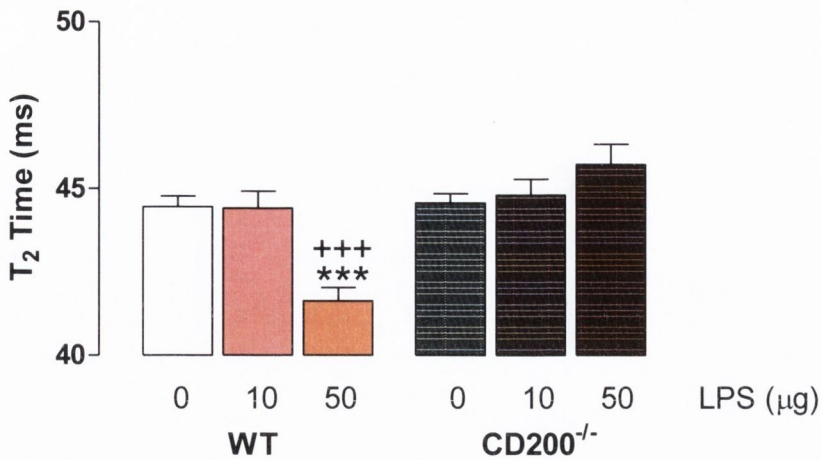


Figure 4.29 The effect of LPS on T₂ relaxation times in the corpus callosum of WT and CD200^{-/-} mice at 3.5 hours.

Groups of WT and CD200^{-/-} mice were injected ip with sterile saline (200µl) or LPS (10µg or 50µg/mouse; 200µl). After 3.5 hours, mice were prepared for MR scanning. T₂ relaxation times of the corpus callosum were measured on 2 adjacent slices of the MSME scan. There was a significant decrease in T₂ relaxation times in 50µg LPS-treated WT mice compared with control-treated WT mice (**p<0.001; ANOVA) and 10µg LPS-treated WT mice (***p<0.001; ANOVA). Data are presented as means ± SEM.

2-way ANOVA: LPS effect F (2, 39) =2.627; p=0.0850, Genotype effect F (1, 39) = 17.19; p=0.0002, Interaction effect F (2, 39) = 12.28; p<0.0001

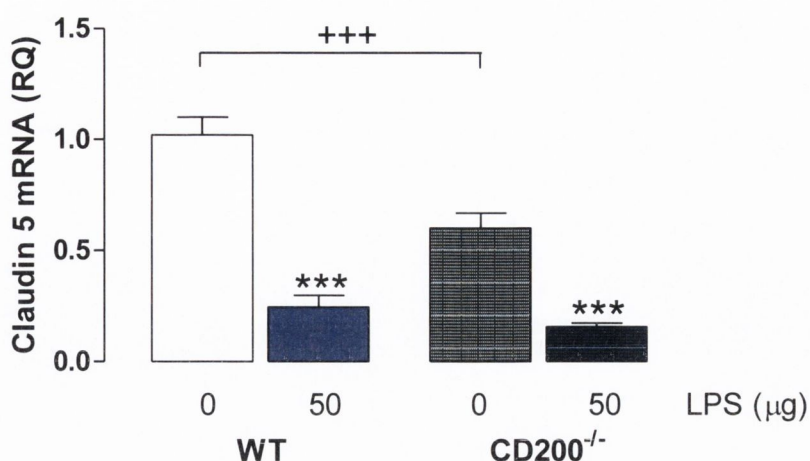


Figure 4.30 The effect of LPS on cortical claudin 5 mRNA expression in WT and CD200^{-/-} mice.

Groups of WT and CD200^{-/-} mice were injected ip with sterile saline (200μl) or LPS (50μg/mouse; 200μl). After 4 hours, mice were sacrificed by decapitation, right cortex dissected free, homogenized and claudin 5 mRNA expression determined by qPCR. Mean claudin 5 mRNA expression was decreased in cortical tissue prepared from LPS-treated WT compared with control-treated mice (**p<0.001; ANOVA) and in LPS-treated CD200^{-/-} mice compared with control-treated CD200^{-/-} mice (**p<0.001; ANOVA). Mean claudin 5 mRNA expression was decreased in cortical tissue prepared from control-treated CD200^{-/-} mice compared with control-treated WT mice (***p<0.001; ANOVA). Values are expressed as relative quantities (RQ) obtained from calculating the ratio of claudin 5 mRNA to an endogenous control and are means ± SEM.

2-way ANOVA: LPS effect $F(1, 25) = 93.12; p < 0.0001$, **Genotype effect** $F(1, 25) = 16.1; p = 0.0005$, **Interaction effect** $F(1, 25) = 6.832; p = 0.0149$

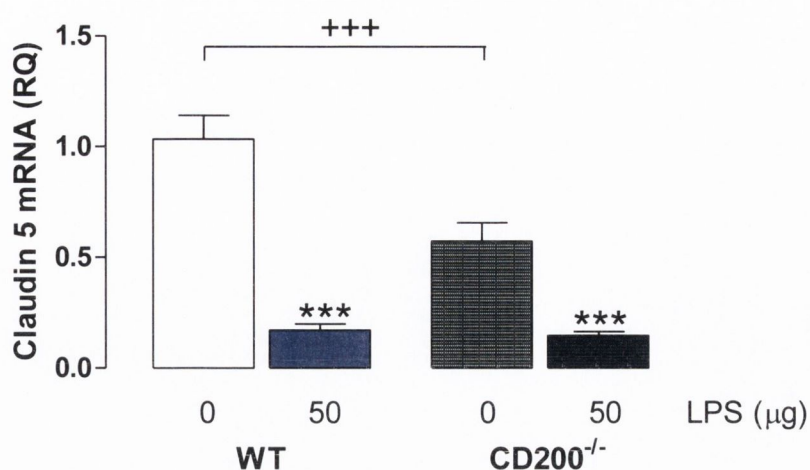


Figure 4.31 The effect of LPS on hippocampal claudin 5 mRNA expression in WT and CD200^{-/-} mice.

Groups of WT and CD200^{-/-} mice were injected ip with sterile saline (200µl) or LPS (50µg/mouse; 200µl). After 4 hours, mice were sacrificed by decapitation, right hippocampus dissected free, homogenized and claudin 5 mRNA expression determined by qPCR. Mean claudin 5 mRNA expression was decreased in hippocampal tissue prepared from LPS-treated WT compared with control-treated mice (**p<0.001; ANOVA) and in LPS-treated CD200^{-/-} mice compared with control-treated CD200^{-/-} mice (**p<0.001; ANOVA). Mean claudin 5 mRNA expression was decreased in cortical tissue prepared from control-treated CD200^{-/-} mice compared with control-treated WT mice (+++p<0.001; ANOVA). Values are expressed as relative quantities (RQ) obtained from calculating the ratio of claudin 5 mRNA to an endogenous control and are means ± SEM.

2-way ANOVA: LPS effect F (1, 24) = 86.44; p<0.0001, Genotype effect F (1, 24) = 12.32; p=0.0018, Interaction effect F (1, 24) = 9.897; p=0.0044

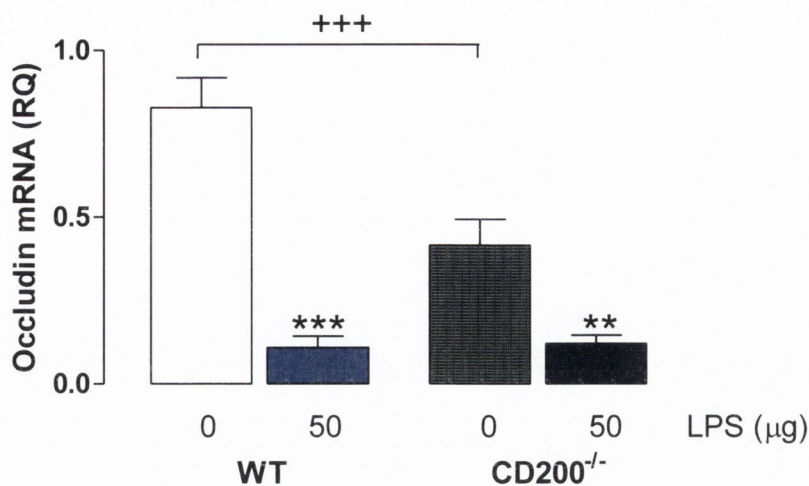


Figure 4.32 The effect of LPS on cortical occludin mRNA expression in WT and CD200^{-/-} mice.

Groups of WT and CD200^{-/-} mice were injected ip with sterile saline (200μl) or LPS (50μg/mouse; 200μl). After 4 hours, mice were sacrificed by decapitation, right cortex dissected free, homogenized and occludin mRNA expression determined by qPCR. Mean occludin mRNA expression was decreased in cortical tissue prepared from LPS-treated WT compared with control-treated mice (**p<0.001; ANOVA) and in LPS-treated CD200^{-/-} mice compared with control-treated CD200^{-/-} mice (**p<0.01; ANOVA). Mean occludin mRNA expression was decreased in cortical tissue prepared from control-treated CD200^{-/-} mice compared with control-treated WT mice (+++p<0.001; ANOVA). Values are expressed as relative quantities (RQ) obtained from calculating the ratio of occludin mRNA to an endogenous control and are means ± SEM.

2-way ANOVA: LPS effect $F(1, 20) = 64.45$; $p < 0.0001$, **Genotype effect** $F(1, 20) = 10.09$; $p = 0.0047$, **Interaction effect** $F(1, 20) = 11.33$; $p = 0.0031$

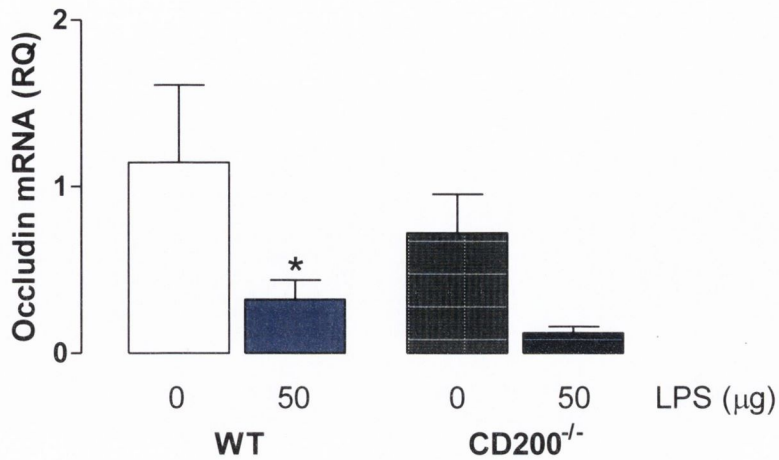


Figure 4.33 The effect of LPS on hippocampal occludin mRNA expression in WT and CD200^{-/-} mice.

Groups of WT and CD200^{-/-} mice were injected ip with sterile saline (200µl) or LPS (50µg/mouse; 200µl). After 4 hours, mice were sacrificed by decapitation, right hippocampus dissected free, homogenized and occludin mRNA expression determined by qPCR. Mean occludin mRNA expression was decreased in hippocampal tissue prepared from LPS-treated WT compared with control-treated mice (*p<0.05; ANOVA). Values are expressed as relative quantities (RQ) obtained from calculating the ratio of occludin mRNA to an endogenous control and are means ± SEM.

2-way ANOVA: LPS effect F (1, 20) = 9.092; p=0.0068, Genotype effect F (1, 20) = 1.753; p=0.2004, Interaction effect F (1, 20) = 0.2209; p=0.6434

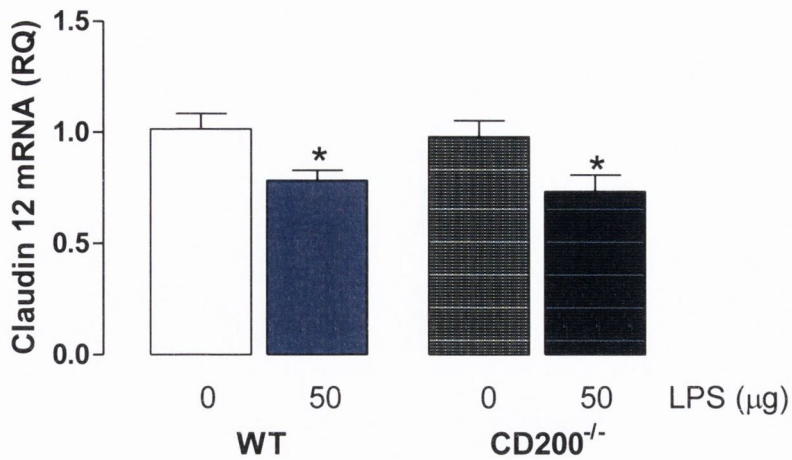


Figure 4.34 The effect of LPS on cortical claudin 12 mRNA expression in WT and CD200^{-/-} mice.

Groups of WT and CD200^{-/-} mice were injected ip with sterile saline (200μl) or LPS (50μg/mouse; 200μl). After 4 hours, mice were sacrificed by decapitation, right cortex dissected free, homogenized and claudin 12 mRNA expression determined by qPCR. Mean claudin 12 mRNA expression was decreased in cortical tissue prepared from LPS-treated WT compared with control-treated mice (*p<0.05; ANOVA) and in LPS-treated CD200^{-/-} mice compared with control-treated CD200^{-/-} mice (*p<0.05; ANOVA). Values are expressed as relative quantities (RQ) obtained from calculating the ratio of claudin 12 mRNA to an endogenous control and are means ± SEM.

2-way ANOVA: LPS effect F (1, 25) = 13.32; p=0.0012, Genotype effect F (1, 25) = 0.4277; p=0.5191, Interaction effect F (1, 25) =0.0131; p=0.9096

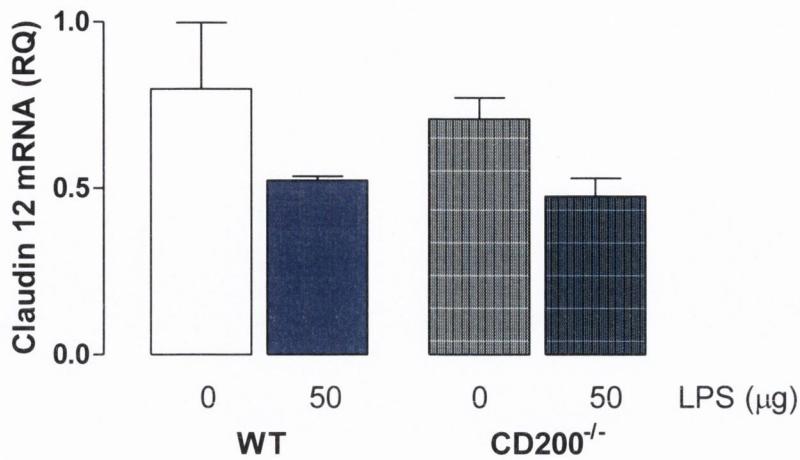


Figure 4.35 The effect of LPS on hippocampal claudin 12 mRNA expression in WT and CD200^{-/-} mice.

Groups of WT and CD200^{-/-} mice were injected ip with sterile saline (200µl) or LPS (50µg/mouse; 200µl). After 4 hours, mice were sacrificed by decapitation, right hippocampus dissected free, homogenized and claudin 12 mRNA expression determined by qPCR. Mean hippocampal claudin 12 mRNA expression was similar in tissue prepared from LPS- and control-treated WT and CD200^{-/-} mice. Values are expressed as relative quantities (RQ) obtained from calculating the ratio of claudin 12 mRNA to an endogenous control and are means ± SEM.

2-way ANOVA: LPS effect F (1, 22) = 5.791; p=0.0249, Genotype effect F (1, 22) = 1.105; p=0.3046, Interaction effect F (1, 22) =0.4035; p=0.5318

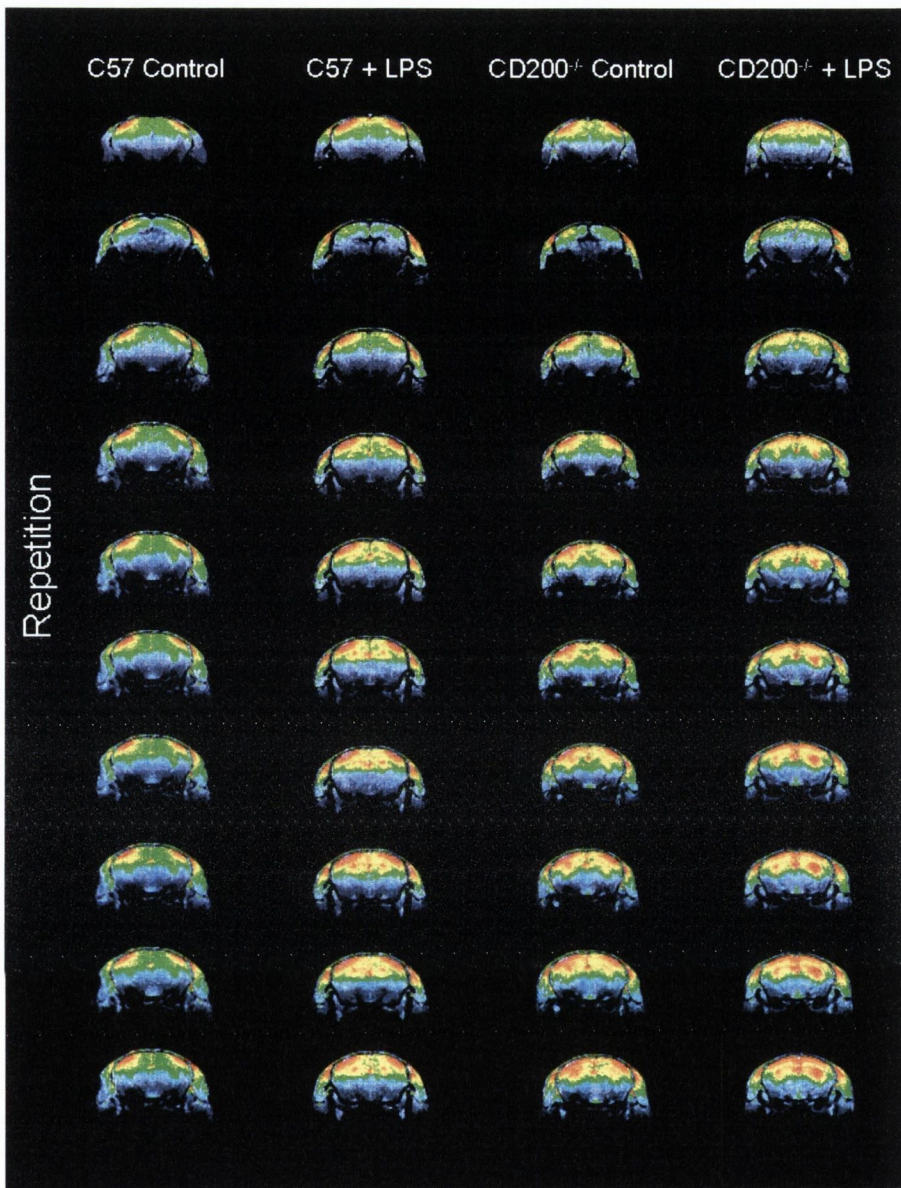


Figure 4.36 Representative contrast MRI data sets from control- and LPS-treated WT and CD200^{-/-} mice injected with gadolinium.

Groups of WT and CD200^{-/-} mice received an ip injection of sterile saline (200μl) or LPS (50μg/mouse; 200μl). Mean signal intensity was similar in control-treated WT mice after gadolinium injection (repetitions 3-10), compared with before injection (repetition 1). Mean SI in post-contrast images was increased in control-treated CD200^{-/-} mice and in LPS-treated WT and CD200^{-/-} mice, after gadolinium injection, compared with before injection. Increased SI is denoted by higher colour intensities.

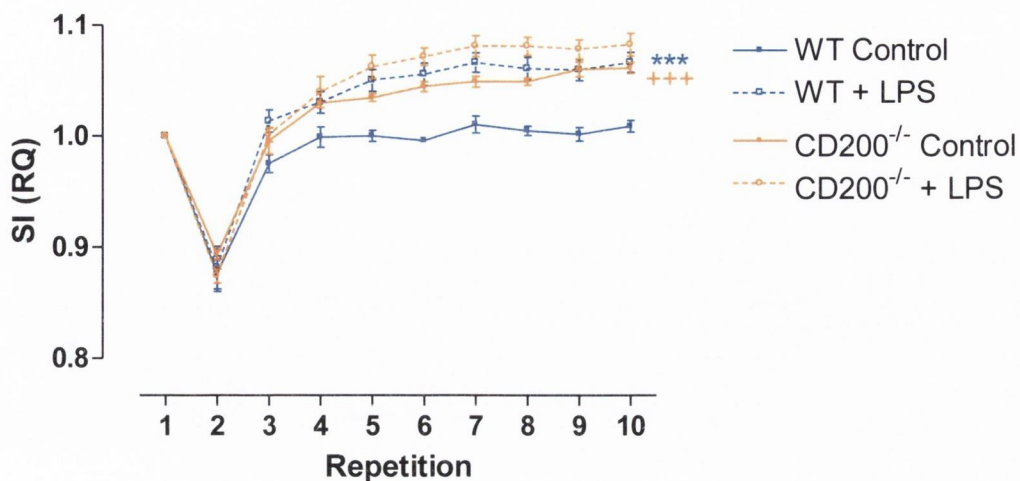


Figure 4.37 Contrast-enhanced SI changes in the right motor cortex of control- and LPS-treated WT and CD200^{-/-} mice.

Groups of WT and CD200^{-/-} mice were injected ip with sterile saline (200μl) or LPS (50μg/mouse; 200μl). After 3.75 hours, mice were prepared for gadolinium-enhanced contrast imaging by tail vein cannulation. Gadolinium (200μl) was injected at the commencement of repetition 2. Mean SI in the post-contrast repetitions was increased in the right motor cortex of LPS-treated, compared with control-treated, WT mice (**p<0.001; ANOVA), and in control-treated CD200^{-/-} mice, compared with control-treated WT mice (+++p<0.001; ANOVA). Treatment with LPS had no significant additional effect on SI values in the motor cortex of CD200^{-/-} mice. Values are presented as a proportion of the baseline, pre-contrast measure (repetition 1) and are means ± SEM.

2-way ANOVA: LPS_{effect} F (1, 18) = 32.58; p<0.0001, Genotype_{effect} F (1, 18) = 20.80; p=0.0002, Interaction_{effect} F (1, 18) = 4.629; p=0.0453

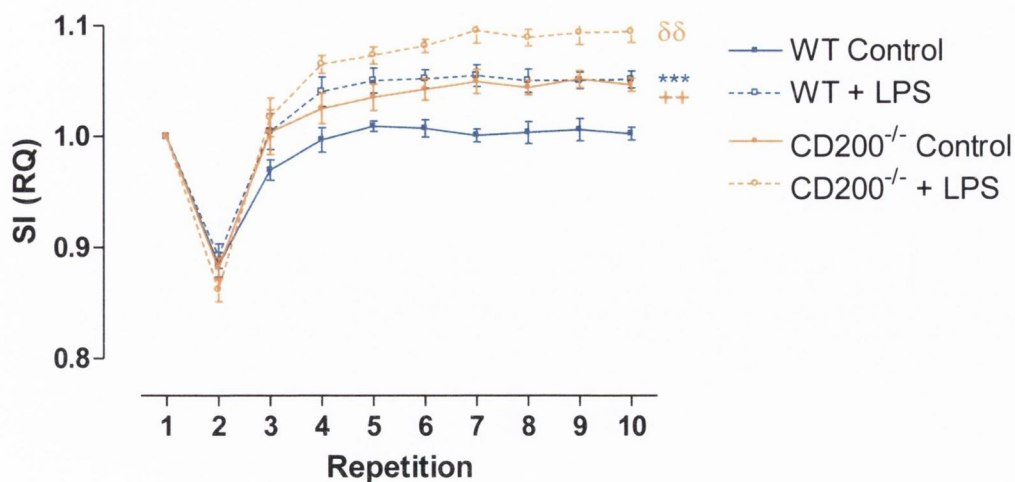


Figure 4.38 Contrast-enhanced SI changes in the right somatosensory cortex of control- and LPS-treated WT and CD200^{-/-} mice.

Groups of WT and CD200^{-/-} mice were injected ip with sterile saline (200μl) or LPS (50μg/mouse; 200μl). After 3.75 hours, mice were prepared for gadolinium-enhanced contrast imaging by tail vein cannulation. Gadolinium (200μl) was injected at the commencement of repetition 2. Mean SI in the post-contrast repetitions was increased in the right somatosensory cortex of LPS-treated, compared with control-treated, WT mice (**p<0.001; ANOVA), and in LPS-treated CD200^{-/-}, compared with control-treated CD200^{-/-}, mice (*p<0.01; ANOVA). SI was also increased in control-treated CD200^{-/-}, compared with control-treated WT, mice (⁺⁺p<0.01; ANOVA) and in LPS-treated CD200^{-/-}, compared with LPS-treated WT, mice (^{δδ}p<0.01; ANOVA). Values are presented as a proportion of the baseline, pre-contrast measure (repetition 1) and are means ± SEM.

2-way ANOVA: LPS_{effect} F (1, 18) = 32.57; p<0.0001, Genotype_{effect} F (1, 18) = 27.53; p<0.0001, Interaction_{effect} F (1, 18) = 0.4182; p=0.8403

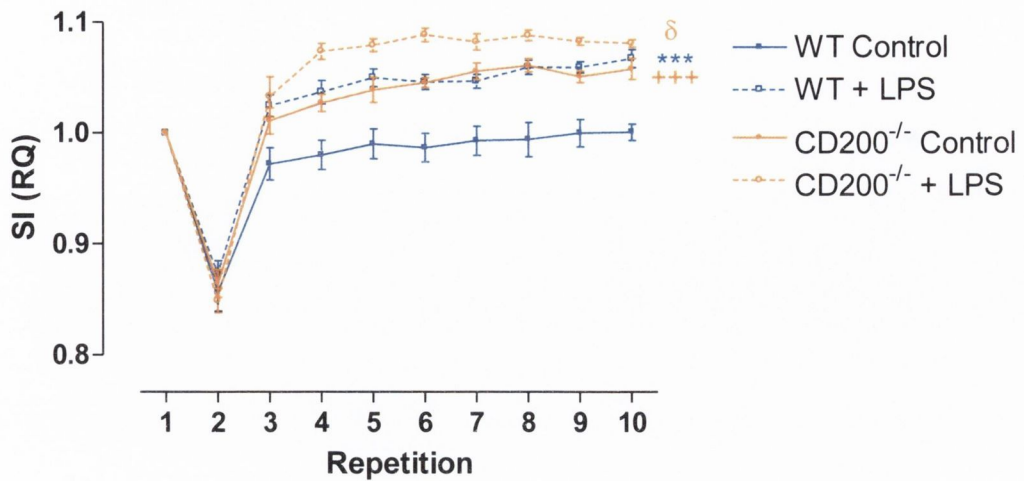


Figure 4.39 Contrast-enhanced SI changes in the right entorhinal cortex of control- and LPS-treated WT and CD200^{-/-} mice.

Groups of WT and CD200^{-/-} mice were injected ip with sterile saline (200μl) or LPS (50μg/mouse; 200μl). After 3.75 hours, mice were prepared for gadolinium-enhanced contrast imaging by tail vein cannulation. Gadolinium (200μl) was injected at the commencement of repetition 2. Mean SI in the post-contrast repetitions was increased in the right entorhinal cortex of LPS-treated, compared with control-treated, WT mice (** $p < 0.001$; ANOVA), and in LPS-treated CD200^{-/-}, compared with control-treated CD200^{-/-}, mice (* $p < 0.05$; ANOVA). SI was increased in the right entorhinal cortex of control-treated CD200^{-/-} mice, compared with control-treated WT mice (+++ $p < 0.001$; ANOVA) and in LPS-treated CD200^{-/-}, compared with LPS-treated WT, mice (* $p < 0.05$; ANOVA). Values are presented as a proportion of the baseline, pre-contrast measure (repetition 1) and are means \pm SEM.

2-way ANOVA: LPS_{effect} F (1, 18) = 36.78; $p < 0.0001$, Genotype_{effect} F (1, 18) = 33.66; $p < 0.0001$, Interaction_{effect} F (1, 18) = 5.458; $p = 0.0312$

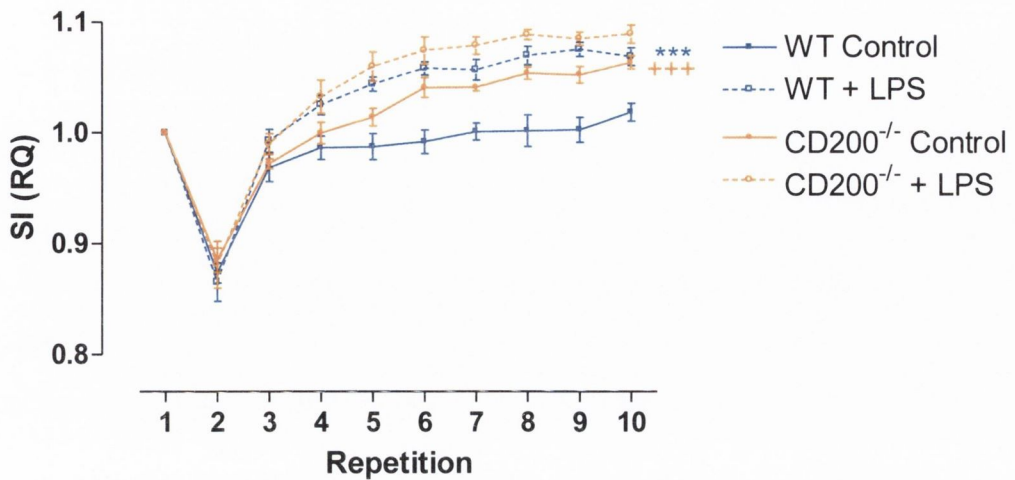


Figure 4.40 Contrast-enhanced SI changes in the right dentate gyrus of control- and LPS-treated WT and CD200^{-/-} mice.

Groups of WT and CD200^{-/-} mice were injected ip with sterile saline (200μl) or LPS (50μg/mouse; 200μl). After 3.75 hours, mice were prepared for gadolinium-enhanced contrast imaging by tail vein cannulation. Gadolinium (200μl) was injected at the commencement of repetition 2. Mean SI in the post-contrast repetitions was increased in the right dentate gyrus of LPS-treated, compared with control-treated, WT mice (**p<0.001; ANOVA), and in LPS-treated CD200^{-/-}, compared with control-treated, mice (*p<0.05; ANOVA). Mean SI was also increased in control-treated CD200^{-/-}, compared with control-treated WT, mice (***p<0.001; ANOVA). LPS had no further effect on hippocampal SI values in CD200^{-/-} mice. Values are presented as a proportion of the baseline, pre-contrast measure (repetition 1) and are means ± SEM.

2-way ANOVA: LPS_{effect} F (1, 18) = 41.61; p<0.0001, Genotype_{effect} F (1, 18) = 19.38; p=0.0003, Interaction_{effect} F (1, 18) = 3.922; p=0.0613

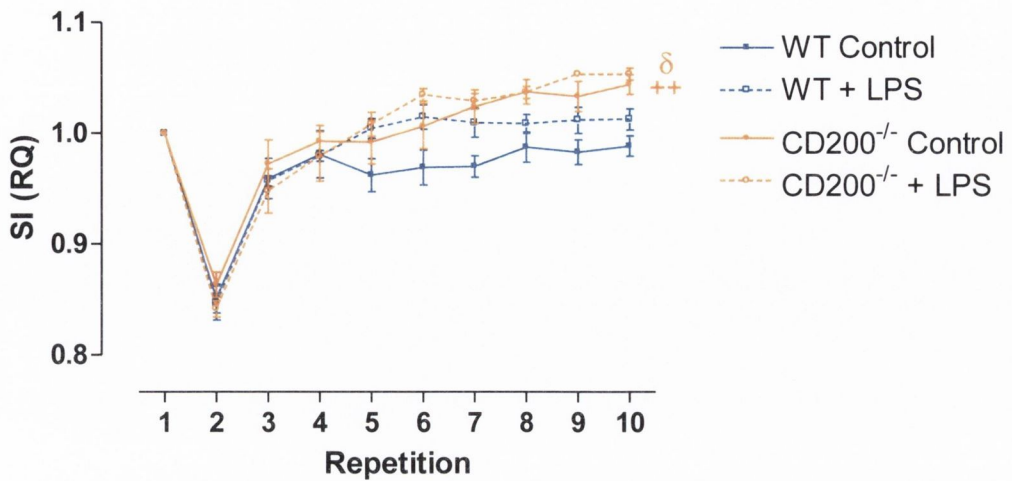


Figure 4.41 Contrast-enhanced SI changes in right ventrolateral thalamus of control- and LPS-treated WT and CD200^{-/-} mice.

Groups of WT and CD200^{-/-} mice were injected ip with sterile saline (200μl) or LPS (50μg/mouse; 200μl). After 3.75 hours, mice were prepared for gadolinium-enhanced contrast imaging by tail vein cannulation. Gadolinium (200μl) was injected at the commencement of repetition 2. Mean SI in the post-contrast repetitions was similar in the right ventrolateral thalamus of LPS-treated, compared with control-treated, WT mice, and in LPS-treated, compared with control-treated, CD200^{-/-} mice. There was an increase in mean SI in control-treated CD200^{-/-}, compared with control-treated WT, mice (⁺⁺p<0.01; ANOVA) and in LPS-treated CD200^{-/-}, compared with LPS-treated WT, mice (^δp<0.05; ANOVA). Values are presented as a proportion of the baseline, pre-contrast measure (repetition 1) and are means ± SEM.

2-way ANOVA: LPS_{effect} F (1, 18) = 4.223; p=0.0547, Genotype_{effect} F (1, 18) = 22.46; p=0.0002, Interaction_{effect} F (1, 18) = 1.240; p=0.2801

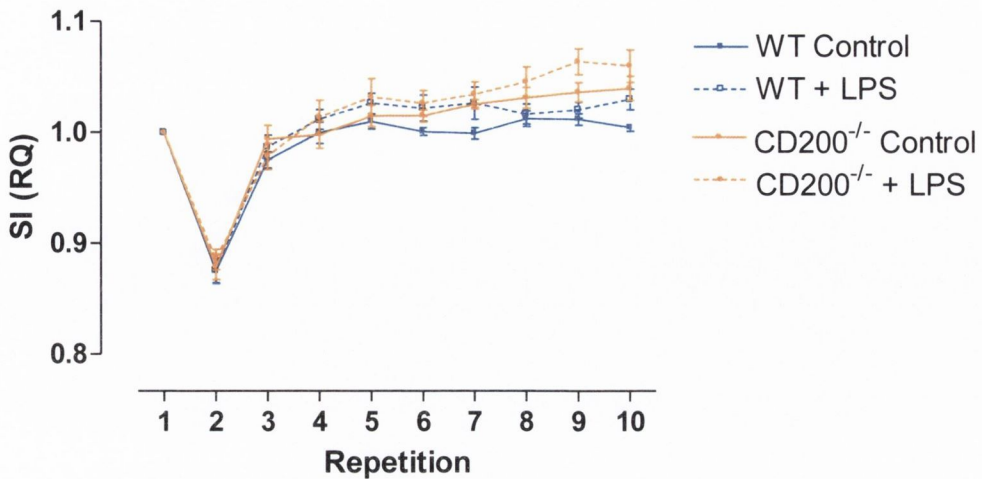


Figure 4.42 Contrast-enhanced SI changes in the right frontal association cortex of control- and LPS-treated WT and CD200^{-/-} mice.

Groups of WT and CD200^{-/-} mice were injected ip with sterile saline (200μl) or LPS (50μg/mouse; 200μl). After 3.75 hours, mice were prepared for gadolinium-enhanced contrast imaging by tail vein cannulation. Gadolinium (200μl) was injected at the commencement of repetition 2. Mean SI in the post-contrast repetitions was similar in the right frontal association cortex of LPS-treated, compared with control-treated, WT mice, and in LPS-treated CD200^{-/-}, compared with control-treated CD200^{-/-}, mice. Mean SI values in the frontal association cortex were similar in control- and LPS-treated CD200^{-/-}, compared with WT, mice. Values are presented as a proportion of the baseline, pre-contrast measure (repetition 1) and are means ± SEM.

2-way ANOVA: LPS_{effect} F (1, 18) = 3.389; p=0.0822, Genotype_{effect} F (1, 18) = 8.483; p=0.0093, Interaction_{effect} F (1, 18) = 0.005802; p=0.9401

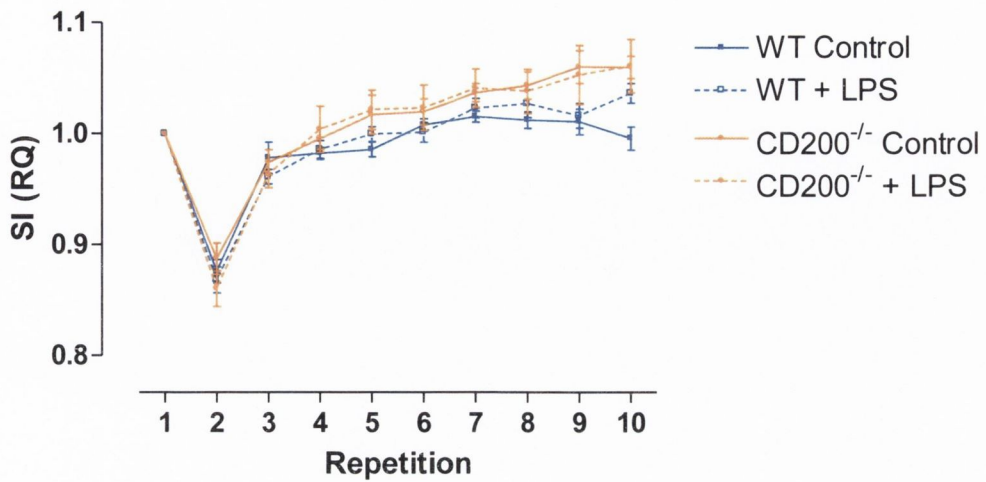


Figure 4.43 Contrast-enhanced SI changes in the right lateral cerebellar nucleus of control- and LPS-treated WT and CD200^{-/-} mice.

Groups of WT and CD200^{-/-} mice were injected ip with sterile saline (200μl) or LPS (50μg/mouse; 200μl). After 3.75 hours, mice were prepared for gadolinium-enhanced contrast imaging by tail vein cannulation. Gadolinium (200μl) was injected at the commencement of repetition 2. Mean SI in the post-contrast repetitions was similar in the right later cerebellar nucleus of LPS-treated, compared with control-treated, WT and CD200^{-/-} mice, and in control- and LPS-treated CD200^{-/-}, compared with WT, mice. Values are presented as a proportion of the baseline, pre-contrast measure (repetition 1) and are means ± SEM.

2-way ANOVA: LPS_{effect} F (1, 18) = 0.367; p=0.5522, Genotype_{effect} F (1, 18) = 6.510; p=0.0200, Interaction_{effect} F (1, 18) = 1.615; p=0.4591

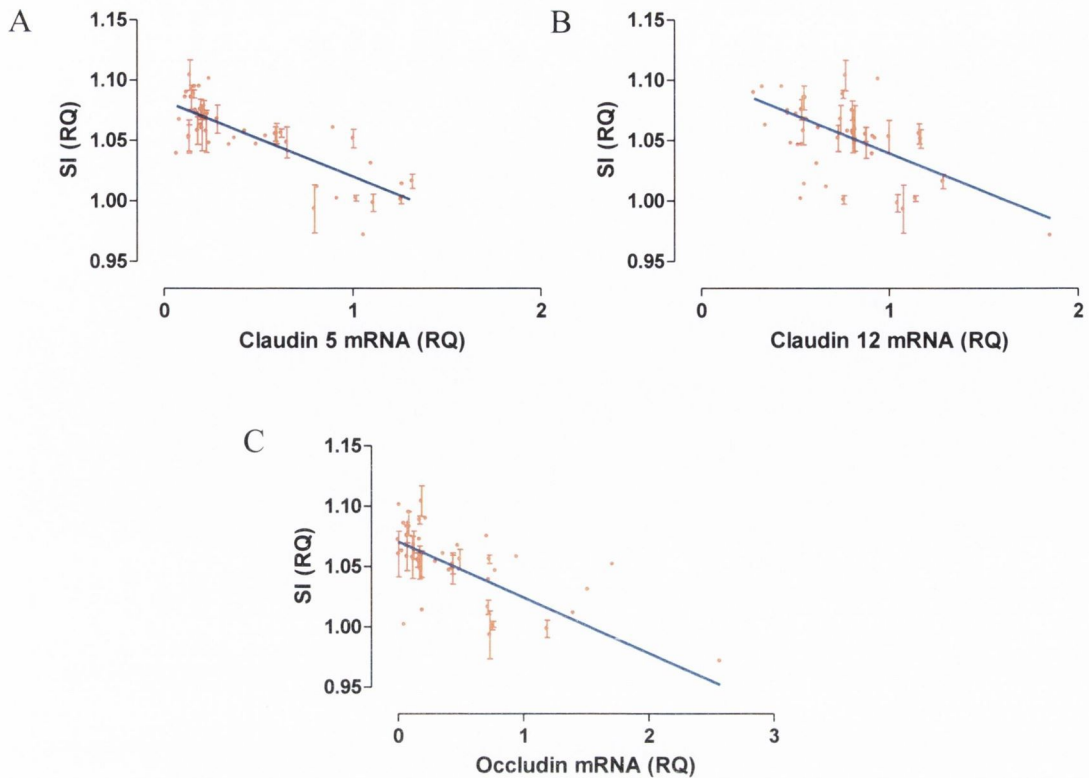


Figure 4.44 Relationship between SI values and claudins 5, 12 and occludin mRNA expression.

Groups of WT and CD200^{-/-} mice were injected ip with sterile saline (200μl) or LPS (50μg/mouse; 200μl). After 3.75 hours, mice were prepared for gadolinium-enhanced contrast imaging by tail vein cannulation. Contrast analysis was carried out on ROIs in the cortex and hippocampus. After 4 hours, mice were sacrificed by decapitation, right cortex and hippocampus dissected free, homogenized and claudins 5, 12 and occludin mRNA expression determined by qPCR. There were significant negative correlations between cortical and hippocampal SI values and the associated mRNA expression of claudins 5 (Figure A), 12 (Figure B) and occludin (Figure C). Values are presented as means ± SEM.

(A) SI and claudin 5 mRNA: Pearson $r = -0.792$, $p < 0.0001$; $n = 44$

(B) SI and claudin 12 mRNA: Pearson $r = -0.5368$, $p = 0.0002$; $n = 44$

(C) SI and occludin mRNA: Pearson $r = -0.6262$, $p < 0.0001$; $n = 44$

4.4 Discussion

One of the fundamental aims of this study was to determine the role that CD200 plays in the maintenance of microglia in a quiescent state in an *in vivo* environment. The expression of CD200 and CD200R on neurons and microglia, respectively, suggests that their interaction may contribute to the preservation of microglia in a resting state. It has recently been reported that the LPS-induced production of pro-inflammatory cytokines is significantly exaggerated in glia prepared from CD200-deficient, compared with WT, mice (Costello *et al.*, 2011). Furthermore, the ability of neurons to modulate LPS- and A β -induced changes in microglial activation is CD200-dependent (Lyons *et al.*, 2007; Lyons *et al.*, 2009). However, the effect of LPS-induced neurotoxicity in CD200^{-/-} mice has yet to be evaluated. The hypothesis proposed is that a deficiency in CD200, coupled with an LPS challenge, will lead to a more profound neuroinflammatory response in CD200-deficient, compared with WT, mice.

It has previously been shown that LPS induces an increase in CD40 gene expression in glia prepared from WT mice in a dose-dependent manner (Qin *et al.*, 2005). Additionally, an increase in CD40 expression has been reported in isolated microglia following A β -treatment, as well as microglia prepared from a mouse model of AD (Tan *et al.*, 1999), which correlates with several other studies indicating an increase in markers of microglial activation in these models (Town *et al.*, 2005). It has also been pointed out that LPS induces CD11b mRNA (Zhou *et al.*, 2009). Increased CD11b expression, the β -integrin marker of microglia, represents microglial activation during neurodegenerative inflammation (Roy *et al.*, 2006). It is pertinent to point out that treatment with 10 μ g LPS had no significant effect on CD40 mRNA expression in cortical or hippocampal in these mice.

In addition to the expression of CD40, activated microglia also up-regulate their expression of CD11b (Roy *et al.*, 2006). In this study, CD11b expression was investigated by RT-PCR and immunostaining. In contrast to the increased expression of CD40 mRNA, CD11b mRNA expression was unchanged in cortical tissue prepared from LPS-treated WT mice. The failure of LPS to affect CD11b mRNA expression is not consistent with other studies, and requires clarification. Previous reports have shown an increase in CD11b mRNA in the treated area following striatal injection of LPS in 8-10 week old WT mice (Roy *et al.*, 2006) and the analysis was undertaken 5 days after

injection. This contrasts with the present study where LPS was delivered intraperitoneally and analysis was undertaken after 4 hours. It is possible that the timing was too short to allow an increase in cortical expression of CD11b.

In this study, the data revealed only a subtle increase in CD11b immunostaining in cortical sections of LPS-treated WT mice. The effects of LPS treatment have been studied in many laboratories, and much of the histological data suggests that accumulation of CD11b-positive microglia reaches a peak as late as 48 hours after treatment (Kalehua *et al.*, 2000). The lack of change in CD11b immunostaining described here may be because changes do not occur as early as 4 hours. Future work should focus on a 48hr timepoint.

LPS initiates a strong immune response both *in vivo* (Nolan *et al.*, 2004) and *in vitro* (Downer *et al.*, 2010) and the evidence suggests that both CD40 and CD11b are increased (Tan *et al.*, 1999; Zhou *et al.*, 2009). The initial step involves activation of TLR4. An up-regulation of TLR4 mRNA has been reported in glia prepared from CD200-deficient mice (Costello *et al.*, 2011) and this probably explains the increased response to LPS in CD200^{-/-} mice.

It is generally accepted that the primary source of inflammatory cytokines is activated microglia and consistent with this is the finding that LPS increased IL-1 β , TNF- α and IL-6 mRNA expression in the cortex and hippocampus of WT mice in parallel with the increase in CD40 mRNA following treatment with 50 μ g LPS. It is important to point out that treatment with 10 μ g LPS, a dose commonly used to initiate sickness behaviour (Combrinck *et al.*, 2002), had no significant effect on cytokine expression. IL-1 β is produced during inflammation, injury, immunological challenge or infection (Dinarello, 1994) and contributes to many of the behavioural responses associated with sickness syndrome (Rachal Pugh *et al.*, 2001). TNF- α is present on neurons around ischemic tissue, is released by phagocytic cells upon activation by LPS, and can cause apoptosis in neurons (Shohami *et al.*, 1997). IL-6 is associated with acute phase reaction of immune responses, and has been noted for its anti-inflammatory effects in mice *in vivo* (Tilg *et al.*, 1994).

A significant finding in this study was that an injection of 50 μ g LPS triggered greater microglial phenotype in the hippocampus of CD200^{-/-}, compared with WT, mice. This was characterized by an up-regulation of CD40 and CD11b mRNA expression, but not CD11b. The LPS-induced increase in CD40 mRNA seen in cortical

tissue prepared from WT mice was exacerbated in CD200^{-/-} mice. This exaggerated response was also found in hippocampal tissue prepared from CD200-deficient mice. Activated microglia are distinguished by the activation of a variety of cell surface receptors. CD40, a member of the TNF receptor family (Harnett, 2004) is one such receptor that, when activated, leads to the up-regulation of pro-inflammatory cytokines, including IL-1 and TNF- α (Stout & Suttles, 1996). The interaction between CD40 (also expressed on endothelial cells) and its cognate ligand CD40L (CD154; expressed on activated T cells) is vital for a productive immune response; CD40-CD154 contact induces the production of chemokines and cytokines as well as the up-regulation of MHC II and CD86 (Schonbeck & Libby, 2001). This study would have benefited from an analysis on MHC II and CD86 expression.

Our data show an increase in CD11b expression in the hippocampus of CD200^{-/-} mice at both the transcription and translation level. The failure of LPS to increase CD11b expression in the cortex of CD200^{-/-} mice suggests a regional difference in microglial activation states, a feature that has been reported to exist in the aged mouse brain (Sandhir *et al.*, 2008).

However there was no exacerbation of the LPS-induced expression of IL-1 β , IL-6 or TNF- α in either the cortex or hippocampus in CD200^{-/-}, compared with WT, mice. The similar response in cytokines may be due to the relatively high dose of LPS used. It is interesting to note that the LPS-induced increase in supernatant concentration of these cytokines was enhanced to a greater extent in mixed glia prepared from CD200-deficient mice compared with WT mice (Costello *et al.*, 2011). The deletion of CD200, which is expressed on astrocytes, induces downstream signalling of CD200R, which is expressed on microglia. On the basis that it is microglial cells that are the most dysregulated following removal of CD200, it was hypothesized that the increase in mRNA expression of these cytokines seen in WT mice would be enhanced in CD200^{-/-} mice.

It is possible that the age of the mice used in this study (6-8 months) had an impact on the LPS-induced cytokine expression. Results from chapter 3 indicated that microglial activation (assessed by CD11b immunohistochemistry) was most evident in 17 month-old CD200^{-/-} mice, whereas a less pronounced genotype difference was observed in younger CD200^{-/-} mice. It would be interesting to repeat this study to assess cytokine expression in both aged and young CD200^{-/-} mice, as it has been shown that

the LPS-induced release of IL-1 β and IL-10 following 4 hours of treatment is exaggerated in aged, compared with adult, mice (Henry *et al.*, 2009). In addition, assessing the production of these pro-inflammatory cytokines by ELISA would be beneficial, as relying on mRNA to predict protein expression is not acceptable. Indeed, one study has shown that only 20-40% of the change in protein expression can be accounted for by changes in mRNA expression (Nie *et al.*, 2006). Together, these results indicate that microglial activation was markedly enhanced in WT mice following a single ip injection of 50 μ g LPS. This was confirmed by an increase in CD40 mRNA expression, as well as CD11b immunostaining. Furthermore, these markers of microglial activation were markedly enhanced, in particular in the hippocampus, in CD200-deficient mice, although they were not reflected in expression of inflammatory cytokines. Taken together, these results indicate that CD200 is involved in dampening the immune response following acute endotoxic challenge at a sufficient potency.

Several studies have shown that removal of the CD200 ligand increases susceptibility to autoimmune disease (Hoek *et al.*, 2000). Conversely, activation of the CD200 receptor initiates a signalling cascade involving recruitment and phosphorylation of adaptor proteins, ultimately leading to a decrease in inflammatory cytokines (Zhang *et al.*, 2004). Furthermore, absence of CD200 markedly enhanced microglial proliferation and markers of activated microglia following *Toxoplasma gondii*-induced encephalitis (Deckert *et al.*, 2006), which suggests that activation of the CD200 receptor provides a mechanism for the control of cell responses following immunological stimuli.

Several studies have indicated that CD200^{-/-} mice are highly susceptible to autoimmune diseases to which microglial cells contribute (Feuer, 2007). While MOG-induced EAE is easily inducible in WT mice, symptoms of the disease are advanced by 3 days in CD200^{-/-} mice (Hoek *et al.*, 2000). Microglial activation, assessed by CD68 immunohistochemistry, was greatly increased in CD200^{-/-} compared with wildtype mice with disease 10 days after immunization. In addition, while incidence of CIA is approximately 10% in WT, about 50% of CD200^{-/-} mice showed evidence of the disease 20 days after injection. This is further evidence that through direct and continuous CD200 interaction with CD200R, macrophage activation is regulated in tissues (Hoek *et al.*, 2000; Deckert *et al.*, 2006)

The present data indicate that GFAP mRNA was increased in WT and CD200^{-/-} mice following injection of the higher dose of LPS. Activated astrocytes were visualized by GFAP immunoreactivity in cortical and hippocampal sections and an increase was observed following injection of 50µg LPS-treated in WT and CD200^{-/-} mice. This finding is consistent with a study by Mori and colleagues (2005) that showed GFAP staining was increased in the olfactory bulb of 8-10 week old mice up to 24 hours after ip injection of 50µg LPS. Interestingly, double-staining with antibodies against GFAP and TNF-α revealed co-localization for up to 6 hours post LPS treatment which disappeared by 24 hours (Mori *et al.*, 2005). This infers that astrocytes also produce TNF-α following ip LPS treatment, and is consistent with the earlier finding in this study that indicated parallel LPS-induced increases in TNF-α mRNA and GFAP mRNA in tissue prepared from WT and CD200^{-/-} mice, 4 hours after treatment.

The absence of any genotype-related effect in GFAP expression is not surprising. Expression of CD200 ligand is reserved for neurons (Hoek *et al.*, 2000), and oligodendrocytes (Liu *et al.*, 2010), on highly reactive astrocytes in human AD brain slices (Walker *et al.*, 2009), and on astrocytes adjacent to plaques in MS patients (Koning *et al.*, 2009). CD200 lacks intracellular signalling motifs, or potential docking sites for adaptor signalling molecules (Gorczyński *et al.*, 2002). This infers, firstly, that immunoregulation by CD200 occurs following engagement with its receptor, and, secondly, that deletion of CD200 only has a significant downstream effect on CD200R⁺ cells like microglia and not on cells expressing the ligand. Thus it might be predicted that astrocytic activation following LPS treatment would be similar in WT and CD200^{-/-} mice.

The data from the relaxometry analysis show that LPS failed to induce the predicted decrease in T₂. In the grey matter regions of the cortex and hippocampus, T₂ values were significantly increased in CD200^{-/-} mice treated with the higher dose of LPS. This is contrary to the hypothesis that a decrease in T₂ values reflects microglial activation. In a study examining the effect of LPS-induced endotoxic shock in rats, Rosengarten and colleagues (2008) found no effect of LPS treatment on T₂ relaxation times 3.5 hours post treatment, which was similar to the timepoint in the current study (Rosengarten *et al.*, 2008). Similarly, it has been reported that intracerebral injection of IL-1β, which greatly increases microglial activation (Cai *et al.*, 2004), had no downstream effect on either T₁ or T₂ relaxometry (Harnett, 2004). However, it has been

shown that T_2 signal loss occurs following uptake of ultra-small particles of iron oxide (USPIO) by phagocytic microglia presumably because the signal loss is spatially coincident with labelled activated microglia (Weinstein *et al.*, 2010). It would be useful to assess T_2 relaxometry following uptake of USPIO in LPS-treated CD200-deficient mice in future studies, as previously assessed in a model of cerebral ischemia (Wiert *et al.*, 2007) although the authors concluded that T_2 relaxometry was unreliable as surrogate marker of microglial activation.

The data in this study show that T_1 relaxation times were increased in cortical and hippocampal tissue prepared from mice following treatment with the higher LPS dose. It is interesting to note that, like GFAP expression, T_1 values were unaffected by the lower LPS dose, but increased following treatment with the higher LPS dose. A significant finding in this study is that there was a moderate, positive correlation between GFAP mRNA and T_1 values in cortical and hippocampal regions. This finding is consistent with numerous reports in the literature (Sibson *et al.*, 2008), as well as results from the previous chapter, which have shown that acute astrocytosis is reflected by an increase in T_1 signal in the rodent brain. It is clear that hyperintensity on T_1 images is due, at least in part, to an abundance of reactive astrocytes. Initially it was proposed that a morphological change in astrocytes, denoted by hypertrophied or large-bodied astrocytes was the cause of the enhanced T_1 signal, however it now seems that this is not the case (Shan, 2004).

Several reports have suggested that accumulation of manganese increases T_1 signal in the rodent brain. Intravenous administration of manganese can provide excellent contrast in the rodent brain, enabling the visualization of neural architecture up to 24 hours after treatment (Lee *et al.*, 2005). In the brain, manganese binds to manganese metalloproteins, most commonly glutamine synthetase on astrocytes. Manganese ions, which enter cells through calcium pathways, will cause a shorter water proton T_1 , which will in turn cause an increase in SI (Lin & Koretsky, 1997). The link between manganese accumulation, reactive astrocyte and T_1 relaxometry has been postulated in several studies by Fujioka and colleagues. This group demonstrated that, using a rat model of ischemic neurodegeneration, manganese accumulation and T_1 signal enhancement continues in the striatum up to 4 weeks after cerebral artery occlusion, in chronological agreement with manganese-expressing reactive astrocytes assessed by GFAP immunostaining (Fujioka *et al.*, 2003). Together, these data suggest

that increased concentration of manganese, coupled with its paramagnetic properties, can contribute to T_1 signal enhancement through accumulation on reactive astrocytes following insult or challenge to the CNS. Staining for manganese reactivity in brain sections would have been beneficial in this study.

Astrocytic activation has not been shown to impact on T_2 values which, according to numerous reports, are more reflective of the presence of paramagnetic substances (Ordidge *et al.*, 1994; Warakaulle & Anslow, 2003). Evidence from this laboratory has shown that the age-related increase in GFAP and T_1 relaxation times are both attenuated by rosiglitazone, a PPAR γ agonist with neuroprotective and anti-inflammatory effects, whereas neither microglial activation nor T_2 values were affected (Cowley *et al.*, 2010).

A major aim in this study was to quantify the BBB permeability to the contrast agent gadolinium in WT and CD200^{-/-} mice following LPS treatment. The results show SI in all cortical and hippocampal ROIs was increased in mice treated with the higher concentration of LPS. Relatively little SI change was observed in the cerebellum and frontal cortex. It is possible that these areas which are further away from the isocentre of the magnet suffer from decreased signal to noise ratio. In this study, according to the method described by Blamire and colleagues (2000) which provides an accurate measurement of signal changes in individual voxels. Therefore, post-contrast values close to 1 in control-treated WT mice are indicative of a lack of signal change and lack of BBB permeability to the contrast agent.

The finding that an acute dose of LPS causes BBB breakdown is consistent with previous reports in the literature that describe time- and dose-dependent changes both *in vitro* (Gaillard *et al.*, 2003) and *in vivo* (Singh & Jiang, 2004). In addition, it has been shown that a single ip injection of LPS in rats (3 mg/kg) can increase the transport of insulin (molecular weight: 5508 Daltons) across the BBB, and this was most evident 16-24 hours post treatment (Xaio *et al.*, 2001). Interestingly, ip injection of LPS in rats at a lower dose (2mg/kg) failed to induce BBB permeability to sucrose (Bickel *et al.*, 1998), which has a low molecular weight of 342 Daltons, suggesting that BBB disruption is only induced following treatment with a high concentration of LPS.

Regulation of BBB homeostasis relies on the formation and efficiency of tight junctions to prevent the movement of molecules and ions between adjacent endothelial cells. The tight junction system consists of several proteins including transmembrane

proteins occludin, the claudin family and junctional adhesion molecule. In this study, LPS decreased expression of claudins 5, 12 and occludin mRNA consistent with previous data showing that a decrease in expression of the BBB tight junction proteins leads to disruption of the protein-protein interactions and increased BBB permeability (Singh *et al.*, 2007). Expression of tight junction proteins is modulated by circulating cytokine expression. The expression of claudin 5 and occludin, for example, can be disrupted by the pro-inflammatory cytokines TNF- α , IL-1 β and IL-17 (Kebir *et al.*, 2007) which is thought to lead to increased permeability for lymphocyte infiltration 24 hours after treatment. These results are consistent with the data in this study, correlating increased mRNA expression of pro-inflammatory cytokines, and decreased tight junction protein expression 4 hours post treatment, resulting in increased BBB permeability.

A novel finding in this study was the observation that BBB permeability was increased in CD200-deficient mice. Assessment in the cortex, hippocampus and thalamus revealed increased signal enhancement in CD200^{-/-}, compared with WT, mice and a further increase as a consequence of LPS treatment. Increased extravasation to the contrast agent in CD200-deficient mice was associated with decreased expression of claudin 5 and occludin mRNA and in every ROI assessed, the LPS-treated CD200^{-/-} mice displayed the greatest degree of SI enhancement to gadolinium with a parallel decrease in claudin 5, 12 and occludin mRNA.

The increase in BBB permeability in CD200-deficient mice is noteworthy. The CD200 glycoprotein provides a control mechanism for microglia in the brain, maintaining their downregulated phenotype (Barclay *et al.*, 2002). Changes in the inflammatory profile in CD200^{-/-} mice were increased compared with WT mice. Accumulating evidence has suggested a role for excessive NO production in BBB disruption, for example during experimental meningitis (Boje & Lakhman, 2000). In this study, it is possible that NO was increased in parallel with microglial activation and that is influenced the BBB permeability.

The results presented demonstrate an increase in glial activity in WT and CD200^{-/-} mice following LPS treatment. T₁ relaxometry and GFAP expression were positively correlated, while T₂ relaxation times did not show the predicted decrease in response to microglial activation induced by treatment with LPS. BBB permeability was increased in WT mice following LPS treatment, and particularly in control- and LPS-

treated CD200-deficient mice and this was accompanied by a concomitant loss in mRNA expression of the tight junction proteins claudin 5 and occludin in CD200-deficient mice. It is concluded that the effects of knocking out CD200 are profound and more wide-reaching than simply an increase in inflammatory phenotype.

Chapter 5

**Analysis of the effect of
inducing BBB permeability
in WT and APP/PS1 mice**

5.1 Introduction

AD is a devastating disease, which leads to deleterious cognitive function and behavioural impairments. The presence of A β plaques, which are formed primarily from fibrillary A β_{42} and contain iron-laden cores, is a primary hallmark of the disease. The development of A β plaques in both AD patients (Rojo *et al.*, 2008) and in mouse models of the disease (Eikelenboom *et al.*, 2002) has been shown to initiate a cascade of events that compromise the neuroinflammatory balance within the brain. This is characterized by the up-regulation of markers of glial activity, including MHC II immunostaining in the mouse brain (Gordon *et al.*, 2002) and astrocytosis (Patel *et al.*, 2005), as well as an increase in oxidative stress (Mattson, 2002) and expression of pro-inflammatory cytokines (Lemere, 2007). It has been proposed that inefficient clearance of the peptide is a possible major mechanism for cerebral A β accumulation in the AD brain.

The development of MRI as a clinical tool has led to its ability to detect subtle changes in the tissue water environment under examination. Evidence from the previous chapters has suggested a relationship between acute astrocytosis and T₁ relaxation times, while the ability of T₂ relaxometry to detect changes in levels of paramagnetic substances like iron could render it an attractive technique for the evaluation of anti-amyloid therapies in mouse models of the disease. Thus, the first aim of this study was to confirm the neuroinflammatory profile and MRI changes of middle-aged APP/PS1 mice, a mouse model of AD, which is characterized by early-stage A β plaque deposition. This was carried out using *in vivo* approaches, including relaxometry, immunohistochemical and molecular analysis techniques.

The BBB is formed by the tight junctions of transmembrane proteins between adjacent endothelial cells and astrocytic end feet. These junctions are formed by the continuous production of tight junction proteins, including claudins and occludin, that are critical for BBB maintenance and coordinated activity of neurons (Persidsky *et al.*, 2006). Endothelial cells regulate the diffusion of circulating microscopic molecules, for example bacteria and large hydrophilic molecules, while permitting the diffusion of small, hydrophobic molecules (Weksler *et al.*, 2005) with a molecular weight less than 400 Daltons (Pardridge, 2007). It has previously been reported that size-selective opening of the BBB is a feature of claudin 5 knockout mice (Nitta *et al.*, 2003), while

siRNA treatment targeting suppression of the claudin 5 gene induces BBB permeability to gadolinium (molecular weight: 742 Daltons)-based contrast agents 48hr after treatment (Campbell *et al.*, 2008). This occurs in a time-dependent manner, with greatest suppression of the claudin 5 gene occurring 48 hours after treatment, and a return to control levels 72 hours after treatment.

The aim of this study was to induce a 48hr opening of the BBB following iv injection of siRNA targeting the tight junction proteins claudin 5 and occludin. The hypothesis was that opening the BBB would allow the movement of larger molecules across the BBB, and in APP/PS1 mice, it was hypothesized that this would induce the movement of soluble A β down the concentration gradient from the brain and into the blood.

5.2 Methods

Groups of middle-aged (13-14 months) APP/PS1 mice and WT littermate mice (30g-56g) were used in this study. WT mice were divided into 4 males and 10 females, while the APP/PS1 mice were divided into 4 males and 13 females. Mice were randomly divided into 2 treatment groups (n=7-9/group). The control groups received a non-target siRNA (400 μ l; 20 μ g/mouse in RNase/ DNase-free water) and the experimental groups received siRNA targeting the two tight junction proteins claudin 5 and occludin (400 μ l; 20 μ g/target/mouse in RNase/DNase-free water). The non-target siRNA-treated and claudin 5 and occludin siRNA-treated groups will be henceforth referred to as “control”-treated and “siRNA”-treated groups, respectively.

Mice were placed in a 60ml volume plastic tube that was fixed to the bench and open ended at one end, and filled with a rubber stopper at the other end. The mouse was placed head first inside this tube, with the mouse’s head positioned underneath the rubber stopper. The protruding tail was warmed for 5 minutes, and injection of siRNA solution was carried out with a 30 gauge needle (Introcan, Ireland) with a 1ml syringe.

Mice were anaesthetized with isoflurane 48 hours after siRNA treatment as previously described (see section 2.1.2) for MR scanning. T₁- and T₂-weighted, high-resolution and contrast-enhanced imaging was carried out on mice in this study (see sections 2.1.5, 2.1.6, 2.1.7 and 2.1.9, respectively). BBB permeability to the contrast-

agent, Magnevist, was investigated using the tail-vein cannulation technique. The MR mouse cradle was removed from the magnet and a heated glove was applied to the mouse tail. The mice remained under anaesthetic during the cannulation process. The right lateral tail veins were cannulated with custom-built cannula tubing consisting of a 30 gauge in-dwelling, paediatric iv cannula needle (Introcan, Ireland) which was connected to a three-way tap, which enabled delivery of saline from one syringe and Magnevist contrast agent solution from a second syringe (Bayer, Ireland; Magnevist to saline ratio; 1:2).

Mice were injected with the contrast agent solution (200 μ l) at the beginning of the second repetition of the 10-repetition contrast scan. This allowed for both pre- and post-contrast measurements to be acquired in the same scan and permitted the accurate placement of ROIs from the pre-contrast scan onto subsequent repetitions.

Following scanning, mice were sacrificed by cervical dislocation and brain tissue was prepared for analysis of inflammatory markers, tight junction protein expression and soluble and insoluble concentrations of A β . Brains were rapidly removed, and placed on a Petri dish that had been filled with ice. Brains were hemisected and prepared for quantified immunohistochemical analysis of CD11b, GFAP and A β plaques (left hemisphere) and mRNA analysis of microglial and astrocytic markers and tight junction proteins by qPCR (left hemisphere). Only cortical tissue was prepared for qPCR analysis (see sections 2.5.1 for specific details). In a parallel set of experiments by other members of the laboratory, soluble and insoluble levels of A β ₄₀ and AB₄₂ were measured in blood serum samples and brain tissue (right hemisphere) of these mice. This is summarised in sections 2.7.7-2.7.9.

Data are presented as means \pm SEM. For the contrast analysis, ROIs consisting of a 2x2 voxel square were manually placed into anatomically distinct regions in the pre-contrast scan and copied into identical positions in post-contrast images. A mouse brain atlas (Paxinos G, 2001) was used to ensure precise positioning of ROIs. Contrast analysis was carried out in cortical, hippocampal, thalamic, and cerebellar regions. These data are presented as a ratio by dividing post-contrast values by the pre-contrast measurement to assess post-contrast SI changes. The last four repetitions of the contrast scan from each mouse were used for statistical analysis. The contrast imaging data presented correspond to the left hemisphere which was taken for analysis of tight

junction protein expression; the data from the contralateral hemisphere are summarised in Table 7.8, Appendix III.

A two-way ANOVA was performed to ascertain whether significant differences existed in the data. Where significance was found, Bonferroni post-hoc tests were used to determine where significant differences lay (see section 2.8 for further details). Where appropriate, a two-tailed Student's t-test for independent means was performed to assess statistical significance between conditions.

5.3 Results

5.3.1 *The effect of genotype on microglial activation*

CD11b is a cell surface marker of activated microglia, and is upregulated in conditions of inflammatory stress (Gonzalez-Scarano & Baltuch, 1999). The present data show that there was a significant increase in CD11b mRNA and protein expression in sections prepared from APP/PS1 mice. Firstly, Figure 5.1 illustrates that there was a significant increase in cortical mRNA expression of CD11b in control-treated APP/PS1 (1.94 ± 0.19 RQ; $n=9$) compared with control-treated WT mice (1.01 ± 0.05 RQ; $n=7$; ** $p<0.01$; ANOVA) and in siRNA-treated APP/PS1 mice (2.11 ± 0.22 RQ; $n=8$) compared with siRNA-treated WT mice (0.92 ± 0.06 RQ; $n=9$; *** $p<0.001$; ANOVA). There was no effect of siRNA treatment on cortical CD11b expression.

Brain tissue from control and siRNA-treated WT and APP/PS1 mice was stained for CD11b and sample micrographs from the cortex and hippocampus are presented in Figures 5.2 and 5.3, respectively. The micrographs displayed are representative of an $N=7-9$ /group. Positive immunoreactivity is denoted by brown staining, while methyl green was used to counterstain the chromatin of the cells. CD11b staining was low in cortical sections prepared from control and siRNA-treated WT mice (Figure 5.2). There was a marked increase in CD11b staining in cortical sections prepared from control and siRNA-treated APP/PS1 mice compared with siRNA-treated WT mice. There was no clear effect of siRNA treatment on cortical expression of CD11b in these mice. There was a significant increase in the ratio of DAB/nuclear area in the cortex of control-

treated APP/PS1, compared with WT, mice (** $p < 0.01$; ANOVA) and in siRNA-treated APP/PS1, compared with WT, mice (***) $p < 0.001$; ANOVA).

A similar trend was observed in hippocampal sections prepared from control- and siRNA-treated WT and APP/PS1 mice (Figure 5.3). There was a significant increase in the ratio of DAB/nuclear area in the hippocampus of control-treated APP/PS1, compared with WT, mice (** $p < 0.01$; ANOVA) and in siRNA-treated APP/PS1, compared with WT, mice (***) $p < 0.001$; ANOVA).

The interaction between CD40 and its ligand, CD154, has been shown to decrease phagocytosis of A β by microglia (Townsend *et al.*, 2005). Here, brain tissue from siRNA-treated WT and APP/PS1 mice was examined for changes in CD40 mRNA expression (Figure 5.4). Genotype was a significant factor in predicting CD40 mRNA expression in this study, with a decrease in expression of cortical CD40 mRNA expression in APP/PS1 mice (* $p < 0.05$; ANOVA). However, mean values were similar in control-treated APP/PS1 mice (0.48 ± 0.09 RQ; $n=8$) compared with WT mice (1.12 ± 0.2 RQ; $n=7$), and in siRNA-treated APP/PS1 mice (0.24 ± 0.04 RQ; $n=7$).

5.3.2 The effect of genotype on GFAP expression

Reactive astrocytosis occurs in response to all forms of CNS injury and disease, and is characterized by cellular hypertrophy and changes in gene expression (Sofroniew, 2005). Figure 5.5 illustrates the changes in GFAP mRNA expression in cortical tissue prepared from control- and siRNA-treated WT and APP/PS1 mice. There was a significant increase in cortical mRNA expression of GFAP in control-treated APP/PS1 mice (4.05 ± 0.33 RQ; $n=9$) compared with control-treated WT mice (1.01 ± 0.07 RQ; $n=7$; ***) $p < 0.001$; ANOVA) and in siRNA-treated APP/PS1 mice (4.38 ± 0.53 RQ; $n=9$) compared with siRNA-treated WT mice (0.95 ± 0.11 RQ; $n=9$; ***) $p < 0.001$; ANOVA). There was no effect of siRNA treatment on cortical mRNA expression of GFAP.

Brain tissue from control- and siRNA-treated WT and APP/PS1 mice was stained for GFAP and sample micrographs from the cortex and hippocampus are presented in Figures 5.6 and 5.7, respectively. The micrographs displayed are representative of an $N=7-9$ /group. Positive immunoreactivity is denoted by brown positive staining, and methyl green was used to counterstain the chromatin of the cells.

Positive GFAP staining was low in cortical sections prepared from control and siRNA-treated WT mice (Figure 5.5). There was a marked increase in GFAP staining in cortical sections prepared from control and siRNA-treated APP/PS1 mice. There was no clear effect of siRNA treatment on GFAP staining in cortical sections prepared from these mice. There was a significant increase in the ratio of DAB/nuclear area in the cortex of control-treated APP/PS1, compared with WT, mice (** $p < 0.01$; ANOVA) and in siRNA-treated APP/PS1, compared with WT, mice (* $p < 0.05$; ANOVA). This result was replicated in hippocampal sections prepared from siRNA-treated WT and APP/PS1 mice (Figure 5.7)

5.3.3 The effect of genotype on IL-1 β , TNF- α , IL-6 mRNA expression

Pro-inflammatory cytokines are thought to play a pathogenic role in the development of several age-related diseases, including AD (Bruunsgaard *et al.*, 2001). Therefore, mRNA expression of the pro-inflammatory cytokines IL-1 β , TNF- α and IL-6 was assessed in cortical tissue prepared from control and siRNA-treated WT and APP/PS1 mice. Figure 5.8 illustrates the effect of genotype on IL-1 β . There was a significant increase in cortical IL-1 β mRNA expression in control-treated APP/PS1 mice (2.21 ± 0.23 RQ; $n=8$) compared with control-treated WT mice (0.89 ± 0.16 RQ; $n=6$; ** $p < 0.01$; ANOVA) and in siRNA-treated APP/PS1 mice (2.11 ± 1.3 RQ; $n=7$) compared with siRNA-treated WT mice (1.05 ± 0.26 RQ; $n=8$; * $p < 0.05$; ANOVA). There was no effect of siRNA treatment on IL-1 β mRNA expression in these mice.

The changes in TNF- α mRNA in WT and APP/PS1 mice are illustrated in Figure 5.9. There was a significant increase in cortical TNF- α mRNA expression in control-treated APP/PS1 mice (2.07 ± 0.44 RQ; $n=8$) compared with control-treated WT mice (0.80 ± 0.15 RQ; $n=6$; ** $p < 0.01$; ANOVA). There was no effect of siRNA treatment on TNF- α mRNA expression.

Figure 5.10 illustrates the difference in IL-6 mRNA expression in cortical tissue prepared from siRNA-treated WT and APP/PS1 mice. Mean IL-6 mRNA expression was similar in control-treated APP/PS1 (1.64 ± 0.28 RQ; $n=9$) and control-treated WT mice (1.02 ± 0.3 RQ; $n=6$). There was a significant increase in cortical mRNA expression of IL-6 in siRNA-treated APP/PS1 mice (1.83 ± 0.53 RQ; $n=6$) compared with siRNA-treated WT mice (0.89 ± 0.27 RQ; $n=8$; * $p < 0.05$; ANOVA).

5.3.4 The effect of genotype on T_2 relaxometry

T_2 relaxation times are determined primarily by water molecule protons, but are also sensitive to macromolecular interactions, including those generated by even small concentrations of paramagnetic material (Haacke *et al.*, 2005). To provide a whole-brain analysis, T_2 measurements were taken in ROIs in the cortex, hippocampus, thalamus and corpus callosum in control- and siRNA-treated WT and APP/PS1 mice. Figure 5.11 illustrates the effect of genotype on T_2 values in the whole cortex of WT and APP/PS1 mice. There was a significant decrease in cortical T_2 values in control-treated APP/PS1 mice (48.49 ± 0.27 ms; $n=8$) compared with control-treated WT mice (49.44 ± 0.31 ms; $n=7$; * $p<0.05$; ANOVA) and siRNA-treated APP/PS1 mice (48.39 ± 0.18 ms; $n=8$) compared with siRNA-treated WT mice (49.37 ± 0.24 ms; $n=7$; * $p<0.05$; ANOVA).

The effect of genotype on T_2 values in the motor and entorhinal cortex in siRNA-treated WT and APP/PS1 mice is presented in Figure 5.12. In the motor cortex, there was a decrease in T_2 values in control-treated APP/PS1 mice (46.36 ± 0.28 ms; $n=8$) compared with control-treated WT mice (49.64 ± 0.62 ms; $n=7$; *** $p<0.001$; ANOVA) and in siRNA-treated APP/PS1 mice (45.87 ± 0.14 ms; $n=8$) compared with siRNA-treated WT mice (49.17 ± 0.41 ms; $n=7$; *** $p<0.001$; ANOVA). A similar genotype difference was observed in the entorhinal cortex of WT and APP/PS1 mice (Figure B); there was a significant decrease in T_2 values in the entorhinal cortex of control-treated APP/PS1 mice (48.79 ± 0.33 ms; $n=8$) compared with control-treated WT mice (50.77 ± 0.28 ms; $n=7$; *** $p<0.001$; ANOVA) and in siRNA-treated APP/PS1 mice (49.27 ± 0.15 ; $n=8$) compared with siRNA-treated WT mice (50.54 ± 0.28 ms; $n=7$; ** $p<0.01$; ANOVA). Treatment with siRNA had no significant effect.

T_2 relaxation times were significantly decreased in the hippocampus of control-treated APP/PS1 mice (48.72 ± 0.37 ms; $n=8$) compared with control-treated WT mice (49.98 ± 0.31 ms; $n=7$; * $p<0.05$; ANOVA; Figure 5.13). Mean T_2 values were similar in the hippocampus of siRNA-treated APP/PS1 mice (49.07 ± 0.35 ms; $n=8$) and siRNA-treated WT mice (49.79 ± 0.13 ms; $n=7$). Treatment with siRNA had no effect.

Figure 5.14 depicts the effect of genotype and treatment on T_2 values in the corpus callosum of WT and APP/PS1 mice. Mean T_2 relaxation times were similar in control-treated APP/PS1 mice (42.61 ± 0.45 ms; $n=8$) and WT mice (43.46 ± 0.2 ms;

n=7), and in siRNA-treated APP/PS1 mice (41.89 ± 0.5 ; n=8) and WT mice (42.37 ± 0.5 ; n=7). Similarly, neither genotype nor treatment had an effect on T_2 data in the thalamus (Figure 5.15); mean T_2 values were similar in the thalamus of control-treated APP/PS1 mice (43.07 ± 0.13 ms; n=8) and WT mice (42.95 ± 0.2 ; n=7) and of siRNA-treated APP/PS1 mice (43.01 ± 0.23 ms; n=8) and WT mice (43.23 ± 0.2 ms; n=7).

5.3.5 The effect of genotype on T_1 relaxometry

Results from the previous chapters, as well as several reports in the literature (Fujioka *et al.*, 2003), have indicated that acute astrocytosis reflects increased T_1 relaxation times in grey matter regions. This potential association was investigated in WT and APP/PS1 mice. Figure 5.16 illustrates the effect of genotype on T_1 values from the whole cortex of WT and APP/PS1 mice. Mean T_1 values were similar in the whole cortex of control-treated APP/PS1 (1663 ± 17.26 ms; n=9) and WT mice (1685 ± 22.99 ms; n=7), and in siRNA-treated APP/PS1 mice (1718 ± 26.39 ms; n=7) and WT mice (1660 ± 5.23 ms; n=6). Treatment with siRNA had no effect.

ROI analysis was also carried out on sub-regions of the cortex. Figure 5.17 illustrates the effect of genotype on T_1 values in the motor (A) and entorhinal (B) cortices. There was an increase in T_1 values in the motor cortex of control-treated APP/PS1 mice (1682 ± 25.36 ms; n=9) compared with WT mice (1579 ± 12.38 ms; n=6; * $p < 0.05$; ANOVA) and in siRNA-treated APP/PS1 mice (1737 ± 32.31 ms; n=7) compared with WT mice (1586 ± 22.99 ms; n=7; *** $p < 0.001$; ANOVA). In contrast, mean T_1 values were similar in the entorhinal cortex of control-treated APP/PS1 mice (1692 ± 16.5 ms; n=9), and WT mice (1689 ± 31.21 ms; n=7) and in siRNA-treated APP/PS1 mice (1771 ± 29.95 ms; n=7) and WT mice (1690 ± 23.9 ms; n=7). There was no significant effect of siRNA treatment on T_1 values in these cortical sub-regions.

There was an increase in T_1 relaxation times in the hippocampus of siRNA-treated APP/PS1 mice (1758 ± 28.99 ms; n=7) compared with WT mice (1626 ± 4.18 ms; n=6; *** $p < 0.001$; ANOVA).

In contrast, mean T_1 values in the corpus callosum were similar in control-treated APP/PS1 mice (1509 ± 25.55 ms; n=9) and WT mice (1535 ± 18.11 ms; n=7), and in siRNA-treated APP/PS1 mice (1511 ± 32.9 ms; n=7) and WT mice (1538 ± 15.71 ms; n=7; Figure 5.19). Finally, the effect of genotype and siRNA treatment on T_1

relaxation times in the thalamus of WT and APP/PS1 mice is presented in Figure 5.19. Mean T_1 values in control-treated APP/PS1 mice (1418 ± 18.58 ms; $n=9$) were similar to that in control-treated WT mice (1369 ± 18.14 ms; $n=7$). However, T_1 values were increased in the thalamus of siRNA-treated APP/PS1 mice (1489 ± 28.05 ms; $n=7$) compared with WT mice (1391 ± 19.41 ms; $n=7$; ** $p<0.01$; ANOVA).

5.3.6 The effect of genotype on anatomic volumetry

One of the aims of this study was to assess high-resolution T_2 -weighted anatomic images for differences in grey matter as an indicator of volumetric alteration in APP/PS1 mice. Grey matter segmentations were spatially registered to a generic C57 template image and between-group voxel-wise statistics were carried out on the resulting registrations. The resulting statistical parametric mapping was thresholded at $p<0.05$ to indicate significance between groups. The sample coronal, sagittal and axial images presented in Figure 5.21 indicate that there were no voxel clusters within the SPM that reached statistical significance between genotypes.

5.3.7 The effect of siRNA treatment on claudins 5, 12 and occludin mRNA expression

Treatment with siRNA targeting suppression of the claudin 5 gene induces transient permeability of the BBB through suppression of proteins associated with endothelial cell tight junctions (Campbell *et al.*, 2008). The effect of siRNA on cortical mRNA expression of claudin 5, occludin and claudin 12 in WT and APP/PS1 mice is presented in Figures 5.22, 5.23 and 5.24, respectively. There was a significant decrease in claudin 5 mRNA expression in cortical tissue prepared from siRNA-treated WT mice (0.45 ± 0.08 RQ; $n=9$) compared with control-treated WT mice (1.03 ± 0.1 RQ; $n=6$; ** $p<0.01$; ANOVA; Figure 5.22). Expression was similar in cortical tissue prepared from siRNA-treated APP/PS1 mice (0.47 ± 0.09 RQ; $n=8$) and control-treated APP/PS1 mice (0.59 ± 0.1 RQ; $n=9$). There was a significant decrease in cortical claudin 5 mRNA expression in control-treated APP/PS1 mice (0.59 ± 0.1 RQ; $n=9$) compared with non-target siRNA-treated WT mice (1.03 ± 0.1 RQ; $n=6$; ** $p<0.01$; ANOVA).

Figure 5.23 illustrates that mean occludin mRNA values were similar in siRNA-treated WT mice (0.68 ± 0.24 RQ; $n=5$) and control-treated WT mice (0.84 ± 0.19 RQ;

n=5). Likewise, mean occludin mRNA values were similar in the cortex of siRNA-treated APP/PS1 mice (0.68 ± 0.24 RQ; n=8) and control-treated APP/PS1 mice (0.66 ± 0.16 RQ; n=8). Genotype was not a factor in predicting occludin mRNA values in these data.

There was a significant decrease in cortical expression of claudin 12 mRNA in siRNA-treated WT mice (0.80 ± 0.07 RQ; n=7) compared with control-treated WT mice (1.02 ± 0.08 RQ; n=7; * $p < 0.05$; ANOVA; Figure 5.24) and in siRNA-treated APP/PS1 mice (0.64 ± 0.01 RQ; n=7) compared with control-treated APP/PS1 mice (0.75 ± 0.04 RQ; n=9; * $p < 0.05$; Student's t-test). Mean claudin 12 mRNA was decreased in cortical tissue prepared from control-treated APP/PS1 mice (0.75 ± 0.04 RQ; n=9) compared with control-treated WT mice (1.02 ± 0.08 RQ; n=7; ++ $p < 0.01$; ANOVA).

5.3.8 The effect of siRNA treatment on BBB permeability to gadolinium

It has previously been shown that siRNA treatment targeting the endothelial cell tight junction protein claudin 5 induces transient disruption of the BBB and the infiltration and deposition of gadolinium-based contrast agents in the brains of treated mice (Campbell *et al.*, 2008). The effects of siRNA treatment are visualized in Figure 5.25. Mean post-contrast SI in control-treated WT mice was similar to the pre-contrast baseline measurement. Treatment with siRNA induced a significant increase in post-contrast SI values in WT mice. Both APP/PS1 siRNA treatment groups displayed increased SI intensities in post-contrast repetitions following gadolinium injection. An increase in SI values in later repetitions is denoted by a change in voxel value in the MR image from yellow to red.

SI changes in anatomical regions were quantified using a similar method to that used in chapter 4. Figures 5.26 – 5.32 illustrate the effects of genotype and siRNA treatment on gadolinium-enhancement in the cortex, dentate gyrus, thalamus, frontal lobe and cerebellum in the left hemisphere of mice. Data from the contra-lateral hemisphere is summarised in Table 7.7, Appendix III.

There was no indication of post-contrast signal enhancement in the left motor cortex of control-treated WT mice following contrast agent injection, compared with the pre-contrast baseline (Figure 5.26). There was an increase in SI in siRNA-treated WT mice (1.03 ± 0.01 RQ; n=6) compared with control-treated WT mice (0.99 ± 0.01 RQ;

n=5; **p<0.01; ANOVA). Mean SI was also increased in siRNA-treated APP/PS1 (1.04 ± 0.01 RQ; n=7) compared with control-treated APP/PS1 (1.01 ± 0.01 RQ; n=6; *p<0.05; ANOVA) but post-contrast SI was similar in the left motor cortex of control-treated APP/PS1 (1.01 ± 0.01 RQ; n=6) and control-treated WT mice (0.99 ± 0.01 RQ; n=5).

There was no significant change in post-contrast SI values in the somatosensory cortex of control-treated WT mice, compared with the pre-contrast measurement. There was an increase in post-contrast SI measurements in siRNA-treated WT mice (1.03 ± 0.01 RQ; n=6) compared with control-treated WT mice (0.99 ± 0.01 RQ; n=5; **p<0.01; ANOVA; Figure 5.27) and in control-treated APP/PS1 mice (1.01 ± 0.005 ; n=6) compared with WT mice (0.99 ± 0.01 RQ; n=5; *p<0.05; ANOVA). Treatment with siRNA failed to significantly increase SI in the somatosensory cortex of APP/PS1 mice (1.04 ± 0.004 RQ; n=7) compared with control-treated APP/PS1 mice (1.01 ± 0.005 RQ; n=6).

Neither control-treated WT or APP/PS1 mice displayed post-contrast SI values indicative of gadolinium extravasation. There was an increase in post-contrast SI values in siRNA-treated WT mice (1.01 ± 0.005 RQ; n=6) compared with control-treated WT mice (0.96 ± 0.01 RQ; n=5; ***p<0.001; ANOVA; Figure 5.28) and in siRNA-treated APP/PS1 mice (1.04 ± 0.007 RQ; n=7) compared with control-treated APP/PS1 mice (0.99 ± 0.008 RQ; n=6; ***p<0.001; ANOVA). Treatment with siRNA exerted a significantly greater increase in post-contrast SI values in APP/PS1 mice (1.04 ± 0.007 RQ; n=7) compared with WT mice (1.01 ± 0.005 RQ; n=6; *p<0.05; ANOVA).

Post-contrast SI values in control-treated WT mice showed no indication of gadolinium extravasation in the dentate gyrus. Neither genotype nor siRNA treatment were a significant factor in predicting SI values and mean SI values were similar in the dentate gyrus of siRNA-treated WT mice (1.04 ± 0.006 RQ; n=6) and control-treated WT mice (1.02 ± 0.01 RQ; n=5) and in siRNA-treated APP/PS1 mice (1.03 ± 0.007 RQ; n=7) and control-treated APP/PS1 mice (1.04 ± 0.06 n=6; Figure 5.29).

No significant alterations in SI post gadolinium injection were observed in the thalamus in either of the control groups. However, mean SI was increased in the thalamus of siRNA-treated WT mice (1.05 ± 0.01 RQ; n=6) compared with control-treated WT mice (1.01 ± 0.01 RQ; n=5; *p<0.05; ANOVA; Figure 5.30). In addition, there was a significant increase in gadolinium-induced SI values in siRNA-treated

APP/PS1 mice (1.06 ± 0.008 RQ; n=7) compared with control-treated APP/PS1 mice (1.02 ± 0.01 RQ; n=6; * $p < 0.05$; ANOVA).

Mean post-contrast SI values were similar in the cerebellum of control-treated APP/PS1 mice (1.01 ± 0.01 RQ; n=6) compared with WT mice (0.98 ± 0.01 RQ; n=5). However, there was a significant increase in post contrast SI values in siRNA-treated WT mice (1.04 ± 0.01 RQ; n=6) compared with control-treated WT mice (0.98 ± 0.01 RQ; n=6; * $p < 0.05$; Figure 5.31). In addition, there was a significant increase in post-contrast SI in the left cerebellar nucleus of siRNA-treated APP/PS1 mice (1.06 ± 0.01 RQ; n=7) compared with control-treated APP/PS1 mice (1.01 ± 0.01 RQ; n=6; * $p < 0.05$; ANOVA).

SI changes following gadolinium injection in the left frontal association cortex of WT and APP/PS1 are presented in Figure 5.32. There was a significant increase in SI in this ROI of siRNA-treated WT mice (1.03 ± 0.005 RQ; n=6) compared with control-treated WT mice (0.97 ± 0.009 RQ; n=5; ** $p < 0.01$; ANOVA). Moreover, there was an increase in post-contrast SI in the left frontal association cortex of control-treated APP/PS1 mice (1.03 ± 0.005 RQ; n=6) compared with WT mice (0.97 ± 0.009 RQ; n=5; ** $p < 0.01$; ANOVA). Treatment with siRNA failed to significantly alter SI values in APP/PS1 mice.

The relationship between SI and mRNA expression of the tight junction proteins claudins 5, 12 and occludin are presented in Figure 5.33. SI values from cortical ROIs were pooled and paired with the associated expression of tight junction proteins claudins 5, 12 and occludin. There were moderate and significant inverse correlations between SI and claudin 5 mRNA expression (Figure A: Pearson $r = -0.571$; ** $p < 0.01$; n=24) and claudin 12 mRNA expression (Figure B: Pearson $r = -0.5985$; ** $p < 0.01$; n=24). There was no correlation between SI and occludin mRNA expression in these data (Figure C: Pearson $r = -0.114$; $p > 0.05$; n=20).

5.3.9 The effect of siRNA treatment on A β levels

The abundance and solubility of A β peptides are critical determinants of amyloidosis in the brains of AD patients (Wang *et al.*, 1999). Insoluble and soluble levels of A β were measured in this study by immunohistochemical staining and by mesoscale analysis. Staining by Congo red, which binds to amyloid fibrils, was carried

out on sections prepared from siRNA-treated WT and APP/PS1 mice and sample images are presented in Figure 5.34. Representative images from the hippocampus (A, B) and cortex (C, D) of control- and siRNA-treated APP/PS1 mice confirm the presence of A β plaques in the brains of both APP/PS1 groups. Sections prepared from control- and siRNA-treated WT mice were completely plaque-free (data not shown).

Plaque quantification was carried out on six half-hemisphere coronal slices per animal from control and siRNA-treated APP/PS1 groups under the same light conditions and averaged per animal. This is summarised in Figure 5.35. Treatment with siRNA had no effect on total plaque number in APP/PS1 mice. Mean plaque count was similar in control-treated APP/PS1 mice (17.86 ± 4.01 ; n=7) compared with siRNA-treated mice (22.11 ± 4.98 ; n=6).

Concentrations of A β_{40} and A β_{42} were measured in serum and cortical tissue and the data are illustrated in Figures 5.36 – 5.38. There was a significant increase in soluble A β_{40} in cortical tissue prepared from control-treated APP/PS1 mice (4058 ± 587.4 pg/ml; n=8) compared with control-treated WT mice (24.68 ± 5.07 pg/ml; n=7; *** p<0.001; ANOVA). Likewise, the concentration of A β_{40} was significantly increased in cortical tissue prepared from siRNA-treated APP/PS1 mice (5129 ± 1039 pg/ml; n=8) compared with WT mice (34.25 ± 11.11 pg/ml; n=7; *** p<0.001; ANOVA). Treatment with siRNA failed to induce a significant change in the concentration of soluble A β_{40} . A similar trend was observed in the concentration of insoluble A β_{40} , where a significant increase was noted in cortical tissue from control-treated APP/PS1 (1779 ± 537.1 pg/ml; n=9), compared with WT, mice (1.37 ± 0.67 pg/ml; n=6; ** p<0.01; ANOVA) and in siRNA-treated APP/PS1 (2221 ± 423.1 pg/ml; n=7), compared with WT, mice (10.86 ± 6.18 pg/ml; n=7; ** p<0.01; ANOVA). Treatment with siRNA had no effect.

A similar finding was noted in the concentration of soluble and insoluble A β_{42} (Figure 5.37). A significant increase in soluble A β_{42} was observed in cortical tissue prepared from control-treated APP/PS1 (2030 ± 274.4 pg/ml; n=9) compared with WT, mice (15.43 ± 5.6 pg/ml; n=7; *** p<0.001; ANOVA) and in siRNA-treated APP/PS1 mice (1976 ± 310.7 pg/ml; n=8) compared with WT mice (20.49 ± 8.09 pg/ml; n=7; *** p<0.001; ANOVA). Likewise, the concentration of insoluble A β_{42} was significantly increased in cortical tissue prepared from control-treated APP/PS1 mice (2497 ± 555.3 pg/ml; n=9) compared with WT mice (0 ± 0 pg/ml; n=6; ** p<0.01; ANOVA) and in siRNA-treated APP/PS1 mice (3274 ± 513 pg/ml; n=8) compared with WT mice (14.41

± 7.77 pg/ml; n=7; ***p<0.001; ANOVA). Treatment with siRNA had no effect on concentrations of soluble or insoluble A β_{42} in cortical tissue.

There was an increase in serum A β_{40} concentration in blood from siRNA-treated APP/PS1 mice (257.8 ± 79.99 pg/ml; n=7) compared with WT mice (18.21 ± 2.64 pg/ml; n=4; *p<0.05; Figure 5.38). Mean concentration of A β_{40} was also upregulated in the blood of control-treated APP/PS1 mice (142.5 ± 53 pg/ml; n=6) and WT mice (17.2 ± 2.3 pg/ml; n=5). Mean serum concentrations of A β_{42} were upregulated in control-treated APP/PS1 mice (22.5 ± 9.39 pg/ml; n=7) and WT mice (0.75 ± 0.46 pg/ml; n=5), and in siRNA-treated APP/PS1 mice (22.31 ± 7.76 pg/ml; n=7) and WT mice (0 ± 0 pg/ml; n=4).

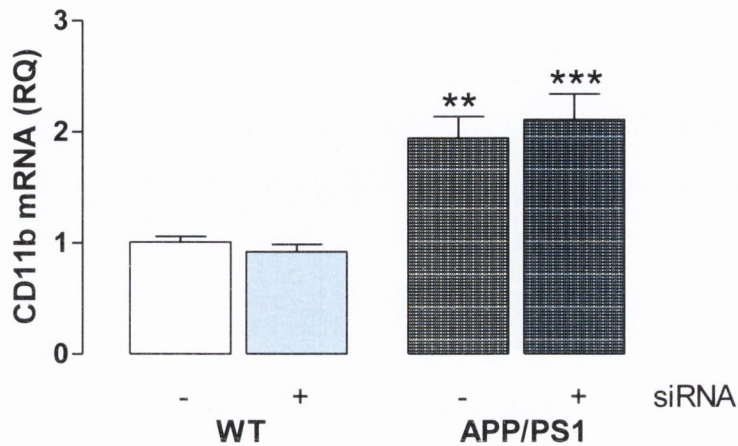


Figure 5.1 Cortical CD11b mRNA expression in WT and APP/PS1 transgenic mice.

Groups of WT and APP/PS1 transgenic mice were injected iv with a control siRNA (400µl; 20µg/mouse) or siRNA targeting claudin 5 and occludin (400µl; 20µg/target/mouse). After 48 hours, mice were sacrificed by decapitation, left cortex dissected free, homogenized and CD11b mRNA expression determined by qPCR. Mean CD11b mRNA expression was increased in cortical tissue prepared from control-treated APP/PS1 mice compared with WT mice (** p<0.01; ANOVA) and in siRNA-treated APP/PS1 mice compared with WT mice (** p<0.001; ANOVA). Values are expressed as relative quantities (RQ) obtained from calculating the ratio of CD11b mRNA to an endogenous control and are means ± SEM.

2-way ANOVA: siRNA effect F (1, 27) = 0.0683; p=0.7958, Genotype effect F (1, 27) = 37.97; p<0.0001, Interaction effect F (1, 27) = 0.5045; p=0.4836

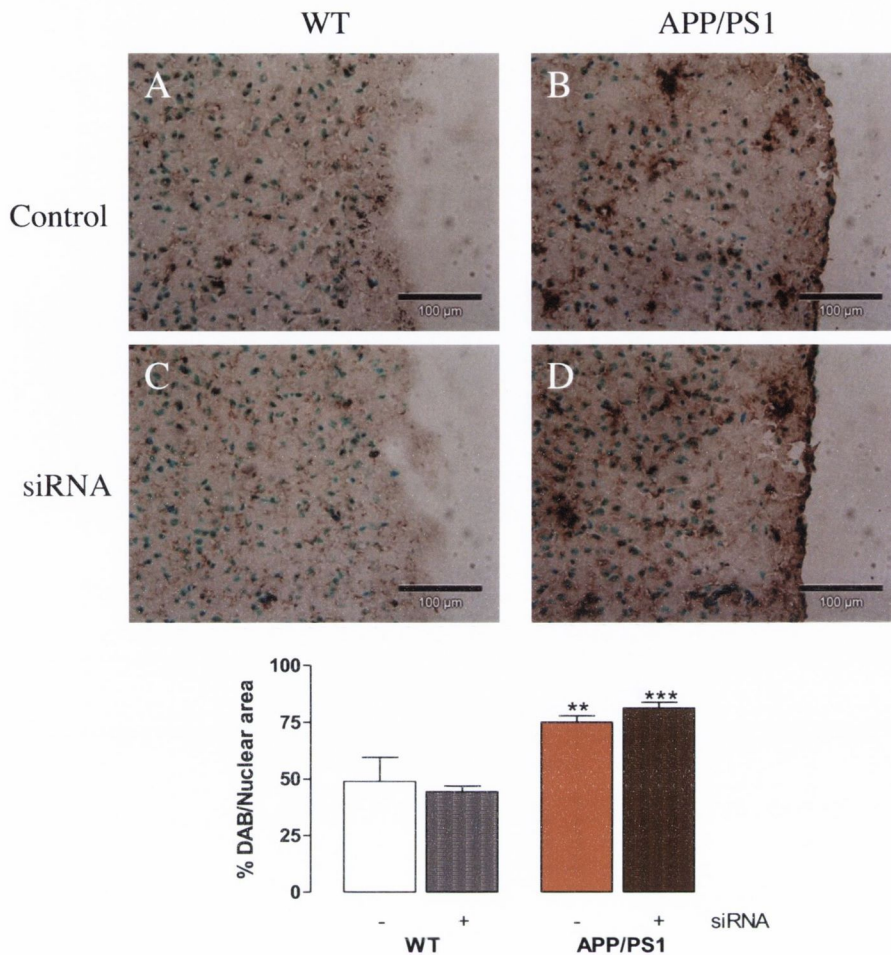


Figure 5.2 CD11b immunoreactivity in the cortex of WT and APP/PS1 mice.

Groups of WT and APP/PS1 mice were injected iv with a control siRNA (400 μ l; 20 μ g/mouse), or siRNA targeting claudin 5 and occludin (400 μ l; 20 μ g/target/mouse). There was a marked increase in DAB-enhanced positive staining in the cortex of APP/PS1, compared with WT, mice. (Magnification 40x, scale bar 100 μ m).

There was a significant increase in the ratio of DAB/nuclear area in the cortex of control-treated APP/PS1, compared with WT, mice (** $p < 0.01$; ANOVA) and in siRNA-treated APP/PS1, compared with WT, mice (** $p < 0.001$; ANOVA).

2-way ANOVA: siRNA effect $F(1, 26) = 0.04$; $p = 0.8669$, Genotype effect $F(1, 26) = 59.92$; $p < 0.0001$, Interaction effect $F(1, 26) = 1.74$; $p = 0.2858$

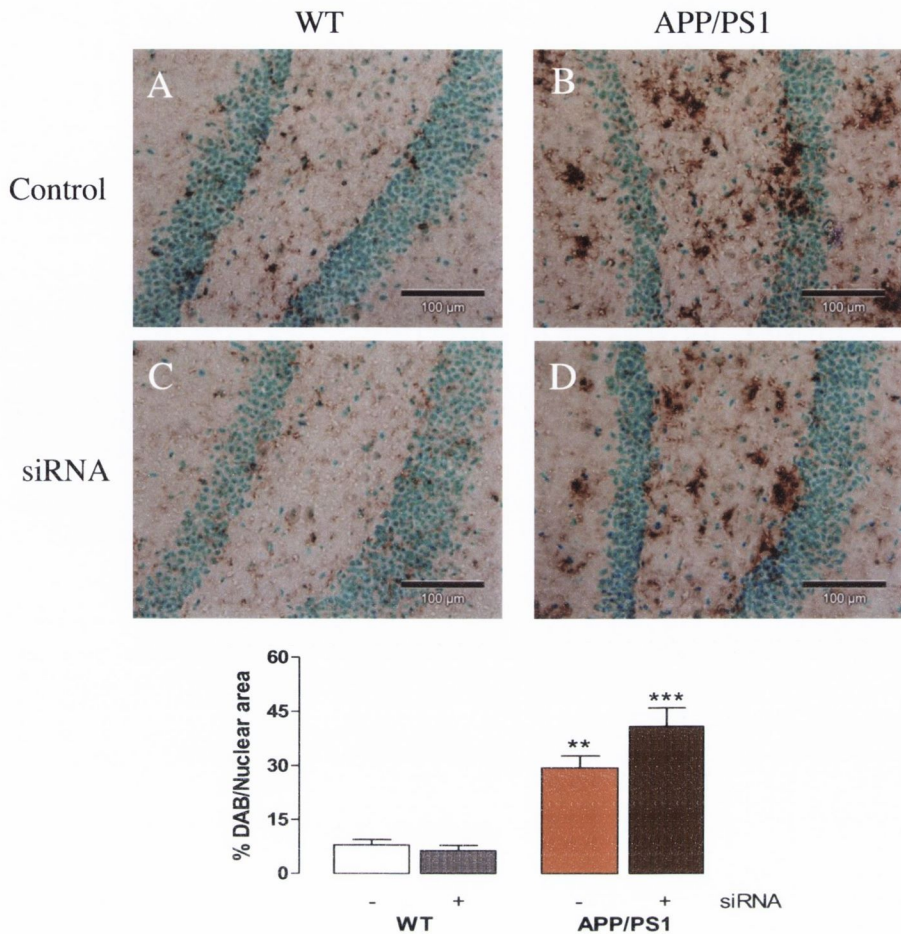


Figure 5.3 CD11b immunoreactivity in the hippocampus of WT and APP/PS1 mice.

Groups of WT and APP/PS1 mice were injected iv with a non-target siRNA (400 μ l; 20 μ g/mouse), or siRNA targeting claudin 5 and occludin (400 μ l; 20 μ g/target/mouse). There was a marked increase in CD11b positive staining in the hippocampus of both APP/PS1 groups. (Magnification 40x, scale bar 100 μ m).

There was a significant increase in the ratio of DAB/nuclear area in the hippocampus of control-treated APP/PS1, compared with WT, mice (** p <0.01; ANOVA) and in siRNA-treated APP/PS1, compared with WT, mice (*** p <0.001; ANOVA).

2-way ANOVA: siRNA effect $F(1, 26) = 1.96$; $p = 0.2123$, Genotype effect $F(1, 26) = 62.27$; $p < 0.0001$, Interaction effect $F(1, 26) = 3.37$; $p = 0.1052$

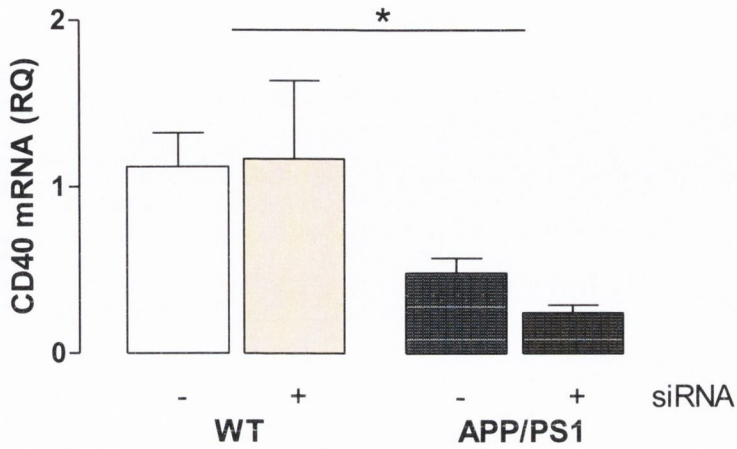


Figure 5.4 Cortical CD40 mRNA expression in WT and APP/PS1 transgenic mice.

Groups of WT and APP/PS1 transgenic mice were injected iv with a control siRNA (400µl; 20µg/mouse) or siRNA targeting claudin 5 and occludin (400µl; 20µg/target/mouse). After 48 hours, mice were sacrificed by decapitation, left cortex dissected free, homogenized and CD40 mRNA expression determined by qPCR. There was a significant effect of genotype on predicting mean CD40 mRNA values (* $p < 0.05$; ANOVA). Values are expressed as relative quantities (RQ) obtained from calculating the ratio of CD40 mRNA to an endogenous control and are means \pm SEM.

2-way ANOVA: siRNA effect $F(1, 27) = 0.1046$; $p = 0.7488$, Genotype effect $F(1, 27) = 6.936$; $p = 0.0138$, Interaction effect $F(1, 27) = 0.2324$; $p = 0.6366$

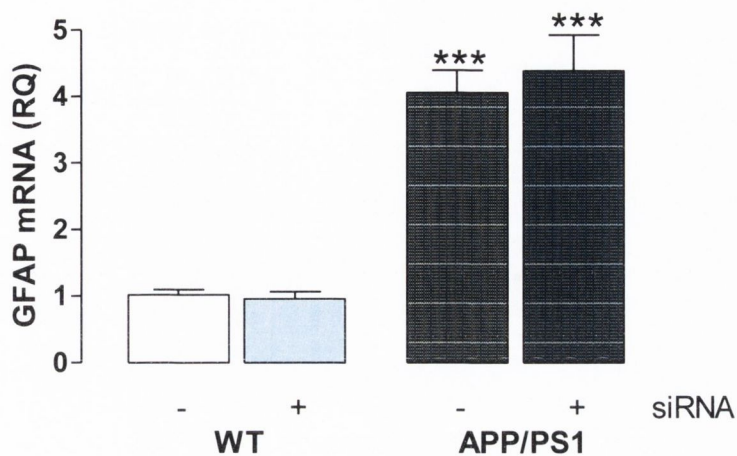


Figure 5.5 Cortical GFAP mRNA expression in WT and APP/PS1 transgenic mice.

Groups of WT and APP/PS1 transgenic mice were injected iv with a control siRNA (400µl; 20µg/mouse) or siRNA targeting claudin 5 and occludin (400µl; 20µg/target/mouse). After 48 hours, mice were sacrificed by decapitation, left cortex dissected free, homogenized and GFAP mRNA expression determined by qPCR. Mean GFAP mRNA expression was increased in cortical tissue prepared from control-treated APP/PS1 mice compared with WT mice (** $p < 0.001$; ANOVA) and in siRNA-treated APP/PS1 mice compared with WT mice (** $p < 0.001$; ANOVA). Values are expressed as relative quantities (RQ) obtained from calculating the ratio of GFAP mRNA to an endogenous control and are means \pm SEM.

2-way ANOVA: siRNA effect $F(1, 27) = 0.07215$; $p = 0.7903$, Genotype effect $F(1, 27) = 88.67$; $p < 0.0001$, Interaction effect $F(1, 27) = 0.4674$; $p = 0.5000$

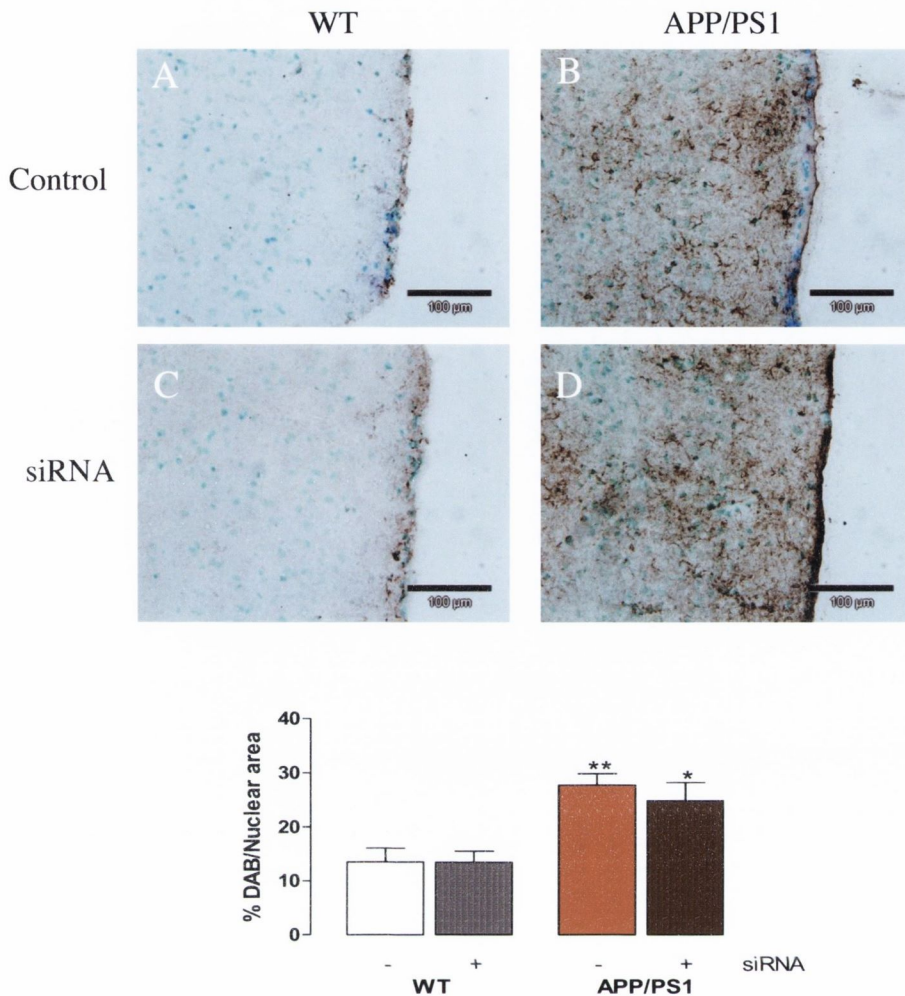


Figure 5.6 GFAP immunoreactivity in the cortex of WT and APP/PS1 mice.

Groups of WT and APP/PS1 mice were injected iv with a control siRNA (400 μl; 20 μg/mouse), or siRNA targeting claudin 5 and occludin (400 μl; 20 μg/target/mouse). There was a marked increase in GFAP positive staining in the cortex of both APP/PS1. (Magnification 40x, scale bar 100 μm).

There was a significant increase in the ratio of DAB/nuclear area in the cortex of control-treated APP/PS1, compared with WT, mice (**p<0.01; ANOVA) and in siRNA-treated APP/PS1, compared with WT, mice (*p<0.05; ANOVA).

2-way ANOVA: siRNA effect F (1, 26) = 0.59; p=0.5996, Genotype effect F (1, 26) = 43.92; p=0.0001, Interaction effect F (1, 26) = 0.53; p=0.62

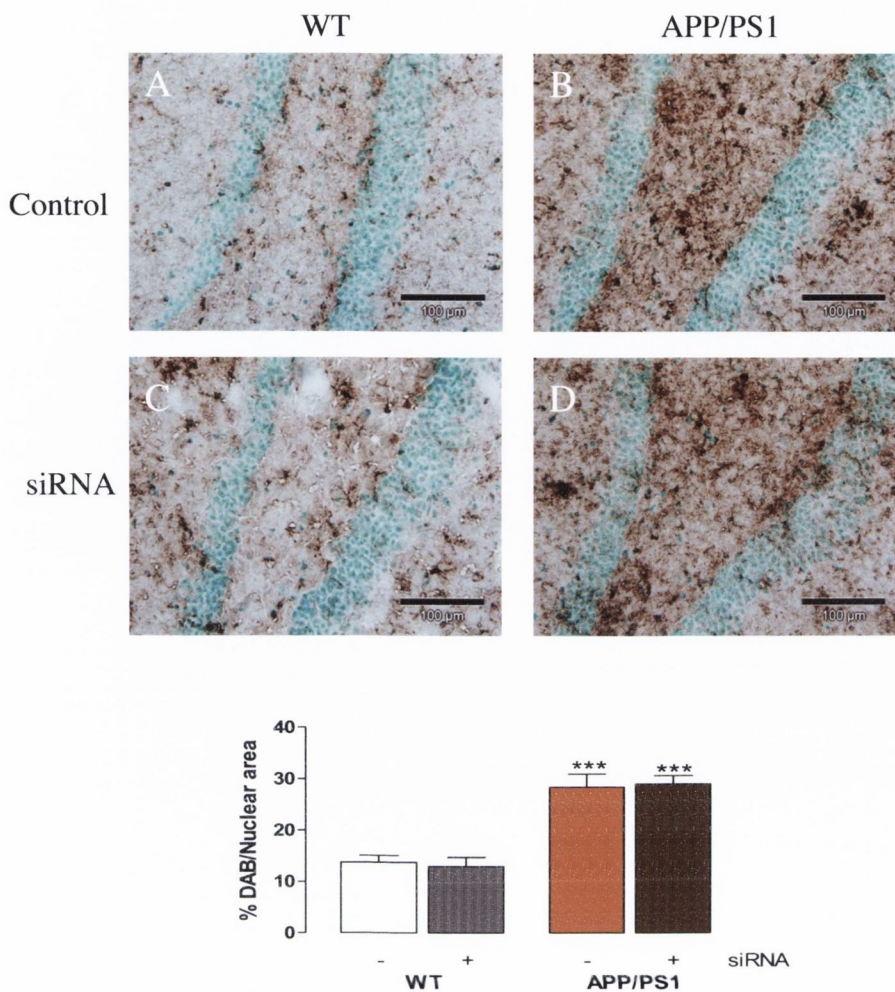


Figure 5.7 GFAP immunoreactivity in the hippocampus of WT and APP/PS1 mice.

Groups of WT and APP/PS1 mice were injected iv with a control siRNA (400 μl; 20 μg/mouse), or siRNA targeting claudin 5 and occludin (400 μl; 20 μg/target/mouse). There was a marked increase in GFAP positive staining in the cortex of both APP/PS1 groups. (Magnification 40x, scale bar 100 μm).

There was a significant increase in the ratio of DAB/nuclear area in the hippocampus of control-treated APP/PS1, compared with WT, mice (** $p < 0.001$; ANOVA) and in siRNA-treated APP/PS1, compared with WT, mice (** $p < 0.001$; ANOVA).

2-way ANOVA: siRNA effect $F(1, 26) = 0.00$; $p = 0.9569$, Genotype effect $F(1, 26) = 67.48$; $p < 0.0001$, Interaction effect $F(1, 26) = 0.13$; $p = 0.7507$

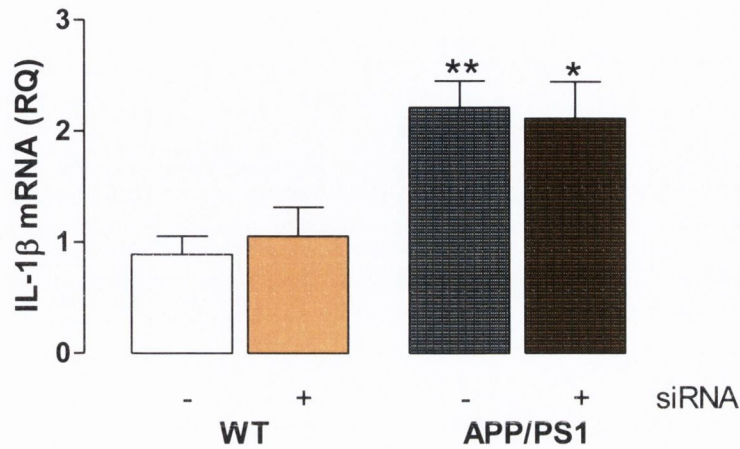


Figure 5.8 Cortical IL-1 β mRNA expression in WT and APP/PS1 transgenic mice.

Groups of WT and APP/PS1 transgenic mice were injected iv with a control siRNA (400 μ l; 20 μ g/mouse) or siRNA targeting claudin 5 and occludin (400 μ l; 20 μ g/target/mouse). After 48 hours, mice were sacrificed by decapitation, left cortex dissected free, homogenized and IL-1 β mRNA expression determined by qPCR. Mean IL-1 β mRNA expression was increased in cortical tissue prepared from control-treated APP/PS1 mice compared with WT mice (** p <0.01; ANOVA) and in siRNA-treated APP/PS1 mice compared with WT mice (* p <0.05; ANOVA). Values are expressed as relative quantities (RQ) obtained from calculating the ratio of IL-1 β mRNA to an endogenous control and are means \pm SEM.

2-way ANOVA: siRNA effect F (1, 25) = 0.0148; p =0.9041, Genotype effect F (1, 25) = 20.45; p <0.0001, Interaction effect F (1, 25) = 0.2463; p =0.6240

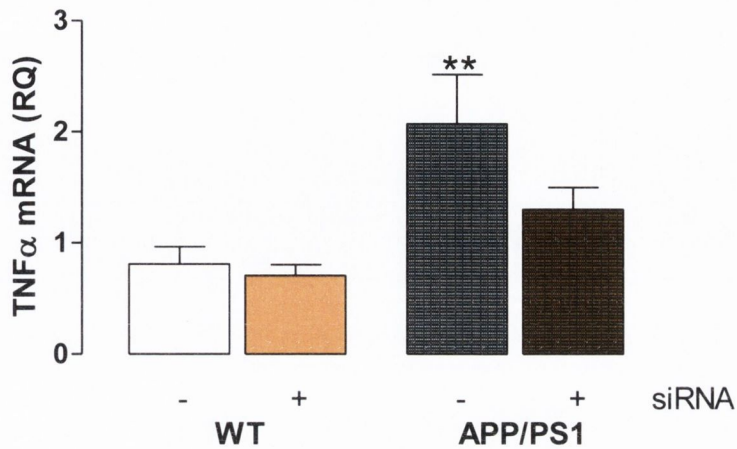


Figure 5.9 Cortical TNF- α mRNA expression in WT and APP/PS1 transgenic mice.

Groups of WT and APP/PS1 transgenic mice were injected iv with a non-target siRNA (400 μ l; 20 μ g/mouse) or siRNA targeting claudin 5 and occludin (400 μ l; 20 μ g/target/mouse). After 48 hours, mice were sacrificed by decapitation, left cortex dissected free, homogenized and TNF α mRNA expression determined by qPCR. Mean TNF- α mRNA expression was increased in cortical tissue prepared from control-treated APP/PS1 mice compared with WT mice (** p <0.01; ANOVA). Values are expressed as relative quantities (RQ) obtained from calculating the ratio of TNF- α mRNA to an endogenous control and are means \pm SEM.

2-way ANOVA: siRNA effect F (1, 25) = 2.877; p =0.1023, Genotype effect F (1, 25) = 9.544; p =0.0049, Interaction effect F (1, 25) = 1.988; p =0.1709

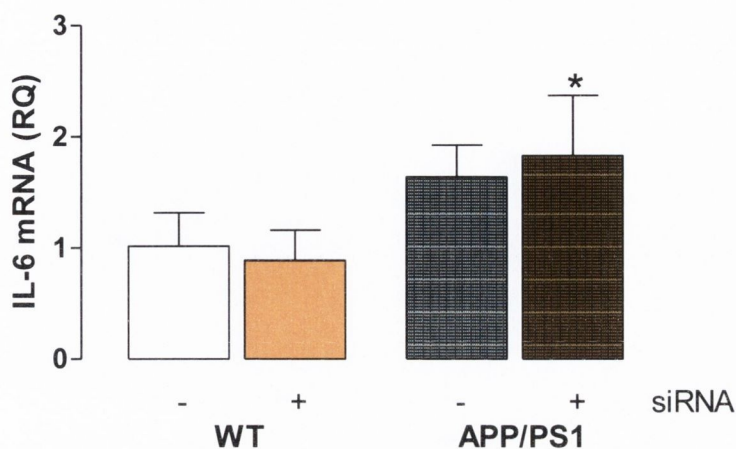


Figure 5.10 Cortical IL-6 mRNA expression in WT and APP/PS1 transgenic mice.

Groups of WT and APP/PS1 transgenic mice were injected iv with a control siRNA (400µl; 20µg/mouse) or siRNA targeting claudin 5 and occludin (400µl; 20µg/target/mouse). After 48 hours, mice were sacrificed by decapitation, left cortex dissected free, homogenized and IL-6 mRNA expression determined by qPCR. Mean IL-6 mRNA expression was increased in cortical tissue prepared from siRNA-treated APP/PS1 mice compared with WT mice (*p<0.05; ANOVA). Values are expressed as relative quantities (RQ) obtained from calculating the ratio of IL-6 mRNA to an endogenous control and are means ± SEM.

2-way ANOVA: siRNA effect F (1, 24) = 0.0617; p=0.8059, Genotype effect F (1, 24) = 7.131; p=0.0134, Interaction effect F (1, 24) = 0.6702; p=0.4210

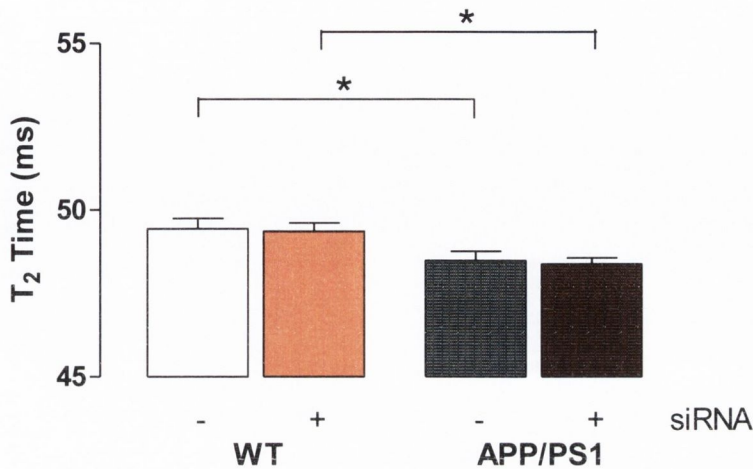


Figure 5.11 T₂ relaxation times in the whole cortex of WT and APP/PS1 mice.

Groups of WT and APP/PS1 transgenic mice received an iv injection of a control siRNA (400µl; 20µg/mouse) or siRNA targeting claudin 5 and occludin (400µl; 20µg/target/mouse). After 48 hours, mice were anaesthetized and prepared for MR scanning. T₂ times were measured bilaterally on the MSME scans, and averaged across 2 adjacent slices. There was a significant decrease in T₂ relaxation times in the whole cortex of control-treated APP/PS1, compared with WT, mice (*p<0.05; ANOVA) and in siRNA treated APP/PS1, compared with WT, mice (*p<0.05; ANOVA). Data are presented as means ± SEM.

2-way ANOVA: siRNA effect F (1, 26) = 0.1125; p=0.7400, Genotype effect F (1, 26) = 14.13; p=0.0009, Interaction effect F (1, 26) = 0.002502; p=0.9605

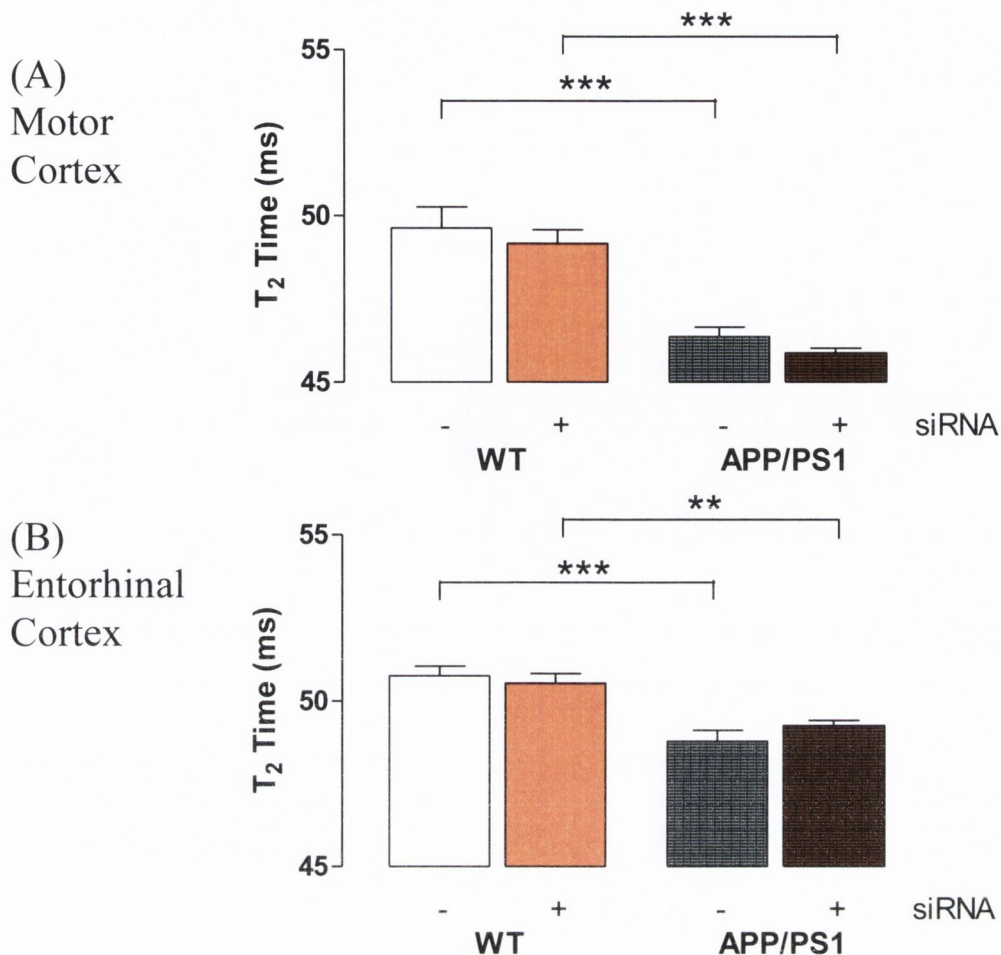


Figure 5.12 T₂ relaxation times in the motor and entorhinal cortex of WT and APP/PS1 mice.

Groups of WT and APP/PS1 transgenic mice received an iv injection of a control siRNA (400µl; 20µg/mouse) or siRNA targeting claudin 5 and occludin (400µl; 20µg/target/mouse). There was a significant decrease in T₂ relaxation times in the motor (A) and entorhinal (B) cortex of control-treated APP/PS1, compared with WT, mice (***p*<0.001; ANOVA) and in siRNA-treated APP/PS1, compared with WT, mice (***p*<0.001; ANOVA) (***p*<0.01; ANOVA). Data are presented as means ± SEM.

(A) 2-way ANOVA: siRNA_{effect} F (1, 26) = 1.511; *p*=0.2300, Genotype_{effect} F (1, 26) = 71.3; *p*<0.0001, Interaction_{effect} F (1, 26) = 0.0008; *p*=0.9768

(B) 2-way ANOVA: siRNA_{effect} F (1, 26) = 0.2302; *p*=0.6558, Genotype_{effect} F (1, 26) = 35.36; *p*<0.0001, Interaction_{effect} F (1, 26) = 1.630; *p*=0.2130

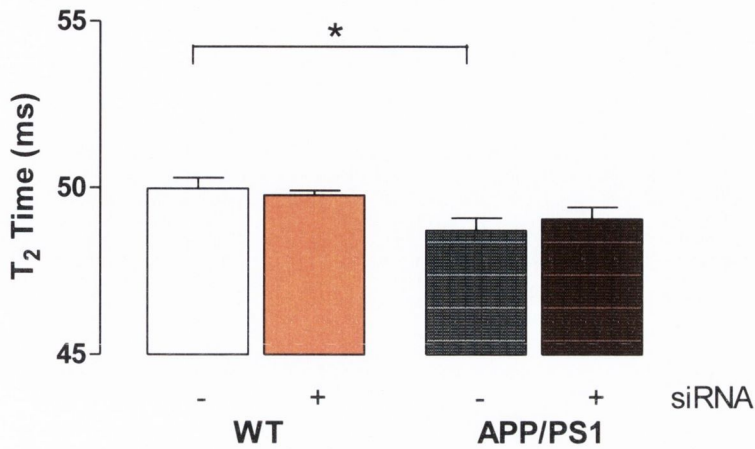


Figure 5.13 T₂ relaxation times in the hippocampus of WT and APP/PS1 mice.

Groups of WT and APP/PS1 transgenic mice received an iv injection of a control siRNA (400µl; 20µg/mouse) or siRNA targeting claudin 5 and occludin (400µl; 20µg/target/mouse). After 48 hours, mice were anaesthetized and prepared for MR scanning. T₂ times were measured bilaterally on the MSME scans, and averaged across 2 adjacent slices. There was a significant decrease in T₂ relaxation times in the hippocampus of control-treated APP/PS1, compared with WT, mice (*p<0.05; ANOVA). Hippocampal T₂ relaxation times were similar in siRNA-treated APP/PS1, and WT, mice. Data are presented as means ± SEM.

2-way ANOVA: siRNA effect F (1, 26) = 0.05807; p=0.8115, Genotype effect F (1, 26) = 9.490; p=0.0048, Interaction effect F (1, 26) = 0.7146; p=0.4056

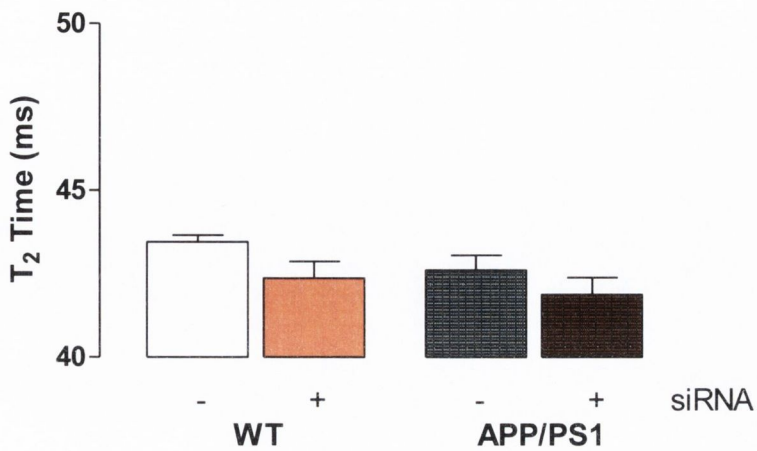


Figure 5.14 T₂ relaxation times in the corpus callosum of WT and APP/PS1 mice.

Groups of WT and APP/PS1 transgenic mice received an iv injection of a control siRNA (400µl; 20µg/mouse) or siRNA targeting claudin 5 and occludin (400µl; 20µg/target/mouse). After 48 hours, mice were anaesthetized and prepared for MR scanning. T₂ times were measured bilaterally on the MSME scans, and averaged across 2 adjacent slices. Mean T₂ relaxation times were similar in the corpus callosum of control, and siRNA-treated APP/PS1, compared with WT, mice. Data are presented as means ± SEM.

2-way ANOVA: siRNA effect F (1, 26) = 4.174; p=0.0513, Genotype effect F (1, 26) = 2.261; p=0.1447, Interaction effect F (1, 26) = 0.1644; p=0.6884

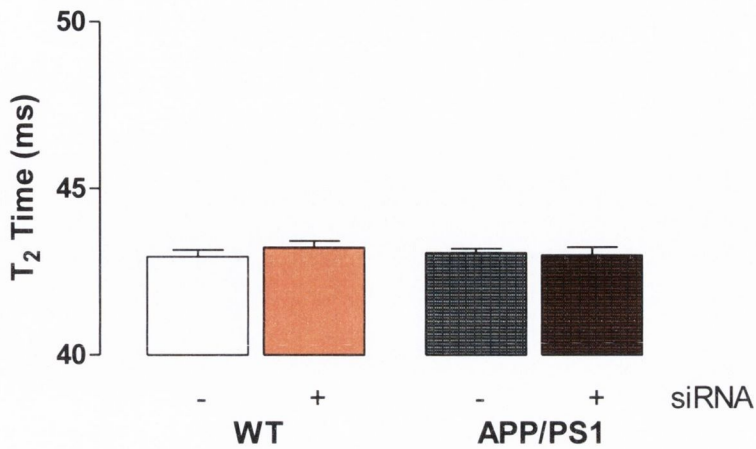


Figure 5.15 T₂ relaxation times in the thalamus of WT and APP/PS1 mice.

Groups of WT and APP/PS1 transgenic mice received an iv injection of a control siRNA (400µl; 20µg/mouse) or siRNA targeting claudin 5 and occludin (400µl; 20µg/target/mouse). After 48 hours, mice were anaesthetized and prepared for MR scanning. T₂ times were measured bilaterally on the MSME scans, and averaged across 2 adjacent slices. Mean T₂ relaxation times were similar in the thalamus of control-, and siRNA-treated APP/PS1, compared with WT, mice. Data are presented as means ± SEM.

2-way ANOVA: siRNA effect F (1, 26) = 0.3199; p=0.5765, Genotype effect F (1, 26) = 0.08339; p=0.7750, Interaction effect F (1, 26) = 0.7368; p=0.3985

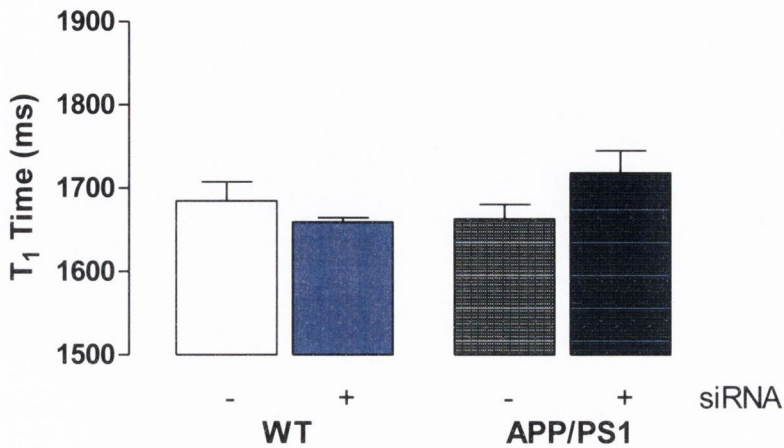


Figure 5.16 T₁ relaxation times in the whole cortex of WT and APP/PS1 mice.

Groups of WT and APP/PS1 transgenic mice received an iv injection of a control siRNA (400µl; 20µg/mouse) or siRNA targeting claudin 5 and occludin (400µl; 20µg/target/mouse). After 48 hours, mice were anaesthetized and prepared for MR scanning. T₁ relaxation times were measured bilaterally on the RARE-VTR scans for each ROI. Mean T₁ relaxation times were similar in control- and siRNA-treated APP/PS1, compared with WT, mice. Data are presented as means ± SEM.

2-way ANOVA: siRNA effect F (1, 25) = 0.5473; p=0.4663, Genotype effect F (1, 25) = 0.8353; p=0.3695, Interaction effect F (1, 25) = 3.907; p=0.0592

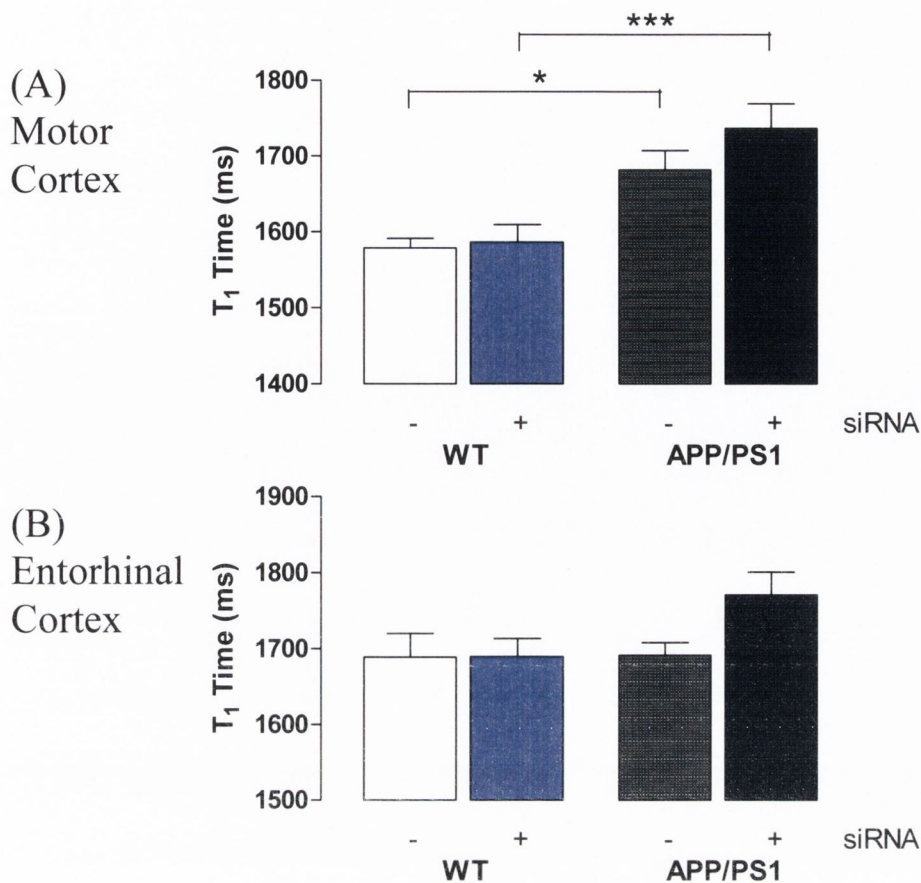


Figure 5.17 T₁ relaxation times in the motor and entorhinal cortex of WT and APP/PS1 transgenic mice.

Groups of WT and APP/PS1 transgenic mice received an iv injection of a control siRNA (400µl; 20µg/mouse) or siRNA targeting claudin 5 and occludin (400µl; 20µg/target/mouse). There was a significant increase in T₁ relaxation times in the motor cortex (A) of control-treated APP/PS1, compared with WT, mice (*p<0.05; ANOVA) and in siRNA-treated APP/PS1, compared with WT, mice (**p<0.001; ANOVA). Mean T₁ values were similar in the entorhinal cortex (B) of control- and siRNA-treated APP/PS1, compared with WT, mice. Data are presented as means ± SEM.

(A) 2-way ANOVA: siRNA effect F (1, 26) = 1.485; p=0.2344, **Genotype effect** F (1, 26) = 24.32; p<0.0001, **Interaction effect** F (1, 26) = 0.8462; p=0.3664

(B) 2-way ANOVA: siRNA effect F (1, 26) = 2.511; p=0.1251, **Genotype effect** F (1, 26) = 2.772; p=0.1079, **Interaction effect** F (1, 26) = 2.423; p=0.1317

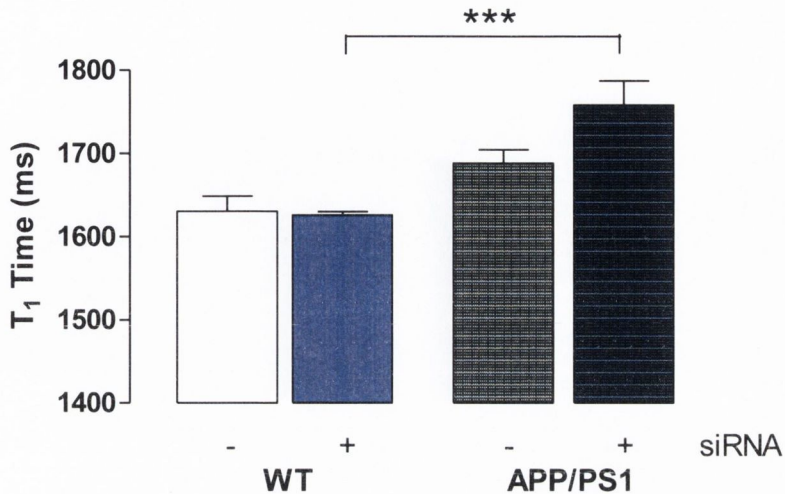


Figure 5.18 T₁ relaxation times in the hippocampus of WT and APP/PS1 mice.

Groups of WT and APP/PS1 transgenic mice received an iv injection of a control siRNA (400µl; 20µg/mouse) or siRNA targeting claudin 5 and occludin (400µl; 20µg/target/mouse). After 48 hours, mice were anaesthetized and prepared for MR scanning. T₁ relaxation times were measured bilaterally on the RARE-VTR scans for each ROI. There was an increase in T₁ relaxation times in siRNA-treated APP/PS1, compared with WT, mice (**p<0.001; ANOVA). Data are presented as means ± SEM.

2-way ANOVA: siRNA effect F (1, 25) = 2.748; p=0.1099, Genotype effect F (1, 25) = 23.99; p<0.0001, Interaction effect F (1, 25) = 3.579; p=0.0702

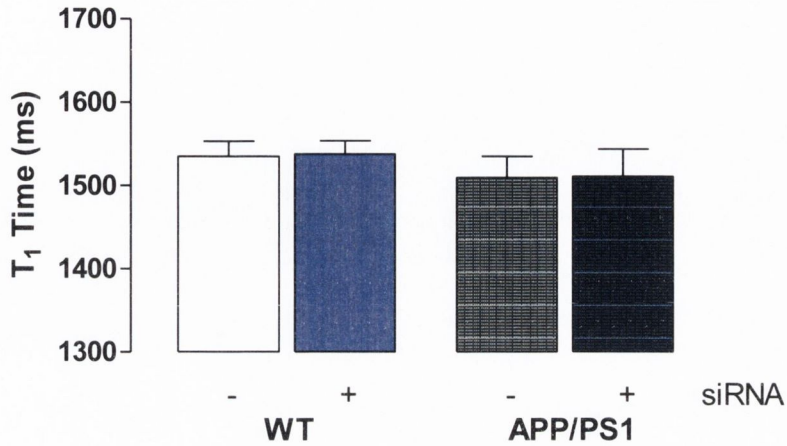


Figure 5.19 T₁ relaxation times in the corpus callosum of WT and APP/PS1 transgenic mice.

Groups of WT and APP/PS1 transgenic mice received an iv injection of a control siRNA (400µl; 20µg/mouse) or siRNA targeting claudin 5 and occludin (400µl; 20µg/target/mouse). After 48 hours, mice were anaesthetized and prepared for MR scanning. T₁ relaxation times were measured bilaterally on the RARE-VTR scans for each ROI. Mean T₁ values were similar in the corpus callosum of control- and siRNA-treated APP/PS1, compared with WT, mice. Data are presented as means ± SEM.

2-way ANOVA: siRNA effect F (1, 26) = 0.0094; p=0.9233, Genotype effect F (1, 26) = 1.146; p=0.2942, Interaction effect F (1, 26) = 0.0008; p=0.9771

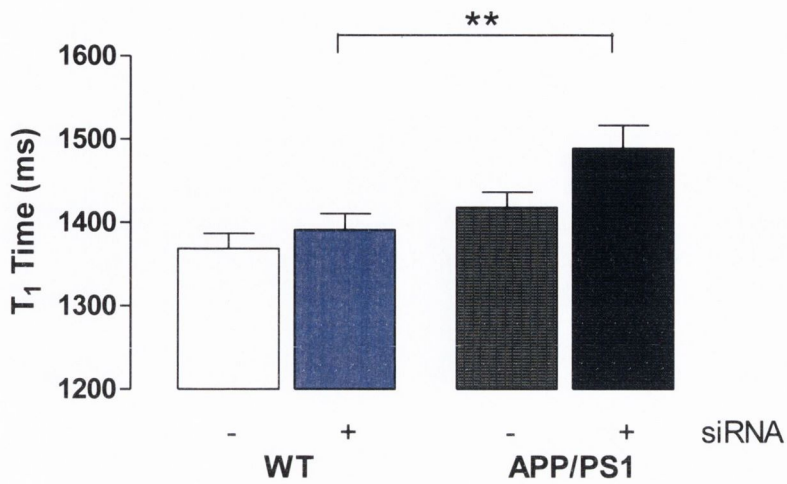


Figure 5.20 T₁ relaxation times in the thalamus of WT and APP/PS1 transgenic mice.

Groups of WT and APP/PS1 transgenic mice received an iv injection of a control siRNA (400µl; 20µg/mouse) or siRNA targeting claudin 5 and occludin (400µl; 20µg/target/mouse). After 48 hours, mice were anaesthetized and prepared for MR scanning. T₁ relaxation times were measured bilaterally on the RARE-VTR scans for each ROI. There was a significant increase in T₁ relaxation times in the thalamus of siRNA-treated APP/PS1, compared with WT, mice (**p<0.01; ANOVA). Data are presented as means ± SEM.

2-way ANOVA: siRNA effect F (1, 26) = 4.832; p=0.0370, Genotype effect F (1, 26) = 11.88; p=0.0019, Interaction effect F (1, 26) = 1.288; p=0.2668

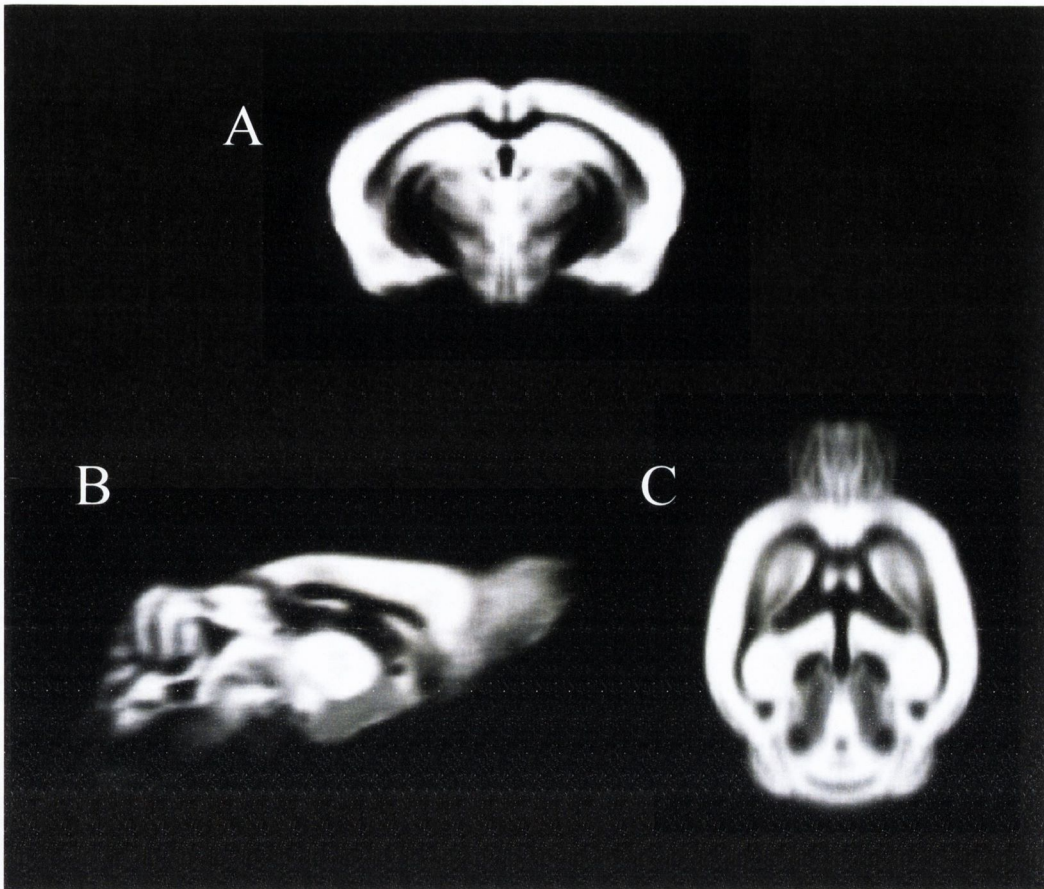


Figure 5.21 The effect of genotype on VBM output

Groups of WT and APP/PS1 mice underwent high-resolution MR scanning at 13-14 months. Anatomic scans were prepared for volumetric analysis by the optimized VBM protocol. Images were spatially registered to a generic C57 template and voxel-wise group comparisons were carried out. The results indicated no significant volumetric differences in APP/PS1 transgenic mice, compared with WT mice. A sample coronal (A), sagittal (B) and axial (C) image from the study template is presented above. Voxel-wise statistics did not reveal significant regions of volumetric difference in APP/PS1 mice.

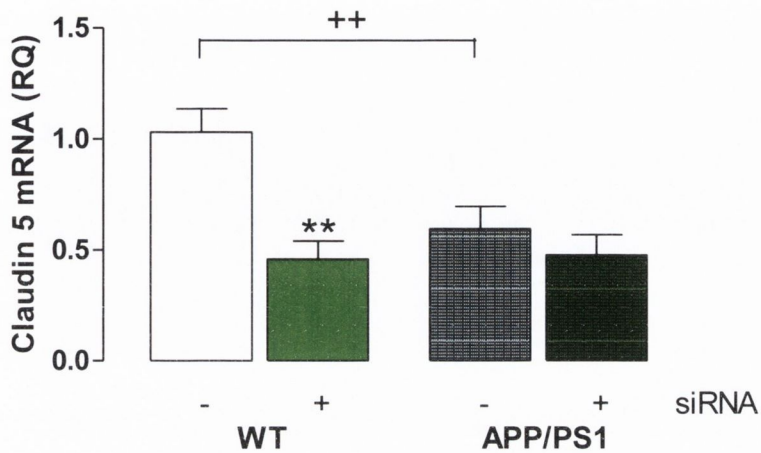


Figure 5.22 The effect of siRNA treatment on cortical claudin 5 mRNA expression in WT and APP/PS1 transgenic mice.

Groups of WT and APP/PS1 transgenic mice were injected iv with a control siRNA (400µl; 20µg/mouse) or siRNA targeting claudin 5 and occludin (400µl; 20µg/target/mouse). After 48 hours, mice were sacrificed by decapitation, left cortex dissected free, homogenized and claudin 5 mRNA expression determined by qPCR. Mean claudin 5 mRNA expression was decreased in cortical tissue prepared from siRNA-treated WT mice (** $p < 0.01$; ANOVA) and in control-treated APP/PS1 mice compared with WT mice (⁺⁺ $p < 0.01$; ANOVA). Treatment with siRNA had no significant effect on claudin 5 expression in APP/PS1 mice. Values are expressed as relative quantities (RQ) obtained from calculating the ratio of claudin 5 mRNA to an endogenous control and are means \pm SEM.

2-way ANOVA: siRNA effect $F(1, 26) = 13.66$; $p = 0.0010$, **Genotype effect** $F(1, 26) = 3.509$; $p = 0.0723$, **Interaction effect** $F(1, 26) = 6.357$; $p = 0.0182$

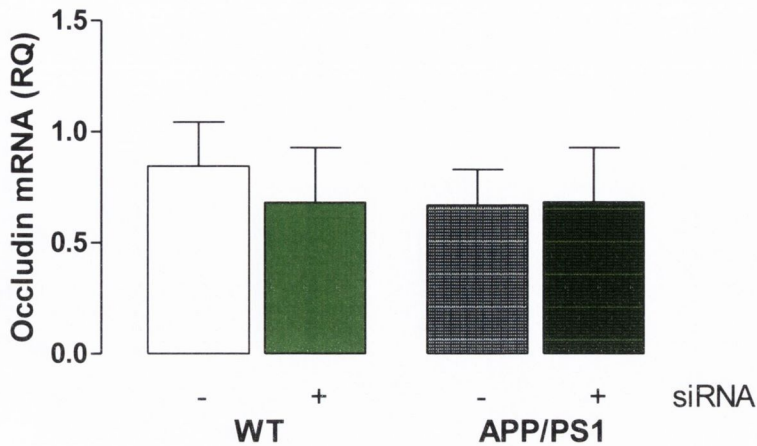


Figure 5.23 The effect of siRNA treatment on cortical occludin mRNA expression in WT and APP/PS1 transgenic mice.

Groups of WT and APP/PS1 transgenic mice were injected iv with a control siRNA (400µl; 20µg/mouse) or siRNA targeting claudin 5 and occludin (400µl; 20µg/target/mouse). After 48 hours, mice were sacrificed by decapitation, left cortex dissected free, homogenized and occludin mRNA expression determined by qPCR. Mean occludin mRNA expression was similar in the cortex of siRNA-treated, compared with control-treated, WT mice. Treatment with siRNA had no effect on cortical occludin mRNA expression in APP/PS1 mice. Values are expressed as relative quantities (RQ) obtained from calculating the ratio of occludin mRNA to an endogenous control and are means ± SEM.

2-way ANOVA: siRNA effect F (1, 22) = 0.1102; p=0.7430, Genotype effect F (1, 22) = 0.1496; p=0.7026, Interaction effect F (1, 22) = 0.1566; p=0.6961

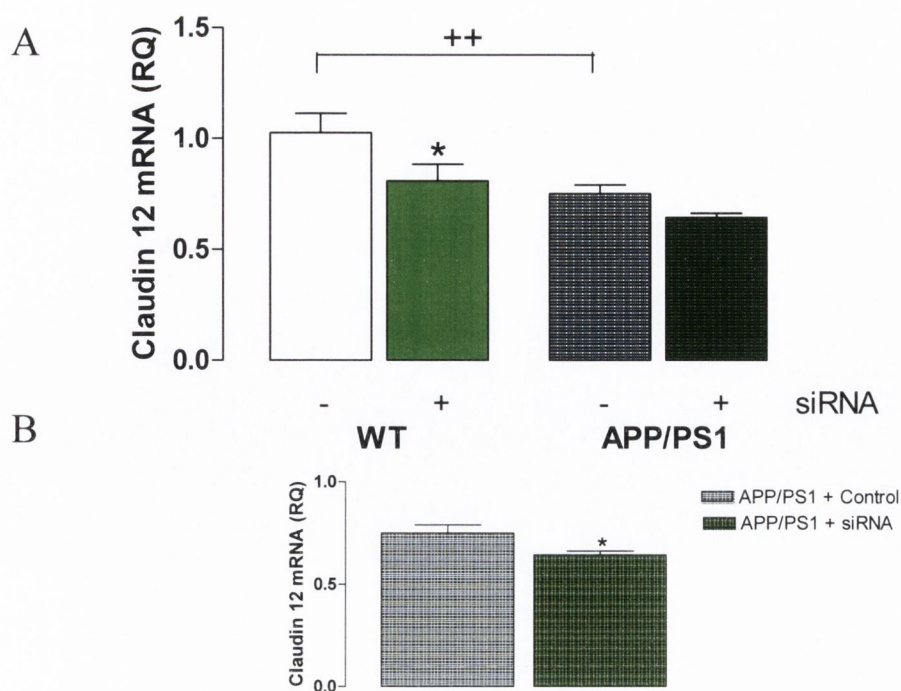


Figure 5.24 The effect of siRNA treatment on cortical claudin 12 mRNA expression in WT and APP/PS1 transgenic mice.

Groups of WT and APP/PS1 transgenic mice were injected iv with a control siRNA (400 μ l; 20 μ g/mouse) or siRNA targeting claudin 5 and occludin (400 μ l; 20 μ g/target/mouse). After 48 hours, mice were sacrificed by decapitation, left cortex dissected free, homogenized and claudin 12 mRNA expression determined by qPCR. Mean claudin 12 mRNA expression was decreased in cortical tissue prepared from siRNA-treated WT mice compared with control-treated WT mice (* p <0.05; ANOVA; Figure A), and in siRNA-treated APP/PS1 mice compared with control-treated APP/PS1 mice (* p <0.05; Student's t-test; Figure B). There was also a decrease in claudin 12 mRNA in control-treated APP/PS1 mice compared with control-treated WT mice (** p <0.01; ANOVA). Values are expressed as relative quantities (RQ) obtained from calculating the ratio of claudin 12 mRNA to an endogenous control and are means \pm SEM.

2-way ANOVA: siRNA effect $F(1, 26) = 7.262$; $p=0.0122$, **Genotype effect** $F(1, 26) = 13.44$; $p=0.0011$, **Interaction effect** $F(1, 26) = 0.8363$; $p=0.3689$

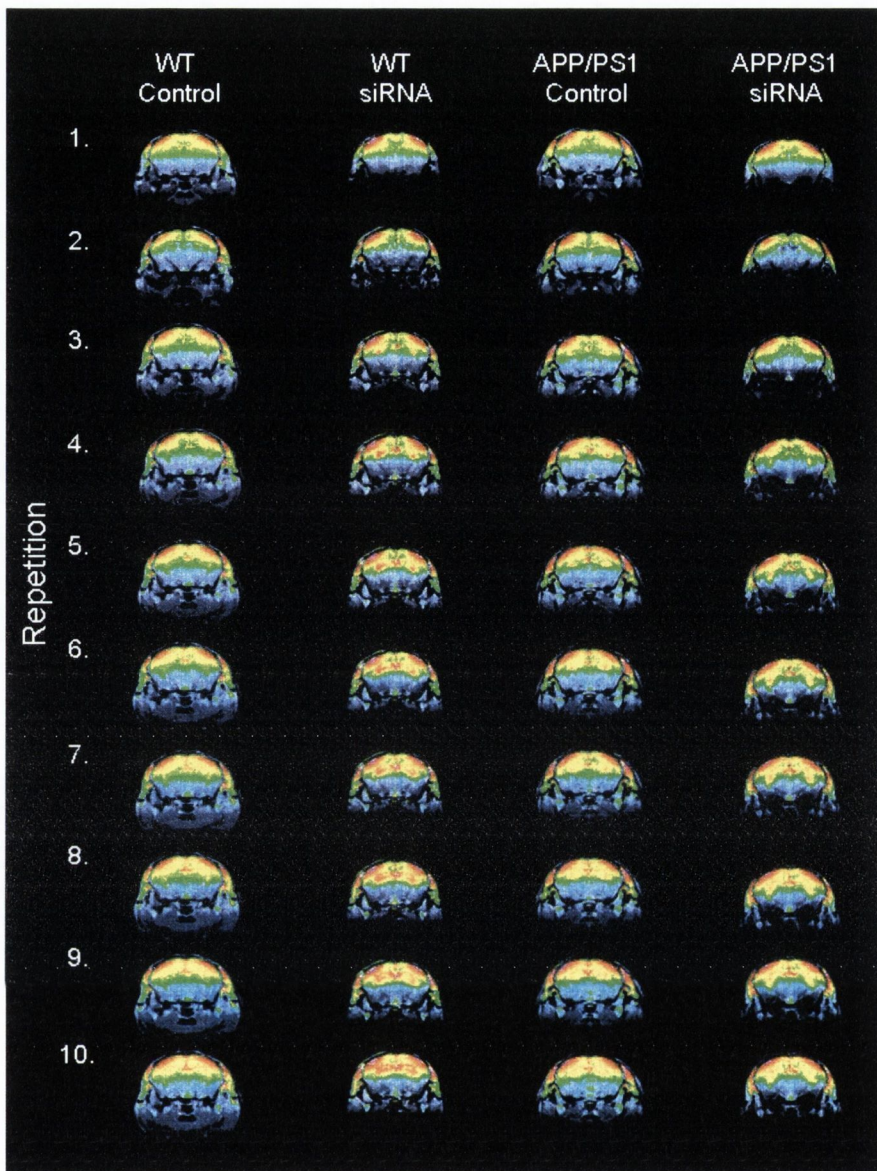


Figure 5.25 Representative contrast MRI data sets from control- and siRNA-treated WT and APP/PS1 mice injected with gadolinium.

Groups of WT and APP/PS1 mice received an iv injection of a control siRNA (400 μ l) or siRNA targeting claudin 5 and occludin (400 μ l; 20 μ g/target/mouse). Mean signal intensity was similar in control-treated WT mice after gadolinium injection (repetitions 3-10), compared with before injection (repetition 1). Mean SI was increased in control-treated APP/PS1 mice, and in siRNA-treated WT and APP/PS1 mice after gadolinium injection, compared with before injection. Increased signal intensity is denoted by a change in voxel colour intensities from yellow to red.

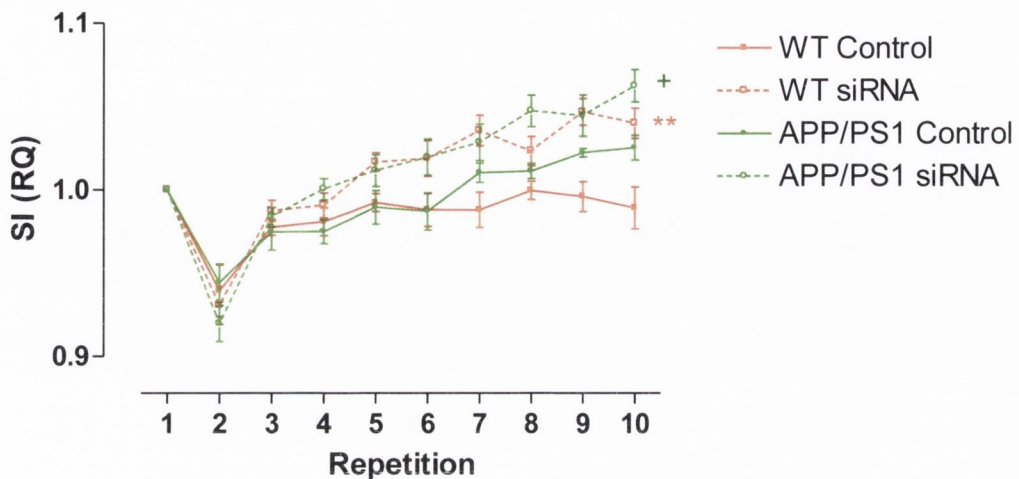


Figure 5.26 Contrast-enhanced SI changes in the left motor cortex of control and siRNA-treated WT and APP/PS1 mice.

Groups of WT and APP/PS1 mice were injected iv with a control siRNA (400 μ l; 20 μ g/mouse), or siRNA targeting claudin 5 and occludin (400 μ l; 20 μ g/target/mouse). After 48 hours, mice were prepared for gadolinium-enhanced contrast imaging by tail vein cannulation. Gadolinium (200 μ l) was injected at the commencement of repetition 2. Mean SI was increased in the left motor cortex of siRNA-treated, compared with control-treated, WT mice (** p <0.01; ANOVA) and APP/PS1 mice (⁺ p <0.05; ANOVA). Mean SI was similar in control-treated APP/PS1, and WT, mice. Values are presented as a proportion of the pre-contrast measure (repetition 1) and are means \pm SEM.

2-way ANOVA: siRNA_{effect} F (1, 20) = 24.53; p <0.0001, Genotype_{effect} F (1, 20) = 5.461; p =0.0300, Interaction_{effect} F (1, 20) = 1.038; p =0.3204

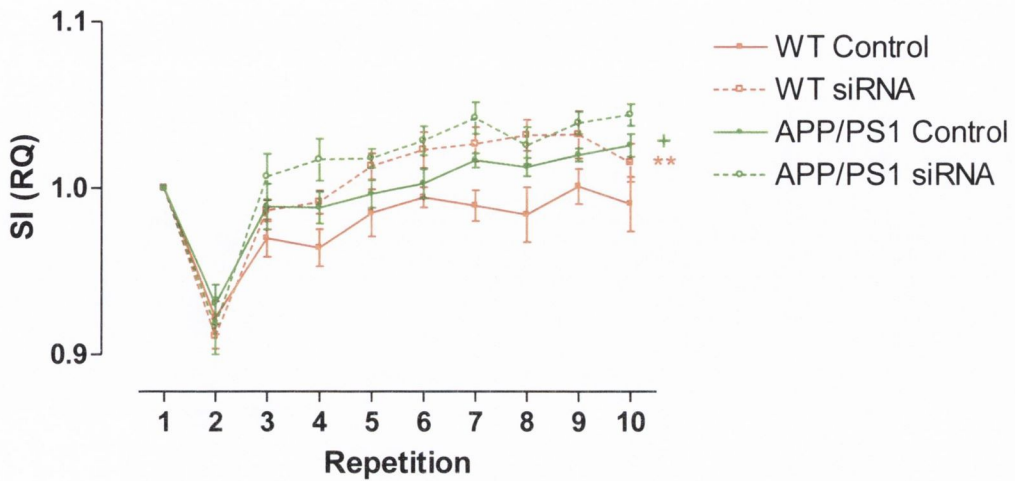


Figure 5.27 Contrast-enhanced SI changes in the left somatosensory cortex of control and siRNA-treated WT and APP/PS1 mice.

Groups of WT and APP/PS1 mice were injected iv with a control siRNA (400µl; 20µg/mouse), or siRNA targeting claudin 5 and occludin (400µl; 20µg/target/mouse). After 48 hours, mice were prepared for gadolinium-enhanced contrast imaging by tail vein cannulation. Gadolinium (200µl) was injected at the commencement of repetition 2. Mean SI was increased in the left somatosensory cortex of siRNA-treated, compared with control-treated, WT mice (**p<0.01; ANOVA), and in control-treated APP/PS1 mice, compared with WT mice (+p<0.05; ANOVA). Mean SI was similar in siRNA-treated APP/PS1, and control-treated, mice. Values are presented as a proportion of the pre-contrast measure and are means ± SEM.

2-way ANOVA: siRNA_{effect} F (1, 20) = 12.77; p=0.0019, Genotype_{effect} F (1, 20) = 6.661; p=0.0178, Interaction_{effect} F (1, 20) = 1.152; p=0.2959

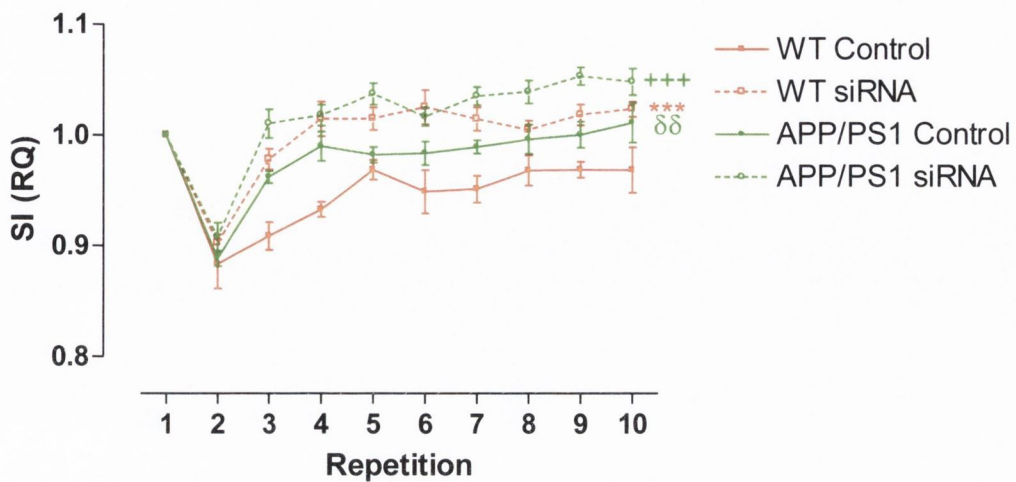


Figure 5.28 Contrast-enhanced SI changes in the left entorhinal cortex of control and siRNA-treated WT and APP/PS1 mice.

Groups of WT and APP/PS1 mice were injected iv with a control siRNA (400µl; 20µg/mouse), or siRNA targeting claudin 5 and occludin (400µl; 20µg/target/mouse). After 48 hours, mice were prepared for gadolinium-enhanced contrast imaging by tail vein cannulation. Gadolinium (200µl) was injected at the commencement of repetition 2. Mean SI was increased in the left entorhinal cortex of siRNA-treated, compared with control-treated, WT mice (** $p < 0.001$; ANOVA) and APP/PS1 mice (+++ $p < 0.001$; ANOVA) and in control-treated APP/PS1 mice, compared with WT mice ($\delta\delta p < 0.01$; ANOVA). Values are presented as a proportion of the pre-contrast measure and are means \pm SEM.

2-way ANOVA: siRNA_{effect} F (1, 20) = 42.44; $p < 0.0001$, Genotype_{effect} F (1, 20) = 17.15; $p = 0.0005$, Interaction_{effect} F (1, 20) = 0.3204; $p = 0.5777$

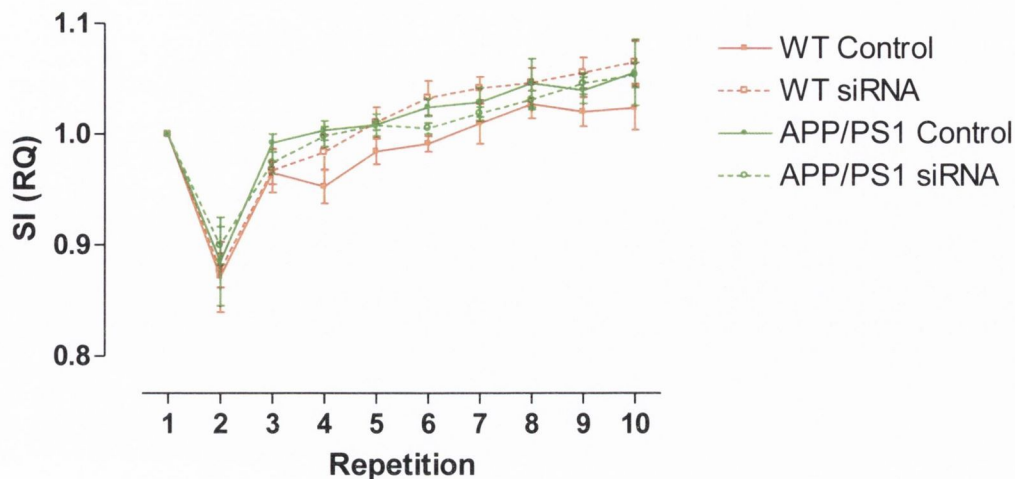


Figure 5.29 Contrast-enhanced SI changes in the left dentate gyrus of control and siRNA-treated WT and APP/PS1 mice.

Groups of WT and APP/PS1 mice were injected iv with a control siRNA (400µl; 20µg/mouse), or siRNA targeting claudin 5 and occludin (400µl; 20µg/target/mouse). After 48 hours, mice were prepared for gadolinium-enhanced contrast imaging by tail vein cannulation. Gadolinium (200µl) was injected at the commencement of repetition 2. Mean SI was similar in siRNA-treated, and control-treated, WT and APP/PS1 mice, and in control-treated APP/PS1 mice, compared with WT mice. Values are presented as a proportion of the pre-contrast measure and are means ± SEM.

2-way ANOVA: siRNA_{effect} F (1, 20) = 0.5466; p=0.4683, Genotype_{effect} F (1, 20) = 0.694; p=0.4147, Interaction_{effect} F (1, 20) = 1.526; p=0.2310

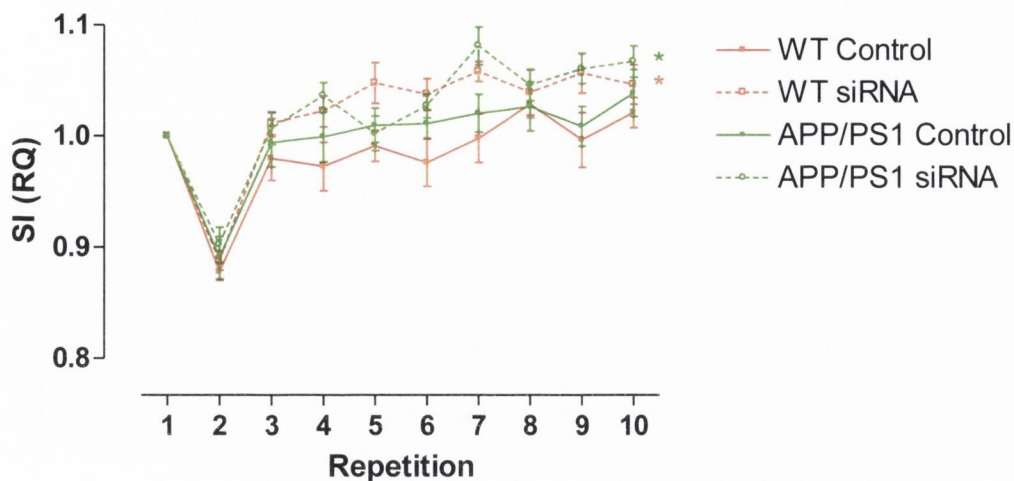


Figure 5.30 Contrast-enhanced SI changes in the left ventrolateral thalamus of control-and siRNA-treated WT and APP/PS1 mice.

Groups of WT and APP/PS1 mice were injected iv with a control siRNA (400 μ l; 20 μ g/mouse), or siRNA targeting claudin 5 and occludin (400 μ l; 20 μ g/target/mouse). After 48 hours, mice were prepared for gadolinium-enhanced contrast imaging by tail vein cannulation. Gadolinium (200 μ l) was injected at the commencement of repetition 2. Mean SI was increased in siRNA-treated, compared with control-treated, WT mice (* p <0.05; ANOVA) and APP/PS1 mice (* p <0.05; ANOVA). Mean SI was similar in control-treated APP/PS1 mice and WT mice. Values are presented as a proportion of the pre-contrast measure and are means \pm SEM.

2-way ANOVA: siRNA_{effect} F (1, 20) = 14.95; p =0.001, Genotype_{effect} F (1, 20) = 1.715; p =0.2052, Interaction_{effect} F (1, 20) = 0.0032; p =0.9553

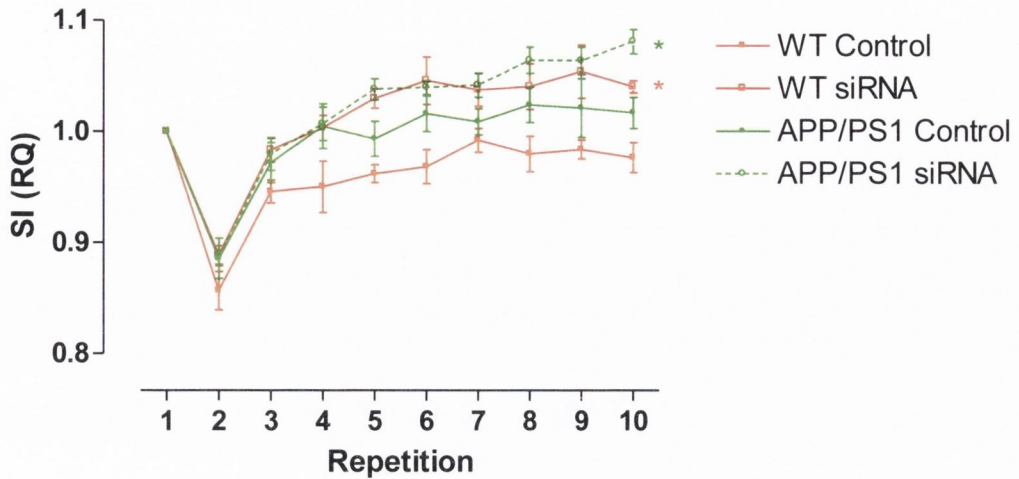


Figure 5.31 Contrast-enhanced SI changes in the left cerebellar nucleus of control- and siRNA-treated WT and APP/PS1 mice.

Groups of WT and APP/PS1 mice were injected iv with a control siRNA (400 μ l; 20 μ g/mouse), or siRNA targeting claudin 5 and occludin (400 μ l; 20 μ g/target/mouse). After 48 hours, mice were prepared for gadolinium-enhanced contrast imaging by tail vein cannulation. Gadolinium (200 μ l) was injected at the commencement of repetition 2. Mean SI was increased in siRNA-treated, compared with control-treated, WT mice (* p <0.05; ANOVA) and APP/PS1 mice (* p <0.05; ANOVA). Mean SI was similar in control-treated APP/PS1 mice and WT mice. Values are presented as a proportion of the pre-contrast measure and are means \pm SEM.

2-way ANOVA: siRNA_{effect} F (1, 20) = 15.53; p =0.0008, Genotype_{effect} F (1, 20) = 4.257; p =0.0523, Interaction_{effect} F (1, 20) = 0.3185; p =0.5788

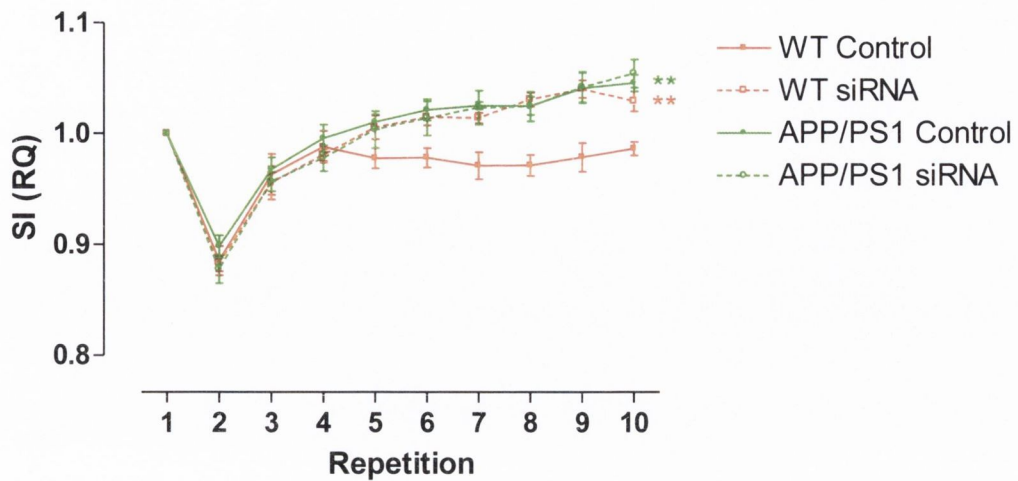


Figure 5.32 Contrast-enhanced SI changes in the left frontal association cortex of control- and siRNA-treated WT and APP/PS1 mice.

Groups of WT and APP/PS1 mice were injected iv with a control siRNA (400 μ l; 20 μ g/mouse), or siRNA targeting claudin 5 and occludin (400 μ l; 20 μ g/target/mouse). After 48 hours, mice were prepared for gadolinium-enhanced contrast imaging by tail vein cannulation. Gadolinium (200 μ l) was injected at the commencement of repetition 2. Mean SI was increased in siRNA-treated, compared with control-treated, WT mice (** p <0.01; ANOVA). Mean SI was also increased in control-treated APP/PS1 mice, compared with WT mice (** p <0.01; ANOVA). Values are presented as a proportion of the pre-contrast measure and are means \pm SEM.

2-way ANOVA: siRNA_{effect} F (1, 20) = 7.826; p =0.0111, Genotype_{effect} F (1, 20) = 11.65; p =0.0028, Interaction_{effect} F (1, 20) = 6.829; p =0.0166

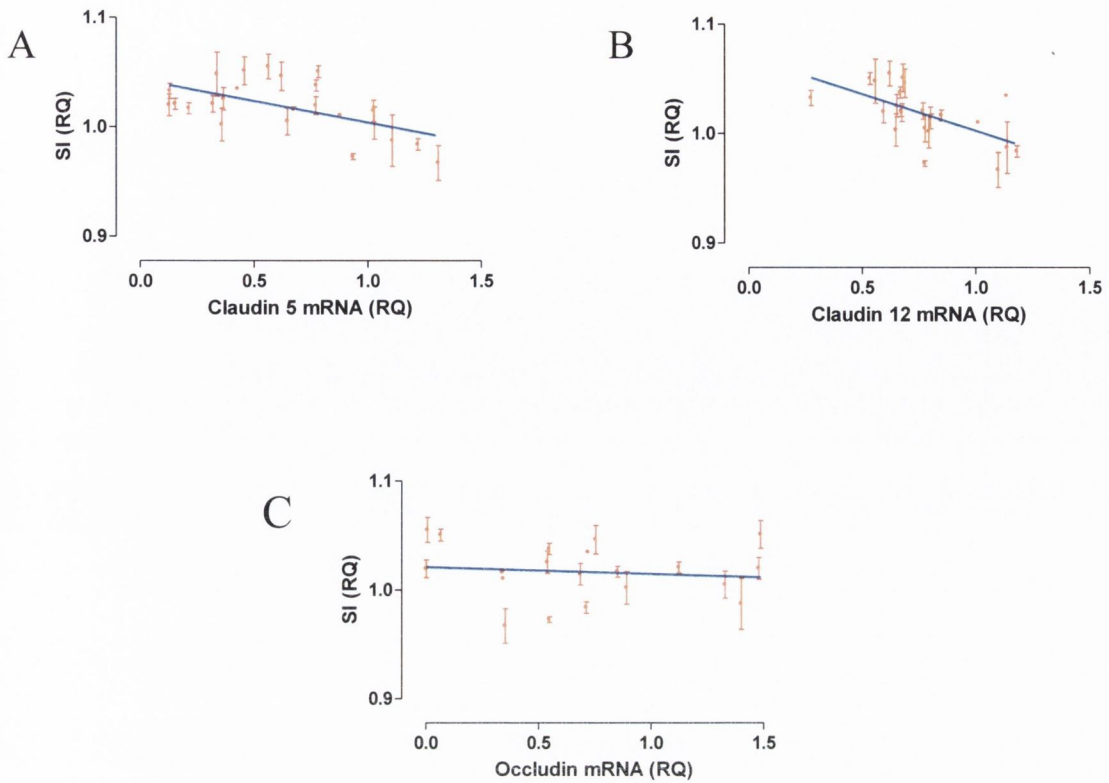


Figure 5.33 Tight junction expression and contrast MRI SI levels.

Groups of WT and APP/PS1 transgenic mice received an iv injection of (400 μ l; 20 μ g/mouse), or siRNA targeting claudin 5 and occludin (400 μ l; 20 μ g/target/mouse). After 48 hours, contrast analysis was carried out on ROIs in the cortex. Mice were sacrificed by decapitation, right cortex dissected free, homogenized and claudins 5, 12 and occludin mRNA expression determined by qPCR. There were moderate and significant negative correlations between cortical SI values and the associated mRNA expression of claudins 5 (A) and 12 (B) respectively but not occludin (C). Values are presented as means \pm SEM.

(A) SI and claudin 5 mRNA: Pearson $r = -0.571$, $p=0.0036$; $n=24$

(B) SI and claudin 12 mRNA: Pearson $r = -0.5985$, $p=0.002$; $n=24$

(C) SI and occludin mRNA: Pearson $r = -0.114$, $p>0.05$; $n=20$

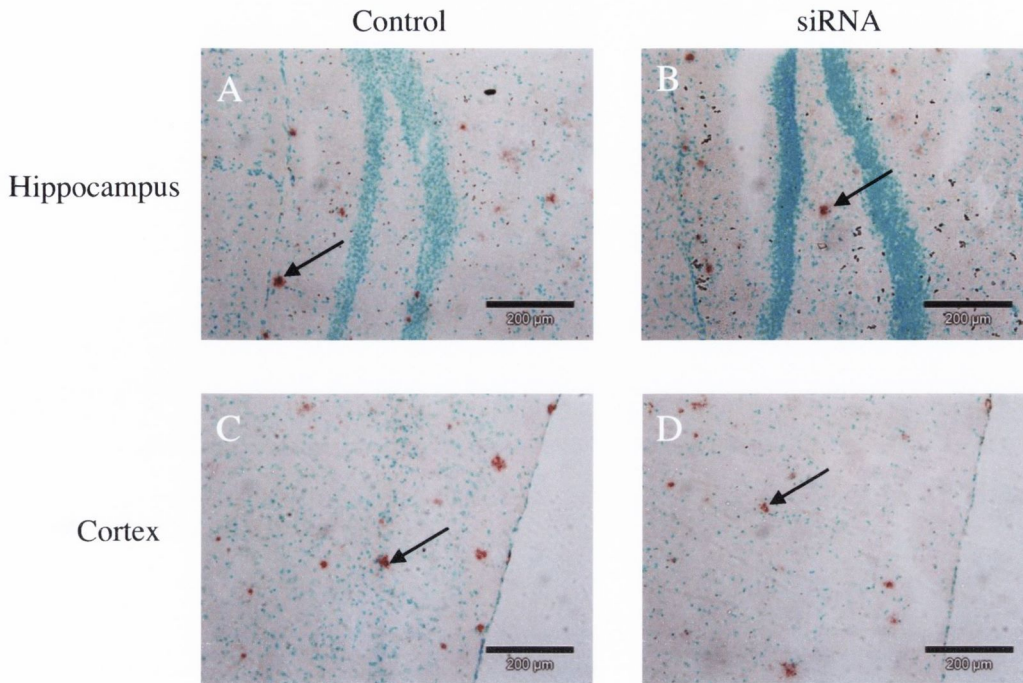


Figure 5.34 Congo Red staining confirms the presence of A β plaques in the brains of APP/PS1 mice.

Groups of WT and APP/PS1 mice were injected iv with a control siRNA (400 μ l; 20 μ g/mouse), or siRNA targeting claudin 5 and occludin (400 μ l; 20 μ g/target/mouse). Mice were sacrificed by decapitation, brain tissue sliced (10 μ m thickness) and prepared for immunohistochemical staining of amyloid beta plaques by the Congo Red method. Images presented here confirm the presence of A β plaques in the hippocampus (A, B) and cortex (C, D) of control (A, C) and siRNA-treated (B, D) APP/PS1 mice. No plaques were observed in either WT groups (data not shown). (Magnification 20x, scale bar 200 μ m).

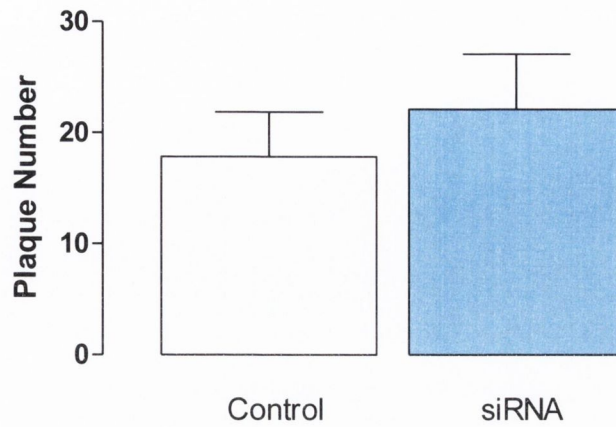


Figure 5.35 Plaque count in siRNA-treated APP/PS1 mice.

Groups of WT and APP/PS1 mice were injected iv with a non-target siRNA (400 μ l; 20 μ g/mouse), or siRNA targeting claudin 5 and occludin (400 μ l; 20 μ g/target/mouse). Brain tissue was sliced and prepared for immunohistochemical staining of A β plaques by the Congo Red method. Plaques were counted in 6 slices under the same light conditions and averaged per animal. Plaque count was similar in control-treated APP/PS1, compared with siRNA-treated, mice. Data are presented as means \pm SEM.

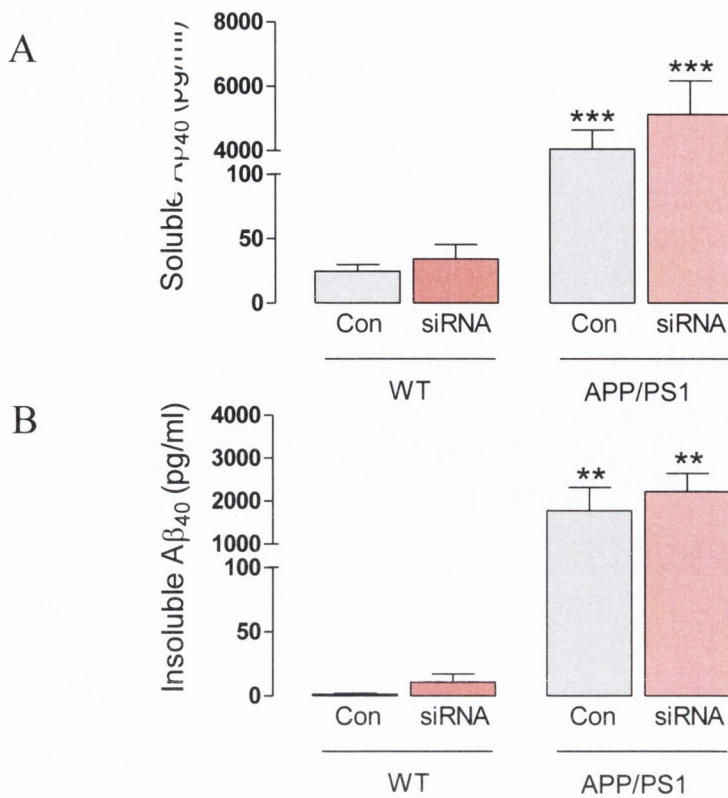


Figure 5.36 Cortical soluble and insoluble Aβ₄₀ expression in control- and siRNA-treated WT and APP/PS1 mice.

Groups of WT and APP/PS1 transgenic mice received an iv injection of control siRNA (400μl; 20μg/mouse), or siRNA targeting claudin 5 and occludin (400μl; 20μg/target/mouse). After 48 hours, mice were sacrificed by decapitation and concentrations of soluble and insoluble Aβ₄₀ measured in cortical tissue by multi-spot ELISA. There were significant increases in the concentrations of soluble and insoluble Aβ₄₀ in cortical tissue prepared from control- and siRNA-treated APP/PS1 mice compared with WT mice. Values are presented as means ± SEM.

(A) 2-way ANOVA siRNA_{effect} F(1, 26) = 0.7184; p=0.4044, Genotype_{effect} F(1, 26) = 50.66; p<0.0001, Interaction_{effect} F(1, 26) = 0.6933; p=0.4126

(B) 2-way ANOVA siRNA_{effect} F(1, 26) = 0.3435; p=0.5628, Genotype_{effect} F(1, 26) = 27.05; p<0.0001, Interaction_{effect} F(1, 26) = 0.322; p=0.5753

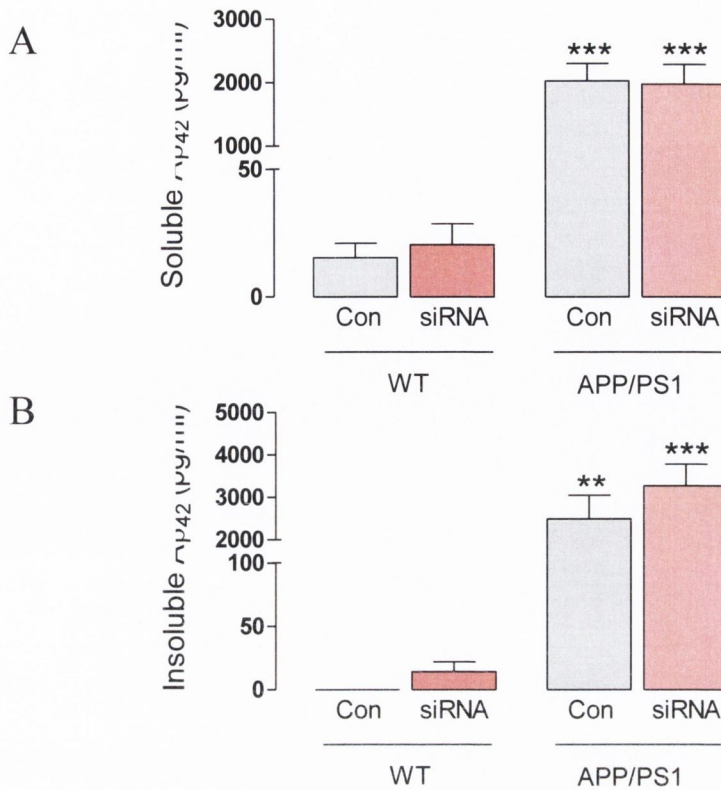


Figure 5.37 Cortical soluble and insoluble $A\beta_{42}$ expression in control- and siRNA-treated WT and APP/PS1 mice.

Groups of WT and APP/PS1 transgenic mice received an iv injection of control siRNA (400 μ l; 20 μ g/mouse), or siRNA targeting claudin 5 and occludin (400 μ l; 20 μ g/target/mouse). After 48 hours, mice were sacrificed by decapitation and concentrations of soluble and insoluble $A\beta_{42}$ measured in cortical tissue by multi-spot ELISA. There were significant increases in concentrations of both forms of $A\beta_{42}$ in tissue prepared from control- and siRNA-treated APP/PS1 mice, compared with WT mice. Values are presented as means \pm SEM.

(A) 2-way ANOVA $siRNA_{effect}$ $F(1, 27) = 0.0112$; $p=0.9162$, $Genotype_{effect}$ $F(1, 27) = 75.29$; $p<0.0001$, $Interaction_{effect}$ $F(1, 27) = 0.0164$; $p=0.8988$

(B) 2-way ANOVA $siRNA_{effect}$ $F(1, 26) = 0.8091$; $p=0.3766$, $Genotype_{effect}$ $F(1, 26) = 42.74$; $p<0.0001$, $Interaction_{effect}$ $F(1, 26) = 0.7513$; $p=0.3940$

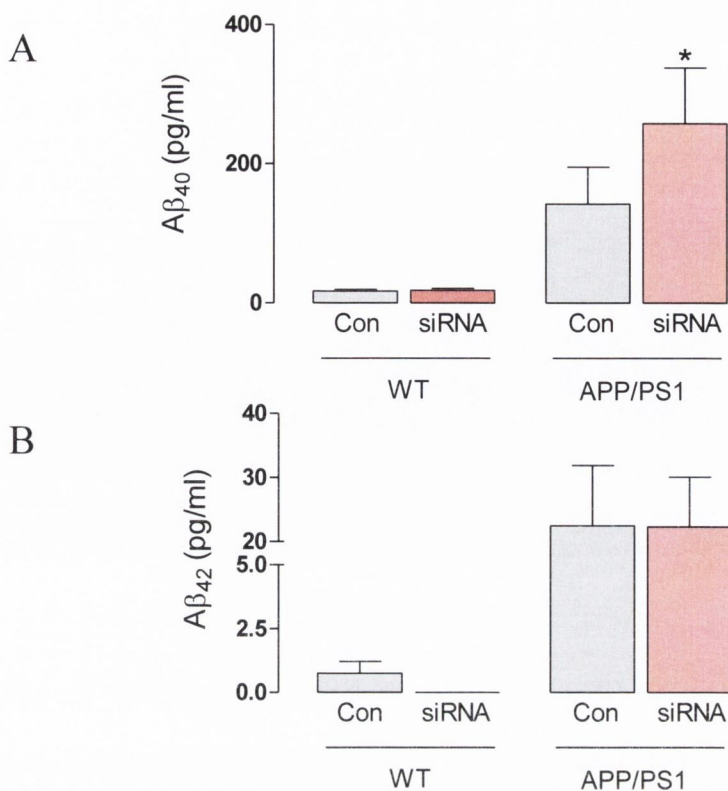


Figure 5.38 Aβ₄₀ and Aβ₄₂ expression in blood serum of control- and siRNA-treated WT and APP/PS1 mice.

Groups of WT and APP/PS1 transgenic mice received an iv injection of control siRNA (400μl; 20μg/mouse), or siRNA targeting claudin 5 and occludin (400μl; 20μg/target/mouse). After 48 hours, mice were sacrificed, serum taken, and concentrations of Aβ₄₀ and Aβ₄₂ measured by multi-spot ELISA. There was a significant increase in Aβ₄₀ in siRNA-treated APP/PS1, compared with WT, mice. Mean Aβ₄₂ concentration was similar in control- and siRNA-treated WT and APP/PS1 mice. Values are presented as means ± SEM.

(A) 2-way ANOVA siRNA_{effect} F(1, 18) = 0.9088; p=0.3531, Genotype_{effect} F(1, 18) = 8.933; p=0.0079, Interaction_{effect} F(1, 18) = 0.8777; p=0.3612

(B) 2-way ANOVA siRNA_{effect} F(1, 21) = 0.0045; p=0.9467, Genotype_{effect} F(1, 21) = 10.01; p=0.0047, Interaction_{effect} F(1, 21) = 0.0016; p=0.9677

5.4 Discussion

The first aim of this study was to assess the neuroinflammatory changes that occur in the APP/PS1 mouse model of AD. This study demonstrated that at 13-14 months, plaque deposition was widespread in cortical and hippocampal sections prepared from APP/PS1 mice. In parallel with this finding, several markers of neuroinflammation were significantly upregulated in brain tissue of transgenic mice, compared with WT mice. Assessment of WT and APP/PS1 mice by MRI indicated that T_2 relaxation times were significantly decreased in grey matter regions of APP/PS1, compared with WT, mice. Conversely, T_1 relaxation times were significantly increased in the same regions of transgenic AD mice.

Congo red immunohistochemistry revealed, unsurprisingly, that $A\beta$ plaque deposition was widespread in cortical and hippocampal sections in APP/PS1 mouse model of AD. Transgenic mice in this particular model of AD are known to develop $A\beta$ plaques from 9 months of age (Jankowsky *et al.*, 2004). There is accumulating evidence that suggests that an increase in levels of $A\beta$ in the brain is central to the pathogenesis of AD. More than 130 known mutations of the PS1 gene result in familial AD (FAD). These mutations increase the deposition and expression of $A\beta_{42}$, as do mutations in the APP gene, which in turn have been significantly correlated with age of disease onset (Duering *et al.*, 2005). The $A\beta$ peptide is also found at low concentrations as a normal constituent of biological fluids, where it is known as soluble $A\beta$ (Haass *et al.*, 1992). Soluble $A\beta$ is elevated in the AD brain, and the elevation appears to precede $A\beta$ plaque formation, which has been reported to start in the hippocampal structure (Wirhns *et al.*, 2001).

Microglial activation, which is assessed by PCR and immunostaining for CD11b, revealed a marked up-regulation in sections prepared from APP/PS1, compared with WT, mice. There was a two-fold increase in CD11b mRNA expression in cortical tissue from APP/PS1, compared with WT, mice and this was paralleled by a marked and significant up-regulation of CD11b immunostaining in cortical and hippocampal sections. These findings are consistent with numerous reports in the literature which have indicated an increased neuroinflammatory profile in mouse models of AD.

According to the amyloid cascade hypothesis proposed by Hardy and Higgins (1992), $A\beta_{42}$ accumulation and deposition as diffuse plaques leads to the activation of

both microglia and astrocytes, consequently leading to synaptic and neuritic injury (Hardy & Higgins, 1992). Critically, expression of CD11b, which is a cell surface marker of activated microglia, has been shown to correlate with severity of microglial activation (Roy *et al.*, 2008). Interestingly, non-steroidal anti-inflammatory drugs (NSAIDs) aimed at treating AD are more likely primed to suppress microglial activation, rather than the formation of senile plaques or neurofibrillary tangles (Mackenzie & Munoz, 1998).

Unlike CD11b, CD40 expression was significantly decreased in the cortex of APP/PS1 mice. It has previously been shown that ligation of CD40 by CD154 significantly decreases phagocytosis of A β by microglia (Townsend *et al.*, 2005), as well as inducing an APC phenotype in microglia (von Bernhardt *et al.*, 2009). A β peptides have been shown to activate microglia through the CD40 pathway, an effect that is attenuated in APP transgenic mice that have a deficient CD40 gene (Tan *et al.*, 1999). Several studies have shown that a reduction in CD40L or CD40 mitigates amyloid deposition and microgliosis in mouse models of AD (Laporte *et al.*, 2008). Taken together, these results suggest an increased phagocytic and decreased APC phenotype in APP/PS1 transgenic mice.

Results from this study indicated that mRNA expression of the pro-inflammatory cytokines IL-1 β , TNF- α and IL-6 were significantly up-regulated in cortical tissue prepared from APP/PS1 mice. In support of these results, numerous reports have suggested an increase in pro-inflammatory cytokine release associated with an A β pathology (Lukiw & Bazan, 2000), suggesting that the AD-affected brain may be in a chronic state of microglia-mediated neuroinflammation. The role of IL-1 β in the AD brain is particularly interesting, and is the focus of increased attention among researchers. In AD, neuronal injury or insults like A β deposition may trigger a self-propagating cytokine cycle, which, when induced, initiates a vicious feedback loop of continuing IL-1 β elevation promoting further neuronal and synaptic dysfunction and plaque deposition (Griffin *et al.*, 1998).

A large body of evidence supports the view that IL-1 β contributes to the pathogenic process of AD (Lemere, 2007), including compelling evidence showing that a single injection of IL-1 β into the rat brain significantly increases A β production when compared with saline-injected controls (Sheng *et al.*, 1996). However, recent work on animal models of the disease has challenged the assumptions of the role played by IL-

1 β in AD. Work by Shaftel and colleagues (2007) showed that APP/PS1 transgenic mice that overexpress the IL-1 β transgene showed a reduction in plaque deposition in the hippocampus, as well as lower insoluble A β levels, compared with mice expressing the APP and PS1 transgenes alone (Shaftel *et al.*, 2007). While levels of APP were actually unchanged, the focal expression of IL-1 β induced a large increase in astrocytic and microglial activation, which in turn could lead stimulate microglia to phagocytose A β deposits. Likewise, APP/PS1 mice that received an intrahippocampal injection of LPS showed a 26% reduction in A β plaque burden, as determined by immunohistochemistry, in addition to the marked increase in the area covered by MHC II immunostaining (DiCarlo *et al.*, 2001). Taken together, these results suggest that phagocytosis of A β by stimulated microglial cells could have a beneficial role in the pathology of AD.

Results from this study indicated that GFAP expression was increased in the cortex of APP/PS1 mice. There was a 4-fold increase in GFAP mRNA expression, coupled with a marked increase in GFAP immunostaining, in tissue prepared from APP/PS1 transgenic mice at 13-14 months. This parallels several reports indicating a profound astrocytic reaction in the brains of both AD patients and mouse models of AD (Malm *et al.*, 2007). Additionally, the total number of GFAP-expressing astrocytes is increased in the hippocampus and amygdala of APP/PS1 mice with the same APP and PS1 mutations as the mice used in this study (Manaye *et al.*, 2007).

Indeed, the pathologic potential of astrocytes was originally suggested by Alois Alzheimer himself in 1910 (Rodriguez *et al.*, 2009). Astrocytosis comes in many guises, including a robust hypertrophy and proliferation, as well multiple immunological changes (Sofroniew, 2005). Cultured glial cells treated with human A β plaques isolated from human AD brains triggers reactive astrogliosis, characterized by an increase in GFAP immunoreactivity around A β plaques (DeWitt *et al.*, 1998). While activated astrocytes are capable of phagocytosing large amyloid deposits in the human brain (Nagele *et al.*, 2003), the phagocytic ability of microglia is significantly attenuated when cultured in the presence of astrocytes, with a coincident increase in their ramification (DeWitt *et al.*, 1998). Thus, on the one hand astrocytes may aid in the removal of deleterious debris like A β while, conversely, they may also be indirectly responsible for the persistence of amyloid plaques in the AD brain.

A major aim of this study was to assess whether the neuroinflammatory changes in APP/PS1 could be evaluated using *in vivo* T_1 and T_2 relaxometry. One of the significant results is that T_2 relaxation times were significantly decreased in grey matter regions of 13-14 month-old APP/PS1 mice. The decrease was most profound in cortical regions, while the hippocampus was least affected. Changes in T_2 relaxometry have been shown to reflect the presence of paramagnetic elements, for example iron in plaque cores, and many researchers have used this fact to study the pathogenesis and development of AD over time. For example, Braakman and colleagues showed that it was possible to non-invasively image $A\beta$ plaques without exogenous application of a contrast agent in the Tg2576 model of AD. These appeared as dark, hypointense lesions on the T_2 scan, and correlated spatially with both $A\beta$ - and iron-labelled plaques in the cortex and hippocampus (Braakman *et al.*, 2006).

The basis for intrinsic MRI contrast (i.e. without a contrast agent) between individual plaques and normal background tissue is presumed to be related to the iron content of plaques, which accelerates the T_2 relaxation rates of tissue water protons in and adjacent to plaques (Jack *et al.*, 2005). The co-localization between iron and amyloid plaques has been shown in several studies, including mouse models and AD patients (Wadghiri *et al.*, 2003). Furthermore, an age-related increase in plaque size and number was correlated with an age-related decrease in T_2 , a feature that is not evident in plaque-free, single transgenic PS1 mice. (Falangola *et al.*, 2007). Interestingly, it has been shown that the global iron content is similar in the brains of PS1 mice, compared with plaque-laden double transgenic APP/PS1 mice (El Tannir El Tayara *et al.*, 2006). This suggests that iron accumulation within plaques results from a redistribution of surrounding diffuse iron, rather than additional iron trapping.

While a decrease in T_2 was noted in the APP/PS1 mice in this study, the T_2 protocol used in this study was not able to identify individual plaques in these transgenic mice. This can be explained by the relative resolutions of the scans used in this study, compared with others. The matrix dimensions of the T_2 scan in this study was 128x128 voxels with an in-field resolution of 141 μ m per voxel, while that used by Braakman and colleagues was a superior 256x256 with an in-field resolution of 78 μ m. The plaques detected by Congo red staining in this study (with an estimated diameter of 30 μ m-40 μ m) inside larger voxels must produce enough local spin dephasing, and thereby signal loss, to cause the voxel to be resolved from surrounded normal tissue.

The greatest T_2 decrease observed in APP/PS1 mice was noted in the regions of the motor and entorhinal cortex (approximately 8% compared with non-transgenic control mice), while the T_2 values in the hippocampus were less affected by genotype (a decrease of approximately 4%). Representative micrographs from the Congo red immunohistochemistry suggest that frequency of $A\beta$ plaque deposition was greater in cortical regions, compared with deposition in the hippocampus. This correlates with the previously-mentioned studies which showed an inverse correlation between plaque number and iron deposition, and T_2 signal; however, a comparison of plaque deposition in different regions would have been beneficial in this study.

Microglial activation, determined by CD11b immunostaining, was markedly enhanced in sections prepared from transgenic APP/PS1 mice. Microglial activation in APP/PS1 brain tissue was characterized by large clumps of CD11b positive staining. Reactive microglial clusters have been observed both in and around senile plaques and amyloid deposits (Haga *et al.*, 1989). Several studies have also demonstrated a decreased T_2 signal arising from iron-accumulating activated microglia. For example, recent evidence from Teipel and colleagues (2011) investigated whether a spatial coincidence existed between decreased T_2 signal with amyloid plaques in conjunction with activated microglia. In this study, double immunohistochemistry of $A\beta$ plaques and Iba-1 (a marker of all microglia) showed that activated microglial only co-localized with $A\beta$ deposits in the 19-20 week-old mice from the APP^{swe}/PS1 AD model (Teipel *et al.*, 2011). Furthermore, the authors suggest that the DAB-enhanced iron staining of both amyloid plaques in combination with activated microglia contribute to the decrease in T_2 signal observed. A decrease in T_2 resulting from activated microglia in human AD was originally suggested (Laakso *et al.*, 1996), however follow-up studies have not fully addressed this question. Moreover, it remains to be seen if activated microglia alone, in the absence of iron-accumulating plaques, can induce paramagnetic susceptibility to a sufficient extent to significantly alter the T_2 signal.

T_1 relaxation times were significantly increased in grey matter regions of APP/PS1 mice at 13-14 months. This was particularly interesting as GFAP immunoreactivity was markedly enhanced in the cortex and hippocampus of APP/PS1 mice. We previously hypothesized that an increase in T_1 relaxation values may reflect acute astrocytosis through net water accumulation following insult or injury. While the association between T_1 increases and acute astrocytosis found in this study

parallels findings described in previous chapters, the data do not correlate with previous reports in the literature investigating T_1 changes in AD transgenic mice. T_1 relaxation values in APP/PS1, PS1 and non-transgenic controls showed no genotype difference at ages up to 10 months (El Tannir El Tayara *et al.*, 2006). A further study confirmed this in mice at 16 months of age (Helpert *et al.*, 2004). The subtle genotype increase found in several regions in the current study may be due to the larger number of mice used in this experiment and consequently a higher powered study. It is pertinent to point out that the increase in T_1 was not constant in all ROIs investigated; the greatest increase was observed in the motor cortex of APP/PS1 mice, an area that showed a marked enhancement in GFAP immunoreactivity.

Results from the VBM analysis revealed no significant volumetric alterations in the APP/PS1 mice at 13-14 months. This is similar to previous observations where volumetric analyses in mouse AD models consistently show a lack of significant volumetric loss in AD transgenic mice. In an *ex vivo* study conducted by Yang and colleagues (2011) comparing 13-17 month old APP/PS1 mice with age-matched non-transgenic controls using the VBM analysis revealed only a small area of significant tissue loss in transgenic mice that was present in the thalamic area of the mid-brain. This was probably due to atrophy in this area of the AD mouse brain (Yang *et al.*, 2011), highlighted as a result of using extremely high-resolution MR imaging with an image resolution of 256x256x256 voxels and a prolonged imaging time of over eight hours. This finding should be considered in the context of studies indicating memory deficits in AD transgenic mice (Trinchese *et al.*, 2004), where it can be concluded that any deficits in hippocampal-based memory tasks in AD mice, for example the Morris water maze (Puolivali *et al.*, 2002), may be due to the presence of A β plaques and the subsequent inflammatory changes and cytokine release, and not due to gross anatomical loss. Furthermore, the consistent lack of volumetric change in mouse models of AD highlights the inherent problems in using models of the disease that do not perfectly correlate with disease symptoms in human patients. Interestingly, results from pathological and MRI studies have indicated that the hippocampal formation undergoes severe atrophy in AD patients (Fox *et al.*, 1996; Burton *et al.*, 2004).

A particular aim of this study was to describe the effect of siRNA targeting the tight junction proteins claudin 5 and occludin on BBB permeability in WT and APP/PS1 mice. The tight junction proteins claudins and occludin have been implicated

in mediating changes in the paracellular conductance of endothelial cells (Balda *et al.*, 2000; Van Itallie *et al.*, 2001). Here, efficient knock-down of claudin 5 was confirmed by PCR on cortical tissue prepared from WT mice, where a decrease of approximately 50% was observed in siRNA-treated mice. This concurs with data from a previous study by Campbell and colleagues (2011) which showed strong and significant suppression (approximately 50%) of the claudin 5 gene in WT mice 48 hours following treatment with siRNA targeting claudin 5 alone (Campbell *et al.*, 2011) and a return to baseline values a further 24 hours later (Campbell *et al.*, 2008).

Interestingly, treatment with siRNA targeting occludin had no significant effect on occludin mRNA levels in WT mice. There was significant variation in these data, suggesting that siRNA treatment may have worked in some, but not all, mice in this study. Follow up experiments has revealed that expression of occludin is significantly suppressed 72 hours after siRNA treatment (Matthew Campbell, personal communication), therefore the timepoint of 48 hours used in this study was too premature. Claudin 12 mRNA was also analysed in these groups, as it was predicted that this tight junction protein would be up-regulated as a compensatory consequence of the claudin 5 suppression. Unexpectedly, claudin 12 mRNA was also decreased in the cortex of siRNA-treated WT mice. This may reflect transcriptional regulation of claudin 12 in response to the controlled suppression of claudin 5, and may be as a result of the different tight junction proteins binding to similar sites to the zonula occludens. Despite our hypothesis that claudin 12 might be up-regulated as a compensatory mechanism to the down-regulation of claudin 5, claudin 12 expression was unchanged in mice deficient in the claudin 5 gene (Nitta *et al.*, 2003).

Transient knock-down of claudin 5 in WT mice, coupled with the unexpected decrease in claudin 12, induced BBB permeability to the 742 Dalton gadolinium-based contrast agent, Magnevist. Extravasation of gadolinium is reflected in significant SI increases, or areas of hyperintense brightness, on T₁-weighted MR images. Our cannulation technique indicated significant SI increases in multiple cortical regions, as well as ROIs in the thalamus, cerebellum and frontal lobe of siRNA-treated WT mice. However, the increase in SI in the dentate gyrus of siRNA-treated WT mice did not reach statistical significance. Again, this result parallels previous work carried out investigating the effect of suppressing expression of claudin 5 alone by siRNA, where the authors found deposition of gadolinium in the brains of WT mice, but no evidence

of permeability to molecules with a molecular weight of 4400 Daltons (Campbell *et al.*, 2008). Overall, siRNA treatment targeting suppression of both claudin 5 and occludin in WT mice had a similar effect as siRNA targeting claudin 5 alone, resulting in transient BBB breakdown 48 hours after treatment and increased paracellular diffusion to compounds with molecular weights larger than would normally be permitted to transverse the highly regulated BBB.

The results from this study indicated that BBB integrity was compromised in cortical regions of APP/PS1 mice and these findings were coupled with a marked decrease in mRNA expression of claudins 5 and 12 in APP/PS1 mice. This suggests that BBB disruption could be a relatively early biomarker of the AD pathology. Numerous cerebrovascular abnormalities can be found in the AD brain, the most obvious of which is cerebral amyloid angiopathy, which is characterized by the deposition of amyloid in small arteries, arterioles and capillaries and found in most AD cases (Ellis *et al.*, 1996; Poduslo *et al.*, 2001). Other changes found in the cerebrovasculature include alterations in pericytes, endothelial cell thinning (Kalaria & Hedera, 1996).

While it is now generally accepted that breach of the BBB occurs in AD patients with high plaque burden (Vinters, 1987), more recent evidence has indicated a similar characteristic in transgenic models of AD. Ujiie and colleagues (2003) have shown that 4 month-old Tg2576 transgenic mice have a compromised BBB integrity in several cortical areas compared to their non-transgenic littermates (Ujiie *et al.*, 2003). This occurs prior to disease-onset and senile plaque deposition which is initiated at 9 months, and was assessed by extravascular detection of the fluorescent compound carboxyfluorescein throughout brain tissue, a dye which has a molecular weight of 376 Daltons (Balice-Gordon *et al.*, 1998). Furthermore, an age-related increase in fluorescence was detected in 10 month-old mice, suggesting that early-stage BBB damage is magnified by the presence of A β plaque deposition in AD mice. In a follow-up study from the same laboratory, Dickstein and colleagues (2006) showed that peripheral administration of anti-A β peptides not only reduced the size and number of A β plaques, but also dramatically restored integrity of the BBB to uptake of the 960 Dalton Evans blue dye (Dickstein *et al.*, 2006). This suggests that once A β is removed, the integrity of the BBB is restored. These results are of particular importance, as determining whether, and when, cerebral microvessels become compromised in AD is

of considerable importance, as it could define an early therapeutic intervention point to slow down the progression of the disease.

Treatment with siRNA induced a 20% decrease in claudin 5 mRNA in the cortex of APP/PS1 mice; however, this did not reach statistical significance. A similar siRNA effect was observed in APP/PS1 mice as in WT mice; the level of occludin mRNA was unchanged and claudin 12 mRNA was unexpectedly decreased in siRNA-treated APP/PS1 mice. In parallel with this was a significant increase in BBB permeability to gadolinium in areas of the cortex, thalamus and cerebellum of transgenic mice. The failure of siRNA to decrease claudin 5 expression in APP/PS1 mice could be as a result of compromised perfusion, which has been reported to occur in the brains of APP/PS1 mice (Faure *et al.*, 2011). Thus the distribution of siRNA may not be as complete as in WT mice. A potential method for correcting for this in future studies may be to increase the concentration of siRNA though this may introduce confounding variables such as activation of innate inflammatory response resulting in IL-12 and IFN- γ release (Kleinman *et al.*, 2008).

Remodelling the BBB by selectively modulating levels of tight junction proteins could have substantial therapeutic potential given that the vast majority of low-molecular weight drugs cannot attain access to neuronal tissues from peripheral circulation. As a corollary, with a more permeable BBB, A β may be able to move down the concentration gradient from the brain and CSF to the plasma more freely. This may present an attractive avenue for anti-amyloid therapies. However in this study, A β levels were unchanged in control- compared with siRNA-treated APP/PS1 mice, indicating that siRNA failed to alter levels of soluble amyloid concentrations. Unsurprisingly, siRNA had no effect on insoluble A β plaque count in transgenic mice. In fact the only effect of siRNA was a significant increase in serum A β ₄₀ concentration in siRNA-treated APP/PS1 mice compared with WT mice. While cortical A β levels were unchanged between control- and siRNA-treated AD mice, any subtle or transient change in concentration here could have a significant impact on serum levels, due to the relatively high concentration of A β in the brain compared with levels in circulating blood.

The relative levels and distribution of A β species in the brain may influence disease progression and so, the failure of siRNA treatment to induce movement of soluble A β to blood serum is disappointing. One possible explanation for this is the

molecular weight of A β peptides relative to the extent of the BBB permeability induced by the siRNA treatment. A β are considered small peptides, with a molecular weight of approximately 4.5kDa (Deane *et al.*, 2009) but BBB disruption as induced here allowed only compounds with a molecular weight less than 1kDa to translocate. Molecular tracer experiments carried out by Campbell and colleagues (2008) revealed that the FITC-labelled dextran, FD-4, which has a molecular weight of 4400 Da, remained within the microvessels of the brain vasculature, and no extravasation was evident at any time-point (Campbell *et al.*, 2008). Thus we can conclude that the size-selective property of the BBB permeability induced by the siRNA prevented the passage of amyloid peptides across into the blood plasma.

It has been suggested that decreased clearance of A β from the brain and CSF is the main cause of amyloid accumulation in sporadic AD (Rosenberg, 2000). Recent evidence has indicated that A β clearance may actually be impaired in AD patients (Tanzi *et al.*, 2004). A β concentration is rigorously regulated by its rapid efflux and clearance across the BBB via low-density lipoprotein receptor related protein-1 (LRP-1) (Deane *et al.*, 2009). The LRP-mediated A β transcytosis across the BBB is initiated at the brain side of the endothelium and is directly responsible for eliminating A β from the brain into the bloodstream (Zlokovic, 2004). The role of LRP in amyloid clearance is supported by findings in an AD mouse model demonstrating that deletion of LRP at the BBB results in doubling of cerebral amyloid (Van Uden *et al.*, 2002). LRP-1, although abundant in young mice, is downregulated in older animals, and this downregulation correlated with regional A β accumulation in brains of AD patients, as well as positive staining of vessels for A β ₄₀ and A β ₄₂ (Shibata *et al.*, 2000).

This study set out to assess the neuroinflammatory profile and BBB permeability of 13-14 month-old APP/PS1 mice. Significant A β plaque deposition was associated with an increase in pro-inflammatory markers, including up-regulation of microglial markers and pro-inflammatory cytokines, as well as enhanced BBB permeability in cortical regions. Treatment with siRNA targeting the tight junction proteins claudin 5 and occludin induced further BBB disruption to the gadolinium-based contrast in some, but not all brain regions, of AD mice, although concentrations of A β ₄₀ and A β ₄₂ were unaffected in the brain. Thus, further work is required to modulate BBB permeability to induce the passage of amyloid peptides down the concentration gradient. This has the

potential to reduce the amyloid burden associated with AD models, and thus attenuate the pro-inflammatory profile of AD mice.

Chapter 6

General Discussion

6.1 General Discussion

The primary objective of this study was to assess characteristics of glial function and BBB permeability in several models of neuroinflammation. Innate responses in the CNS, which are dependent on glial activation, are critical to first line defence against infection and injury (Babcock *et al.*, 2003), and have been implicated in the pathogenesis of several neurodegenerative disorders. These include MS (Barnett & Prineas, 2004), AD (Nagele *et al.*, 2004) and PD (Hirsch *et al.*, 1998). The secondary objective of this study was to evaluate the utility of MR relaxometry parameters in the assessment of neuroinflammatory changes in our selected models. The characteristics of glial activation and function and subsequent effects on MR parameters were analysed in three models of neuroinflammation: Young and aged WT and CD200-deficient mice, LPS-challenged WT and CD200-deficient mice, APP/PS1 model of AD associated with widespread plaque deposition.

The most significant finding was that the age-related increase in microglial activation in WT mice was enhanced in CD200^{-/-} mice. In addition, treatment with 50µg LPS induced an increase in microglial activation, denoted by CD11b and CD40 mRNA, that was exaggerated in the hippocampus of CD200^{-/-}, compared with WT, mice. The data from the relaxometry analysis show that LPS failed to have the expected decrease in T₂ relaxation times. However, the data from the second study suggests a positive correlation between GFAP expression and T₁ relaxometry. BBB permeability to exogenous contrast agents was increased in CD200^{-/-} mice, and in LPS-treated WT mice, which was coupled with a decrease in the expression of the tight junction proteins claudins 5 and 12, and occludin. Finally, siRNA targeting suppression of the tight junction proteins induced BBB permeability up to compounds <1kDa, but failed to induce movement of the larger Aβ molecule out of the brain.

The data show that markers of glial cells are up-regulated in states of neuroinflammatory stress and peripheral challenge. Microglial activation was assessed by immunohistochemical staining for CD11b, as well as analysis of cell surface marker expression by PCR. CD11b expression was increased in the cortex and hippocampus of 17 month, compared with 4 and 13 month-old, WT mice. This age-related increase was further enhanced in CD200^{-/-} mice. There was a dose-dependent response in CD11b staining following LPS treatment in both WT and CD200-deficient mice. Treatment

with 50µg LPS induced a significantly greater increase in CD40 mRNA expression when assessed in CD200-deficient mice. In the third model, neuroinflammatory changes were also evident. Specifically, there was a two-fold increase in CD11b mRNA expression in the cortex of APP/PS1 mice, coupled with a marked increase in CD11b immunostaining which tended to occur in large clumps, possibly in proximity to plaques, although a co-localization was not performed. In addition, the expression of pro-inflammatory cytokines IL-1β, TNF-α and IL-6 was significantly up-regulated in tissue and serum prepared from APP/PS1 mice.

Astrocytic immunoreactivity was assessed by immunostaining for GFAP, an intermediate filament protein thought to be specific for these cells in the CNS (Eng, 1985), and mRNA expression by PCR analysis. There was an age-related increase in GFAP immunostaining in the cortex, but not hippocampus, of WT mice. GFAP staining was more pronounced in sections prepared from 4 month-old CD200-deficient mice and LPS increased GFAP mRNA and immunostaining in a dose-dependent manner in both WT and CD200^{-/-} mice. Similarly, GFAP expression was significantly increased in the cortex and hippocampus of 13-14 month-old APP/PS1 mice.

The effect of ageing on glial activation has been well documented in previous studies. The ageing brain is defined by a decrease in weight and volume in grey matter regions, presumably as a result of a loss of neurons and myelinated axons (Conde & Streit, 2006). Furthermore, the accumulation of reactive oxygen species over one's lifetime is one of the most profound causative factors in ageing (Nakanishi & Wu, 2009) and has been proposed to negatively affect cell function (Harman, 1956).

It is significant that the age-related increase in microglial activation was more profound in CD200-deficient mice. Microglial cells comprise a network of immunocompetent cells that pervade the brain and spinal cord; their primary function is to provide a continuous surveillance of the parenchyma and protect the CNS against injury and disease (Streit *et al.*, 2005). Microglia are referred to as activated when they show an up-regulation of particular antigens, and when they develop processes which are more shorter and stouter than those in the resident population. Studies in aged rats have shown an increase in numbers of microglia in these animals, as well as an up-regulation of MHC II expression in both grey and white matter (Perry *et al.*, 1993), as well as an age-related increase in concentration of the pro-inflammatory cytokine IL-1β

in the hippocampus (Lynch, 1999). Conversely, secretion of the anti-inflammatory cytokine IL-10 is decreased in the brains of aged mice (Barbier *et al.*, 2005).

Ageing is associated with the up-regulation of TLRs (Letiembre *et al.*, 2007) which are innate immune receptors that recognize special motifs on components of viral or bacterial pathogens (Jack *et al.*, 2005). However, A β is also known to bind to TLR2 and TLR4 (Richard *et al.*, 2008). Receptor binding initiates a pronounced inflammatory cascade aimed at killing invading organisms (Fassbender *et al.*, 2004). In the absence of cerebral pathology, ageing of the mouse brain is associated with an increase in TLRs 1-7, with TLR4 showing the greatest age-related increase (Letiembre *et al.*, 2007). This was associated with an increase in expression of pro-inflammatory cytokines like TNF- α . Consequently, it has been proposed that down-regulation of TLRs, including TLR9, might be a mechanism for dampening inflammatory responses (Godbout & Johnson, 2004). This may be consistent with microglial dystrophy, characterized by deramification, spheroid formation and fragmentation of processes in the brains of the elderly (Streit *et al.*, 2004). Thus, the age-related increase in CD11b expression seen in WT mice can be considered is probably reflective of an increased pro-inflammatory environment with age.

Several studies have proposed an important role for CD200, like CD22 and CD47 (Tian *et al.*, 2009), in the maintenance of microglia in a quiescent state. CD200R is a member of a group of proteins expressed on myeloid cells, including microglia (Wright *et al.*, 2003). CD200R recruits docking protein 1 (Dok 1) and Dok 2 which leads to recruitment of Ras GTPase-activating protein (RasGap) and downstream inhibition of the JNK and MAPK pathways (Zhang *et al.*, 2004). The reduced activation of these MAPKs is believed to be responsible for the observed inhibition of cytokine production by CD200R⁺ cells (Gorczynski *et al.*, 2004). Conversely, deletion of CD200 renders microglia in an activated state, characterized by an increase in many features of reactive microglia (Neumann, 2001). From these data, it was predicted that neuroinflammatory changes induced by the ageing process would be enhanced in CD200^{-/-} mice. The present data convincingly showed that CD200-deficient mice had an exaggerated response to LPS; this is consistent with recently published data (Costello *et al.*, 2011). In addition, age-related changes were more pronounced in CD200^{-/-} mice and one possibility is that the more profound age-induced increase in microglial activation

may be mediated by enhanced TLR4 expression in CD200^{-/-} mice, as previously reported (Costello *et al.*, 2011).

ROI analysis on T₂-weighted images revealed an age-related decrease in this parameter in cortical and hippocampal regions of WT mice. We hypothesized that this may be due to an age-related increase in microglial-mediated expression of ferritin since it has been shown that microglia have the capacity to store iron (Zecca *et al.*, 2004). Indeed, reactive microglia are more positively stained with anti-ferritin immunohistochemistry (Kaneko *et al.*, 1989). An age-related increase in iron staining in microglia has also been documented in the cortex, hippocampus, cerebellum and amygdala (Connor *et al.*, 1990). Interestingly, it has been postulated that increased iron accumulation may be a risk factor in age-related degenerative brain diseases, for example AD (Bartzokis *et al.*, 2007). However, the enhanced increase in microglial activation seen in aged CD200^{-/-} mice was not coupled with a decrease in T₂ relaxometry. This suggests that whereas the age-related decrease in T₂ values of WT and CD200-deficient mice may be reflective of the increase in overall iron accumulation (Floyd & Carney, 1991; Gerlach *et al.*, 1994), this was not correlated with the extent of activation of microglial cells.

The effect of ageing on astrocytic function has been extensively examined; the activation of these cells is widely accepted to play a role in the brain's inflammatory reaction (Abraham, 2001). The age-related increase in GFAP staining in the cortex of WT and CD200^{-/-} mice should be considered in terms of the role astrocytes play in neuronal repair in normal, ageing tissue in the absence of neurodegenerative disease. GFAP expression is highly sensitive to neuronal impairments, as shown by astrocytic hypertrophy after local neuron death and by rapid induction of GFAP-containing astrocytic processes following pharmacological blockade of neuronal impulses (Canady *et al.*, 1994). Reciprocally, neuronal outgrowth, which is impaired with the onset of ageing (Hall *et al.*, 2001), is inhibited in sites of neuronal hyperactivity, for example after spinal cord lesions (Rozovsky *et al.*, 2005). It is unclear whether the activation state of astrocytes described here in aged mice and CD200^{-/-} mice is reflective of degenerative change or indicative of an effort to induce reparative changes.

CD200 is expressed on neurons, endothelial cells (Copland *et al.*, 2007), and on reactive and un-stimulated astrocytes (Koning *et al.*, 2009; Costello *et al.*, 2011). Multiple lines of evidence support a model whereby CD200 ligation of CD200R results

in immune regulation of CD200R⁺ cells, with a downstream effect of attenuating both inflammation and autoimmunity (Rosenblum *et al.*, 2006). However, CD200 itself lacks a cytoplasmic domain with obvious intracellular signalling motifs (Gorczyński *et al.*, 2004). Thus, cells deficient in CD200 in knockout mice do not show obvious signs of increased reactivity, with reactivity reserved for cells expressing CD200R alone. However, the age-related increase in GFAP staining in cortical tissue of WT mice was more pronounced in CD200-deficient mice. This may be reflective of exaggerated neuronal stress in CD200^{-/-} mice, which is a possibility considering the significant volumetric changes in CD200-deficient mice revealed by the VBM analysis.

Assessment of T₁-weighted imaging revealed an increase in this MR parameter in the cortex and hippocampus of 4 month-old CD200-deficient mice and no age-related changes were observed. T₁ values have been shown to reflect acute astrocytosis (Sibson *et al.*, 2008) and GFAP staining was significantly increased in these regions of CD200-deficient mice at this timepoint.

LPS-mediated activation of microglial activation was more profound in CD200-deficient mice; this effect was more profound in the hippocampal formation than in the cortex which suggests an enhanced susceptibility to acute inflammatory challenge in the hippocampus of CD200^{-/-} mice.

Treatment with LPS did not induce the predicted decrease in T₂ values in WT or CD200^{-/-} mice. Considering that LPS is a potent activator of microglial activation, and that the microglial response was more pronounced in CD200-deficient mice, it must be concluded that changes in T₂ relaxometry do not reflect changes in the physiological state of microglial cells. Combining these T₂ data with results from chapter 3, it is deduced that the decrease in T₂ may be reflective of changes in microglial iron accumulation but are unlikely to be mediated simply by the activation state of microglia. This contrasts with the findings of Justicia and colleagues (2008) who reported that iron accumulation in reactive microglia can reduce the local T₂ relaxation time on MR images in a rat model of stroke (Justicia *et al.*, 2008).

Although LPS can not enter the brain when administered peripherally, ip treatment with LPS induced the expected significant increase in astrocytic activation and this paralleled the increase in T₁ relaxation values in grey matter regions. *In vivo* administration of LPS has been shown to induce astrocytic activation (Qiao *et al.*, 2001), as astrocytes also express the TLR4 pattern recognition receptor, albeit at lower

levels than microglia (Kipp *et al.*, 2008). To investigate this relationship further, this study would have benefited from pre-treatment of WT and CD200^{-/-} mice with an inhibitor of astrocytic activation, for example arundic acid (Mori *et al.*, 2005). Indeed, the positive correlation between GFAP mRNA and T₁ values in this study is encouraging, as it demonstrates the inherent potential of MRI as an *in vivo* assessment of some aspects of neuroinflammatory change.

The neuroinflammatory changes of 13-14 month-old APP/PS1 mice, a mouse model of AD associated with widespread plaque deposition at this age, was also investigated. Unsurprisingly, extensive plaque deposition was associated with up-regulation of numerous markers of inflammation including markers of glial activation (CD11b and GFAP) as well as expression of pro-inflammatory cytokines IL-1 β , TNF- α and IL-6. According to the amyloid cascade hypothesis, A β accumulation and deposition as diffuse plaques leads to the activation of both microglia and astrocytes, consequently leading to synaptic and neuritic injury (Hardy & Higgins, 1992). These data suggest that the AD brain is in a chronic state of glia-mediated neuroinflammation.

Assessment by MRI revealed significant alterations in T₁ and T₂ relaxation values. There was a significant increase in T₁ values in grey matter regions of APP/PS1 mice and based on the parallel between astrocytic activation and T₁ observed in CD200-deficient mice, it is suggested that the observed changes in T₁ in APP/PS1 mice may be because of the observed astrocytic activation. On the contrary, T₂ relaxation times were significantly decreased in AD transgenic mice. All evidence suggests that this occurs as a result of greater accumulation of iron in the AD brain. This is borne out by the fact that total iron load is increased with amyloid deposition in APP/PS1 mice, an age-related phenomenon that correlates with a decrease in T₂ signal in these mice (El Tannir El Tayara *et al.*, 2006).

Combining the T₂ data from the three models of inflammation, our results suggest further the already established link between T₂ alterations and changes in the concentration of iron from A β plaques in brain tissue. However, the utility of T₂ as a surrogate bio-marker of microglial activation must be optimized. Thus, established approaches like that provided by USPIO technologies, which take advantage of the phagocytic abilities of activated microglia and the paramagnetic effects of iron oxide, are more likely to be identified as proxy markers of activation.

In this study a novel tail-vein cannulation method was used for the assessment of BBB permeability to exogenous contrast agents. This allowed the quantification of both pre- and post-contrast SI measurements in the same scan. Data using this technique showed that BBB permeability is induced by 50µg LPS treatment in WT mice. Gadolinium extravasation in tissue only occurs under conditions of vascular leakage, brought about by disruption of tight junctions of the BBB. WT mice treated with 50µg LPS displayed decreased levels of the tight junction proteins claudin 5, 12 and occludin, thereby inducing BBB permeability to the 742 Dalton gadolinium-based contrast agent, Magnevist. This decrease may have occurred as a result of circulating cytokine expression induced by LPS treatment since it has been shown that claudin 5 and occludin expression is disrupted by the pro-inflammatory cytokines IL-1β and IL-17 (Kebir *et al.*, 2007). Like microglia, endothelial cells also express TLR4 and release pro-inflammatory cytokines (Boyle *et al.*, 1997) and may contribute to LPS-induced signalling (Nagai *et al.*, 2002).

An unexpected but interesting finding in this study was that BBB permeability was increased in 6-8 month-old CD200-deficient mice where levels of permeability to gadolinium were nearly as great as those seen in LPS-treated WT mice. Unsurprisingly, follow-up analysis revealed decreases in claudin 5 and occludin mRNA expression in CD200^{-/-} mice. CD200 is expressed on endothelial cells, however as far as the authors are aware, this is the first study to indicate that endothelial cell function is impaired with CD200-deficiency. However, as deletion of CD200 renders CD200R⁺ microglia in an activated state (Costello *et al.*, 2011), this impairment in BBB permeability may be mediated by microglia. In conjunction with the release of pro-inflammatory cytokines, activated microglia also up-regulate their production of NO, as do endothelial cells. Thus, the enhanced BBB permeability in knockout mice could be as a result of the pro-inflammatory environment of CD200-deficient mice; for example, where increased levels of the pro-inflammatory cytokines IL-13 and IL-17 released by activated microglia have been shown to disrupt expression of the tight junction proteins.

BBB disruption could lead to the passage of Aβ from areas of high concentration in the brain, to areas of lower concentration in the blood. However, the increase in BBB permeability induced by siRNA treatment was not sufficient to propagate a movement in soluble amyloid peptides down the concentration gradient. Perhaps this is unsurprising, since treatment with siRNA targeting claudin 5 alone only induces

permeability to compounds less than 1kDa (Campbell *et al.*, 2008). A β has a molecular weight of 4.5kDa, and is thus too large to cross the BBB by paracellular transport. Interestingly, treatment with siRNA had no effect on levels of microglial or astrocytic activation, thus we can conclude that there was no significant movement of pro-inflammatory molecules from the periphery to the brain of APP/PS1 mice.

The evidence presented in this study highlights the utility of non-invasive MR imaging in the assessment of several models of neuroinflammation. A consistent result in this study is that T₁ relaxometry positively correlated with acute astrocytosis in the CNS, and this was evident following peripheral challenge of LPS, and at basal levels in the brains of APP/PS1 AD mice. However, the association between decreased T₂ signal and activated microglia was not borne out in the data, and the T₂ decreases reported here are more likely to reflect greater iron accumulation in the aged and AD brain; however, this was not investigated and is therefore of further analysis. Contrast imaging revealed that BBB function is impaired in CD200-deficient and APP/PS1 mice, and this was associated with a decrease in proteins associated with endothelial cell tight junctions. Overall, this study highlights the fact that MRI can be used in the assessment of astrocyte function and BBB integrity in several models of neuroinflammation. Future experiments should investigate the utility of USPIO technologies in the assessment of microglial activation by MR scanning.

References

- Abbott N. (2002). Astrocyte-endothelial interactions and blood-brain barrier permeability. *J Anat* **200**, 527.
- Abbott NJ, Patabendige AA, Dolman DE, Yusof SR & Begley DJ. (2010). Structure and function of the blood-brain barrier. *Neurobiol Dis* **37**, 13-25.
- Abbott NJ, Ronnback L & Hansson E. (2006). Astrocyte-endothelial interactions at the blood-brain barrier. *Nat Rev Neurosci* **7**, 41-53.
- Abraham CR. (2001). Reactive astrocytes and alpha1-antichymotrypsin in Alzheimer's disease. *Neurobiol Aging* **22**, 931-936.
- Acton RD, Dahlberg PS, Uknis ME, Klaerner HG, Fink GS, Norman JG & Dunn DL. (1996). Differential sensitivity to Escherichia coli infection in mice lacking tumor necrosis factor p55 or interleukin-1 p80 receptors. *Arch Surg* **131**, 1216-1221.
- Aderem A & Ulevitch RJ. (2000). Toll-like receptors in the induction of the innate immune response. *Nature* **406**, 782-787.
- Aderem A & Underhill DM. (1999). Mechanisms of phagocytosis in macrophages. *Annu Rev Immunol* **17**, 593-623.
- al-Ali SY & al-Hussain SM. (1996). An ultrastructural study of the phagocytic activity of astrocytes in adult rat brain. *J Anat* **188 (Pt 2)**, 257-262.
- Allin M, Matsumoto H, Santhouse AM, Nosarti C, AlAsady MH, Stewart AL, Rifkin L & Murray RM. (2001). Cognitive and motor function and the size of the cerebellum in adolescents born very pre-term. *Brain* **124**, 60-66.
- Alliot F, Godin I & Pessac B. (1999). Microglia derive from progenitors, originating from the yolk sac, and which proliferate in the brain. *Brain Res Dev Brain Res* **117**, 145-152.

- Aloisi F, De Simone R, Columba-Cabezas S, Penna G & Adorini L. (2000). Functional maturation of adult mouse resting microglia into an APC is promoted by granulocyte-macrophage colony-stimulating factor and interaction with Th1 cells. *J Immunol* **164**, 1705-1712.
- Aloisi F, Penna G, Polazzi E, Minghetti L & Adorini L. (1999). CD40-CD154 interaction and IFN-gamma are required for IL-12 but not prostaglandin E2 secretion by microglia during antigen presentation to Th1 cells. *J Immunol* **162**, 1384-1391.
- Alonso G. (2001). Proliferation of progenitor cells in the adult rat brain correlates with the presence of vimentin-expressing astrocytes. *Glia* **34**, 253-266.
- Anderson VM, Fox NC & Miller DH. (2006). Magnetic resonance imaging measures of brain atrophy in multiple sclerosis. *J Magn Reson Imaging* **23**, 605-618.
- Arai H, Higuchi S, Matsushita S, Yuzuriha T, Trojanowski JQ & Lee VM. (1994). Expression of beta-amyloid precursor protein in the developing human spinal cord. *Brain Res* **642**, 132-136.
- Araujo DM & Cotman CW. (1992). Beta-amyloid stimulates glial cells in vitro to produce growth factors that accumulate in senile plaques in Alzheimer's disease. *Brain Res* **569**, 141-145.
- Ashburner J & Friston KJ. (2000). Voxel-based morphometry--the methods. *Neuroimage* **11**, 805-821.
- Azevedo FA, Carvalho LR, Grinberg LT, Farfel JM, Ferretti RE, Leite RE, Jacob Filho W, Lent R & Herculano-Houzel S. (2009). Equal numbers of neuronal and nonneuronal cells make the human brain an isometrically scaled-up primate brain. *J Comp Neurol* **513**, 532-541.

- Babcock AA, Kuziel WA, Rivest S & Owens T. (2003). Chemokine expression by glial cells directs leukocytes to sites of axonal injury in the CNS. *J Neurosci* **23**, 7922-7930.
- Balda MS, Flores-Maldonado C, Cerejido M & Matter K. (2000). Multiple domains of occludin are involved in the regulation of paracellular permeability. *J Cell Biochem* **78**, 85-96.
- Balice-Gordon RJ, Bone LJ & Scherer SS. (1998). Functional gap junctions in the schwann cell myelin sheath. *J Cell Biol* **142**, 1095-1104.
- Banati RB & Graeber MB. (1994). Surveillance, intervention and cytotoxicity: is there a protective role of microglia? *Dev Neurosci* **16**, 114-127.
- Banks WA, Kastin AJ, Brennan JM & Vallance KL. (1999). Adsorptive endocytosis of HIV-1 gp120 by blood-brain barrier is enhanced by lipopolysaccharide. *Exp Neurol* **156**, 165-171.
- Barbier EL, Liu L, Grillon E, Payen JF, Lebas JF, Segebarth C & Remy C. (2005). Focal brain ischemia in rat: acute changes in brain tissue T1 reflect acute increase in brain tissue water content. *NMR Biomed* **18**, 499-506.
- Barclay AN, Wright GJ, Brooke G & Brown MH. (2002). CD200 and membrane protein interactions in the control of myeloid cells. *Trends Immunol* **23**, 285-290.
- Barnes D, McDonald WI, Landon DN & Johnson G. (1988). The characterization of experimental gliosis by quantitative nuclear magnetic resonance imaging. *Brain* **111 (Pt 1)**, 83-94.
- Barnett MH & Prineas JW. (2004). Relapsing and remitting multiple sclerosis: pathology of the newly forming lesion. *Ann Neurol* **55**, 458-468.

- Bauer J, Huitinga I, Zhao W, Lassmann H, Hickey WF & Dijkstra CD. (1995). The role of macrophages, perivascular cells, and microglial cells in the pathogenesis of experimental autoimmune encephalomyelitis. *Glia* **15**, 437-446.
- Bear MF, Connors BW & Paradiso MA. (1996). *Neuroscience: exploring the brain*.
- Beaumont M, Lemasson B, Farion R, Segebarth C, Remy C & Barbier EL. (2009). Characterization of tumor angiogenesis in rat brain using iron-based vessel size index MRI in combination with gadolinium-based dynamic contrast-enhanced MRI. *J Cereb Blood Flow Metab* **29**, 1714-1726.
- Becher B, Prat A & Antel JP. (2000). Brain-immune connection: immuno-regulatory properties of CNS-resident cells. *Glia* **29**, 293-304.
- Beets-Tan RG, Beets GL, Borstlap AC, Oei TK, Teune TM, von Meyenfeldt MF & van Engelshoven JM. (2000). Preoperative assessment of local tumor extent in advanced rectal cancer: CT or high-resolution MRI? *Abdom Imaging*.
- Belayev L, Busto R, Zhao W & Ginsberg MD. (1996). Quantitative evaluation of blood-brain barrier permeability following middle cerebral artery occlusion in rats. *Brain Res* **739**, 88-96.
- Benkovic SA & Connor JR. (1993). Ferritin, transferrin, and iron in selected regions of the adult and aged rat brain. *J Comp Neurol* **338**, 97-113.
- Benveniste EN. (1992). Inflammatory cytokines within the central nervous system: sources, function, and mechanism of action. *Am J Physiol* **263**, C1-16.
- Benveniste EN. (1998). Cytokine actions in the central nervous system. *Cytokine Growth Factor Rev* **9**, 259-275.

- Benveniste EN & Benos DJ. (1995). TNF-alpha- and IFN-gamma-mediated signal transduction pathways: effects on glial cell gene expression and function. *FASEB J* **9**, 1577-1584.
- Beutler B, Du X & Poltorak A. (2001). Identification of Toll-like receptor 4 (Tlr4) as the sole conduit for LPS signal transduction: genetic and evolutionary studies. *J Endotoxin Res* **7**, 277-280.
- Bickel U, Grave B, Kang YS, del Rey A & Voigt K. (1998). No increase in blood-brain barrier permeability after intraperitoneal injection of endotoxin in the rat. *J Neuroimmunol* **85**, 131-136.
- Biella G & de Curtis M. (2000). Olfactory inputs activate the medial entorhinal cortex via the hippocampus. *J Neurophysiol* **83**, 1924-1931.
- Biamond P, van Eijk HG, Swaak AJ & Koster JF. (1984). Iron mobilization from ferritin by superoxide derived from stimulated polymorphonuclear leukocytes. Possible mechanism in inflammation diseases. *J Clin Invest* **73**, 1576-1579.
- Blamire AM, Anthony DC, Rajagopalan B, Sibson NR, Perry VH & Styles P. (2000). Interleukin-1beta -induced changes in blood-brain barrier permeability, apparent diffusion coefficient, and cerebral blood volume in the rat brain: a magnetic resonance study. *J Neurosci* **20**, 8153-8159.
- Bluthe RM, Dantzer R & Kelley KW. (1992). Effects of interleukin-1 receptor antagonist on the behavioral effects of lipopolysaccharide in rat. *Brain Res* **573**, 318-320.
- Boddaert N, Chabane N, Gervais H, Good CD, Bourgeois M, Plumet MH, Barthelemy C, Mouren MC, Artiges E, Samson Y, Brunelle F, Frackowiak RS & Zilbovicius M. (2004). Superior temporal sulcus anatomical abnormalities in childhood autism: a voxel-based morphometry MRI study. *Neuroimage* **23**, 364-369.

- Boje KM & Lakhman SS. (2000). Nitric oxide redox species exert differential permeability effects on the blood-brain barrier. *J Pharmacol Exp Ther* **293**, 545-550.
- Bowman CC, Rasley A, Tranguch SL & Marriott I. (2003). Cultured astrocytes express toll-like receptors for bacterial products. *Glia* **43**, 281-291.
- Boyle EM, Jr., Pohlman TH, Johnson MC & Verrier ED. (1997). Endothelial cell injury in cardiovascular surgery: the systemic inflammatory response. *Ann Thorac Surg* **63**, 277-284.
- Braakman N, Matysik J, van Duinen SG, Verbeek F, Schliebs R, de Groot HJ & Alia A. (2006). Longitudinal assessment of Alzheimer's beta-amyloid plaque development in transgenic mice monitored by in vivo magnetic resonance microimaging. *J Magn Reson Imaging* **24**, 530-536.
- Brahmachari S, Fung YK & Pahan K. (2006). Induction of glial fibrillary acidic protein expression in astrocytes by nitric oxide. *J Neurosci* **26**, 4930-4939.
- Briellmann RS, Kalnins RM, Berkovic SF & Jackson GD. (2002). Hippocampal pathology in refractory temporal lobe epilepsy: T2-weighted signal change reflects dentate gliosis. *Neurology* **58**, 265-271.
- Broderick C, Hoek RM, Forrester JV, Liversidge J, Sedgwick JD & Dick AD. (2002). Constitutive retinal CD200 expression regulates resident microglia and activation state of inflammatory cells during experimental autoimmune uveoretinitis. *Am J Pathol* **161**, 1669-1677.
- Broom KA, Anthony DC, Blamire AM, Waters S, Styles P, Perry VH & Sibson NR. (2005). MRI reveals that early changes in cerebral blood volume precede blood-brain barrier breakdown and overt pathology in MS-like lesions in rat brain. *J Cereb Blood Flow Metab* **25**, 204-216.

- Bruck W, Bitsch A, Kolenda H, Bruck Y, Stiefel M & Lassmann H. (1997). Inflammatory central nervous system demyelination: correlation of magnetic resonance imaging findings with lesion pathology. *Ann Neurol* **42**, 783-793.
- Bruck W & Stadelmann C. (2003). Inflammation and degeneration in multiple sclerosis. *Neurol Sci* **24 Suppl 5**, S265-267.
- Brugg B, Dubreuil YL, Huber G, Wollman EE, Delhay-Bouchaud N & Mariani J. (1995). Inflammatory processes induce beta-amyloid precursor protein changes in mouse brain. *Proc Natl Acad Sci U S A* **92**, 3032-3035.
- Bruunsgaard H, Pedersen M & Pedersen BK. (2001). Aging and proinflammatory cytokines. *Curr Opin Hematol* **8**, 131-136.
- Burton EJ, McKeith IG, Burn DJ, Williams ED & O'Brien JT. (2004). Cerebral atrophy in Parkinson's disease with and without dementia: a comparison with Alzheimer's disease, dementia with Lewy bodies and controls. *Brain* **127**, 791-800.
- Butt AM, Jones HC & Abbott NJ. (1990). Electrical resistance across the blood-brain barrier in anaesthetized rats: a developmental study. *J Physiol* **429**, 47-62.
- Cai Z, Lin S, Pang Y & Rhodes PG. (2004). Brain injury induced by intracerebral injection of interleukin-1beta and tumor necrosis factor-alpha in the neonatal rat. *Pediatr Res* **56**, 377-384.
- Campbell M, Humphries MM, Kiang AS, Nguyen AT, Gobbo OL, Tam LC, Suzuki M, Hanrahan F, Ozaki E, Farrar GJ, Kenna PF & Humphries P. (2011). Systemic low-molecular weight drug delivery to pre-selected neuronal regions. *EMBO Mol Med* **3**, 235-245.

- Campbell M, Kiang AS, Kenna PF, Kerskens C, Blau C, O'Dwyer L, Tivnan A, Kelly JA, Brankin B, Farrar GJ & Humphries P. (2008). RNAi-mediated reversible opening of the blood-brain barrier. *J Gene Med* **10**, 930-947.
- Campbell M, Nguyen AT, Kiang AS, Tam LC, Gobbo OL, Kerskens C, Ni Dhubhghail S, Humphries MM, Farrar GJ, Kenna PF & Humphries P. (2009). An experimental platform for systemic drug delivery to the retina. *Proc Natl Acad Sci U S A* **106**, 17817-17822.
- Campbell M, Ozaki E & Humphries P. (2010). Systemic delivery of therapeutics to neuronal tissues: a barrier modulation approach. *Expert Opin Drug Deliv* **7**, 859-869.
- Canady KS, Hyson RL & Rubel EW. (1994). The astrocytic response to afferent activity blockade in chick nucleus magnocellularis is independent of synaptic activation, age, and neuronal survival. *J Neurosci* **14**, 5973-5985.
- Carson MJ & Sutcliffe JG. (1999). Balancing function vs. self defense: the CNS as an active regulator of immune responses. *J Neurosci Res* **55**, 1-8.
- Carswell EA, Old LJ, Kassel RL, Green S, Fiore N & Williamson B. (1975). An endotoxin-induced serum factor that causes necrosis of tumors. *Proc Natl Acad Sci U S A* **72**, 3666-3670.
- Caviness VS, Jr., Lange NT, Makris N, Herbert MR & Kennedy DN. (1999). MRI-based brain volumetrics: emergence of a developmental brain science. *Brain Dev* **21**, 289-295.
- Cella M, Scheidegger D, Palmer-Lehmann K, Lane P, Lanzavecchia A & Alber G. (1996). Ligation of CD40 on dendritic cells triggers production of high levels of interleukin-12 and enhances T cell stimulatory capacity: T-T help via APC activation. *J Exp Med* **184**, 747-752.

- Chan A, Magnus T & Gold R. (2001). Phagocytosis of apoptotic inflammatory cells by microglia and modulation by different cytokines: mechanism for removal of apoptotic cells in the inflamed nervous system. *Glia* **33**, 87-95.
- Chapman PF, White GL, Jones MW, Cooper-Blacketer D, Marshall VJ, Irizarry M, Younkin L, Good MA, Bliss TV, Hyman BT, Younkin SG & Hsiao KK. (1999). Impaired synaptic plasticity and learning in aged amyloid precursor protein transgenic mice. *Nat Neurosci* **2**, 271-276.
- Chen G & Goeddel DV. (2002). TNF-R1 signaling: a beautiful pathway. *Science* **296**, 1634-1635.
- Chen K, Iribarren P, Hu J, Chen J, Gong W, Cho EH, Lockett S, Dunlop NM & Wang JM. (2006). Activation of Toll-like receptor 2 on microglia promotes cell uptake of Alzheimer disease-associated amyloid beta peptide. *J Biol Chem* **281**, 3651-3659.
- Chen S, Le WD, Xie WJ, Alexianu ME, Engelhardt JI, Siklos L & Appel SH. (1998). Experimental destruction of substantia nigra initiated by Parkinson disease immunoglobulins. *Arch Neurol* **55**, 1075-1080.
- Chen Y & Swanson RA. (2003). Astrocytes and brain injury. *J Cereb Blood Flow Metab* **23**, 137-149.
- Chitnis T, Imitola J, Wang Y, Elyaman W, Chawla P, Sharuk M, Raddassi K, Bronson RT & Khoury SJ. (2007). Elevated neuronal expression of CD200 protects Wlds mice from inflammation-mediated neurodegeneration. *Am J Pathol* **170**, 1695-1712.
- Cho S, Jones D, Reddick WE, Ogg RJ & Steen RG. (1997). Establishing norms for age-related changes in proton T1 of human brain tissue in vivo. *Magn Reson Imaging* **15**, 1133-1143.

- Chow JC, Young DW, Golenbock DT, Christ WJ & Gusovsky F. (1999). Toll-like receptor-4 mediates lipopolysaccharide-induced signal transduction. *J Biol Chem* **274**, 10689-10692.
- Chung DW, Yoo KY, Hwang IK, Kim DW, Chung JY, Lee CH, Choi JH, Choi SY, Youn HY, Lee IS & Won MH. (2010). Systemic administration of lipopolysaccharide induces cyclooxygenase-2 immunoreactivity in endothelium and increases microglia in the mouse hippocampus. *Cell Mol Neurobiol* **30**, 531-541.
- Combrinck MI, Perry VH & Cunningham C. (2002). Peripheral infection evokes exaggerated sickness behaviour in pre-clinical murine prion disease. *Neuroscience* **112**, 7-11.
- Conde JR & Streit WJ. (2006). Microglia in the aging brain. *J Neuropathol Exp Neurol* **65**, 199-203.
- Connor JR, Menzies SL, St Martin SM & Mufson EJ. (1990). Cellular distribution of transferrin, ferritin, and iron in normal and aged human brains. *J Neurosci Res* **27**, 595-611.
- Copland DA, Calder CJ, Raveney BJ, Nicholson LB, Phillips J, Cherwinski H, Jenmalm M, Sedgwick JD & Dick AD. (2007). Monoclonal antibody-mediated CD200 receptor signaling suppresses macrophage activation and tissue damage in experimental autoimmune uveoretinitis. *Am J Pathol* **171**, 580-588.
- Costello DA, Lyons A, Browne T, Denieffe S, Cox FF & Lynch MA. (2011). Long-term potentiation is impaired in CD200-deficient mice: a role for Toll-like receptor activation. *J Biol Chem*.
- Cotrina ML & Nedergaard M. (2002). Astrocytes in the aging brain. *J Neurosci Res* **67**, 1-10.

- Cowley TR, O'Sullivan J, Blau C, Deighan BF, Jones R, Kerskens C, Richardson JC, Virley D, Upton N & Lynch MA. (2010). Rosiglitazone attenuates the age-related changes in astrocytosis and the deficit in LTP. *Neurobiol Aging*.
- D'Aversa TG, Weidenheim KM & Berman JW. (2002). CD40-CD40L interactions induce chemokine expression by human microglia: implications for human immunodeficiency virus encephalitis and multiple sclerosis. *Am J Pathol* **160**, 559-567.
- D'Esposito M, Deouell LY & Gazzaley A. (2003). Alterations in the BOLD fMRI signal with ageing and disease: a challenge for neuroimaging. *Nat Rev Neurosci* **4**, 863-872.
- Dantzer R. (2001). Cytokine-induced sickness behavior: where do we stand? *Brain Behav Immun* **15**, 7-24.
- Dantzer R, O'Connor JC, Freund GG, Johnson RW & Kelley KW. (2008). From inflammation to sickness and depression: when the immune system subjugates the brain. *Nat Rev Neurosci* **9**, 46-56.
- Dar MS. (1997). Mouse cerebellar adenosinergic modulation of ethanol-induced motor incoordination: possible involvement of cAMP. *Brain Res* **749**, 263-274.
- Davis GW. (2006). Homeostatic control of neural activity: from phenomenology to molecular design. *Annu Rev Neurosci* **29**, 307-323.
- de Armond SJ, Eng LF & Rubinstein LJ. (1980). The application of glial fibrillary acidic (GFA) protein immunohistochemistry in neurooncology. A progress report. *Pathol Res Pract* **168**, 374-394.
- Deakin AM, Payne AN, Whittle BJ & Moncada S. (1995). The modulation of IL-6 and TNF-alpha release by nitric oxide following stimulation of J774 cells with LPS and IFN-gamma. *Cytokine* **7**, 408-416.

- Deane R, Bell RD, Sagare A & Zlokovic BV. (2009). Clearance of amyloid-beta peptide across the blood-brain barrier: implication for therapies in Alzheimer's disease. *CNS Neurol Disord Drug Targets* **8**, 16-30.
- Deckert M, Sedgwick JD, Fischer E & Schluter D. (2006). Regulation of microglial cell responses in murine Toxoplasma encephalitis by CD200/CD200 receptor interaction. *Acta Neuropathol* **111**, 548-558.
- Deutsch LH, Bylsma FW, Rovner BW, Steele C & Folstein MF. (1991). Psychosis and physical aggression in probable Alzheimer's disease. *Am J Psychiatry* **148**, 1159-1163.
- DeWitt DA, Perry G, Cohen M, Doller C & Silver J. (1998). Astrocytes regulate microglial phagocytosis of senile plaque cores of Alzheimer's disease. *Exp Neurol* **149**, 329-340.
- Diamond MS, Garcia-Aguilar J, Bickford JK, Corbi AL & Springer TA. (1993). The I domain is a major recognition site on the leukocyte integrin Mac-1 (CD11b/CD18) for four distinct adhesion ligands. *J Cell Biol* **120**, 1031-1043.
- DiCarlo G, Wilcock D, Henderson D, Gordon M & Morgan D. (2001). Intrahippocampal LPS injections reduce Abeta load in APP+PS1 transgenic mice. *Neurobiol Aging* **22**, 1007-1012.
- Dickstein DL, Biron KE, Ujiie M, Pfeifer CG, Jeffries AR & Jefferies WA. (2006). Abeta peptide immunization restores blood-brain barrier integrity in Alzheimer disease. *FASEB J* **20**, 426-433.
- Dinarello CA. (1992). The biology of interleukin-1. *Chem Immunol* **51**, 1-32.
- Dinarello CA. (1994). The biological properties of interleukin-1. *Eur Cytokine Netw* **5**, 517-531.

- Ding XQ, Kucinski T, Wittkugel O, Goebell E, Grzyska U, Gorg M, Kohlschutter A & Zeumer H. (2004). Normal brain maturation characterized with age-related T2 relaxation times: an attempt to develop a quantitative imaging measure for clinical use. *Invest Radiol* **39**, 740-746.
- Dixon WT, Du LN, Faul DD, Gado M & Rossnick S. (1986). Projection angiograms of blood labeled by adiabatic fast passage. *Magn Reson Med* **3**, 454-462.
- Dong Y & Benveniste EN. (2001). Immune function of astrocytes. *Glia* **36**, 180-190.
- Dousset V, Ballarino L, Delalande C, Coussemacq M, Canioni P, Petry KG & Caille JM. (1999). Comparison of ultrasmall particles of iron oxide (USPIO)-enhanced T2-weighted, conventional T2-weighted, and gadolinium-enhanced T1-weighted MR images in rats with experimental autoimmune encephalomyelitis. *AJNR Am J Neuroradiol* **20**, 223-227.
- Downer EJ, Cowley TR, Lyons A, Mills KH, Berezin V, Bock E & Lynch MA. (2010). A novel anti-inflammatory role of NCAM-derived mimetic peptide, FGL. *Neurobiol Aging* **31**, 118-128.
- Drewes G, Ebneith A & Mandelkow EM. (1998). MAPs, MARKs and microtubule dynamics. *Trends Biochem Sci* **23**, 307-311.
- Driscoll I, Howard SR, Stone JC, Monfils MH, Tomanek B, Brooks WM & Sutherland RJ. (2006). The aging hippocampus: a multi-level analysis in the rat. *Neuroscience* **139**, 1173-1185.
- Du X, Poltorak A, Silva M & Beutler B. (1999). Analysis of Tlr4-mediated LPS signal transduction in macrophages by mutational modification of the receptor. *Blood Cells Mol Dis* **25**, 328-338.

- Duering M, Grimm MO, Grimm HS, Schroder J & Hartmann T. (2005). Mean age of onset in familial Alzheimer's disease is determined by amyloid beta 42. *Neurobiol Aging* **26**, 785-788.
- Eikelenboom P, Bate C, Van Gool WA, Hoozemans JJ, Rozemuller JM, Veerhuis R & Williams A. (2002). Neuroinflammation in Alzheimer's disease and prion disease. *Glia* **40**, 232-239.
- El Tannir El Tayara N, Delatour B, Le Cudennec C, Guegan M, Volk A & Dhenain M. (2006). Age-related evolution of amyloid burden, iron load, and MR relaxation times in a transgenic mouse model of Alzheimer's disease. *Neurobiol Dis* **22**, 199-208.
- El Tayara Nel T, Volk A, Dhenain M & Delatour B. (2007). Transverse relaxation time reflects brain amyloidosis in young APP/PS1 transgenic mice. *Magn Reson Med* **58**, 179-184.
- Ellis RJ, Olichney JM, Thal LJ, Mirra SS, Morris JC, Beekly D & Heyman A. (1996). Cerebral amyloid angiopathy in the brains of patients with Alzheimer's disease: the CERAD experience, Part XV. *Neurology* **46**, 1592-1596.
- Eng LF. (1985). Glial fibrillary acidic protein (GFAP): the major protein of glial intermediate filaments in differentiated astrocytes. *J Neuroimmunol* **8**, 203-214.
- Ershler WB & Keller ET. (2000). Age-associated increased interleukin-6 gene expression, late-life diseases, and frailty. *Annu Rev Med* **51**, 245-270.
- Evin G, Zhu A, Holsinger RM, Masters CL & Li QX. (2003). Proteolytic processing of the Alzheimer's disease amyloid precursor protein in brain and platelets. *J Neurosci Res* **74**, 386-392.

- Falangola MF, Dyakin VV, Lee SP, Bogart A, Babb JS, Duff K, Nixon R & Helpert JA. (2007). Quantitative MRI reveals aging-associated T2 changes in mouse models of Alzheimer's disease. *NMR Biomed* **20**, 343-351.
- Falangola MF, Lee SP, Nixon RA, Duff K & Helpert JA. (2005). Histological co-localization of iron in Aβ plaques of PS/APP transgenic mice. *Neurochem Res* **30**, 201-205.
- Fann MJ & Patterson PH. (1994). Neurotrophic cytokines and activin A differentially regulate the phenotype of cultured sympathetic neurons. *Proc Natl Acad Sci U S A* **91**, 43-47.
- Fantuzzi G, Zheng H, Faggioni R, Benigni F, Ghezzi P, Sipe JD, Shaw AR & Dinarello CA. (1996). Effect of endotoxin in IL-1 beta-deficient mice. *J Immunol* **157**, 291-296.
- Farquhar MG & Palade GE. (1963). Junctional complexes in various epithelia. *J Cell Biol* **17**, 375-412.
- Fassbender K, Walter S, Kuhl S, Landmann R, Ishii K, Bertsch T, Stalder AK, Muehlhauser F, Liu Y, Ulmer AJ, Rivest S, Lentsch A, Gulbins E, Jucker M, Staufenbiel M, Brechtel K, Walter J, Multhaup G, Penke B, Adachi Y, Hartmann T & Beyreuther K. (2004). The LPS receptor (CD14) links innate immunity with Alzheimer's disease. *FASEB J* **18**, 203-205.
- Fattori E, Cappelletti M, Costa P, Sellitto C, Cantoni L, Carelli M, Faggioni R, Fantuzzi G, Ghezzi P & Poli V. (1994). Defective inflammatory response in interleukin 6-deficient mice. *J Exp Med* **180**, 1243-1250.
- Faure A, Verret L, Bozon B, El Tannir El Tayara N, Ly M, Kober F, Dhenain M, Rampon C & Delatour B. (2011). Impaired neurogenesis, neuronal loss, and brain functional deficits in the APPxPS1-Ki mouse model of Alzheimer's disease. *Neurobiol Aging* **32**, 407-418.

- Feuer R. (2007). Tickling the CD200 receptor: A remedy for those irritating macrophages. *Am J Pathol* **171**, 396-398.
- Fisher E, Rudick RA, Simon JH, Cutter G, Baier M, Lee JC, Miller D, Weinstock-Guttman B, Mass MK, Dougherty DS & Simonian NA. (2002). Eight-year follow-up study of brain atrophy in patients with MS. *Neurology* **59**, 1412-1420.
- Fliegner KH & Liem RK. (1991). Cellular and molecular biology of neuronal intermediate filaments. *Int Rev Cytol* **131**, 109-167.
- Floyd RA & Carney JM. (1991). Age influence on oxidative events during brain ischemia/reperfusion. *Arch Gerontol Geriatr* **12**, 155-177.
- Fox NC, Warrington EK, Freeborough PA, Hartikainen P, Kennedy AM, Stevens JM & Rossor MN. (1996). Presymptomatic hippocampal atrophy in Alzheimer's disease. A longitudinal MRI study. *Brain* **119 (Pt 6)**, 2001-2007.
- Frei K, Siepl C, Groscurth P, Bodmer S, Schwerdel C & Fontana A. (1987). Antigen presentation and tumor cytotoxicity by interferon-gamma-treated microglial cells. *Eur J Immunol* **17**, 1271-1278.
- Fujioka M, Taoka T, Matsuo Y, Mishima K, Ogoshi K, Kondo Y, Tsuda M, Fujiwara M, Asano T, Sakaki T, Miyasaki A, Park D & Siesjo BK. (2003). Magnetic resonance imaging shows delayed ischemic striatal neurodegeneration. *Ann Neurol* **54**, 732-747.
- Fulton D, Gratton JP, McCabe TJ, Fontana J, Fujio Y, Walsh K, Franke TF, Papapetropoulos A & Sessa WC. (1999). Regulation of endothelium-derived nitric oxide production by the protein kinase Akt. *Nature* **399**, 597-601.

- Furuse M, Hirase T, Itoh M, Nagafuchi A, Yonemura S & Tsukita S. (1993). Occludin: a novel integral membrane protein localizing at tight junctions. *J Cell Biol* **123**, 1777-1788.
- Gadient RA & Otten U. (1994). Identification of interleukin-6 (IL-6)-expressing neurons in the cerebellum and hippocampus of normal adult rats. *Neurosci Lett* **182**, 243-246.
- Gadient RA & Otten UH. (1997). Interleukin-6 (IL-6)--a molecule with both beneficial and destructive potentials. *Prog Neurobiol* **52**, 379-390.
- Gaillard PJ, de Boer AB & Breimer DD. (2003). Pharmacological investigations on lipopolysaccharide-induced permeability changes in the blood-brain barrier in vitro. *Microvasc Res* **65**, 24-31.
- Gasperini C, Paolillo A, Giugni E, Galgani S, Bagnato F, Mainero C, Onesti E, Bastianello S & Pozzilli C. (2002). MRI brain volume changes in relapsing-remitting multiple sclerosis patients treated with interferon beta-1a. *Mult Scler* **8**, 119-123.
- Gatehouse PD & Bydder GM. (2003). Magnetic resonance imaging of short T2 components in tissue. *Clin Radiol* **58**, 1-19.
- Geinisman Y, Detoledo-Morrell L, Morrell F & Heller RE. (1995). Hippocampal markers of age-related memory dysfunction: behavioral, electrophysiological and morphological perspectives. *Prog Neurobiol* **45**, 223-252.
- Gerlach M, Ben-Shachar D, Riederer P & Youdim MB. (1994). Altered brain metabolism of iron as a cause of neurodegenerative diseases? *J Neurochem* **63**, 793-807.
- Giulian D, Vaca K & Corpuz M. (1993). Brain glia release factors with opposing actions upon neuronal survival. *J Neurosci* **13**, 29-37.

- Godbout JP & Johnson RW. (2004). Interleukin-6 in the aging brain. *J Neuroimmunol* **147**, 141-144.
- Golde DW & Gasson JC. (1988). Hormones that stimulate the growth of blood cells. *Sci Am* **259**, 62-71.
- Goldmann E. (1913). Vitalfa"rbung am Zentralnervensystem. *Abhandl Konigl preuss Akad Wiss.*
- Gomi H, Yokoyama T, Fujimoto K, Ikeda T, Katoh A, Itoh T & Itohara S. (1995). Mice devoid of the glial fibrillary acidic protein develop normally and are susceptible to scrapie prions. *Neuron* **14**, 29-41.
- Gonzalez-Scarano F & Baltuch G. (1999). Microglia as mediators of inflammatory and degenerative diseases. *Annu Rev Neurosci* **22**, 219-240.
- Good CD, Johnsrude IS, Ashburner J, Henson RN, Friston KJ & Frackowiak RS. (2001). A voxel-based morphometric study of ageing in 465 normal adult human brains. *Neuroimage* **14**, 21-36.
- Gorczynski R, Chen Z, Kai Y, Lee L, Wong S & Marsden PA. (2004a). CD200 is a ligand for all members of the CD200R family of immunoregulatory molecules. *J Immunol* **172**, 7744-7749.
- Gorczynski RM, Chen Z, Clark DA, Kai Y, Lee L, Nachman J, Wong S & Marsden P. (2004b). Structural and functional heterogeneity in the CD200R family of immunoregulatory molecules and their expression at the fetomaternal interface. *Am J Reprod Immunol* **52**, 147-163.
- Gorczynski RM, Chen Z, Lee L, Yu K & Hu J. (2002). Anti-CD200R ameliorates collagen-induced arthritis in mice. *Clin Immunol* **104**, 256-264.

- Gordon MN, Holcomb LA, Jantzen PT, DiCarlo G, Wilcock D, Boyett KW, Connor K, Melachrinou J, O'Callaghan JP & Morgan D. (2002). Time course of the development of Alzheimer-like pathology in the doubly transgenic PS1+APP mouse. *Exp Neurol* **173**, 183-195.
- Greenfield JP, Tsai J, Gouras GK, Hai B, Thinakaran G, Checler F, Sisodia SS, Greengard P & Xu H. (1999). Endoplasmic reticulum and trans-Golgi network generate distinct populations of Alzheimer beta-amyloid peptides. *Proc Natl Acad Sci U S A* **96**, 742-747.
- Griffin R, Nally R, Nolan Y, McCartney Y, Linden J & Lynch MA. (2006). The age-related attenuation in long-term potentiation is associated with microglial activation. *J Neurochem* **99**, 1263-1272.
- Griffin WS, Sheng JG, Royston MC, Gentleman SM, McKenzie JE, Graham DI, Roberts GW & Mrazek RE. (1998). Glial-neuronal interactions in Alzheimer's disease: the potential role of a 'cytokine cycle' in disease progression. *Brain Pathol* **8**, 65-72.
- Guha M & Mackman N. (2001). LPS induction of gene expression in human monocytes. *Cell Signal* **13**, 85-94.
- Guix FX, Uribealago I, Coma M & Munoz FJ. (2005). The physiology and pathophysiology of nitric oxide in the brain. *Prog Neurobiol* **76**, 126-152.
- Haacke EM, Cheng NY, House MJ, Liu Q, Neelavalli J, Ogg RJ, Khan A, Ayaz M, Kirsch W & Obenaus A. (2005). Imaging iron stores in the brain using magnetic resonance imaging. *Magn Reson Imaging* **23**, 1-25.
- Haas J, Storch-Hagenlocher B, Biessmann A & Wildemann B. (2002). Inducible nitric oxide synthase and argininosuccinate synthetase: co-induction in brain tissue of patients with Alzheimer's dementia and following stimulation with beta-amyloid 1-42 in vitro. *Neurosci Lett* **322**, 121-125.

- Haass C, Schlossmacher MG, Hung AY, Vigo-Pelfrey C, Mellon A, Ostaszewski BL, Lieberburg I, Koo EH, Schenk D, Teplow DB & et al. (1992). Amyloid beta-peptide is produced by cultured cells during normal metabolism. *Nature* **359**, 322-325.
- Haga S, Akai K & Ishii T. (1989). Demonstration of microglial cells in and around senile (neuritic) plaques in the Alzheimer brain. An immunohistochemical study using a novel monoclonal antibody. *Acta Neuropathol* **77**, 569-575.
- Hall KE, Sheng HC, Srinivasan S, Spitsbergen JM, Tuttle JB, Steers WD & Wiley JW. (2001). Treatment of aged rat sensory neurons in short-term, serum-free culture with nerve growth factor reverses the effect of aging on neurite outgrowth, calcium currents, and neuronal survival. *Brain Res* **888**, 128-137.
- Hansen LA, Armstrong DM & Terry RD. (1987). An immunohistochemical quantification of fibrous astrocytes in the aging human cerebral cortex. *Neurobiol Aging* **8**, 1-6.
- Haorah J, Knipe B, Leibhart J, Ghorpade A & Persidsky Y. (2005). Alcohol-induced oxidative stress in brain endothelial cells causes blood-brain barrier dysfunction. *J Leukoc Biol* **78**, 1223-1232.
- Hardy JA & Higgins GA. (1992). Alzheimer's disease: the amyloid cascade hypothesis. *Science* **256**, 184-185.
- Harman D. (1956). Aging: a theory based on free radical and radiation chemistry. *J Gerontol* **11**, 298-300.
- Harnett MM. (2004). CD40: a growing cytoplasmic tale. *Sci STKE* **2004**, pe25.

- Harris GJ, Lewis RF, Satlin A, English CD, Scott TM, Yurgelun-Todd DA & Renshaw PF. (1996). Dynamic susceptibility contrast MRI of regional cerebral blood volume in Alzheimer's disease. *Am J Psychiatry* **153**, 721-724.
- Hashimoto C, Hudson KL & Anderson KV. (1988a). The Toll gene of *Drosophila*, required for dorsal-ventral embryonic polarity, appears to encode a transmembrane protein. *Cell* **52**, 269-279.
- Hashimoto K, Yamagata S, Minamikawa J, Watanabe Y, Kaneshiro M & Kikuchi H. (1988b). [The effect of Gd-DTPA on magnetic resonance imaging: a potential blood-brain barrier indicator]. *No To Shinkei* **40**, 461-466.
- Hattiangady B & Shetty AK. (2008). Aging does not alter the number or phenotype of putative stem/progenitor cells in the neurogenic region of the hippocampus. *Neurobiol Aging* **29**, 129-147.
- Heiland S, Sartor K, Martin E, Bardenheuer HJ & Plaschke K. (2002). In vivo monitoring of age-related changes in rat brain using quantitative diffusion magnetic resonance imaging and magnetic resonance relaxometry. *Neurosci Lett* **334**, 157-160.
- Heinrich PC, Behrmann I, Haan S, Hermanns HM, Muller-Newen G & Schaper F. (2003). Principles of interleukin (IL)-6-type cytokine signalling and its regulation. *Biochem J* **374**, 1-20.
- Helpert JA, Lee SP, Falangola MF, Dyakin VV, Bogart A, Ardekani B, Duff K, Branch C, Wisniewski T, de Leon MJ, Wolf O, O'Shea J & Nixon RA. (2004). MRI assessment of neuropathology in a transgenic mouse model of Alzheimer's disease. *Magn Reson Med* **51**, 794-798.
- Henry CJ, Huang Y, Wynne AM & Godbout JP. (2009). Peripheral lipopolysaccharide (LPS) challenge promotes microglial hyperactivity in aged mice that is

associated with exaggerated induction of both pro-inflammatory IL-1beta and anti-inflammatory IL-10 cytokines. *Brain Behav Immun* **23**, 309-317.

Hickey WF & Kimura H. (1988). Perivascular microglial cells of the CNS are bone marrow-derived and present antigen in vivo. *Science* **239**, 290-292.

Hide I, Tanaka M, Inoue A, Nakajima K, Kohsaka S, Inoue K & Nakata Y. (2000). Extracellular ATP triggers tumor necrosis factor-alpha release from rat microglia. *J Neurochem* **75**, 965-972.

Hideshima T, Nakamura N, Chauhan D & Anderson KC. (2001). Biologic sequelae of interleukin-6 induced PI3-K/Akt signaling in multiple myeloma. *Oncogene* **20**, 5991-6000.

Hirsch EC, Hunot S, Damier P & Faucheux B. (1998). Glial cells and inflammation in Parkinson's disease: a role in neurodegeneration? *Ann Neurol* **44**, S115-120.

Hoek RM, Ruuls SR, Murphy CA, Wright GJ, Goddard R, Zurawski SM, Blom B, Homola ME, Streit WJ, Brown MH, Barclay AN & Sedgwick JD. (2000). Down-regulation of the macrophage lineage through interaction with OX2 (CD200). *Science* **290**, 1768-1771.

Hofman FM, Hinton DR, Johnson K & Merrill JE. (1989). Tumor necrosis factor identified in multiple sclerosis brain. *J Exp Med* **170**, 607-612.

Hornak JP. (1996). *The Basics of MRI*.

Hu J, Akama KT, Krafft GA, Chromy BA & Van Eldik LJ. (1998). Amyloid-beta peptide activates cultured astrocytes: morphological alterations, cytokine induction and nitric oxide release. *Brain Res* **785**, 195-206.

Hunter RL, Liu M, Choi DY, Cass WA & Bing G. (2008). Inflammation and age-related iron accumulation in F344 rats. *Curr Aging Sci* **1**, 112-121.

- Idriss HT & Naismith JH. (2000). TNF alpha and the TNF receptor superfamily: structure-function relationship(s). *Microsc Res Tech* **50**, 184-195.
- Imon Y, Yamaguchi S, Katayama S, Oka M, Murata Y, Kajima T, Yamamura Y & Nakamura S. (1998). A decrease in cerebral cortex intensity on T2-weighted with ageing images of normal subjects. *Neuroradiology* **40**, 76-80.
- Ingelsson M, Fukumoto H, Newell KL, Growdon JH, Hedley-Whyte ET, Frosch MP, Albert MS, Hyman BT & Irizarry MC. (2004). Early Abeta accumulation and progressive synaptic loss, gliosis, and tangle formation in AD brain. *Neurology* **62**, 925-931.
- Iravani MM, Leung CC, Sadeghian M, Haddon CO, Rose S & Jenner P. (2005). The acute and the long-term effects of nigral lipopolysaccharide administration on dopaminergic dysfunction and glial cell activation. *Eur J Neurosci* **22**, 317-330.
- Jack CR, Jr., Wengenack TM, Reyes DA, Garwood M, Curran GL, Borowski BJ, Lin J, Preboske GM, Holasek SS, Adriany G & Poduslo JF. (2005a). In vivo magnetic resonance microimaging of individual amyloid plaques in Alzheimer's transgenic mice. *J Neurosci* **25**, 10041-10048.
- Jack CS, Arbour N, Manusow J, Montgrain V, Blain M, McCrea E, Shapiro A & Antel JP. (2005b). TLR signaling tailors innate immune responses in human microglia and astrocytes. *J Immunol* **175**, 4320-4330.
- Jacobs RE & Cherry SR. (2001). Complementary emerging techniques: high-resolution PET and MRI. *Curr Opin Neurobiol* **11**, 621-629.
- Jana M, Palencia CA & Pahan K. (2008). Fibrillar amyloid-beta peptides activate microglia via TLR2: implications for Alzheimer's disease. *J Immunol* **181**, 7254-7262.

- Janeway CA, Jr. & Medzhitov R. (1998). Introduction: the role of innate immunity in the adaptive immune response. *Semin Immunol* **10**, 349-350.
- Jankowsky JL, Fadale DJ, Anderson J, Xu GM, Gonzales V, Jenkins NA, Copeland NG, Lee MK, Younkin LH, Wagner SL, Younkin SG & Borchelt DR. (2004). Mutant presenilins specifically elevate the levels of the 42 residue beta-amyloid peptide in vivo: evidence for augmentation of a 42-specific gamma secretase. *Hum Mol Genet* **13**, 159-170.
- Jarrett JT, Berger EP & Lansbury PT, Jr. (1993). The C-terminus of the beta protein is critical in amyloidogenesis. *Ann N Y Acad Sci* **695**, 144-148.
- Jellinger K, Paulus W, Grundke-Iqbal I, Riederer P & Youdim MB. (1990). Brain iron and ferritin in Parkinson's and Alzheimer's diseases. *J Neural Transm Park Dis Dement Sect* **2**, 327-340.
- Jenmalm MC, Cherwinski H, Bowman EP, Phillips JH & Sedgwick JD. (2006). Regulation of myeloid cell function through the CD200 receptor. *J Immunol* **176**, 191-199.
- Johnson FB, Sinclair DA & Guarente L. (1999). Molecular biology of aging. *Cell* **96**, 291-302.
- Justicia C, Ramos-Cabrer P & Hoehn M. (2008). MRI detection of secondary damage after stroke: chronic iron accumulation in the thalamus of the rat brain. *Stroke* **39**, 1541-1547.
- Kalaria RN & Hedera P. (1996). beta-Amyloid vasoactivity in Alzheimer's disease. *Lancet* **347**, 1492-1493.
- Kalehua AN, Taub DD, Baskar PV, Hengemihle J, Munoz J, Trambadia M, Speer DL, De Simoni MG & Ingram DK. (2000). Aged mice exhibit greater mortality concomitant to increased brain and plasma TNF-alpha levels following

intracerebroventricular injection of lipopolysaccharide. *Gerontology* **46**, 115-128.

Kamenetz F, Tomita T, Hsieh H, Seabrook G, Borchelt D, Iwatsubo T, Sisodia S & Malinow R. (2003). APP processing and synaptic function. *Neuron* **37**, 925-937.

Kaneko Y, Kitamoto T, Tateishi J & Yamaguchi K. (1989). Ferritin immunohistochemistry as a marker for microglia. *Acta Neuropathol* **79**, 129-136.

Kato K, Suzuki F, Morishita R, Asano T & Sato T. (1990). Selective increase in S-100 beta protein by aging in rat cerebral cortex. *J Neurochem* **54**, 1269-1274.

Kebir H, Kreymborg K, Ifergan I, Dodelet-Devillers A, Cayrol R, Bernard M, Giuliani F, Arbour N, Becher B & Prat A. (2007). Human TH17 lymphocytes promote blood-brain barrier disruption and central nervous system inflammation. *Nat Med* **13**, 1173-1175.

Kelly M, Blau C, Bechara R, Lynch M & Kerskens C. (2009b). Bolus-tracking arterial spin labeling; a new marker for age and age related diseases. *J Cereb Blood Flow Metab* **29**.

Kelly ME, Blau CW, Gobbo OL, Griffin KM, Jones JF & Kerskens CM. (2009a). Functional bolus-tracking arterial spin labeling: a new approach to quantitative fMRI. *Neuroimage* **47**.

Kelly ME, Blau CW, Griffin KM, Gobbo OL, Jones JF & Kerskens CM. (2010). Quantitative functional magnetic resonance imaging of brain activity using bolus-tracking arterial spin labeling. *J Cereb Blood Flow Metab* **30**, 913-922.

Kelly ME, Blau CW & Kerskens CM. (2009b). Bolus-tracking arterial spin labelling: theoretical and experimental results. *Phys Med Biol* **54**, 1235-1251.

- Kennedy DN, Makris N, Herbert MR, Takahashi T & Caviness VS, Jr. (2002). Basic principles of MRI and morphometry studies of human brain development. *Developmental Science* **5**, 268-278.
- Kennedy MB. (1989). Regulation of neuronal function by calcium. *Trends Neurosci* **12**, 417-420.
- Kent S, Bluth RM, Dantzer R, Hardwick AJ, Kelley KW, Rothwell NJ & Vannice JL. (1992). Different receptor mechanisms mediate the pyrogenic and behavioral effects of interleukin 1. *Proc Natl Acad Sci U S A* **89**, 9117-9120.
- Khanna R, Cooper L, Kienzle N, Moss DJ, Burrows SR & Khanna KK. (1997). Engagement of CD40 antigen with soluble CD40 ligand up-regulates peptide transporter expression and restores endogenous processing function in Burkitt's lymphoma cells. *J Immunol* **159**, 5782-5785.
- Kim KY, Kim MY, Choi HS, Jin BK, Kim SU & Lee YB. (2002). Thrombin induces IL-10 production in microglia as a negative feedback regulator of TNF- α release. *Neuroreport* **13**, 849-852.
- Kim SU & de Vellis J. (2005). Microglia in health and disease. *J Neurosci Res* **81**, 302-313.
- Kipp M, Norkute A, Johann S, Lorenz L, Braun A, Hieble A, Gingele S, Pott F, Richter J & Beyer C. (2008). Brain-region-specific astroglial responses in vitro after LPS exposure. *J Mol Neurosci* **35**, 235-243.
- Kircher MF, Mahmood U, King RS, Weissleder R & Josephson L. (2003). A multimodal nanoparticle for preoperative magnetic resonance imaging and intraoperative optical brain tumor delineation. *Cancer Res* **63**, 8122-8125.
- Kitamura T. (1973). The origin of brain macrophages--some considerations on the microglia theory of Del Rio-Hortega. *Acta Pathol Jpn* **23**, 11-26.

- Klein C, Nekolla SG, Bengel FM, Momose M, Sammer A, Haas F, Schnackenburg B, Delius W, Mudra H, Wolfram D & Schwaiger M. (2002). Assessment of myocardial viability with contrast-enhanced magnetic resonance imaging: comparison with positron emission tomography. *Circulation* **105**, 162-167.
- Kleinman ME, Yamada K, Takeda A, Chandrasekaran V, Nozaki M, Baffi JZ, Albuquerque RJ, Yamasaki S, Itaya M, Pan Y, Appukuttan B, Gibbs D, Yang Z, Kariko K, Ambati BK, Wilgus TA, DiPietro LA, Sakurai E, Zhang K, Smith JR, Taylor EW & Ambati J. (2008). Sequence- and target-independent angiogenesis suppression by siRNA via TLR3. *Nature* **452**, 591-597.
- Kohama SG, Goss JR, Finch CE & McNeill TH. (1995). Increases of glial fibrillary acidic protein in the aging female mouse brain. *Neurobiol Aging* **16**, 59-67.
- Kondo Y, Ogawa N, Asanuma M, Ota Z & Mori A. (1995). Regional differences in late-onset iron deposition, ferritin, transferrin, astrocyte proliferation, and microglial activation after transient forebrain ischemia in rat brain. *J Cereb Blood Flow Metab* **15**, 216-226.
- Koning N, Swaab DF, Hoek RM & Huitinga I. (2009). Distribution of the immune inhibitory molecules CD200 and CD200R in the normal central nervous system and multiple sclerosis lesions suggests neuron-glia and glia-glia interactions. *J Neuropathol Exp Neurol* **68**, 159-167.
- Krasowska-Zoladek A, Banaszewska M, Kraszpulski M & Konat GW. (2007). Kinetics of inflammatory response of astrocytes induced by TLR 3 and TLR4 ligation. *J Neurosci Res* **85**, 205-212.
- Kreutzberg GW. (1996). Microglia: a sensor for pathological events in the CNS. *Trends Neurosci* **19**, 312-318.

- Krizbai IA, Bauer H, Bresgen N, Eckl PM, Farkas A, Szatmari E, Traweger A, Wejksza K & Bauer HC. (2005). Effect of oxidative stress on the junctional proteins of cultured cerebral endothelial cells. *Cell Mol Neurobiol* **25**, 129-139.
- Kubota K, Furuse M, Sasaki H, Sonoda N, Fujita K, Nagafuchi A & Tsukita S. (1999). Ca(2+)-independent cell-adhesion activity of claudins, a family of integral membrane proteins localized at tight junctions. *Curr Biol* **9**, 1035-1038.
- Laakso MP, Partanen K, Soininen H, Lehtovirta M, Hallikainen M, Hanninen T, Helkala EL, Vainio P & Riekkinen PJ, Sr. (1996). MR T2 relaxometry in Alzheimer's disease and age-associated memory impairment. *Neurobiol Aging* **17**, 535-540.
- Laporte V, Ait-Ghezala G, Volmar CH, Ganey C, Ganey N, Wood M & Mullan M. (2008). CD40 ligation mediates plaque-associated tau phosphorylation in beta-amyloid overproducing mice. *Brain Res* **1231**, 132-142.
- Larsson HB, Stubgaard M, Frederiksen JL, Jensen M, Henriksen O & Paulson OB. (1990). Quantitation of blood-brain barrier defect by magnetic resonance imaging and gadolinium-DTPA in patients with multiple sclerosis and brain tumors. *Magn Reson Med* **16**, 117-131.
- Lee CK, Weindruch R & Prolla TA. (2000). Gene-expression profile of the ageing brain in mice. *Nat Genet* **25**, 294-297.
- Lee JH, Silva AC, Merkle H & Koretsky AP. (2005). Manganese-enhanced magnetic resonance imaging of mouse brain after systemic administration of MnCl₂: dose-dependent and temporal evolution of T1 contrast. *Magn Reson Med* **53**, 640-648.
- Lee MA, Smith S, Palace J, Narayanan S, Silver N, Minicucci L, Filippi M, Miller DH, Arnold DL & Matthews PM. (1999). Spatial mapping of T2 and gadolinium-

enhancing T1 lesion volumes in multiple sclerosis: evidence for distinct mechanisms of lesion genesis? *Brain* **122** (Pt 7), 1261-1270.

Lemere CA. (2007). A beneficial role for IL-1 beta in Alzheimer disease? *J Clin Invest* **117**, 1483-1485.

Lemere CA, Lopera F, Kosik KS, Lendon CL, Ossa J, Saido TC, Yamaguchi H, Ruiz A, Martinez A, Madrigal L, Hincapie L, Arango JC, Anthony DC, Koo EH, Goate AM & Selkoe DJ. (1996). The E280A presenilin 1 Alzheimer mutation produces increased A beta 42 deposition and severe cerebellar pathology. *Nat Med* **2**, 1146-1150.

Letiembre M, Hao W, Liu Y, Walter S, Mihaljevic I, Rivest S, Hartmann T & Fassbender K. (2007). Innate immune receptor expression in normal brain aging. *Neuroscience* **146**, 248-254.

LeVine SM. (1997). Iron deposits in multiple sclerosis and Alzheimer's disease brains. *Brain Res* **760**, 298-303.

Liang Z & Lauterbur PC. (2000). *Principles of Magnetic Resonance Imaging: A Signal Processing Perspective*. IEEE Press Series in Biomedical Engineering.

Lieberman AP, Pitha PM, Shin HS & Shin ML. (1989). Production of tumor necrosis factor and other cytokines by astrocytes stimulated with lipopolysaccharide or a neurotropic virus. *Proc Natl Acad Sci U S A* **86**, 6348-6352.

Liedtke W, Edelmann W, Bieri PL, Chiu FC, Cowan NJ, Kucherlapati R & Raine CS. (1996). GFAP is necessary for the integrity of CNS white matter architecture and long-term maintenance of myelination. *Neuron* **17**, 607-615.

Lim DA, Huang YC & Alvarez-Buylla A. (2007). The adult neural stem cell niche: lessons for future neural cell replacement strategies. *Neurosurg Clin N Am* **18**, 81-92, ix.

- Lin YJ & Koretsky AP. (1997). Manganese ion enhances T1-weighted MRI during brain activation: an approach to direct imaging of brain function. *Magn Reson Med* **38**, 378-388.
- Ling EA & Wong WC. (1993). The origin and nature of ramified and amoeboid microglia: a historical review and current concepts. *Glia* **7**, 9-18.
- Linnemann D & Skarsfelt T. (1994). Regional changes in expression of NCAM, GFAP, and S100 in aging rat brain. *Neurobiol Aging* **15**, 651-655.
- Liu T, McDonnell PC, Young PR, White RF, Siren AL, Hallenbeck JM, Barone FC & Feurestein GZ. (1993). Interleukin-1 beta mRNA expression in ischemic rat cortex. *Stroke* **24**, 1746-1750; discussion 1750-1741.
- Liu Y, Bando Y, Vargas-Lowy D, Elyaman W, Khoury SJ, Huang T, Reif K & Chitnis T. (2010). CD200R1 agonist attenuates mechanisms of chronic disease in a murine model of multiple sclerosis. *J Neurosci* **30**, 2025-2038.
- Long JM, Kalehua AN, Muth NJ, Calhoun ME, Jucker M, Hengemihle JM, Ingram DK & Mouton PR. (1998). Stereological analysis of astrocyte and microglia in aging mouse hippocampus. *Neurobiol Aging* **19**, 497-503.
- Lopes KO, Sparks DL & Streit WJ. (2008). Microglial dystrophy in the aged and Alzheimer's disease brain is associated with ferritin immunoreactivity. *Glia* **56**, 1048-1060.
- Louis JC, Magal E, Takayama S & Varon S. (1993). CNTF protection of oligodendrocytes against natural and tumor necrosis factor-induced death. *Science* **259**, 689-692.

- Lue LF, Kuo YM, Roher AE, Brachova L, Shen Y, Sue L, Beach T, Kurth JH, Rydel RE & Rogers J. (1999). Soluble amyloid beta peptide concentration as a predictor of synaptic change in Alzheimer's disease. *Am J Pathol* **155**, 853-862.
- Lukiw WJ & Bazan NG. (2000). Neuroinflammatory signaling upregulation in Alzheimer's disease. *Neurochem Res* **25**, 1173-1184.
- Lund S, Christensen KV, Hedtjarn M, Mortensen AL, Hagberg H, Falsig J, Hasseldam H, Schrattenholz A, Porzgen P & Leist M. (2006). The dynamics of the LPS triggered inflammatory response of murine microglia under different culture and in vivo conditions. *J Neuroimmunol* **180**, 71-87.
- Lynch AM, Loane DJ, Minogue AM, Clarke RM, Kilroy D, Nally RE, Roche OJ, O'Connell F & Lynch MA. (2007). Eicosapentaenoic acid confers neuroprotection in the amyloid-beta challenged aged hippocampus. *Neurobiol Aging* **28**, 845-855.
- Lynch MA. (1999). What is the biological significance of an age-related increase in IL-1beta in hippocampus? *Mol Psychiatry* **4**, 15-18.
- Lynch MA. (2010). Age-related neuroinflammatory changes negatively impact on neuronal function. *Front Aging Neurosci* **1**, 6.
- Lyons A, Downer EJ, Crotty S, Nolan YM, Mills KH & Lynch MA. (2007). CD200 ligand receptor interaction modulates microglial activation in vivo and in vitro: a role for IL-4. *J Neurosci* **27**, 8309-8313.
- Lyons A, Lynch AM, Downer EJ, Hanley R, O'Sullivan JB, Smith A & Lynch MA. (2009a). Fractalkine-induced activation of the phosphatidylinositol-3 kinase pathway attenuates microglial activation in vivo and in vitro. *J Neurochem* **110**, 1547-1556.

- Lyons A, McQuillan K, Deighan BF, O'Reilly JA, Downer EJ, Murphy AC, Watson M, Piazza A, O'Connell F, Griffin R, Mills KH & Lynch MA. (2009b). Decreased neuronal CD200 expression in IL-4-deficient mice results in increased neuroinflammation in response to lipopolysaccharide. *Brain Behav Immun* **23**, 1020-1027.
- Ma Y, Hof PR, Grant SC, Blackband SJ, Bennett R, Slate L, McGuigan MD & Benveniste H. (2005). A three-dimensional digital atlas database of the adult C57BL/6J mouse brain by magnetic resonance microscopy. *Neuroscience* **135**, 1203-1215.
- Mackenzie IR & Munoz DG. (1998). Nonsteroidal anti-inflammatory drug use and Alzheimer-type pathology in aging. *Neurology* **50**, 986-990.
- Malm TM, Iivonen H, Goldsteins G, Keksa-Goldsteine V, Ahtoniemi T, Kanninen K, Salminen A, Auriola S, Van Groen T, Tanila H & Koistinaho J. (2007). Pyrrolidine dithiocarbamate activates Akt and improves spatial learning in APP/PS1 mice without affecting beta-amyloid burden. *J Neurosci* **27**, 3712-3721.
- Manaye KF, Wang PC, O'Neil JN, Huang SY, Xu T, Lei DL, Tizabi Y, Ottinger MA, Ingram DK & Mouton PR. (2007). Neuropathological quantification of dtg APP/PS1: neuroimaging, stereology, and biochemistry. *Age (Dordr)* **29**, 87-96.
- Mandelkow EM & Mandelkow E. (1998). Tau in Alzheimer's disease. *Trends Cell Biol* **8**, 425-427.
- Mandeville JB & Rosen BR. (2002). *Brain Mapping: The Methods*. Academic Press.
- Markesbery WR. (1997). Oxidative stress hypothesis in Alzheimer's disease. *Free Radic Biol Med* **23**, 134-147.

- Marshak DR, Pesce SA, Stanley LC & Griffin WS. (1992). Increased S100 beta neurotrophic activity in Alzheimer's disease temporal lobe. *Neurobiol Aging* **13**, 1-7.
- Martin DS, Lonergan PE, Boland B, Fogarty MP, Brady M, Horrobin DF, Campbell VA & Lynch MA. (2002). Apoptotic changes in the aged brain are triggered by interleukin-1beta-induced activation of p38 and reversed by treatment with eicosapentaenoic acid. *J Biol Chem* **277**, 34239-34246.
- Masocha W. (2009). Systemic lipopolysaccharide (LPS)-induced microglial activation results in different temporal reduction of CD200 and CD200 receptor gene expression in the brain. *J Neuroimmunol* **214**, 78-82.
- Matter K & Balda MS. (2003). Holey barrier: claudins and the regulation of brain endothelial permeability. *J Cell Biol* **161**, 459-460.
- Mattila KM, Forsell C, Pirttila T, Rinne JO, Lehtimaki T, Roytta M, Lilius L, Eerola A, St George-Hyslop PH, Frey H & Lannfelt L. (1998). The Glu318Gly mutation of the presenilin-1 gene does not necessarily cause Alzheimer's disease. *Ann Neurol* **44**, 965-967.
- Mattson MP. (2002). Oxidative stress, perturbed calcium homeostasis, and immune dysfunction in Alzheimer's disease. *J Neurovirol* **8**, 539-550.
- Maurer K, Volk S & Gerbaldo H. (1997). Auguste D and Alzheimer's disease. *Lancet* **349**, 1546-1549.
- McCandless EE, Budde M, Lees JR, Dorsey D, Lyng E & Klein RS. (2009). IL-1R signaling within the central nervous system regulates CXCL12 expression at the blood-brain barrier and disease severity during experimental autoimmune encephalomyelitis. *J Immunol* **183**, 613-620.

- McFarland HF. (1998). The lesion in multiple sclerosis: clinical, pathological, and magnetic resonance imaging considerations. *J Neurol Neurosurg Psychiatry* **64** Suppl 1, S26-30.
- McRobbie DW, Moore EA & Graves MJ. (2003). *MRI from picture to proton*. Cambridge University Press.
- Medzhitov R & Janeway CA, Jr. (1997). Innate immunity: impact on the adaptive immune response. *Curr Opin Immunol* **9**, 4-9.
- Medzhitov R, Preston-Hurlburt P & Janeway CA, Jr. (1997). A human homologue of the Drosophila Toll protein signals activation of adaptive immunity. *Nature* **388**, 394-397.
- Merrill JE & Benveniste EN. (1996). Cytokines in inflammatory brain lesions: helpful and harmful. *Trends Neurosci* **19**, 331-338.
- Micheau O & Tschopp J. (2003). Induction of TNF receptor I-mediated apoptosis via two sequential signaling complexes. *Cell* **114**, 181-190.
- Miller SI, Ernst RK & Bader MW. (2005). LPS, TLR4 and infectious disease diversity. *Nat Rev Microbiol* **3**, 36-46.
- Milner B, Corkin S & Teuber HL. (1968). Further analysis of the hippocampal amnesic syndrome: 14-year follow-up study of H.M. *Neuropsychologia*.
- Milner R & Campbell IL. (2003). The extracellular matrix and cytokines regulate microglial integrin expression and activation. *J Immunol* **170**, 3850-3858.
- Minas KaL, J. (2006). Is The CD200/CD200 Receptor Interaction More Than Just a Myeloid Cell Inhibitory Signal? *Crit Rev Immunol* **26**, 213.

- Ming GL & Song H. (2005). Adult neurogenesis in the mammalian central nervous system. *Annu Rev Neurosci* **28**, 223-250.
- Minogue AM, Lynch AM, Loane DJ, Herron CE & Lynch MA. (2007). Modulation of amyloid-beta-induced and age-associated changes in rat hippocampus by eicosapentaenoic acid. *J Neurochem* **103**, 914-926.
- Molina-Holgado F, Lledo A & Guaza C. (1997). Anandamide suppresses nitric oxide and TNF-alpha responses to Theiler's virus or endotoxin in astrocytes. *Neuroreport* **8**, 1929-1933.
- Mori K, Kaneko YS, Nakashima A, Nagatsu I, Takahashi H & Ota A. (2005a). Peripheral lipopolysaccharide induces apoptosis in the murine olfactory bulb. *Brain Res* **1039**, 116-129.
- Mori T, Town T, Tan J, Tateishi N & Asano T. (2005b). Modulation of astrocytic activation by arundic acid (ONO-2506) mitigates detrimental effects of the apolipoprotein E4 isoform after permanent focal ischemia in apolipoprotein E knock-in mice. *J Cereb Blood Flow Metab* **25**, 748-762.
- Morita K, Sasaki H, Furuse M & Tsukita S. (1999). Endothelial claudin: claudin-5/TMVCF constitutes tight junction strands in endothelial cells. *J Cell Biol* **147**, 185-194.
- Morrison JH & Hof PR. (1997). Life and death of neurons in the aging brain. *Science* **278**, 412-419.
- Mouton PR, Long JM, Lei DL, Howard V, Jucker M, Calhoun ME & Ingram DK. (2002). Age and gender effects on microglia and astrocyte numbers in brains of mice. *Brain Res* **956**, 30-35.

- Nagai Y, Akashi S, Nagafuku M, Ogata M, Iwakura Y, Akira S, Kitamura T, Kosugi A, Kimoto M & Miyake K. (2002). Essential role of MD-2 in LPS responsiveness and TLR4 distribution. *Nat Immunol* **3**, 667-672.
- Nagele RG, D'Andrea MR, Lee H, Venkataraman V & Wang HY. (2003). Astrocytes accumulate A beta 42 and give rise to astrocytic amyloid plaques in Alzheimer disease brains. *Brain Res* **971**, 197-209.
- Nagele RG, Wegiel J, Venkataraman V, Imaki H & Wang KC. (2004). Contribution of glial cells to the development of amyloid plaques in Alzheimer's disease. *Neurobiol Aging* **25**, 663-674.
- Nagyoszi P, Wilhelm I, Farkas AE, Fazakas C, Dung NT, Hasko J & Krizbai IA. (2010). Expression and regulation of toll-like receptors in cerebral endothelial cells. *Neurochem Int* **57**, 556-564.
- Nakamura Y, Si QS & Kataoka K. (1999). Lipopolysaccharide-induced microglial activation in culture: temporal profiles of morphological change and release of cytokines and nitric oxide. *Neurosci Res* **35**, 95-100.
- Nakanishi H & Wu Z. (2009). Microglia-aging: roles of microglial lysosome- and mitochondria-derived reactive oxygen species in brain aging. *Behav Brain Res* **201**, 1-7.
- Nathan C. (2002). Points of control in inflammation. *Nature* **420**, 846-852.
- Natoli G, Costanzo A, Ianni A, Templeton DJ, Woodgett JR, Balsano C & Levrero M. (1997). Activation of SAPK/JNK by TNF receptor 1 through a noncytotoxic TRAF2-dependent pathway. *Science* **275**, 200-203.
- Neumann H. (2001). Control of glial immune function by neurons. *Glia* **36**, 191-199.

- Nichols NR. (1999). Glial responses to steroids as markers of brain aging. *J Neurobiol* **40**, 585-601.
- Nichols NR, Day JR, Laping NJ, Johnson SA & Finch CE. (1993). GFAP mRNA increases with age in rat and human brain. *Neurobiol Aging* **14**, 421-429.
- Nichols TE & Holmes AP. (2002). Nonparametric permutation tests for functional neuroimaging: a primer with examples. *Hum Brain Mapp* **15**, 1-25.
- Nitta T, Hata M, Gotoh S, Seo Y, Sasaki H, Hashimoto N, Furuse M & Tsukita S. (2003). Size-selective loosening of the blood-brain barrier in claudin-5-deficient mice. *J Cell Biol* **161**, 653-660.
- Nolan Y, Martin D, Campbell VA & Lynch MA. (2004). Evidence of a protective effect of phosphatidylserine-containing liposomes on lipopolysaccharide-induced impairment of long-term potentiation in the rat hippocampus. *J Neuroimmunol* **151**, 12-23.
- Nunomura A, Castellani RJ, Zhu X, Moreira PI, Perry G & Smith MA. (2006). Involvement of oxidative stress in Alzheimer disease. *J Neuropathol Exp Neurol* **65**, 631-641.
- O'Donnell E, Vereker E & Lynch MA. (2000). Age-related impairment in LTP is accompanied by enhanced activity of stress-activated protein kinases: analysis of underlying mechanisms. *Eur J Neurosci* **12**, 345-352.
- Oddo S, Caccamo A, Shepherd JD, Murphy MP, Golde TE, Kaye R, Metherate R, Mattson MP, Akbari Y & LaFerla FM. (2003). Triple-transgenic model of Alzheimer's disease with plaques and tangles: intracellular Abeta and synaptic dysfunction. *Neuron* **39**, 409-421.

- Ogata T, Chuai M, Morino T, Yamamoto H, Nakamura Y & Schubert P. (2003). Adenosine triphosphate inhibits cytokine release from lipopolysaccharide-activated microglia via P2y receptors. *Brain Res* **981**, 174-183.
- Ogura K, Ogawa M & Yoshida M. (1994). Effects of ageing on microglia in the normal rat brain: immunohistochemical observations. *Neuroreport* **5**, 1224-1226.
- Oitzl MS, van Oers H, Schobitz B & de Kloet ER. (1993). Interleukin-1 beta, but not interleukin-6, impairs spatial navigation learning. *Brain Res* **613**, 160-163.
- Ordidge RJ, Gorell JM, Deniau JC, Knight RA & Helpert JA. (1994). Assessment of relative brain iron concentrations using T2-weighted and T2*-weighted MRI at 3 Tesla. *Magn Reson Med* **32**, 335-341.
- Otto D & Unsicker K. (1994). FGF-2 in the MPTP model of Parkinson's disease: effects on astroglial cells. *Glia* **11**, 47-56.
- Owens T. (2003). The enigma of multiple sclerosis: inflammation and neurodegeneration cause heterogeneous dysfunction and damage. *Curr Opin Neurol* **16**, 259-265.
- Ozinsky A, Underhill DM, Fontenot JD, Hajjar AM, Smith KD, Wilson CB, Schroeder L & Aderem A. (2000). The repertoire for pattern recognition of pathogens by the innate immune system is defined by cooperation between toll-like receptors. *Proc Natl Acad Sci U S A* **97**, 13766-13771.
- Pardridge WM. (2003). Blood-brain barrier drug targeting: the future of brain drug development. *Mol Interv* **3**, 90-105, 151.
- Pardridge WM. (2007). Blood-brain barrier delivery. *Drug Discov Today* **12**, 54-61.

- Parry A, Clare S, Jenkinson M, Smith S, Palace J & Matthews PM. (2002). White matter and lesion T1 relaxation times increase in parallel and correlate with disability in multiple sclerosis. *J Neurol* **249**, 1279-1286.
- Patel NV, Gordon MN, Connor KE, Good RA, Engelman RW, Mason J, Morgan DG, Morgan TE & Finch CE. (2005). Caloric restriction attenuates Abeta-deposition in Alzheimer transgenic models. *Neurobiol Aging* **26**, 995-1000.
- Paxinos G FK. (2001). The Mouse Brain in Stereotaxic Coordinates.
- Pell GS, Briellmann RS, Waites AB, Abbott DF & Jackson GD. (2004). Voxel-based relaxometry: a new approach for analysis of T2 relaxometry changes in epilepsy. *Neuroimage* **21**, 707-713.
- Penkowa M, Giralt M, Lago N, Camats J, Carrasco J, Hernandez J, Molinero A, Campbell IL & Hidalgo J. (2003). Astrocyte-targeted expression of IL-6 protects the CNS against a focal brain injury. *Exp Neurol* **181**, 130-148.
- Perry EK, Tomlinson BE, Blessed G, Bergmann K, Gibson PH & Perry RH. (1978). Correlation of cholinergic abnormalities with senile plaques and mental test scores in senile dementia. *Br Med J* **2**, 1457-1459.
- Perry VH, Andersson PB & Gordon S. (1993a). Macrophages and inflammation in the central nervous system. *Trends Neurosci* **16**, 268-273.
- Perry VH, Matyszak MK & Fearn S. (1993b). Altered antigen expression of microglia in the aged rodent CNS. *Glia* **7**, 60-67.
- Persidsky Y, Ramirez SH, Haorah J & Kanmogne GD. (2006). Blood-brain barrier: structural components and function under physiologic and pathologic conditions. *J Neuroimmune Pharmacol* **1**, 223-236.

- Peters A. (2002). The effects of normal aging on myelin and nerve fibers: a review. *J Neurocytol* **31**, 581-593.
- Pike CJ, Cummings BJ, Monzavi R & Cotman CW. (1994). Beta-amyloid-induced changes in cultured astrocytes parallel reactive astrocytosis associated with senile plaques in Alzheimer's disease. *Neuroscience* **63**, 517-531.
- Pilegaard K & Ladefoged O. (1996). Total number of astrocytes in the molecular layer of the dentate gyrus of rats at different ages. *Anal Quant Cytol Histol* **18**, 279-285.
- Poduslo JF, Curran GL, Wengenack TM, Malester B & Duff K. (2001). Permeability of proteins at the blood-brain barrier in the normal adult mouse and double transgenic mouse model of Alzheimer's disease. *Neurobiol Dis* **8**, 555-567.
- Ponomarev ED, Shriver LP & Dittel BN. (2006). CD40 expression by microglial cells is required for their completion of a two-step activation process during central nervous system autoimmune inflammation. *J Immunol* **176**, 1402-1410.
- Porchet R, Probst A, Bouras C, Draberova E, Draber P & Riederer BM. (2003). Analysis of glial acidic fibrillary protein in the human entorhinal cortex during aging and in Alzheimer's disease. *Proteomics* **3**, 1476-1485.
- Preston S, Wright GJ, Starr K, Barclay AN & Brown MH. (1997). The leukocyte/neuron cell surface antigen OX2 binds to a ligand on macrophages. *Eur J Immunol* **27**, 1911-1918.
- Price JL & Morris JC. (1999). Tangles and plaques in nondemented aging and "preclinical" Alzheimer's disease. *Ann Neurol* **45**, 358-368.
- Puolivali J, Wang J, Heikkinen T, Heikkila M, Tapiola T, van Groen T & Tanila H. (2002). Hippocampal A beta 42 levels correlate with spatial memory deficit in APP and PS1 double transgenic mice. *Neurobiol Dis* **9**, 339-347.

- Qiao X, Cummins DJ & Paul SM. (2001). Neuroinflammation-induced acceleration of amyloid deposition in the APPV717F transgenic mouse. *Eur J Neurosci* **14**, 474-482.
- Qin H, Wilson CA, Lee SJ, Zhao X & Benveniste EN. (2005). LPS induces CD40 gene expression through the activation of NF-kappaB and STAT-1alpha in macrophages and microglia. *Blood* **106**, 3114-3122.
- Rachal Pugh C, Fleshner M, Watkins LR, Maier SF & Rudy JW. (2001). The immune system and memory consolidation: a role for the cytokine IL-1beta. *Neurosci Biobehav Rev* **25**, 29-41.
- Rahner C, Mitic LL & Anderson JM. (2001). Heterogeneity in expression and subcellular localization of claudins 2, 3, 4, and 5 in the rat liver, pancreas, and gut. *Gastroenterology* **120**, 411-422.
- Ramakrishnan M, Wengenack TM, Kandimalla KK, Curran GL, Gilles EJ, Ramirez-Alvarado M, Lin J, Garwood M, Jack CR, Jr. & Poduslo JF. (2008). Selective contrast enhancement of individual Alzheimer's disease amyloid plaques using a polyamine and Gd-DOTA conjugated antibody fragment against fibrillar Abeta42 for magnetic resonance molecular imaging. *Pharm Res* **25**, 1861-1872.
- Ransom B, Behar T & Nedergaard M. (2003). New roles for astrocytes (stars at last). *Trends Neurosci* **26**, 520-522.
- Reiser MF, Bongartz GP, Erlemann R, Schneider M, Pauly T, Sittek H & Peters PE. (1989). Gadolinium-DTPA in rheumatoid arthritis and related diseases: first results with dynamic magnetic resonance imaging. *Skeletal Radiol* **18**, 591-597.
- Relton JK, Strijbos PJ, Cooper AL & Rothwell NJ. (1993). Dietary N-3 fatty acids inhibit ischaemic and excitotoxic brain damage in the rat. *Brain Res Bull* **32**, 223-226.

- Renshaw M, Rockwell J, Engleman C, Gewirtz A, Katz J & Sambhara S. (2002). Cutting edge: impaired Toll-like receptor expression and function in aging. *J Immunol* **169**, 4697-4701.
- Richard KL, Filali M, Prefontaine P & Rivest S. (2008). Toll-like receptor 2 acts as a natural innate immune receptor to clear amyloid beta 1-42 and delay the cognitive decline in a mouse model of Alzheimer's disease. *J Neurosci* **28**, 5784-5793.
- Ridet JL, Malhotra SK, Privat A & Gage FH. (1997). Reactive astrocytes: cellular and molecular cues to biological function. *Trends Neurosci* **20**, 570-577.
- Ring S, Weyer SW, Kilian SB, Waldron E, Pietrzik CU, Filippov MA, Herms J, Buchholz C, Eckman CB, Korte M, Wolfer DP & Muller UC. (2007). The secreted beta-amyloid precursor protein ectodomain APPs alpha is sufficient to rescue the anatomical, behavioral, and electrophysiological abnormalities of APP-deficient mice. *J Neurosci* **27**, 7817-7826.
- Risau W & Wolburg H. (1990). Development of the blood-brain barrier. *Trends Neurosci* **13**, 174-178.
- Roberts TP & van Bruggen N. (2003). In *Biomedical Imaging In Experimental Neuroscience*, ed. van Bruggen N & Roberts T. CRC Press.
- Rock RB, Gekker G, Hu S, Sheng WS, Cheeran M, Lokensgard JR & Peterson PK. (2004). Role of microglia in central nervous system infections. *Clin Microbiol Rev* **17**, 942-964, table of contents.
- Rodriguez JJ, Olabarria M, Chvatal A & Verkhratsky A. (2009). Astroglia in dementia and Alzheimer's disease. *Cell Death Differ* **16**, 378-385.

- Rodriguez JJ, Witton J, Olabarria M, Noristani HN & Verkhratsky A. (2010). Increase in the density of resting microglia precedes neuritic plaque formation and microglial activation in a transgenic model of Alzheimer's disease. *Cell Death Dis* **1**, e1.
- Rojo LE, Fernandez JA, Maccioni AA, Jimenez JM & Maccioni RB. (2008). Neuroinflammation: implications for the pathogenesis and molecular diagnosis of Alzheimer's disease. *Arch Med Res* **39**, 1-16.
- Rosenberg RN. (2000). The molecular and genetic basis of AD: the end of the beginning: the 2000 Wartenberg lecture. *Neurology* **54**, 2045-2054.
- Rosenblum MD, Yancey KB, Olasz EB & Truitt RL. (2006). CD200, a "no danger" signal for hair follicles. *J Dermatol Sci* **41**, 165-174.
- Rosengarten B, Walberer M, Allendoerfer J, Mueller C, Schwarz N, Bachmann G & Gerriets T. (2008). LPS-induced endotoxic shock does not cause early brain edema formation - an MRI study in rats. *Inflamm Res* **57**, 479-483.
- Rothwell NJ & Hopkins SJ. (1995). Cytokines and the nervous system II: Actions and mechanisms of action. *Trends Neurosci* **18**, 130-136.
- Roy A, Fung YK, Liu X & Pahan K. (2006). Up-regulation of microglial CD11b expression by nitric oxide. *J Biol Chem* **281**, 14971-14980.
- Roy A, Jana A, Yatish K, Freidt MB, Fung YK, Martinson JA & Pahan K. (2008). Reactive oxygen species up-regulate CD11b in microglia via nitric oxide: Implications for neurodegenerative diseases. *Free Radic Biol Med* **45**, 686-699.
- Rozovsky I, Wei M, Morgan TE & Finch CE. (2005). Reversible age impairments in neurite outgrowth by manipulations of astrocytic GFAP. *Neurobiol Aging* **26**, 705-715.

- Rubinstein LJ. (1986). [Contribution of immunohistochemical methods to the study of central nervous system tumors]. *Ann Pathol* **6**, 157-163.
- Rugg-Gunn FJ, Boulby PA, Symms MR, Barker GJ & Duncan JS. (2005). Whole-brain T2 mapping demonstrates occult abnormalities in focal epilepsy. *Neurology* **64**, 318-325.
- Rutka JT, Murakami M, Dirks PB, Hubbard SL, Becker LE, Fukuyama K, Jung S, Tsugu A & Matsuzawa K. (1997). Role of glial filaments in cells and tumors of glial origin: a review. *J Neurosurg* **87**, 420-430.
- Saitou M, Furuse M, Sasaki H, Schulzke JD, Fromm M, Takano H, Noda T & Tsukita S. (2000). Complex phenotype of mice lacking occludin, a component of tight junction strands. *Mol Biol Cell* **11**, 4131-4142.
- Sakaeda T, Tada Y, Sugawara T, Ryu T, Hirose F, Yoshikawa T, Hirano K, Kupczyk-Subotkowska L, Siahaan TJ, Audus KL & Stella VJ. (2001). Conjugation with L-Glutamate for in vivo brain drug delivery. *J Drug Target* **9**, 23-37.
- Sandhir R, Onyszchuk G & Berman NE. (2008). Exacerbated glial response in the aged mouse hippocampus following controlled cortical impact injury. *Exp Neurol* **213**, 372-380.
- Sandhir R, Puri V, Klein RM & Berman NE. (2004). Differential expression of cytokines and chemokines during secondary neuron death following brain injury in old and young mice. *Neurosci Lett* **369**, 28-32.
- Sanz JM & Di Virgilio F. (2000). Kinetics and mechanism of ATP-dependent IL-1 beta release from microglial cells. *J Immunol* **164**, 4893-4898.
- Sawada M, Suzumura A & Marunouchi T. (1992). TNF alpha induces IL-6 production by astrocytes but not by microglia. *Brain Res* **583**, 296-299.

- Sawiak SJ, Wood NI, Williams GB, Morton AJ & Carpenter TA. (2009). Voxel-based morphometry in the R6/2 transgenic mouse reveals differences between genotypes not seen with manual 2D morphometry. *Neurobiol Dis* **33**, 20-27.
- Scheuner D, Eckman C, Jensen M, Song X, Citron M, Suzuki N, Bird TD, Hardy J, Hutton M, Kukull W, Larson E, Levy-Lahad E, Viitanen M, Peskind E, Poorkaj P, Schellenberg G, Tanzi R, Wasco W, Lannfelt L, Selkoe D & Younkin S. (1996). Secreted amyloid beta-protein similar to that in the senile plaques of Alzheimer's disease is increased in vivo by the presenilin 1 and 2 and APP mutations linked to familial Alzheimer's disease. *Nat Med* **2**, 864-870.
- Schipper HM. (2004). Brain iron deposition and the free radical-mitochondrial theory of ageing. *Ageing Res Rev* **3**, 265-301.
- Schlachetzki JC & Hull M. (2009). Microglial activation in Alzheimer's disease. *Curr Alzheimer Res* **6**, 554-563.
- Schlageter KE, Molnar P, Lapin GD & Groothuis DR. (1999). Microvessel organization and structure in experimental brain tumors: microvessel populations with distinctive structural and functional properties. *Microvasc Res* **58**, 312-328.
- Schmitt P, Griswold MA, Jakob PM, Kotas M, Gulani V, Flentje M & Haase A. (2004). Inversion recovery TrueFISP: quantification of T(1), T(2), and spin density. *Magn Reson Med* **51**, 661-667.
- Schonbeck U & Libby P. (2001). The CD40/CD154 receptor/ligand dyad. *Cell Mol Life Sci* **58**, 4-43.
- Shafteel SS, Kyrkanides S, Olschowka JA, Miller JN, Johnson RE & O'Banion MK. (2007). Sustained hippocampal IL-1 beta overexpression mediates chronic neuroinflammation and ameliorates Alzheimer plaque pathology. *J Clin Invest* **117**, 1595-1604.

- Shaked I, Tchoresh D, Gersner R, Meiri G, Mordechai S, Xiao X, Hart RP & Schwartz M. (2005). Protective autoimmunity: interferon-gamma enables microglia to remove glutamate without evoking inflammatory mediators. *J Neurochem* **92**, 997-1009.
- Shan DE. (2004). Hemichorea-hemiballism associated with hyperintense putamen on T1-weighted MR images: an update and a hypothesis. *Acta Neurol Taiwan* **13**, 170-177.
- Sheng JG, Ito K, Skinner RD, Mrazek RE, Rovnaghi CR, Van Eldik LJ & Griffin WS. (1996). In vivo and in vitro evidence supporting a role for the inflammatory cytokine interleukin-1 as a driving force in Alzheimer pathogenesis. *Neurobiol Aging* **17**, 761-766.
- Sheng JG, Mrazek RE & Griffin WS. (1994). S100 beta protein expression in Alzheimer disease: potential role in the pathogenesis of neuritic plaques. *J Neurosci Res* **39**, 398-404.
- Shibata M, Yamada S, Kumar SR, Calero M, Bading J, Frangione B, Holtzman DM, Miller CA, Strickland DK, Ghiso J & Zlokovic BV. (2000). Clearance of Alzheimer's amyloid- β (1-40) peptide from brain by LDL receptor-related protein-1 at the blood-brain barrier. *J Clin Invest* **106**, 1489-1499.
- Shivers BD, Hilbich C, Multhaup G, Salbaum M, Beyreuther K & Seeburg PH. (1988). Alzheimer's disease amyloidogenic glycoprotein: expression pattern in rat brain suggests a role in cell contact. *EMBO J* **7**, 1365-1370.
- Shohami E, Gallily R, Mechoulam R, Bass R & Ben-Hur T. (1997). Cytokine production in the brain following closed head injury: dexanabinol (HU-211) is a novel TNF- α inhibitor and an effective neuroprotectant. *J Neuroimmunol* **72**, 169-177.

- Sibson NR, Lowe JP, Blamire AM, Martin MJ, Obrenovitch TP & Anthony DC. (2008). Acute astrocyte activation in brain detected by MRI: new insights into T(1) hypointensity. *J Cereb Blood Flow Metab* **28**, 621-632.
- Sies H. (1997). Oxidative stress: oxidants and antioxidants. *Exp Physiol* **82**, 291-295.
- Singh AK & Jiang Y. (2004). How does peripheral lipopolysaccharide induce gene expression in the brain of rats? *Toxicology* **201**, 197-207.
- Singh AK, Jiang Y, Gupta S & Benlhabib E. (2007). Effects of chronic ethanol drinking on the blood brain barrier and ensuing neuronal toxicity in alcohol-preferring rats subjected to intraperitoneal LPS injection. *Alcohol Alcohol* **42**, 385-399.
- Small DH. (1998). The role of the amyloid protein precursor (APP) in Alzheimer's disease: does the normal function of APP explain the topography of neurodegeneration? *Neurochem Res* **23**, 795-806.
- Smith SM, Jenkinson M, Woolrich MW, Beckmann CF, Behrens TE, Johansen-Berg H, Bannister PR, De Luca M, Drobnjak I, Flitney DE, Niazy RK, Saunders J, Vickers J, Zhang Y, De Stefano N, Brady JM & Matthews PM. (2004). Advances in functional and structural MR image analysis and implementation as FSL. *Neuroimage* **23 Suppl 1**, S208-219.
- Sofroniew MV. (2005). Reactive astrocytes in neural repair and protection. *Neuroscientist* **11**, 400-407.
- Sohal RS & Weindruch R. (1996). Oxidative stress, caloric restriction, and aging. *Science* **273**, 59-63.
- Sonobe Y, Takeuchi H, Kataoka K, Li H, Jin S, Mimuro M, Hashizume Y, Sano Y, Kanda T, Mizuno T & Suzumura A. (2009). Interleukin-25 expressed by brain capillary endothelial cells maintains blood-brain barrier function in a protein kinase C epsilon-dependent manner. *J Biol Chem* **284**, 31834-31842.

- Spangelo BL, Judd AM, Isakson PC & MacLeod RM. (1991). Interleukin-1 stimulates interleukin-6 release from rat anterior pituitary cells in vitro. *Endocrinology* **128**, 2685-2692.
- Steensberg A, Fischer CP, Keller C, Moller K & Pedersen BK. (2003). IL-6 enhances plasma IL-1ra, IL-10, and cortisol in humans. *Am J Physiol Endocrinol Metab* **285**, E433-437.
- Steinman L. (2001). Multiple sclerosis: a two-stage disease. *Nat Immunol* **2**, 762-764.
- Stephan A, Laroche S & Davis S. (2001). Generation of aggregated beta-amyloid in the rat hippocampus impairs synaptic transmission and plasticity and causes memory deficits. *J Neurosci* **21**, 5703-5714.
- Stoll G, Jung S, Jander S, van der Meide P & Hartung HP. (1993). Tumor necrosis factor-alpha in immune-mediated demyelination and Wallerian degeneration of the rat peripheral nervous system. *J Neuroimmunol* **45**, 175-182.
- Stout RD & Suttles J. (1996). The many roles of CD40 in cell-mediated inflammatory responses. *Immunol Today* **17**, 487-492.
- Streit WJ. (2002). Microglia as neuroprotective, immunocompetent cells of the CNS. *Glia* **40**, 133-139.
- Streit WJ. (2006). Microglial senescence: does the brain's immune system have an expiration date? *Trends Neurosci* **29**, 506-510.
- Streit WJ, Conde JR, Fendrick SE, Flanary BE & Mariani CL. (2005). Role of microglia in the central nervous system's immune response. *Neurol Res* **27**, 685-691.
- Streit WJ, Sammons NW, Kuhns AJ & Sparks DL. (2004). Dystrophic microglia in the aging human brain. *Glia* **45**, 208-212.

- Sugama S, Yang L, Cho BP, DeGiorgio LA, Lorenzl S, Albers DS, Beal MF, Volpe BT & Joh TH. (2003). Age-related microglial activation in 1-methyl-4-phenyl-1,2,3,6-tetrahydropyridine (MPTP)-induced dopaminergic neurodegeneration in C57BL/6 mice. *Brain Res* **964**, 288-294.
- Suzuki T, Hide I, Ido K, Kohsaka S, Inoue K & Nakata Y. (2004). Production and release of neuroprotective tumor necrosis factor by P2X7 receptor-activated microglia. *J Neurosci* **24**, 1-7.
- Swift ME, Burns AL, Gray KL & DiPietro LA. (2001). Age-related alterations in the inflammatory response to dermal injury. *J Invest Dermatol* **117**, 1027-1035.
- Szczepaniak LS, Sargeson A, Creasey II, Geue RJ, Tweedle M & Bryant RG. (1992). Nuclear magnetic spin-lattice relaxation of water protons caused by metal cage compounds. *Bioconjug Chem* **3**, 27-31.
- Takeda K, Kaisho T & Akira S. (2003). Toll-like receptors. *Annu Rev Immunol* **21**, 335-376.
- Takeuchi O, Hoshino K, Kawai T, Sanjo H, Takada H, Ogawa T, Takeda K & Akira S. (1999). Differential roles of TLR2 and TLR4 in recognition of gram-negative and gram-positive bacterial cell wall components. *Immunity* **11**, 443-451.
- Tan J, Town T, Paris D, Mori T, Suo Z, Crawford F, Mattson MP, Flavell RA & Mullan M. (1999). Microglial activation resulting from CD40-CD40L interaction after beta-amyloid stimulation. *Science* **286**, 2352-2355.
- Tanzi RE, Moir RD & Wagner SL. (2004). Clearance of Alzheimer's Abeta peptide: the many roads to perdition. *Neuron* **43**, 605-608.
- Taylor N, McConachie K, Calder C, Dawson R, Dick A, Sedgwick JD & Liversidge J. (2005). Enhanced tolerance to autoimmune uveitis in CD200-deficient mice

correlates with a pronounced Th2 switch in response to antigen challenge. *J Immunol* **174**, 143-154.

- Teipel SJ, Kaza E, Hadlich S, Bauer A, Bruning T, Plath AS, Krohn M, Scheffler K, Walker LC, Lotze M & Pahnke J. (2011). Automated detection of amyloid-beta-related cortical and subcortical signal changes in a transgenic model of Alzheimer's disease using high-field MRI. *J Alzheimers Dis* **23**, 221-237.
- Testa C, Laakso MP, Sabbatoli F, Rossi R, Beltramello A, Soininen H & Frisoni GB. (2004). A comparison between the accuracy of voxel-based morphometry and hippocampal volumetry in Alzheimer's disease. *J Magn Reson Imaging* **19**, 274-282.
- Thompson PM, MacDonald D, Mega MS, Holmes CJ, Evans AC & Toga AW. (1997). Detection and mapping of abnormal brain structure with a probabilistic atlas of cortical surfaces. *J Comput Assist Tomogr* **21**, 567-581.
- Tilg H, Trehu E, Atkins MB, Dinarello CA & Mier JW. (1994). Interleukin-6 (IL-6) as an anti-inflammatory cytokine: induction of circulating IL-1 receptor antagonist and soluble tumor necrosis factor receptor p55. *Blood* **83**, 113-118.
- Town T, Nikolic V & Tan J. (2005). The microglial "activation" continuum: from innate to adaptive responses. *J Neuroinflammation* **2**, 24.
- Townsend KP, Town T, Mori T, Lue LF, Shytle D, Sanberg PR, Morgan D, Fernandez F, Flavell RA & Tan J. (2005). CD40 signaling regulates innate and adaptive activation of microglia in response to amyloid beta-peptide. *Eur J Immunol* **35**, 901-910.
- Trinchese F, Liu S, Battaglia F, Walter S, Mathews PM & Arancio O. (2004). Progressive age-related development of Alzheimer-like pathology in APP/PS1 mice. *Ann Neurol* **55**, 801-814.

- Truyen L, van Waesberghe JH, van Walderveen MA, van Oosten BW, Polman CH, Hommes OR, Ader HJ & Barkhof F. (1996). Accumulation of hypointense lesions ("black holes") on T1 spin-echo MRI correlates with disease progression in multiple sclerosis. *Neurology* **47**, 1469-1476.
- Tsukita S, Furuse M & Itoh M. (2001). Multifunctional strands in tight junctions. *Nat Rev Mol Cell Biol* **2**, 285-293.
- Ujiie M, Dickstein DL, Carlow DA & Jefferies WA. (2003). Blood-brain barrier permeability precedes senile plaque formation in an Alzheimer disease model. *Microcirculation* **10**, 463-470.
- van der Ley P, Steeghs L, Hamstra HJ, ten Hove J, Zomer B & van Alphen L. (2001). Modification of lipid A biosynthesis in *Neisseria meningitidis* lpxL mutants: influence on lipopolysaccharide structure, toxicity, and adjuvant activity. *Infect Immun* **69**, 5981-5990.
- van Groen T & Kadish I. (2005). Transgenic AD model mice, effects of potential anti-AD treatments on inflammation and pathology. *Brain Res Brain Res Rev* **48**, 370-378.
- Van Itallie C, Rahner C & Anderson JM. (2001). Regulated expression of claudin-4 decreases paracellular conductance through a selective decrease in sodium permeability. *J Clin Invest* **107**, 1319-1327.
- van Kooten C & Banchereau J. (2000). CD40-CD40 ligand. *J Leukoc Biol* **67**, 2-17.
- Van Uden E, Mallory M, Veinbergs I, Alford M, Rockenstein E & Masliah E. (2002). Increased extracellular amyloid deposition and neurodegeneration in human amyloid precursor protein transgenic mice deficient in receptor-associated protein. *J Neurosci* **22**, 9298-9304.

- van Walderveen MA, Kamphorst W, Scheltens P, van Waesberghe JH, Ravid R, Valk J, Polman CH & Barkhof F. (1998). Histopathologic correlate of hypointense lesions on T1-weighted spin-echo MRI in multiple sclerosis. *Neurology* **50**, 1282-1288.
- Vanhoutte G, Dewachter I, Borghgraef P, Van Leuven F & Van der Linden A. (2005). Noninvasive in vivo MRI detection of neuritic plaques associated with iron in APP[V717I] transgenic mice, a model for Alzheimer's disease. *Magn Reson Med* **53**, 607-613.
- Vela JM, Dalmau I, Gonzalez B & Castellano B. (1995). Morphology and distribution of microglial cells in the young and adult mouse cerebellum. *J Comp Neurol* **361**, 602-616.
- Vereker E, Campbell V, Roche E, McEntee E & Lynch MA. (2000). Lipopolysaccharide inhibits long term potentiation in the rat dentate gyrus by activating caspase-1. *J Biol Chem* **275**, 26252-26258.
- Verma S, Nakaoke R, Dohgu S & Banks WA. (2006). Release of cytokines by brain endothelial cells: A polarized response to lipopolysaccharide. *Brain Behav Immun* **20**, 449-455.
- Vigo-Pelfrey C, Seubert P, Barbour R, Blomquist C, Lee M, Lee D, Coria F, Chang L, Miller B, Lieberburg I & et al. (1995). Elevation of microtubule-associated protein tau in the cerebrospinal fluid of patients with Alzheimer's disease. *Neurology* **45**, 788-793.
- Vinters HV. (1987). Cerebral amyloid angiopathy. A critical review. *Stroke* **18**, 311-324.
- von Bernhardi R, Tichauer JE & Eugenin J. (2009). Aging-dependent changes of microglial cells and their relevance for neurodegenerative disorders. *J Neurochem* **112**, 1099-1114.

- Wadghiri YZ, Sigurdsson EM, Sadowski M, Elliott JI, Li Y, Scholtzova H, Tang CY, Aguinaldo G, Pappolla M, Duff K, Wisniewski T & Turnbull DH. (2003). Detection of Alzheimer's amyloid in transgenic mice using magnetic resonance microimaging. *Magn Reson Med* **50**, 293-302.
- Walker DG, Dalsing-Hernandez JE, Campbell NA & Lue LF. (2009). Decreased expression of CD200 and CD200 receptor in Alzheimer's disease: a potential mechanism leading to chronic inflammation. *Exp Neurol* **215**, 5-19.
- Wang J, Dickson DW, Trojanowski JQ & Lee VM. (1999). The levels of soluble versus insoluble brain Abeta distinguish Alzheimer's disease from normal and pathologic aging. *Exp Neurol* **158**, 328-337.
- Wang XJ, Ye M, Zhang YH & Chen SD. (2007). CD200-CD200R regulation of microglia activation in the pathogenesis of Parkinson's disease. *J Neuroimmune Pharmacol* **2**, 259-264.
- Warakulle DR & Anslow P. (2003). Differential diagnosis of intracranial lesions with high signal on T1 or low signal on T2-weighted MRI. *Clin Radiol* **58**, 922-933.
- Weinstein JR, Koerner IP & Moller T. (2010). Microglia in ischemic brain injury. *Future Neurol* **5**, 227-246.
- Weishaupt D, Kochli VD & Marincek B. (2008). *How Does MRI Work?* Springer.
- Weiss N, Miller F, Cazaubon S & Couraud PO. (2009). The blood-brain barrier in brain homeostasis and neurological diseases. *Biochim Biophys Acta* **1788**, 842-857.
- Weisskoff R & Rosen BR. (1995). Functional magnetic resonance imaging. *Acad Radiol* **2 Suppl 2**, S133-135.

- Wekerle H, Sun D, Oropeza-Wekerle RL & Meyermann R. (1987). Immune reactivity in the nervous system: modulation of T-lymphocyte activation by glial cells. *J Exp Biol* **132**, 43-57.
- Weksler BB, Subileau EA, Perriere N, Charneau P, Holloway K, Leveque M, Tricoire-Leignel H, Nicotra A, Bourdoulous S, Turowski P, Male DK, Roux F, Greenwood J, Romero IA & Couraud PO. (2005). Blood-brain barrier-specific properties of a human adult brain endothelial cell line. *FASEB J* **19**, 1872-1874.
- Westergaard E. (1977). The blood-brain barrier to horseradish peroxidase under normal and experimental conditions. *Acta Neuropathol* **39**, 181-187.
- Wiert M, Davoust N, Pialat JB, Desestret V, Moucharrafié S, Cho TH, Mutin M, Langlois JB, Beuf O, Honnorat J, Nighoghossian N & Berthezene Y. (2007). MRI monitoring of neuroinflammation in mouse focal ischemia. *Stroke* **38**, 131-137.
- Williams K, Ulvestad E & Antel J. (1994). Immune regulatory and effector properties of human adult microglia studies in vitro and in situ. *Adv Neuroimmunol* **4**, 273-281.
- Williams RW. (2000). Mapping genes that modulate mouse brain development: a quantitative genetic approach. *Results Probl Cell Differ* **30**, 21-49.
- Wirhth O, Multhaup G, Czech C, Blanchard V, Moussaoui S, Tremp G, Pradier L, Beyreuther K & Bayer TA. (2001). Intraneuronal Abeta accumulation precedes plaque formation in beta-amyloid precursor protein and presenilin-1 double-transgenic mice. *Neurosci Lett* **306**, 116-120.
- Wolburg H & Lippoldt A. (2002). Tight junctions of the blood-brain barrier: development, composition and regulation. *Vascul Pharmacol* **38**, 323-337.

- Wright GJ, Cherwinski H, Foster-Cuevas M, Brooke G, Puklavec MJ, Bigler M, Song Y, Jenmalm M, Gorman D, McClanahan T, Liu MR, Brown MH, Sedgwick JD, Phillips JH & Barclay AN. (2003). Characterization of the CD200 receptor family in mice and humans and their interactions with CD200. *J Immunol* **171**, 3034-3046.
- Wright GJ, Jones M, Puklavec MJ, Brown MH & Barclay AN. (2001). The unusual distribution of the neuronal/lymphoid cell surface CD200 (OX2) glycoprotein is conserved in humans. *Immunology* **102**, 173-179.
- Wright GJ, Puklavec MJ, Willis AC, Hoek RM, Sedgwick JD, Brown MH & Barclay AN. (2000). Lymphoid/neuronal cell surface OX2 glycoprotein recognizes a novel receptor on macrophages implicated in the control of their function. *Immunity* **13**, 233-242.
- Wright SD, Ramos RA, Tobias PS, Ulevitch RJ & Mathison JC. (1990). CD14, a receptor for complexes of lipopolysaccharide (LPS) and LPS binding protein. *Science* **249**, 1431-1433.
- Xaio H, Banks WA, Niehoff ML & Morley JE. (2001). Effect of LPS on the permeability of the blood-brain barrier to insulin. *Brain Res* **896**, 36-42.
- Yamada M & Hatanaka H. (1994). Interleukin-6 protects cultured rat hippocampal neurons against glutamate-induced cell death. *Brain Res* **643**, 173-180.
- Yan P, Bero AW, Cirrito JR, Xiao Q, Hu X, Wang Y, Gonzales E, Holtzman DM & Lee JM. (2009). Characterizing the appearance and growth of amyloid plaques in APP/PS1 mice. *J Neurosci* **29**, 10706-10714.
- Yang J, Wadghiri YZ, Hoang DM, Tsui W, Sun Y, Chung E, Li Y, Wang A, de Leon M & Wisniewski T. (2011). Detection of amyloid plaques targeted by USPIO-Abeta1-42 in Alzheimer's disease transgenic mice using magnetic resonance microimaging. *Neuroimage* **55**, 1600-1609.

- Ye P, Wang ZJ, Zhang XJ & Zhao YL. (2005). Age-related decrease in expression of peroxisome proliferator-activated receptor alpha and its effects on development of dyslipidemia. *Chin Med J (Engl)* **118**, 1093-1098.
- Yoshida T, Tanaka M, Sotomatsu A & Hirai S. (1995). Activated microglia cause superoxide-mediated release of iron from ferritin. *Neurosci Lett* **190**, 21-24.
- Zecca L, Youdim MB, Riederer P, Connor JR & Crichton RR. (2004). Iron, brain ageing and neurodegenerative disorders. *Nat Rev Neurosci* **5**, 863-873.
- Zhang S, Cherwinski H, Sedgwick JD & Phillips JH. (2004). Molecular mechanisms of CD200 inhibition of mast cell activation. *J Immunol* **173**, 6786-6793.
- Zhang Y, Brady M & Smith S. (2001). Segmentation of brain MR images through a hidden Markov random field model and the expectation-maximization algorithm. *IEEE Trans Med Imaging* **20**, 45-57.
- Zhou H, Andonegui G, Wong CH & Kubes P. (2009). Role of endothelial TLR4 for neutrophil recruitment into central nervous system microvessels in systemic inflammation. *J Immunol* **183**, 5244-5250.
- Zhou X, Gao XP, Fan J, Liu Q, Anwar KN, Frey RS & Malik AB. (2005). LPS activation of Toll-like receptor 4 signals CD11b/CD18 expression in neutrophils. *Am J Physiol Lung Cell Mol Physiol* **288**, L655-662.
- Zlokovic BV. (2004). Clearing amyloid through the blood-brain barrier. *J Neurochem* **89**, 807-811.
- Zlokovic BV. (2008). The blood-brain barrier in health and chronic neurodegenerative disorders. *Neuron* **57**, 178-201.

Appendix

Appendix I: Animal Weights

(g)	Species	
	WT	CD200 ^{-/-}
4 months	20.75 ± 0.36	25.37 ± 1.32
9 months	31.50 ± 1.57	28.40 ± 1.03
13 months	34.38 ± 1.47	31.30 ± 0.93
17 months	33.28 ± 1.75	30.00 ± 2.09

Table 7.1 Average weights of WT and CD200^{-/-} mice throughout longitudinal study. Values are expressed as means ± SEM.

(g)	Species	
	WT	APP/PS1
Control	37.29 ± 3.29	46.50 ± 3.79
siRNA	42.00 ± 2.58	43.60 ± 4.78

Table 7.2 Average WT and APP/PS1 weights in siRNA study. Values are expressed as means ± SEM.

Appendix II: Mean Data

ms	Mouse Treatments			
	C57 Control	C57 + LPS (50µg)	CD200 ^{-/-} Control	CD200 ^{-/-} + LPS (50µg)
Whole Cortex	1663±17.3	1655±14.16	1758±18.9	1710±20.48
Motor Cortex	1665±29.6	1645±21.08	1827±26.6	1701±14.47
Entorhinal	1611±14.9	1680±19.22	1735±17.6	1734±28.12
Hippocampus	1633±16.7	1617±30.01	1673±15.1	1660±21.00
Thalamus	1346±15.5	1400±13.35	1395±16.1	1413±17.90
C. Callosum	1508±36.2	1454±17.65	1561±33.5	1539±14.34

Table 7.3 Average T₁ relaxation times from control- and LPS-treated WT and CD200^{-/-} mice 2.5 hours after treatment. Values are expressed as means ± SEM.

ms	Mouse Treatments			
	C57 Control	C57 + LPS (50µg)	CD200 ^{-/-} Control	CD200 ^{-/-} + LPS (50µg)
Whole Cortex	1576±23.9	1671±25.67	1633±13.0	1707±19.96
Motor Cortex	1588±18.0	1671±25.05	1654±14.7	1711±24.81
Entorhinal	1521±25.7	1690±29.52	1592±17.9	1744±22.80
Hippocampus	1593±14.1	1671±19.32	1622±13.2	1793±18.34
Thalamus	1367±14.2	1427±20.32	1337±25.9	1416±25.51
C. Callosum	1472±27.40	1483±20.06	1500±9.32	1556±16.82

Table 7.4 Average T₁ relaxation times from control- and LPS-treated WT and CD200^{-/-} mice 3.5 hours after treatment. Values are expressed as means ± SEM.

Appendix II: Mean Data

ms	Mouse Treatments			
	C57 Control	C57 + LPS (50µg)	CD200 ^{-/-} Control	CD200 ^{-/-} + LPS (50µg)
Whole Cortex	49.93±0.2	50.02±0.24	50.67±0.19	50.84±0.16
Motor Cortex	51.72±0.3	48.54±0.36	52.47±0.31	49.72±0.26
Entorhinal	49.37±0.1	52.22±0.19	50.10±0.22	53.14 ± 0.19
Hippocampus	50.29±0.2	49.93±0.30	50.04±0.18	50.48±0.26
Thalamus	43.57±0.1	44.25±0.14	43.50±0.17	44.44±0.12
C. Callosum	44.77±0.4	41.36±0.29	44.73±0.37	44.96±0.57

Table 7.5 Average T₂ relaxation times from control- and LPS-treated WT and CD200^{-/-} mice. 2.5 hours after treatment. Values are expressed as means ± SEM.

ms	Mouse Treatments			
	C57 Control	C57 + LPS (50µg)	CD200 ^{-/-} Control	CD200 ^{-/-} + LPS (50µg)
Whole Cortex	49.78±0.21	50.58±0.36	50.31±0.21	51.47±0.19
Motor Cortex	51.41±0.23	49.02±0.47	51.03±0.31	50.10±0.32
Entorhinal	49.31±0.1	52.56±0.28	49.32±0.18	53.38±0.17
Hippocampus	50.42±0.16	50.35±0.47	49.82±0.24	50.95±0.27
Thalamus	44.50±0.19	44.48±0.24	43.97±0.19	44.75±0.18
C. Callosum	44.46±0.31	41.63±0.47	44.57±0.28	45.72±0.61

Table 7.6 Average T₂ relaxation times from control- and LPS-treated WT and CD200^{-/-} mice. 3.5 hours after treatment. Values are expressed as means ± SEM.

Appendix III: Mean Data

RQ		Mouse Treatments			
		C57 Control	C57 + LPS	CD200 ^{-/-} Control	CD200 ^{-/-} + LPS
Left	Motor Cortex	1.007 ± 0.01	1.063 ± 0.01	1.055 ± 0.01	1.081 ± 0.01
	Somatosensory	0.99 ± 0.005	1.04 ± 0.005	1.06 ± 0.007	1.08 ± 0.005
	Entorhinal	0.99 ± 0.006	1.05 ± 0.009	1.06 ± 0.005	1.08 ± 0.004
	Dentate Gyrus	1.00 ± 0.001	1.06 ± 0.006	1.05 ± 0.005	1.08 ± 0.07
	Thalamus	0.99 ± 0.006	1.02 ± 0.009	1.04 ± 0.002	1.04 ± 0.01
	Frontal Cortex	1.01 ± 0.003	1.03 ± 0.004	1.04 ± 0.01	1.04 ± 0.01
	Cerebellum	1.00 ± 0.005	1.01 ± 0.01	1.03 ± 0.01	1.03 ± 0.02
Right	Motor Cortex	1.01 ± 0.01	1.06 ± 0.01	1.05 ± 0.01	1.08 ± 0.01
	Somatosensory	1.00 ± 0.01	1.05 ± 0.01	1.04 ± 0.01	1.09 ± 0.01
	Entorhinal	0.99 ± 0.01	1.05 ± 0.01	1.05 ± 0.01	1.08 ± 0.01
	Dentate Gyrus	1.01 ± 0.01	1.06 ± 0.01	1.05 ± 0.01	1.08 ± 0.01
	Thalamus	0.98 ± 0.01	1.01 ± 0.01	1.03 ± 0.01	1.04 ± 0.01
	Frontal Cortex	1.01 ± 0.01	1.02 ± 0.01	1.03 ± 0.01	1.05 ± 0.01
	Cerebellum	1.01 ± 0.01	1.02 ± 0.01	1.05 ± 0.01	1.05 ± 0.02

Table 7.7 Average SI values post-gadolinium injection in control- and LPS-treated WT and CD200^{-/-} mice. Values are expressed as means ± SEM.

Appendix III: Mean Data

RQ		Mouse Treatments			
		WT Control	WT + siRNA	APP/PS1 Control	APP/PS1 + siRNA
Left	Motor Cortex	0.99 ± 0.01	1.03 ± 0.01	1.01 ± 0.01	1.04 ± 0.01
	Somatosensory	0.99 ± 0.01	1.03 ± 0.01	1.01 ± 0.005	1.04 ± 0.004
	Entorhinal	0.96 ± 0.01	1.01 ± 0.005	0.99 ± 0.008	1.04 ± 0.007
	Dentate Gyrus	1.02 ± 0.01	1.04 ± 0.006	1.04 ± 0.06	1.03 ± 0.007
	Thalamus	1.01 ± 0.01	1.05 ± 0.01	1.02 ± 0.01	1.06 ± 0.008
	Frontal Cortex	0.97 ± 0.009	1.03 ± 0.005	1.03 ± 0.005	1.03 ± 0.01
	Cerebellum	0.98 ± 0.01	1.04 ± 0.01	1.01 ± 0.01	1.06 ± 0.01
Right	Motor Cortex	0.98 ± 0.01	1.02 ± 0.01	1.02 ± 0.004	1.05 ± 0.01
	Somatosensory	0.97 ± 0.01	1.02 ± 0.009	1.01 ± 0.005	1.03 ± 0.004
	Entorhinal	0.97 ± 0.01	1.01 ± 0.006	1.01 ± 0.006	1.03 ± 0.004
	Dentate Gyrus	1.01 ± 0.009	1.03 ± 0.009	1.03 ± 0.01	1.02 ± 0.005
	Thalamus	0.99 ± 0.01	1.01 ± 0.01	1.003 ± 0.01	1.03 ± 0.007
	Frontal Cortex	1.002 ± 0.01	1.03 ± 0.01	1.005 ± 0.01	1.03 ± 0.006
	Cerebellum	0.97 ± 0.01	1.03 ± 0.01	1.01 ± 0.01	1.04 ± 0.01

Table 7.8 Average SI values post-gadolinium injection in control- and siRNA-treated WT and APP/PS1^{-/-} mice. Values are expressed as means ± SEM.

Appendix IV: Company Addresses

Abbott, UK

Abbott Laboratories Ltd
Abbott House
Vanwall Business Park
Vanwall Road
Maidenhead SL6 4XE

Bruker, Germany

Bruker BioSpin GmbH
Silberstreifen 4
76287 Rheinstetten

Sigma-aldrich, UK

Sigma-Aldrich Company Ltd.
The Old Brickyard
New Road
Gillingham
Dorset
SP8 4XT

Merck, US

Merck Corporate Headquarters,
One Merck Drive,
P.O. Box 100
Whitehouse Station, NJ 08889-0100 USA

Bayer, Ireland

The Atrium
Blackthorn Road
Dublin 18

Alexis Biochemicals, Switzerland/

Enzo Life Sciences (UK) LTD.
Palatine House
Matford Court
Exeter EX2 8NL
United Kingdom

VWR, UK

Hunter Boulevard
Magna Park
Lutterworth
Leicestershire LE17 4XN
England

S. A. Instruments, USA

SA Instruments, Inc.
65 Main Street
Stony Brook, NY 11790